CROSSHOLE ELECTRICAL IMAGING OF AQUIFER PROPERTIES AND PREFERENTIAL FLOW PATHS AT THE BOLIVAR ASR SITE

A Ph.D. Thesis

by

Jingping Zhe

B.Sc (Jiaotong University, China), M.Sc (The Flinders University of SA, Australia)

Department of Geology and Geophysics
The University of Adelaide
SA 5005, Australia

Submitted in fulfillment of the requirements for
The degree of Doctor of Philosophy

April 2002

CONTENTS

ABSTRACT

This PhD project is a comprehensive application of crosshole resistivity tomography to image aquifer properties and preferential flow paths at the Bolivar ASR site, north of Adelaide. This site is being used to demonstrate the possibility of artificial recharge and recovery operations from a 50m thick aquifer, 100m below ground surface. The project involved consideration of hydrology, well logging, resistivity surveying, electrical modelling and inversion, data processing and interpretation, and, designing and building a 3-D physical resistivity modelling system.

I have derived all formulas for 3-D numerical resistivity modelling and developed a 3-D resistivity modelling program. I also modified 2.5-D numerical resistivity modelling and inversion programs for speeding the calculation, handling large size inversions and filtering out artefacts in the inversion results. These programs had very important roles in numerical resistivity modelling and inversion for interpretation of synthetic data as well as real field data.

The project has entailed significant experimentation and testing of numerical resistivity modelling and inversion to simulate the field surveys and some special model effects, such as the water effect in a crosshole survey and the possibility of inverting a vertical contact of two layers between two wells. These experiments are very helpful in interpreting the field surveys, especially for the Bolivar time-lapse crosshole resistivity surveys. These experiments also disclosed some very interesting features, such as turning points in an apparent resistivity profile and stacked profile patterns.

I built multi-electrode cables and collected lots of surface, surface-to-borehole, and borehole-to-borehole electrical survey data at the Bolivar Test Site as a part of the ASR trial project. Specifically, seven time-lapse crosshole resistivity surveys at different stages of fresh water injection partly reveal the injected water flow direction. I processed all survey data and interpreted them with the aid of the above numerical resistivity modelling and inversion experiments.

I designed a fully automatic 3-D physical resistivity modelling system with a large water tank. To obtain high efficiency for modelling, the system was designed to be fully automatic, which includes automatic positioning of electrodes, automatic current injection

(on and off) and automatic data logging. Unfortunately, I did not completely finish building the system due to the lack of technical support. The intention to complete it is a late (post-doctoral) project.

STATEMENT

This work contains no material which has been accepted for the award of any degree of diploma in any university or other tertiary institution and, to the best of my knowledge and belief, contains no material previously published or written by another person, except where due reference has been made in the text.

I give consent to this copy of my thesis, when deposited in the University Library, being available for loan and photocopying.

Jingping Zhe

April 09, 2002

Revised October, 2002

ACKNOWLEDGMENTS

This thesis would have been impossible without the help and support of my supervisor, Professor Stewart Greenhalgh, who has given me a lot of valuable suggestions, encouragement and financial support on my studies. He also spent a huge amount of time on correcting the text and the formulations of this thesis so as to reach its present state.

Particularly, I thank Dr. Peter Dillon and Mr Paul Pavelic for fruitful discussions and providing me with all sorts of the scientific monitoring data of the Bolivar ASR trial site.

I also greatly appreciate the following people: Dr. Bing Zhou and Dr. Deepak Raj for their wonderful support and advice during my PhD study.

Finally, I wish to thank my daughter, Sophia Zhe, for her help and support in completing the thesis.

Chapter 1

INTRODUCTION

1.1 BASIC PRINCIPLE OF THE RESISTIVITY METHOD

The resistivity method is one of the principal electrical methods used in geophysical exploration (Keller & Frischknecht, 1966; Kunetz, 1966; Bhattacharya and Patra, 1968; Mooney, 1980; Telford et al., 1990). It uses an artificial DC power source to create an electric field in the subsurface by injecting electricity into the ground between two current electrodes. By measuring and analysing the potential (voltage) response on the ground surface or underground, one can obtain a resistivity distribution map of the subsurface. This map is then used with other information to help identify and delineate geological structures.

The electrical resistivity method is based on the fact that resistivities of Earth materials vary widely. By finding the resistivity distribution, one can detect or locate ore bodies, the water table, sand and gravel lenses, and other geologic features in the subsurface. In general, the resistivity of rocks is related to the amount of water and dissolved salts present. Dense rocks with few voids, little moisture, and negligible amounts of dissolved salts (free ions) will have high resistivity. Soft saturated clay will have a low resistivity, particularly if any decomposed organic matter or soluble salts are present (Parkhomenko, 1967).

The resistivity of rocks varies over a very wide range of 12 orders of magnitude. It is dependent on a number of natural geological and hydrogeological factors: the mineralogical composition, porosity and degree of water saturation of the rocks, mineralisation of the water filling the pores, the structure and texture of the rocks, temperature and pressure.

In general, electric current is passed through the ground in three ways: electronic (movement of free electrons), electrolytic (movement of ions) and dielectric polarisation (Telford, 1990). The latter is an AC phenomena, and only ionic (electrolytic) conduction and electronic conduction are important in DC prospecting. So in the electric DC resistivity method, only the first two ways are considered.

Electronic conduction occurs in connection with metallic ore deposits and so this is an important mode of conduction in mineral exploration. The more metal contained in a rock, the greater the conductivity. But for most rocks, especially in hydrogeology, electrolytic conduction is the dominant mode of passing electricity through the ground.

With electrolytic conduction, the electric current is carried by the free ions present in the fluids (mainly water) of porous rocks. In most rock materials, the porosity and the chemical content of the water filling the pore spaces are more important in governing resistivity than the conductivity of the mineral grains of which the rock itself is composed. The salinity of the water in the pores is probably the most critical factor determining the resistivity (Dobrin, 1988). Normally, the greater the moisture content and the higher the salinity (dissolved chlorides and sulfates in the rocks), the higher the conductivity. Archie (1942) introduced the following formula relating rock resistivity to hydrologic parameters (Telford, 1990):

$$\rho_e = \frac{a\rho_w}{\phi^m S^n} \tag{1.1}$$

Here ϕ is the fractional pore volume (porosity), S is the fraction of the pores containing water (saturation), ρ_w is the resistivity of the pore water, $n \approx 2$, and a, m are constants in the range, $0.5 \le a \le 2.5$, $1.3 \le m \le 2.5$. From the formula, one can see that the resistivity of rocks is mainly affected by the resistivity of the contained water, the porosity and the degree of water saturation.

From the preceding discussion, it is clear that electrolytic conduction is very important in detecting underground water. This accounts for the popularity of the resistivity method in hydrologic studies. Also since temperature affects the movement of ions, the higher the temperature, the lower the viscosity and hence the ion mobility is increased. So an increase in temperature will cause an increase in conductivity.

1.2 APPLICATIONS OF THE RESISTIVITY METHOD TO HYDROGEOLOGY

The relative simplicity of the resistivity method, low equipment cost and the ease of use combine to make the method a useful prospecting technique in hydrologic engineering, mining exploration, and environmental and groundwater investigations. It has become a popular method in hydrological applications. In the past, the resistivity method has been used for locating groundwater (Yang et al., 1994; Sandberg, 1993; Meekes, 1993); detecting groundwater pollution and contamination (Urish, 1983; Osiensky, & Donaldson, 1995;

Ebraheen et al., 1997; Buselli, and Lu, 2000; Benson et al., 1997; Slater et al., 1997a; Kemna and Binley, 1996); measuring groundwater flow directions (White, 1994; Sill, and Sjostrom, 1990; Odins et al., 1985; Slater et al., 1997b; Binley et al., 1996; Ramirez et al., 1996); estimating hydraulic parameters of aquifers (de Lima, & Niwas, 2000; Yang, and Lee, 1998; Barker, 1990; Dasey, & Acworth, 2000); detecting seepage paths in earth dams (Pantholu et al., 2001; Binley et al., 1997); finding out soil characterisations (McCartre, & Desmazer, 1997; West et al., 1997; Stewart et al., 1997); and assorted engineering investigations (Barker, 1988).

In the following chapters, I will be describing crosshole resistivity tomography for imaging aquifer properties and detecting the water flow directions for a local ASR (Aquifer Storage and Recovery) trial by means of the time-lapse resistivity experiments.

In recent years, the resistivity tomography technique has been used to routinely produce 2-D resistivity images from surface survey data (Hauck, and Vonder Muhll, 1999; Shima, and Saito, 1988). However it has not been used very often for crosshole resistivity surveys. There is still no standard crosshole survey configuration. Some researchers (Zhou, and Greenhalgh, 2000; Yi et al., 1997; Spies, and Ellis, 1995; LaBrecque et al., 1996) have done some basic research in the area. Zhou (2000) shows the different effects from the different crosshole electrode configurations with 2.5D numerical resistivity modelling and inversion programs. Yi (1997) analysed the borehole effect in imaging the borehole resistivity survey data. Spies and Ellis (1995) gave a real data example of the crosshole resistivity tomography technique. LaBrecque et al., (1996) analysed the noise effect on Occam's inversion of resistivity tomography data.

The basic principle of detecting the water flow direction with the resistivity method is that the resistivity distribution in an area is changed when the water passes through it. This idea has been applied to detect leakage of liquids, such as water leakage in dams and leakage from waste ponds. White (1994) used the resistivity method to measure ground water flow direction and velocity. Frangos (1994) found leaks in lined waste ponds with the electrical resistivity method. Greenhalgh et al. (2001) applied cross-hole electric imaging for monitoring aquifer artificial recharge.

1.3 AQUIFER STORAGE AND RECOVERY

Aquifer storage and recovery (ASR), which is a form of artificial recharge of groundwater that makes use of a single well to inject and recover water, was the motivation for the present study. A common way to store water is to build a dam on the Earth's surface. However this is expensive and suffers from the added problem of significant evaporation in hot climates like South Australia. Storing water underground in an aquifer and recovering it later was first raised by Pyne (1995). This technique has the potential to substantially reduce the cost for storing water in comparison to the construction and maintenance of above-ground storage facilities. However it is still in the experimental stage. ASR is especially useful in regions where there is a seasonal shortfall between water availability and supply.

An ASR research project commenced in July 1997 at the Bolivar site on the Northern Adelaide Plains in South Australia. This trial was undertaken to help develop and demonstrate the ASR technique. The intention was to examine the feasibility of injecting the winter excess of reclaimed water into the aquifers beneath the North Adelaide Plains and recover the water in summer for use in irrigating the crops grown in the Virginia Horticultural area to the immediate north. A parallel aim was to examine the quality change of the injected water and its effect on the present water resources.

1.4 SURFACE AND CROSSHOLE RESISTIVITY METHODS

The surface resistivity method is a popular and mature geophysical method in mineral exploration, hydrology and environment application (Pritchard, and Renick, 1981). It has many different survey configurations (eg. Wenner, Schlumberger and dipole-dipole) for vertical sounding and lateral profiling (Telford et al., 1990). Modern systems use automatic electronic techniques to operate resistivity acquisition equipment. Multi-electrode arrays for efficient data acquisition have been built and are being gradually used. This greatly increases the field survey coverage and makes 3-D surface resistivity surveys easier. With the help of the resistivity pseudosection (Ritz et al., 1999; Roy, 1978), it is easy to display and graph surface survey data. With the development of resistivity modelling and inversion techniques (Loke and Barker, 1996; Sasaki, 1994; Smith and Vozoff, 1984), the direct interpretation of the surface resistivity survey data is possible. So the surface resistivity method is widely used today.

As with all other surface geophysical methods, the surface resistivity method suffers from decreasing detectability and resolution with increasing depth because the injected current can

only penetrate into the subsurface to a very limited extent. Furthermore, problems of suppression and equivalence mean that the target must get progressively larger with depth (Kunetz, 1966; Keller and Frischknecht, 1966). So crosshole resistivity tomography has to be used to obtain reliable resistivity information at depth. The Bureau de Recherches Geologiques et Minieres (BRGM) (Lesur et al., 1999) introduced a crosshole resistivity technique twelve years ago. The first problem for crosshole resistivity surveys is how to display the survey data. Unlike the resistivity surface survey situation, the pseudosection can not be produced for crosshole resistivity data. So the interpretation of the crosshole survey data becomes problematic. In fact, this fact prevented crosshole resistivity surveying being readily adopted, prior to the advent of 2-D resistivity inversion. Nowadays, the resistivity inversion technique can convert the crosshole survey data into a resistivity distribution map and greatly helps the interpretation of the crosshole electric survey. So the crosshole resistivity method is becoming more popular.

Slater et al. (1996) used the crosshole electric inversion method to determinate hydraulically conductive pathways in fractured limestone. Slater et al. (2000), in a later paper, completed a physical resistivity modelling experiment with a large tank facility (10x10x3m). They used the 2-D crosshole electric inversion method to monitor a controlled saline tracer injection in a layered model with a dipole-dipole configuration in four boreholes. They put two current electrodes in one borehole and two potential electrodes in the other borehole. Such a configuration is not very sensitive in practical surveying (Zhou,1998). Spies and Robert (1995) sucessifully employed 3-D DC crosshole resistivity tomography method to monitor the melting and solidification processes of an in-situ vitrification experiment with six boreholes augered on the circumference of a circle of radius approximately 6.5m from the centre. The resistivity contrast in the experiment was very high, over 1000 times. Middleton and Binley (2001) employed a 3-D cross-borehole electric resistivity tomography imaging to detect the characterisation of unsaturated zone recharge mechanisms. Binley et al. (2001a and 2001b) used crosshole radar and resistivity tomography to observe seasonal dynamics in the vadose zone and to determinate hydraulic parameterisation. Daily and Ramirez (1995) used 2-D crosshole electrical resistivity tomography to monitor in-situ remediation processes for removal of volatile organic compounds from subsurface water and soil. Five boreholes were used for this experiment. The distances between the boreholes were less than 20m and the accessable range in each borehole was 61m. In addition, they used four electrodes on the surface. Air sparging and water infiltration both changed the subsurface resistivity sufficiently to be imaged by electrical resistivity tomography. However, all of the above

time-lapse experiments and surveys were completed in a relatively short time, a few days or weeks. So they were not affected adversely by background environment changes.

For monitoring the water flow direction in the Bolivar ARS Trial, we had to use the crosshole resistivity method since the T2 aquifer is too deep (100m below surface) for use of the surface resistivity method. Specifically, the bipole-bipole configuration (all four electrodes are in the boreholes) had to be used in order to reduce the effect of the top layers in time-lapse surveys. In total, seven time-lapse crosshole surveys were conducted and a lot of resistivity modelling and inversions were done in order to find the water flow direction at the Bolivar ASR Trial.

Detecting the injected water flow direction in an aquifer is harder than finding seepage paths in earth dams or measuring groundwater flow directions due to the different resistivity contrasts present in each situation. Before the fresh water is injected into an aquifer, the aquifer is already full of underground water. The injected water, having a different resistivity, may change the resistivity distribution in the aquifer, but it can not make a large contrast interface in the aquifer unless water with a much higher or lower resistivity is injected. In other words, the resistivity contrast between the injected water and the underground water in an aquifer is relatively small, but the resistivity contrast between leaking liquids and the background rocks is normally quite large.

1.5 RESISTIVITY MODELLING AND INVERSION

Numerical modelling of the electrical resistivity response of the Earth has been widely used in the exploration industry because it aids the interpretation of such data in terms of more realistic geologic structures (Hobbs, 1992; Spitzer, and Kumpel, 1997; Lesur, 1999). Lesur (1999) systematically describes the forward problem of 2-D and 3-D electric tomography and Spitzer and Kumpel (1997) used 3D FD resistivity modelling to simulate the effect of a highly resistive phonolitic body.

Compared with 2D resistivity modelling, 2.5D and 3D numerical modelling are especially useful for practical interpretation since the calculated potential values can be compared with real survey data directly. Such modelling uses the point source assumption instead of the implicit line source in 2D modelling (Mufti, 1976; Dey and Morrison 1979a; Zhou, 1998). Therefore 2.5-D and 3-D resistivity inversion based on the 2.5-D and 3-D forward modelling will be much more accurate than 2-D resistivity inversion which is based on a line source

assumption (Zhou, 1998). So development of 2.5D and 3D resistivity modelling techniques is very important.

Inversion is a critical tool in the interpretation of the resistivity survey data since it can convert resistivity survey data into an understandable resistivity distribution map and greatly helps field survey data interpretation. So a lot of research has been done in this area. Worthington (1984) presented a basic introduction to geophysical tomography and considered matrix inversion, Fourier transform, convolutional, and algebraic reconstruction methods. Sasaki (1994) introduced a 3-D resistivity inversion by using the finite element method. Zhou and Greenhalgh (1998 and 1999) developed a new method to calculate the Frechet and second derivatives in 2.5-D Helmholtz equation inversion and devised a 2.5-D resistivity inversion program. Lesur (1999) systematically describes the inverse problem of 2-D and 3-D electric tomography. Zimmer (1999) tried to find water saturated fractures with the resistivity inversion method.

1.6 RESISTIVITY PHYSICAL MODELLING

Resistivity physical small scale modelling in the laboratory is not popularly used today, despite being a very useful tool in interpretation of field survey data, since it can provide real voltage responses for various 3-D models. Apparao (1979) conducted model tank experiments on resolution of resistivity anomalies using metal sheets in water to simulate conductive dykes or ore bodies. Joshi (1984) did research on the scale factor in 3-D physical modelling with a thin vertical conductor below a conductive overburden layer. Other references are given in Section 5.1.

Physical resistivity modelling is usually done in a water tank or bath. Water or sand with different levels of salt provides the resistivity background of the host rock for modelling. Then some solid materials, such as rocks, metal, or wood, are used to simulate the anomalous field situation. The four electrodes are used to simulate the field survey. Then the potential measurements are compared with the field measurements to help interpret the field data.
3-D physical modelling has played a very important role in exploration geophysics, especially at times and in those areas where resistivity numerical modelling and inversion techniques have not been maturely developed. For the resistivity method, 3-D numerical modelling and inversion are still limited to small mesh sizes due to the currently available computer capacity. So 3-D resistivity physical modelling is still very useful to obtain the responses of some special geological models.

1.7 OBJECTIVES OF THE THESIS

The primary objective of this thesis was to use the resistivity tomography technique to find the flow paths of the injected fresh water at the Bolivar ASR trial site. To achieve this goal, a lot of research had to be done. Firstly, various resistivity survey tests had to be designed and conducted to obtain basic resistivity information about the ASR test site. Secondly, numerous crosshole time-lapse resistivity experiments needed to be finished. Then, to interpret the survey data, numerical resistivity modelling and inversion programs were developed. A 3-D resistivity physical modelling system was also designed and partly finished. Next, a lot of numerical resistivity modelling and inversion experiments were conducted to support the interpretation of the survey data. Finally, the field crosshole time-lapse resistivity survey data had to be processed and interpreted.

1.8 THESIS OUTLINE

Chapter 1 provides an introduction to the principle of and the motivation for the present study. It includes a brief literature review, resistivity method, basic methodology and groundwater applications. The related research areas for this PhD project include crosshole resistivity surveys, survey data processing and interpretation, numerical resistivity forward modelling and inversion research on the method and experiments, and a 3-D automatic physical resistivity modelling system.

Chapter 2 reviews the basic mathematical theory of the resistivity method, and derives the equations and formulas, which are used in later chapters. It also provides a summary of the different surface and borehole survey configurations.

In Chapter 3, I discuss in detail 2.5-D and 3-D numerical resistivity forward modelling techniques and derive all formulas for computer implementation. Then a number of 2.5-D and 3-D models are studied to test the programs and provide some support information for the later interpretation of the survey data.

In Chapter 4, I review the 2.5-D resistivity inversion technique and derive all formulas for completing the inversion technique. This chapter also gives the theoretical derivation for the 3-D imaging method. Some experimental inversion results are presented from the modelled

data of Chapter 3, which are intended to provide insight into image resolution and simulate the Bolivar field situation.

Chapter 5 shows all design details of a 3-D automatic electric modelling laboratory system. The whole design was completed, but the construction is only partly finished due to a lack of time and technician support.

Chapters 6 and 7 provide background information on the Bolivar ASR trial site and other relevant hydrogeological information. The electrical field tests were conducted and the results were given for preliminary surface, surface-to-borehole and borehole-to-borehole resistivity surveys prior to water injection.

Chapters 8 and 9 examine all numerical resistivity modelling and inversion experiments we did for interpreting the survey data for the crosshole resistivity experiments using both the chord and radial configurations in the water injection period. Each chapter deals with a different set of experiments and evaluates either chord measurements (Chapter 8) or radial measurements (chapter 9) across the circular monitor boreholes centred on the injection well. The measurements were repeated at different stages of water injection to look for differences in resistivity values with time. The experimental results from these two chapters are very useful in interpreting the field data.

In Chapters 10 and 11, I interpret all survey data of the two main water injection periods and introduce a few new ways for analysing and interpreting the data. These chapters provide much field data and interpretation results.

The final chapter summarises the whole study and gives the main findings. The research offers some possible improvements in future resistivity surveying.

Chapter 2

BASIC THEORY OF THE RESISTIVITY METHOD

2.1 THE BASIC EQUATIONS OF THE DC ELECTRICAL RESISTIVITY METHOD

In the DC electrical resistivity method, we assume that the underground electric field is static and the electric current flows steadily. According to the Continuity Law (Moon & Spencer, 1965), we have the following equation:

$$\oint_S \vec{j} \cdot d\Gamma = \begin{cases} -I, & (inside \quad S) \\ 0, & (outside \quad S). \end{cases} \tag{2.1}$$

where $\vec{j}$ is the current density, S is an arbitrary closed surface surrounding the current electrode in the region Ω, and I is the injected current magnitude through S (refer to Fig. 2.1).

According to Ohm's law, we have

$$\vec{j} = \sigma \mathbf{E}, \tag{2.2}$$

where σ is the conductivity of the medium (=1/ρ, ρ=resistivitity, Ω.m) and $\mathbf{E}$ is the electric field in volts per meter. Since the electric field $\mathbf{E}$ is the gradient of a scalar potential U, that is

$$\mathbf{E} = -\nabla U, \tag{2.3}$$

where ∇ is the 3-D gradient operator, we have

$$\vec{j} = -\sigma \nabla U. \tag{2.4}$$

According to Gauss' integral theorem, equation (2.4) is equivalent to

$$\nabla \cdot (\sigma \nabla U) = -I\delta(r - r_c) \qquad r, r_c \in \Omega \tag{2.5}$$

where $\vec{r}_c = (x_c, y_c, z_c)$ is the location of the current electrode in Ω. Equation (2.5) is the basic equation for the DC resistivity method. Most numerical DC resistivity modelling and inversions are based on this equation.

If the conductivity σ is constant in the region Ω, Equation (2.5) becomes

$$\sigma \nabla^2 U = -I\delta(r - r_c) \qquad r, r_c \in \Omega \tag{2.6}$$

This is the governing equation for uniform media, or at least media made up of sub-volumes in which the resistivity is constant (a different constant in each sub-volume).

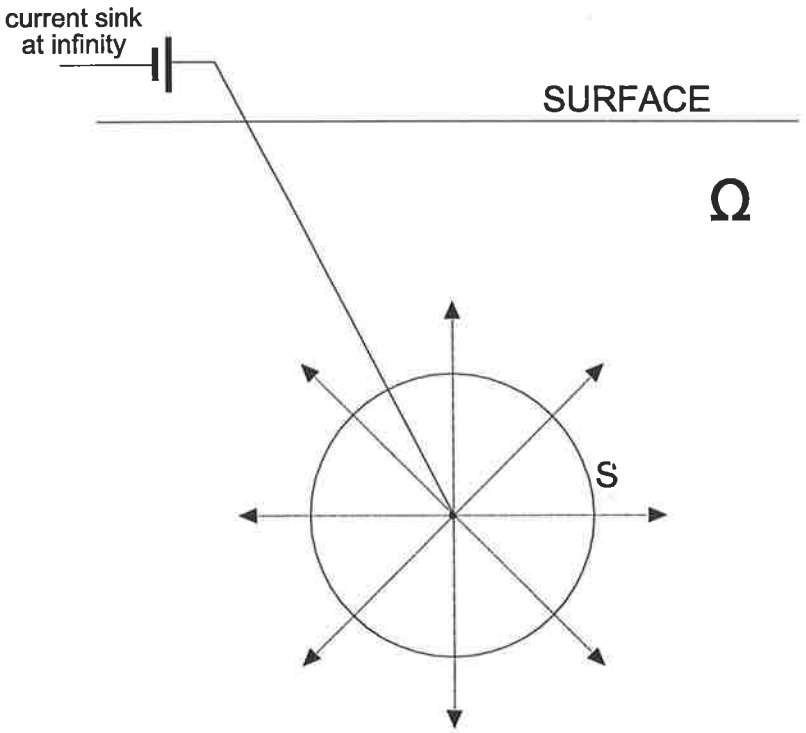

Figure 2.1 Diagram showing position relationship for injecting current into the ground.

2.2 THE FORMULAS FOR CALCULATING THE APPARENT RESISTIVITY AND THE GEOMETRIC FACTOR

In a uniform medium, equation (2.6) has a solution:

$$U(r_c, r) = \frac{I}{4\pi\sigma|r - r_c|} . \tag{2.7}$$

This formula can be used to calculate the potential distribution U with a single current electrode inside the rock volume.

The above solution ignores the boundary reflection effect of the Earth's surface, i.e. the image source, which is "reflected" in the free surface and located an equal distance away on the far side of the boundary. This is analogous to an optical image in a mirror. When the current source moves toward the Earth's surface, the boundary reflection effect of the Earth's surface will become stronger. In the extreme case in which the current electrode is moved to the Earth's surface, the current source overlays with the image current source on the surface. Equation (2.7) then becomes

$$U(r_c, r) = \frac{I}{2\pi\sigma \mid r - r_c \mid} \tag{2.8}$$

In practical situations, a pair of current electrodes has to be used to produce an underground electric field. One electrode injects current into ground and the other works as the current sink. They produce two additive voltages in the ground, expressed as follows (if both current electrodes are on the surface):

$$U_A(r_A, r) = \frac{I}{2\pi\sigma \mid r - r_A \mid} \tag{2.9}$$

$$U_B(r_B, r) = \frac{-I}{2\pi\sigma \mid r - r_B \mid} \tag{2.10}$$

where r_A and r_B are the positions of two current electrodes respectively (r_A is the source location and r_B is the sink location). Then by superposition, the combined voltage distribution should be:

$$U\ (r_A, r_B, r) = U_A(r_A, r) + U_B(r_B, r) = \frac{I}{2\pi\sigma}\ (\frac{1}{D_A} - \frac{1}{D_B}) \tag{2.11}$$

where $D_A = |r - r_A|$ and $D_B = |r - r_B|$.

Therefore the potential difference (observed voltage drop) between any two points M and N is given by:

$$U_{MN}(r_A, r_B, r_M, r_N) = U_M(r_A, r_B, r_M) - U_N(r_A, r_B, r_N) = \frac{I}{2\pi\sigma}(\frac{1}{D_{AM}} - \frac{1}{D_{BM}} - \frac{1}{D_{AN}} + \frac{1}{D_{BN}}) \tag{2.12}$$

where r_A, r_B, r_M and r_N stand for the positions of the two current electrodes A and B, and the two potential electrodes M and N respectively; and D_{AM} , D_{BM} , D_{AN} and D_{BN} represent the distances between the two relative electrodes respectively, as indicated by the subscripts. Equation (2.12) is very useful to get the potential difference distribution for any electrode array on the Earth surface. We can change the above formula into the following forms:

$$\sigma = \frac{I}{2\pi\ U_{MN}(r_A, r_B, r_M, r_N)}(\frac{1}{D_{AM}} - \frac{1}{D_{BM}} - \frac{1}{D_{AN}} + \frac{1}{D_{BN}}) \tag{2.13}$$

or

$$\rho = [\frac{I}{2\pi U_{MN}(r_A, r_B, r_M, r_N)}(\frac{1}{D_{AM}} - \frac{1}{D_{BM}} - \frac{1}{D_{AN}} + \frac{1}{D_{BN}})]^{-1}. \quad (2.14)$$

These two formulas can be used to calculate the true conductivity or resistivity of a uniform medium, for example, the conductivity of water.

The second part of the formula (2.14), $(\frac{1}{D_{AM}} - \frac{1}{D_{BM}} - \frac{1}{D_{AN}} + \frac{1}{D_{BN}})$, is called the geometric factor, because it relates directly to the positions of the four electrodes. This factor is very important in numerical modelling, inversion and practical applications. By calculating the factor, one can easily remove the geometric effect (separation of electrodes) from the measured potential value U.

Keep in mind, the above formulas can only be used where both current electrodes are on the surface. If any one current electrode is in the subsurface, the image plane (Earth's surface) reflection should be considered.

For more complicated media (non-constant conductivity or resistivity), equation (2.5) has to be solved in conjunction with a boundary condition by some numerical method to obtain the electrical potential field (Dey and Morrison, 1979).

If the medium is not uniform, then equation (2.14) no longer strictly applies. However, in practice, the formula is still used to calculate the resistivity. But we do not call it the true resistivity, but rather the "apparent resistivity". Apparent resistivity is the combined effect of all the layer resistivities. It normalises the measured voltage for the current level and for the electrode geometry effect. It is not strictly an average value, but is sometimes treated as such. Variations in apparent resistivity indicate departures from a uniform Earth. Values of apparent resistivity often vary between the minimum and maximum true resistivity of the medium. If the medium is of constant resistivity, the calculated apparent resistivity should be equal to the true resistivity of the medium.

For borehole surveys, formula (2.14) is still valid except we must change the constant from 2π to 4π as follows, to account for the full space as opposed to the half space.

$$\rho = [\frac{I}{4\pi U_{MN}(r_A, r_B, r_M, r_N)}(\frac{1}{D_{AM}} - \frac{1}{D_{BM}} - \frac{1}{D_{AN}} + \frac{1}{D_{BN}})]^{-1} \quad (2.15)$$

If the current sources in the boreholes are not very deep, the Earth's surface boundary effect has to be considered. This means that we have to add an extra part into the above formula. So equation (2.15) becomes:

$$\rho = \{ \frac{I}{4\pi U_{MN}(r_A, r_B, r_M, r_N)} [(\frac{1}{D_{AM}} - \frac{1}{D_{BM}} - \frac{1}{D_{AN}} + \frac{1}{D_{BN}}) + (\frac{1}{D_{A'M}} - \frac{1}{D_{B'M}} - \frac{1}{D_{A'N}} + \frac{1}{D_{B'N}})] \}^{-1} \quad (2.15A)$$

where A' and B' stand for the image current source above the Earth's surface, and the D_{IJ} stands for the distance from current electrode I to potential electrode J. If the current electrodes and the potential electrodes are placed very deep in the boreholes, the term $(\frac{1}{D_{A'M}} - \frac{1}{D_{B'M}} - \frac{1}{D_{A'N}} + \frac{1}{D_{B'N}})$ will be close to zero, since $D_{A'M}$ will be close to $D_{A'N}$ and $D_{B'M}$ will be close to $D_{B'N}$. So equation (2.15) will be valid for this situation. Another extreme case is that where current electrodes are placed on the Earth's surface. The image current source should then be on the Earth's surface as well. So the term $(\frac{1}{D_{A'M}} - \frac{1}{D_{B'M}} - \frac{1}{D_{A'N}} + \frac{1}{D_{B'N}})$ is equal to the term $(\frac{1}{D_{AM}} - \frac{1}{D_{BM}} - \frac{1}{D_{AN}} + \frac{1}{D_{BN}})$ and equation (2.15A) reduces to (2.14). Therefore we can say that equation (2.15A) is a general equation for calculating apparent resistivity.

For borehole resistivity surveys, with different combinations of the current electrodes and the potential electrodes, there are four kinds of basic configuration and they are: pole-pole, bipole-pole, pole-bipole and bipole-bipole (Zhou and Greenhalgh, 2000). However, in practical situations, it is impossible to form an electrical current loop with a single current electrode or obtain the voltage from a single potential electrode. So in any real field resistivity survey, at least two current electrodes and two potential electrodes are used. So formula (2.15A) can always be used in all sorts of resistivity survey. To simulate pole-pole, bipole-pole or pole-bipole configurations, one has to put one current electrode or/and one potential electrode very far away from the survey area to simulate the infinite situation ie, to ignore the effects of the second current electrode and assume that the second potential electrode is at zero volts. For example, in the mise-a-la-masse configuration, one current electrode and one potential electrode are put far away from the other electrodes. So the formula to calculate the apparent resistivity for the mise-a-la-masse configuration will be (derived from equation (2.15A)):

$$\rho \approx [\frac{I}{4\pi U_{MN}(r_A, r_B, r_M, r_N)} ((\frac{1}{D_{AM}} - \frac{1}{D_{AN}}) + (\frac{1}{D_{A'M}} - \frac{1}{D_{A'N}}))]^{-1} \quad (2.16)$$

since D_{BM}, D_{BN}, $D_{B'M}$ and $D_{B'N}$ are 'infinite'. Because of the finite distances D_{BM} and D_{BN} in practical situations, the calculated apparent resistivity using formula (2.16) will contain some errors.

For surface-to-borehole resistivity surveys (if the current electrode A and the potential electrode M are on the Earth's surface, and the current electrode B and the potential electrode N are in the borehole), $D_{AM}=D_{A'M}$ and $D_{AN}=D_{A'N}$. Then formula (2.15A) reduces to

$$\rho = \{ \frac{I}{4\pi U_{MN}(r_A, r_B, r_M, r_N)} [(\frac{2}{D_{AM}} - \frac{2}{D_{BM}} - \frac{1}{D_{AN}} + \frac{1}{D_{BN}} - \frac{1}{D_{B'M}} + \frac{1}{D_{B'N}})] \}^{-1} \quad (2.16A)$$

2.3 2.5-D APPROXIMATION

From a methodology viewpoint, resistivity imaging is based on the solution of one kind of partial differential equation. The governing equation for the 3-D direct current (DC) electric potential is equation (2.5). The numerical solution of the equation is not very difficult and has been performed by several researchers (Lee, 1975; Daniels, 1977; Pridmore, 1981; Sasaki, 1994; Shima, 1992; Spitzer, 1995) with a limited grid mesh. However, the real applications of the numerical solution of the 3D equation in both modelling and inversion is still very limited due to the huge computational requirement, such as memory size, computing time, etc.

The 2-D (x-z plane) form of the equation (2.6) is:

$$\sigma \nabla^2 U(x,z) = -I\delta(r - r_c) \qquad r, r_c \in \Omega \quad . \quad (2.17)$$

It has been widely used in industry (Chunduru, 1996; Dey, 1979; Lee, 1975; Mufti, 1976; Mundry, 1984; Snyder, 1976) because of the lesser requirements for the computer memory and computer speed, subject to the assumption of a line source in the y direction for the 3D geometry. With this assumption, the 2D solution cannot match with the real potential values in practical surveys, and makes the inversion very difficult. But the shape of the calculated potential distribution from the 2D equation is basically correct, and can be used to verify the survey data.

The 2.5-D approximation for 3-D situations considers the source to be a point source (not a line source as in the 2-D situation) and the medium properties to be 2-D or non-changing in the strike (out-of-plane) or y-direction. According to the 2.5-D approximation, the current

electrode is restricted to a single point, and the conductivity σ model is considered to be 2-D, that is, the variation of the conductivity depends upon only the x- and z-coordinates: $\sigma = \sigma(x,z)$ in equation (2.5). To remove the second derivative of the y-coordinate from equation (2.5), we set the current source at $(x_c,0,z_c)$ and take the Fourier-cosine transform with respect to the y-coordinate, which transforms equation (2.5) into:

$$\nabla\cdot(\sigma\nabla\overline{U})-k_y^2\,\sigma\,\overline{U}=-\frac{I}{2}\delta(x-x_c)\delta(z-z_c) \tag{2.18}$$

where

$$\overline{U}(x,z,k_y)=\int_0^{\infty}U(x,y,z)\cos(k_y y)dy\ . \tag{2.19}$$

From equation (2.19), the spectrum $\overline{U}(x,\ z,\ k_y)$ is the wavenumber-domain form of the 3-D electric potential and is a real valued function. Equation (2.18) becomes the governing equation for the DC electric potential computation with the 2.5-D approximation.

Then the 3-D potential can be calculated by performing the pseudo 2-D or 2.5-D computations. The solution from the pseudo 2-D will match with the measured potential values of the real survey data. So, it is natural to treat the modeling or inversion with the 2.5-D approximation in the interpretation of the data. Nowadays, the 2.5-D approximation is widely accepted in DC resistivity modeling and inversion. To analyze crosshole data, the 2.5-D approximation is a reasonable compromise in terms of practical considerations.

2.4 DIFFERENT ELECTRODE ARRAYS IN SURFACE RESISTIVITY SURVEYING

The commonly used electrode arrays in the surface resistivity surveys are the Wenner array, Schlumberger array, pole-dipole array and dipole-dipole array (Telford et al., 1990).

In the Wenner Array (refer to Fig 2.2), we can use formula (2.14) to calculate the apparent resistivity as follows:

$$\sigma=\frac{I}{2\pi\,U_{MN}(r_A,r_B,r_M,r_N)}\left(\frac{1}{D_{AM}}-\frac{1}{D_{BM}}-\frac{1}{D_{AN}}+\frac{1}{D_{BN}}\right)=\frac{I}{2\pi\,aU_{MN}(r_A,r_B,r_M,r_N)} \tag{2.20}$$

or

$$\rho=1/\sigma=2\pi\,aU_{MN}(r_A,r_B,r_M,r_N)/I \tag{2.21}$$

where $D_{AM}=D_{BN}=a$ and $D_{BM}=D_{AN}=2a$.

This formula is the one normally used in Wenner surveying (Telford et al., 1990).

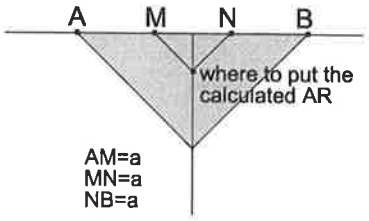

Figure 2.2 Wenner array. A and B are current electrodes, and M and N are potential electrodes.

However, what does this calculated apparent resistivity mean? As mentioned before, the calculated apparent resistivity mainly is a combined effect of the resistivities of the local area (shaded region) in the vicinity of the electrodes, as shown in Figure 2.2. As we know, the larger the distance between A and B, the deeper the current penetrates into the ground (Telford et al., 1990). So at large spacings the effect of deep layers will be added to the calculated apparent resistivity. Based on such considerations, the 2-D pseudosection was introduced. It is a way of assigning apparent resistivities for different electrode spacings to different depths and horizontal positions in the subsurface. Keep in mind that the calculated apparent resistivity in any position of a pseudosection does not mean the resistivity at that depth. It means the combined resistivity effect of the local subsurface, but influenced more or less by the region surrounding the assigned point, with the greatest influence at that point.

Similarly, we can obtain the following formula from equation (2.14) to calculate the apparent resistivity for the Schlumberger array (refer to Figure 2.3):

$$\sigma = \frac{I}{2\pi\, U_{MN}(r_A, r_B, r_M, r_N)\,|} K \tag{2.22}$$

or

$$\rho = 1/\sigma = 2\pi\, U_{MN}(r_A, r_B, r_M, r_N)/(KI) \tag{2.23}$$

where

$$K = \frac{1}{L-x-l} - \frac{1}{L+x+l} - \frac{1}{L-x+l} + \frac{1}{L+x-l}. \tag{2.24}$$

With the same principle as in the Wenner Array, one can produce a pseudosection to present all survey data in 2-D graph form.

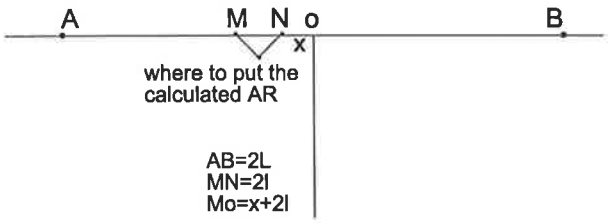

Figure 2.3 Schlumberger array. A and B are current electrodes and M and N are potential electrodes.

Finally for the double-dipole array (refer to Figure 2.4), we have

$$\rho = 1/\sigma = 2\pi\, U_{MN}(r_A, r_B, r_M, r_N)/(KI) \tag{2.25}$$

where

$$K = \frac{1}{2l}\left(\frac{2}{n} - \frac{1}{n+1} - \frac{1}{n-1}\right). \tag{2.26}$$

A pseudosection can be produced in a similar way, by drawing 45-degree lines from the centre of each dipole, and assigning the apparent resistivity to the intersecting point of the two lines. (Fig 2.4)

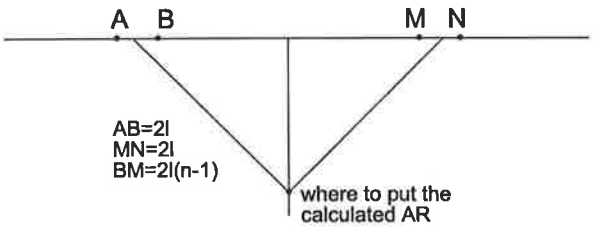

Figure 2.4 Double-dipole array. A and B are current electrodes, and M and N are potential electrodes.

2.5 DIFFERENT ELECTRODE ARRAYS IN BOREHOLE ELECTRIC RESISTIVITY SURVEYING

The borehole resistivity method has not been widely used in practice, mainly due to the lack of a proper way to display the survey data and the lack of a practical inversion technique. Mise-a-la-masse is not a true borehole resistivity method since only one current electrode is in the borehole and normally it is put in a position at the level of the conductive orebody (Telford et al, 1990). Similarly, it has the problem of displaying all the survey data in one 2-D graph, especially if the current electrode is moved to several different positions. For example, one is in the orebody, and the other is out of the orebody.

In borehole resistivity surveys, there are four basic configurations: pole-pole, bipole-pole, pole-bipole and bipole-bipole (Zhou and Greenhalgh, 2000). The same approach can be used to derive the formula to calculate the apparent resistivity. However we have to use equation (2.15A) for borehole resistivity surveys instead of equation (2.14), since both current electrodes are in the borehole and the current can spread into the full 3-D space and it is reflected from the Earth's surface. The derived formula for calculating apparent resistivity for each configuration with the consideration of the surface boundary reflection is as follows:

$$\rho = K\frac{\Delta U}{I} \tag{2.27}$$

where K is a geometry factor and it is calculated with the following formulas:

for pole-pole: $$K = 4\pi\left(\frac{1}{D_{AM}} + \frac{1}{D_{A'M}}\right)^{-1} \tag{2.28}$$

for pole-bipole: $$K = 4\pi\left(\frac{1}{D_{AM}} - \frac{1}{D_{AN}} + \frac{1}{D_{A'M}} - \frac{1}{D_{A'N}}\right)^{-1} \tag{2.29}$$

for bipole-pole: $$K = 4\pi\left(\frac{1}{D_{AM}} - \frac{1}{D_{BM}} + \frac{1}{D_{A'M}} - \frac{1}{D_{B'M}}\right)^{-1} \tag{2.30}$$

for bipole-bipole:

$$K = 4\pi\left(\frac{1}{D_{AM}} - \frac{1}{D_{BM}} - \frac{1}{D_{AN}} + \frac{1}{D_{BN}} + \frac{1}{D_{A'M}} - \frac{1}{D_{B'M}} - \frac{1}{D_{A'N}} + \frac{1}{D_{B'N}}\right)^{-1}. \tag{2.31}$$

Here A and B stand for the two current electrode positions, A' and B' are the image current electrode positions reflected from the surface, and M and N stands for the two potential electrode positions. So D_{IJ} means the distance from the current electrode I to the potential electrode J.

Once an apparent resistivity is calculated from a borehole survey, there is the problem of where to place or assign the value in the 2-D section, ie. how to construct the pseudosection is still a problem. For example, for a measured value in a bipole-bipole configuration, it mainly represents the combined effect of the resistivities in the area surrounded by and near the four electrodes. But where should we put the value in the 2-D section?

So far no one has suggested a satisfactory way to display crosshole survey data properly. In my opinion, the only effective way to use the crosshole data is by inversion.

The mise-a-la-masse (surface to borehole) array is another popular array used in resistivity surveying. However it is neither a surface survey nor a borehole survey, rather, it is a mixed or combination type of survey because it puts one current electrode in a borehole and puts one or

two potential electrodes on the surface. For each current electrode position in the borehole, one can obtain the potential distribution (for one potential electrode) or the potential difference distribution (for two potential electrodes) in the survey area. Such a technique has been used for correlating different parts of the mineralisation, isolating different ore lenses, and determining dip, pitch and extent as well as other geometrical parameters of an orebody (Daniel, 1977). However it is very hard to combine all sets of the data together and put them in one 2-D profile. This makes it hard to display and interpret mise-à-la-masse survey data. The best way to interpret such data is by 3-D modeling and inversion.

Chapter 3

2.5-D AND 3-D NUMERICAL RESISTIVITY FORWARD MODELLING

3.1 INTRODUCTION

Numerical modelling of the electrical resistivity response of the Earth has been widely used in the exploration industry because it aids the interpretation of such data in terms of more realistic geologic structures. Compared with 2D resistivity modelling, 2.5D and 3D numerical modelling are especially useful for practical interpretation since the calculated potential values can be compared with real survey data directly. They use the point source assumption instead of the implicit line source in 2D modelling. Therefore 2.5-D and 3-D resistivity inversion based on the 2.5-D and 3-D forward modelling will be much more accurate than 2-D resistivity inversion which is based on a line source assumption. So developing 2.5D and 3D resistivity modelling techniques is very important.

Three different algorithms for resistivity modelling have been employed: the integral equation method (Okabe, 1981; Das and Parnasis, 1987; Xu et al., 1988), the finite-difference method (FDM) (Mundry, 1984; James, 1985; Lowry et al., 1989; Zhao and Yedlin, 1996) and the finite-element method (FEM) (Pridmore et al., 1981; Holcombe and Jiracek, 1984; Queralt et al., 1991; Zhou, 1998; Zhou and Greenhalgh., 2000)

The integral equation algorithm involves finding a boundary integral solution of Laplace's equation, with the implicit assumption of a uniform subsurface. This method is limited to only very simple models and is normally not used for forward modelling calculation in resistivity inversion. However for some simple models, it may be the best choice since it uses much less computation time and memory.

The other two algorithms are based on solving the following differential equation

$$\nabla \cdot (\sigma \nabla U) = -I\delta(r - r_c) \qquad r, r_c \in \Omega \tag{3.0}$$

where U is potential, σ is the conductivity of the medium, and $\vec{r}_c = (x_c, y_c, z_c)$ is the location of the current electrode in Ω. This equation can be used to study any complicated models. The

potential values in the modelling area are approximated with the finite difference or finite element method. However the disadvantage of the two algorithms is the large cost of computer resources: CPU time and memory.

In this chapter, the basic principle of the FEM of resistivity modelling method is given. Detailed formulae are derived for completing the 2.5D and 3D numerical modelling programs with the FEM algorithm. Then a few 2.5D and 3D modelling results are demonstrated by way of synthetic examples. Some of the modelling results are used to support the interpretation work of the Bolivar ASR project.

3.2 THE GALERKIN SOLUTION OF THE FINITE ELEMENT METHOD

The calculation of the electrical potential distribution by the finite-element algorithm is usually based on a variational principle that considers the potential as a stationary function corresponding to the energy associated with the electric field (Coggon, 1971; Pridmore et al., 1981). From a mathematical viewpoint, the FEM method is more practical and more reliable for solving differential equations than the other two algorithms.

Firstly, let us define the differential equation problem as follows:

$$\begin{cases} L\Phi(r) = f, & r \in \Omega, \\ \dfrac{\partial\, \Phi(r)}{\partial\, n} + B\Phi(r) = 0, & r \in \partial\, \Omega, \end{cases} \tag{3.1}$$

where f is a known function, L is a differential operator, Φ (r) is the exact solution, B stands for the boundary condition, and n is the normal to the bounding surface.

An approximation to Φ may be expressed by

$$\tilde{\Phi}(r) = \sum_{i}^{n} N_i(r)\tilde{\Phi}_i \tag{3.2}$$

where $\tilde{\Phi}_i$ are the unknown nodal values of $\tilde{\Phi}$ in the FEM mesh and $N_i(r)$ are the chosen shape functions. Then we form a residual function R(r) as follows:

$$R(r) = L\tilde{\Phi}(r) - f \quad . \tag{3.3}$$

By using the weighted residuals approach (Kenneth, 1975) and choosing m linearly independent weighting functions, W_j , we wish to set the sum (integral) of the weighted residuals to zero:

$$\int_{\Omega} W_j(r)R(r)dr = \int_{\Omega} W_j(r)[L\tilde{\Phi}(r) - f]dr = 0 \quad (j = 1,2,3,...m). \tag{3.4}$$

According to Galerkin's method (Kenneth, 1975), the weighting functions W_j are chosen to be the same as the approximation functions N_i used in equation (3.2), that is, $W_j = N_i$ for i=j=1,2,…,n. So equation (3.4) becomes

$$\int_{\Omega} N_j(r)R(r)dr = \int_{\Omega} N_j(r)[L\tilde{\Phi}(r) - f]dr = 0 \qquad (j = 1,2,3,...n). \tag{3.5}$$

Next, by substituting equation (3.2) into the above equation, we obtain a general equation for solving a differential equation with the FEM algorithm:

$$\sum_{i}^{n} \int_{\Omega} N_j(r)[LN_i(r)]\tilde{\Phi}_i dr = \int_{\Omega} N_j(r) f dr \qquad (j = 1,2,3,...n). \tag{3.6}$$

3.3 2.5-D RESISTIVITY MODELLING

In the following section, I will derive the formulas needed for the 3-D FEM resistivity modelling program, which I wrote. The 2.5-D treatment will be given first. It is due largely to Zhou (1998) but the 3-D derivation is entirely my own.

3.3.1 Derivation of Formulas

The partial differential equation used in 2.5-D modelling of the potential distribution with a point current source was given as equation (2.18):

$$\nabla \cdot (\sigma \nabla \overline{U}) - k_y^2 \sigma \overline{U} = -\frac{I}{2}\delta(x - x_c)\delta(z - z_c) \tag{3.7}$$

where $\sigma = \sigma(x,z)$ stands for electrical conductivity of medium, $\nabla = (\partial_x, \partial_z)$ stands for the 2D gradient operator in the (x,z)-plane, (x_c, z_c) are the source position and the function $\overline{U}$, given by

$$\overline{U}(x,k_y,z) = \int_0^{\infty} U(x,y,z)\cos(k_y y)dy \tag{3.8}$$

is the wavenumber-domain spectral form of the 3-D electric potential U(x,y,z), and is a real valued function.

We set the differential operator L to

$$L = \nabla \cdot (\sigma \nabla) - k_y^2 \sigma \tag{3.9}$$

and the function f in equ 3.1 to

$$f = -\frac{I}{2}\delta(x-x_c)\delta(z-z_c)\,. \tag{3.10}$$

Substituting the operator L, and the function f into equation (3.6), we obtain

$$\sum_{i}^{n} \int_{\Omega} N_j(r)[\nabla(\sigma\,\nabla N_i(r)) - k_y\sigma\, N_i(r)]\overline{U}_i dr = -\frac{I}{2}\int_{\Omega} N_j(r)\,\delta(x-x_c)(z-z_c)\,dr \;(j=1,2,3,...n) \tag{3.11}$$

By applying the boundary condition (equation 3.1) and using Gauss' Divergence Theorem:

$$\int_{\Omega} \nabla\vec{a}\,dr = \int_{\partial\Omega} \vec{a}_i\cdot\vec{n}\,d\Gamma \tag{3.12}$$

and rearranging equation (3.11), we have

$$\sum_{i}\{\int_{\Omega}[\sigma\nabla N_i\cdot\nabla N_j - \sigma k_y^2 N_i N_j]dr + \int_{\partial\Omega}\sigma N_j B N_i d\Gamma\}\,\overline{U}_i = \frac{I}{2}N_j\delta_{js} \tag{3.13}$$
$$(j=1,2,3,...,n),$$

where δ_{js} =1, if r_j=r_s, otherwise δ_{js} =0, and B stands for the boundary condition which is derived in the next section. Equation (3.13) is the basic equation of the FEM algorithm for 2.5D resistivity modelling.

3.3.2 Creating the Shape Functions for the Whole Calculation Mesh

Normally the modelling area is set to a rectangle for computational convenience. Then the model area is divided into equal spaced rectangular cells with a constant conductivity in each cell. In order to avoid the artificial boundary reflections from the edge of the model grid, the modelling area is usually extended to the left, right and bottom. The cells in the extended area may not be equally spaced for two reasons: 1). The resistivity in the extended area is constant; 2) the larger the cells in the extended area, the more distant the area of interest is from the artificial grid. As such, the actual calculation area for the resistivity modelling looks like that shown in Fig. 3.1.

From the figure, it can be seen that the whole calculation area is Ω and the central shaded area is the modelling area of interest. Γ_a represents the artificial boundary of the calculation area and Γ_s represents the surface boundary of the calculation area.

Fig. 3.2 shows that each cell in the whole calculation area is cut into 4 separate triangular segments in order to form the easiest FEM calculation cells – triangles. The basic requirement for the shape functions is that their value should be 1 at corresponding nodes and should be 0 at

other nodes. Therefore for each triangle, we can choose the following three shape functions for each node in the triangle (for example, in the first left-most triangle):

$$N_k^{(1)}(x,z) = \frac{1}{2\Delta_e^{(1)}}[a_k^{(1)} + b_k^{(1)}x + c_k^{(1)}z] \tag{3.14}$$

$$N_l^{(1)}(x,z) = \frac{1}{2\Delta_e^{(1)}}[a_l^{(1)} + b_l^{(1)}x + c_l^{(1)}z] \tag{3.15}$$

$$N_c^{(1)}(x,z) = \frac{1}{2\Delta_e^{(1)}}[a_c^{(1)} + b_c^{(1)}x + c_c^{(1)}z] \tag{3.16}$$

The corresponding coefficients a, b, c of the shape functions N are obtained with the following formulas.

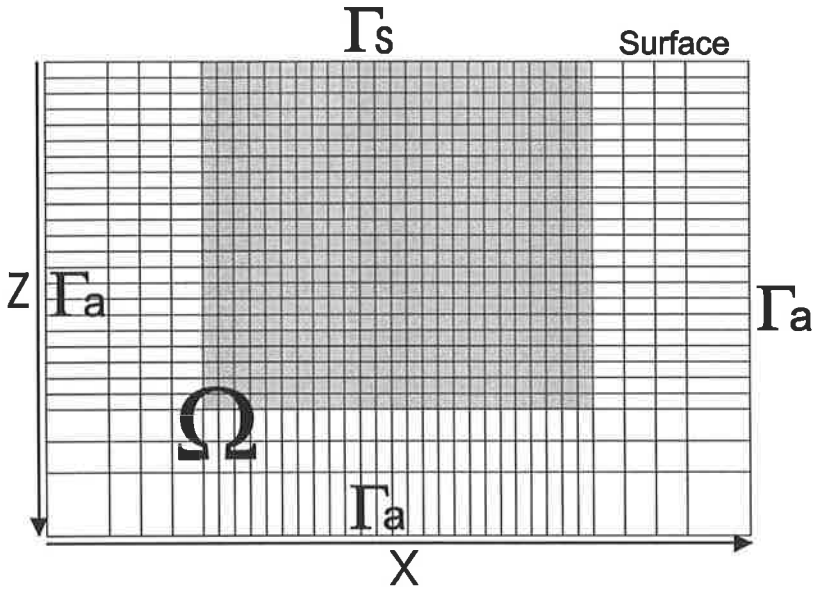

Figure 3.1 The diagram shows the whole calculated area of the FEM algorithm, where the active model area (shaded) has been extended to the left, right and bottom to reduce boundary effects.

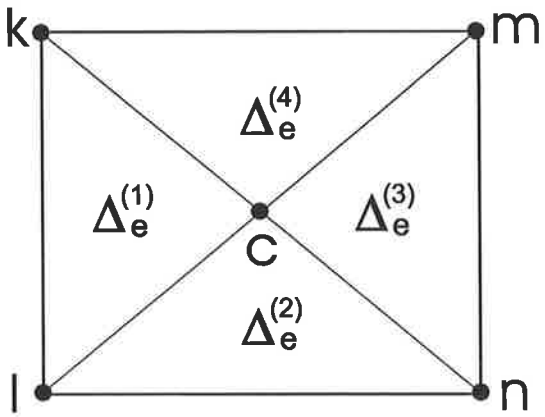

Figure 3.2 Each cell in the calculation area is resliced as above into 4 equal sized triangles.

$$a_k^{(1)} = x_l z_c - z_l x_c, \qquad b_k^{(1)} = \Delta z/2, \qquad c_k^{(1)} = \Delta x/2 \tag{3.17}$$

$$a_l^{(1)} = x_c z_k - z_c x_k, \qquad b_l^{(1)} = \Delta z/2, \qquad c_l^{(1)} = \Delta x/2 \tag{3.18}$$

$$a_c^{(1)} = x_k z_l - z_k x_l, \qquad b_c^{(1)} = \Delta z/2, \qquad c_c^{(1)} = \Delta x/2 \tag{3.19}$$

where points (x_k,z_k), (x_l,z_l) and (x_c,z_c) are the coordinates of the nodes of the triangle.

As with all FEM forward modelling methods, the range is limited by the computational effort. So a computation range Ω has to be set up and the artificial boundaries have to be handled during the calculation. For this situation, we set the top boundary as a natural boundary, that is B=0 since the DC current can not pass into the air. On the other boundaries (left, right and bottom), the following mixed (Dirichelet-Neumann)-boundary condition (Dey and Morrison, 1979a, b; Zhou, 1998) is used

$$B = k_y[\frac{K_1(r\,k_y)\cos\theta_1 + K_1(r'k_y)\cos\theta_2}{K_0(rk_y) + K_0(r'k_y)}] \tag{3.20}$$

where K_0 and K_1 are the modified Bessel functions of the second kind and the quantities r, r', θ_1 and θ_2 are shown in Fig. 3.3. The distances r and angles θ relate to the field point and the current source and its image.

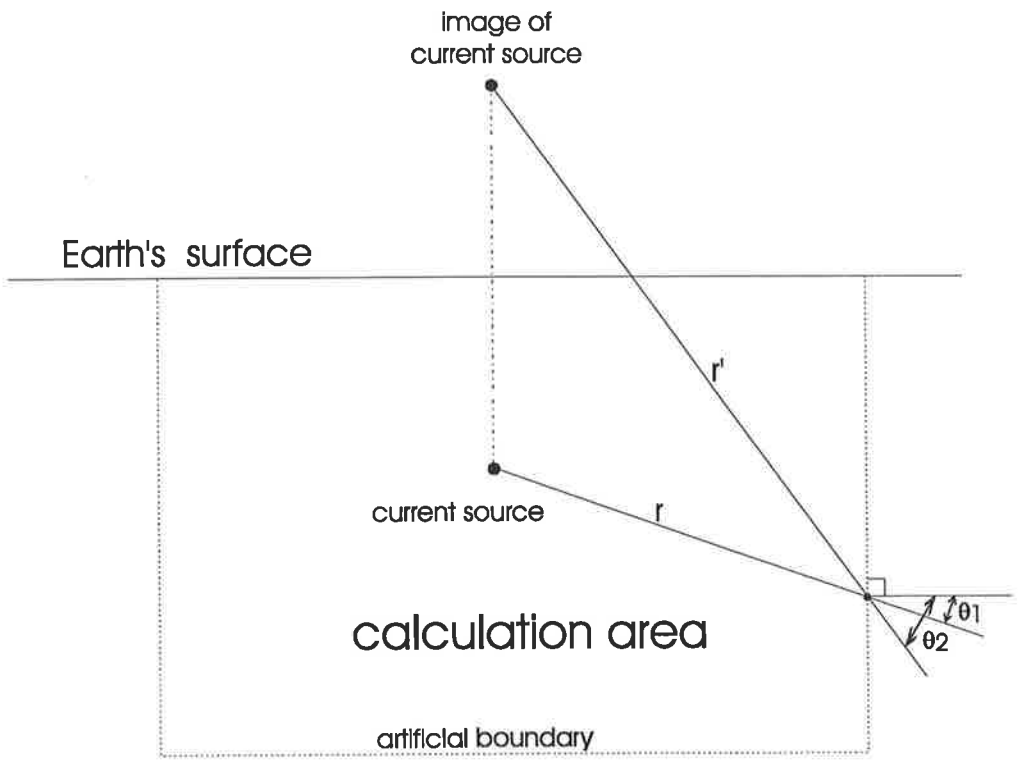

Figure 3.3 Geometric relations among r, r', θ_1 and θ_2 where distances and angles are measured from the field point to the source and its image.

For the left, right and bottom boundaries, the following triangular shape functions (1-D) are used according to the diagram in Fig. 3.4

$$N_i(l) = 1 - \frac{s}{\Gamma_e} \tag{3.21}$$

$$N_j(l) = \frac{s}{\Gamma_e} \tag{3.22}$$

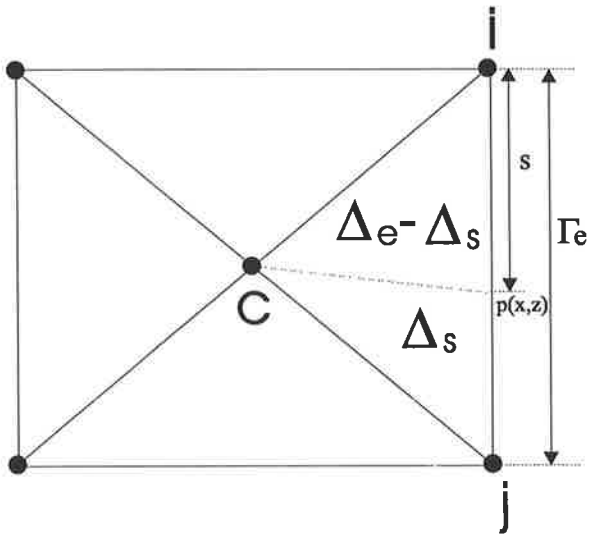

Figure 3.4 The diagram shows how the boundary triangular shape function is formed.

3.3.3 The Final Formulae for 2.5D FEM Resistivity Modelling with FEM

By rewriting equation (3.13) and assuming σ is constant in each cell, the following equations can be obtained

$$M\overline{U} = C_s \tag{3.23}$$

where

$$M = (M_{ij})_{n\times n} \quad \text{and} \quad M_{ij} = \sum_e (A_{ij}^e + T_{ij}^e) \tag{3.24}$$

$$\overline{U} = \{\overline{U}_i\}^T \qquad (i = 1,2,\ldots..,N) \tag{3.25}$$

$$C_s = \{I_s N_i\, \delta_{is}\}^T \qquad (i = 1,2,\ldots..,N) \tag{3.26}$$

$$A_{ij}^e = \int_{\Omega_e} \sigma\, [\nabla N_i \cdot \nabla N_j + \sigma k_y^2 N_i N_j]dr \tag{3.27}$$

$$T_{ij}^e = \int_{\partial\Omega} \sigma\ N_j B N_i d\Gamma \quad . \tag{3.28}$$

Matrices A and T are called the inner element matrix and the boundary element matrix, respectively (Zhou, 1998).

For each inner element (Fig 3.2), we substitute the above shape functions (3.14), (3.15) and (3.16) into equation (3.27) and remove the central node from the formulas (Zhou, 1998), to obtain the following formula to calculate A^e_{ij} for one rectangular cell e:

$$A^e_{ij} = E^e_{ij} - \frac{E^e_{ic} E^e_{jc}}{E^e_{cc}} \qquad \text{(i,j=k,l,m,n)} \qquad (3.29)$$

where

$$E^e_{kk} = \frac{\sigma_e}{2}[\frac{\Delta z}{\Delta x} + \frac{\Delta x}{\Delta z} + \frac{k_y^2}{6}\Delta x \Delta z] \qquad (3.30)$$

$$E^e_{ll} = \frac{\sigma_e}{2}[\frac{\Delta z}{\Delta x} + \frac{\Delta x}{\Delta z} + \frac{k_y^2}{6}\Delta x \Delta z] \qquad (3.31)$$

$$E^e_{mm} = \frac{\sigma_e}{2}[\frac{\Delta z}{\Delta x} + \frac{\Delta x}{\Delta z} + \frac{k_y^2}{6}\Delta x \Delta z] \qquad (3.32)$$

$$E^e_{nn} = \frac{\sigma_e}{2}[\frac{\Delta z}{\Delta x} + \frac{\Delta x}{\Delta z} + \frac{k_y^2}{6}\Delta x \Delta z] \qquad (3.33)$$

$$E^e_{kl} = \frac{\sigma_e}{2}[\frac{\Delta z}{\Delta x} - \frac{\Delta x}{\Delta z} + \frac{k_y^2}{12}\Delta x \Delta z] \qquad (3.34)$$

$$E^e_{km} = \frac{\sigma_e}{2}[\frac{\Delta x}{\Delta z} - \frac{\Delta z}{\Delta x} + \frac{k_y^2}{12}\Delta x \Delta z] \qquad (3.35)$$

$$E^e_{\ln} = \frac{\sigma_e}{2}[\frac{\Delta x}{\Delta z} - \frac{\Delta z}{\Delta x} + \frac{k_y^2}{12}\Delta x \Delta z] \qquad (3.36)$$

$$E^e_{mn} = \frac{\sigma_e}{2}[\frac{\Delta z}{\Delta x} - \frac{\Delta x}{\Delta z} + \frac{k_y^2}{12}\Delta x \Delta z] \qquad (3.37)$$

$$E^e_{kn} = 0 \qquad (3.38)$$

$$E^e_{ml} = 0 \qquad (3.39)$$

$$E^e_{kc} = \sigma_e[\frac{\Delta z}{\Delta x} + \frac{\Delta x}{\Delta z} + \frac{k_y^2}{12}\Delta x \Delta z] \qquad (3.40)$$

$$E^e_{lc} = \sigma_e[-\frac{\Delta z}{\Delta x} - \frac{\Delta x}{\Delta z} + \frac{k_y^2}{12}\Delta x \Delta z] \qquad (3.41)$$

$$E^e_{mc} = \sigma_e[-\frac{\Delta z}{\Delta x} - \frac{\Delta x}{\Delta z} + \frac{k_y^2}{12}\Delta x \Delta z] \qquad (3.42)$$

$$E^e_{nc} = \sigma_e[-\frac{\Delta z}{\Delta x} - \frac{\Delta x}{\Delta z} + \frac{k_y^2}{12}\Delta x \Delta z] \qquad (3.43)$$

$$E^e_{cc} = 4\sigma_e[\frac{\Delta z}{\Delta x} + \frac{\Delta x}{\Delta z} + \frac{k_y^2}{12}\Delta x \Delta z]. \qquad (3.44)$$

Since $E_{ij}^e = E_{ji}^e \quad (i, j = k, l, m, n, c)$, there are in total 25 E_{ij}^e (i, j=k, l, m, n, c) for formula (3.29). So it is easy to calculate A^e_{ij} from the above equations.

For each boundary element (Fig 3.4), by substituting equation (3.20), (3.21) and (3.22) into equation (3.28), T_{ij}^e can be calculated in the following way:

$$T_{ij}^e = \frac{1}{6}\sigma_e B_e L_e (1+\delta_{ij}). \tag{3.45}$$

After A_{ij}^e and T_{ij}^e are calculated, equation (3.23) can be formed. Then the banded Cholesky decomposition ($M=LL^T$) is used to solve the equation (Zhou, 1998) and the transferred potential $\overline{U}(x, k_y, z)$ in the k_y domain with one electric current source is obtained. This yields Galerkin's solution of the 2.5-D Helmholtz equation.

3.3.4 Inverse Fourier Transformation to Obtain the Potential

After the transformed potential $\overline{U}(x, k_y, z)$ is calculated, an inverse Fourier transform has to be performed to obtain the potential U(x,y,z) in the 3D space domain. The following inverse Fourier transform formula is used to complete the task

$$U(x, z, y) = \frac{2}{\pi}\int_0^\infty \overline{U}(x, k_y, z)\cos(k_y y)dk_y . \tag{3.46}$$

3.3.5 2.5-D Modelling Examples

Four sets of numerical resistivity modelling computations have been undertaken with the 2.5-D program to obtain some knowledge and improved understanding about cross well resistivity tomography. The first three modelling examples were chosen to roughly simulate the aquifer field situation under investigation. The last example is to examine sensitivity to small resistive or conductive targets.

3.3.5.1 Example 1 – Horizontal vs Vertical Boundaries

The first example is intended to highlight the difference between horizontal and vertical discontinuities in cross well resistivity surveys. Two numerical models have been studied for this purpose. The first model consists of two horizontal layers as shown in Figure 3.5. Layer resistivities are 30 Ω-m and 100 Ω-m. The second model has two media with a vertical contact as shown in Figure 3.6. Again the resistivity contrast is 100:30.

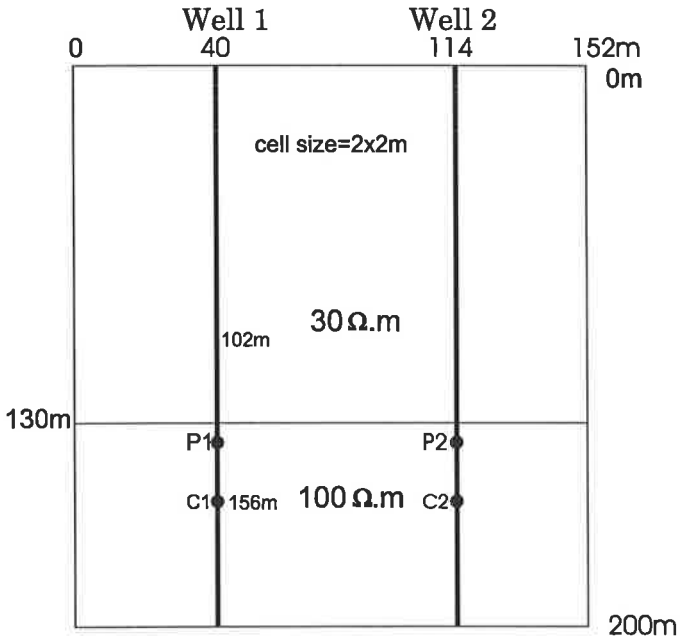

Figure 3.5 The model layout of the first 2.5-D model - model 1-1.

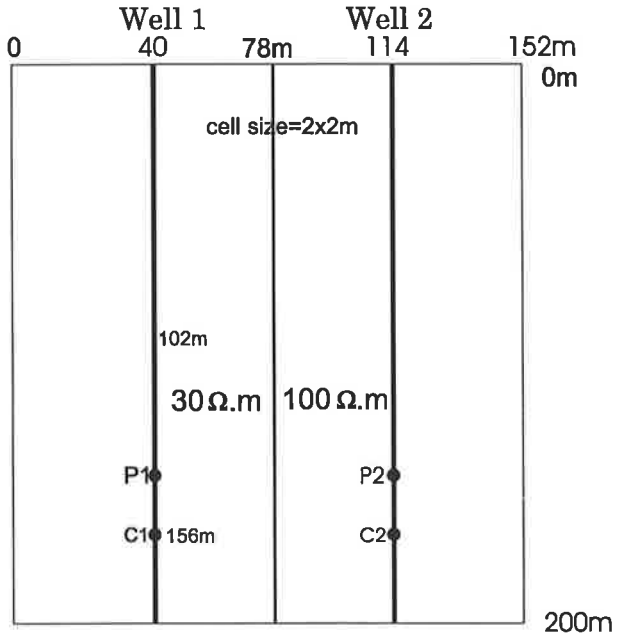

Figure 3.6 The model layout of the second 2.5-D model - model 1-2.

The survey layout for the modelling is shown in the both figures. The bipole bipole configuration is employed with a current electrode (C) and a potential electrode (P) in each borehole. Electrodes C1 and P1 are in Well 1 and electrodes C2 and P2 are in Well 2. The distance between C_1 and P_1, and C_2 and P_2 is 14m. The 'survey' range is from depth 102m to 156m. So there are only 21 acquisition positions in this range in each well when the electrode moving interval is 2 meters.

A cross well multi-scanning method is applied here as explained below. Electrodes C_2, and P_2 are moved upwards at 2 metre intervals from depth 156m to 102m (21 shifts) when electrodes *C_1 and P_1* are at a fixed position in the other well. Then electrodes C_1 and P_1 are shifted upward 2 metres and the procedure is repeated again by progressively moving C2 and P2 until electrode P_1 reaches the top of the 'survey' range (at depth 102m). So in total we obtain 21×21=441 data points of electric potential. The potentials are converted to apparent resistivity using formulae given in chapter 2.

The apparent resistivity data of the modelling are displayed in Figure 3.7 and Figure 3.8 for the first and second model, respectively. From the figures, it can be clearly seen that the dynamic range of the first model data is much larger than that of the second model data. The range of the apparent resistivity in the first model is from about 40 Ω.m to 80 Ω.m. But the range of the apparent resistivity in the second model is only about half an Ω.m, from 64 Ω-m to 64.5 Ω-m. Figure 3.7 also shows that the apparent resistivity gets larger when the electrodes move towards the bottom of the well where the higher resistivity layer is located. This is consistent with the resistivity change trend in the first model. The interesting thing in the figure is that the middle part of the profiles is flat in all profiles. This occurs when two electrodes in the same well are in different layers. By contrast, for the vertical interface model, it seems very hard to deduce the resistivity structure from the apparent resistivity stacked profiles in Figure 3.8. The voltage range of this modelling is less than 10mV when the injected current is 1A.

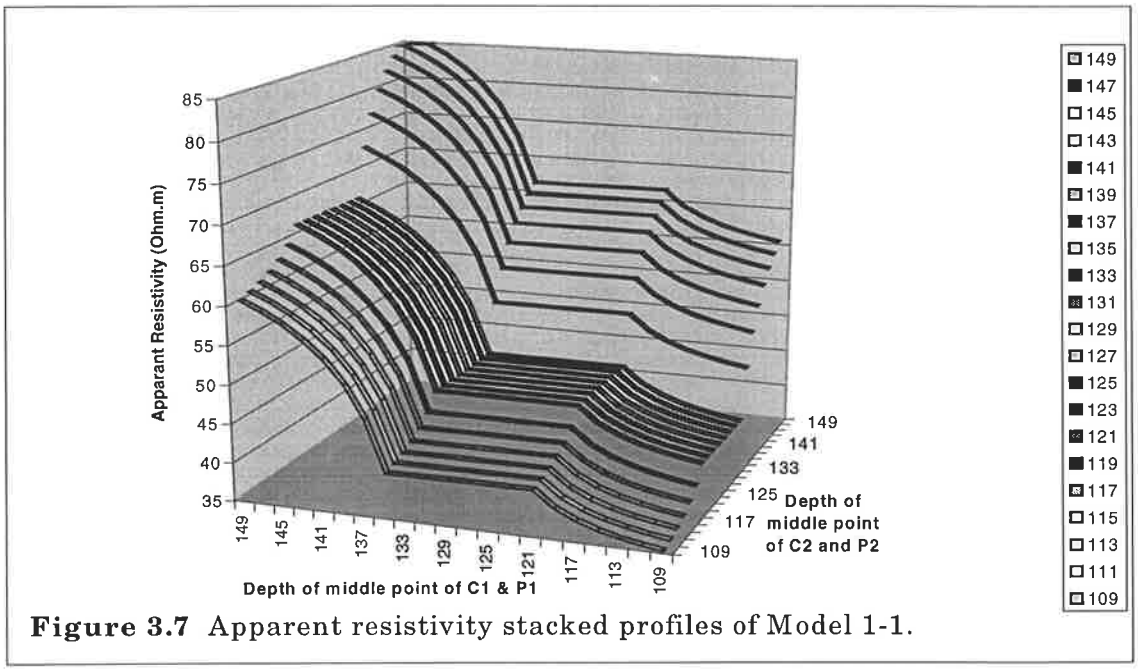

Figure 3.7 Apparent resistivity stacked profiles of Model 1-1.

From Figure 3.7 and Figure 3.8, one may see that the horizontal boundary has much stronger responses than the vertical boundary in apparent resistivity with this crosshole configuration. In the next chapter, these two sets of data will be inverted to construct the resistivity distribution. Then we can get a better answer for this.

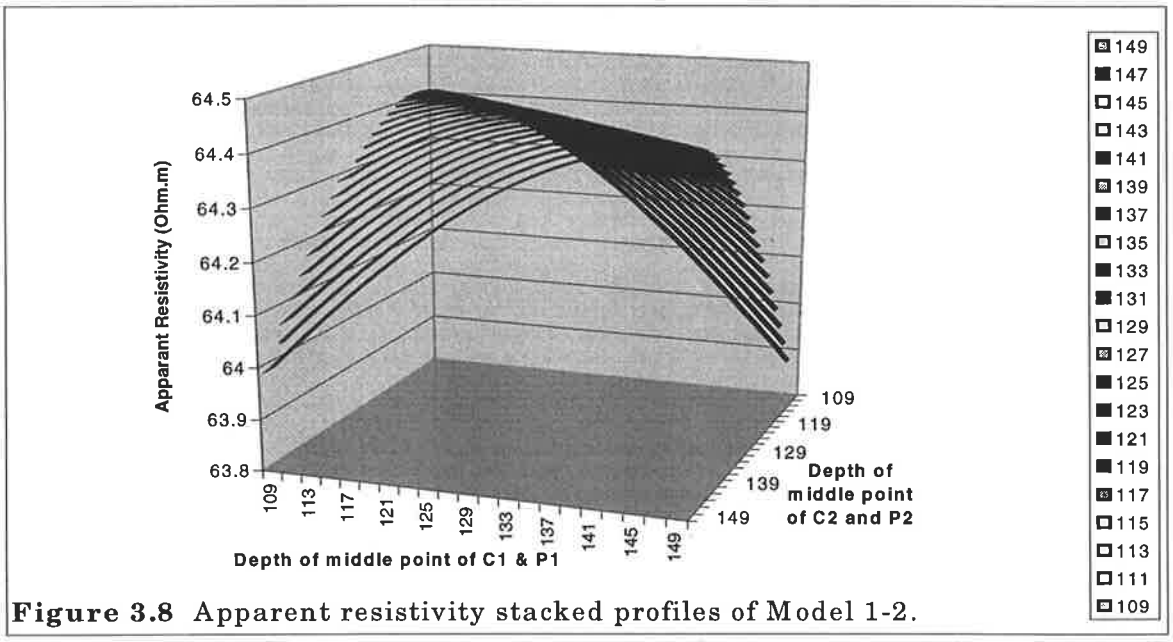

Figure 3.8 Apparent resistivity stacked profiles of Model 1-2.

3.3.5.2 Example 2- Four layer model with an embedded high resistivity layer

From our Bolivar test survey data (refer to Chapter 6 and 8), we noticed that the apparent resistivity stacked profiles are always high->low->high->low along each profile, as shown in Figure 3.9. According to our initial knowledge, we thought that there is a low resistivity zone in the middle part of the section We simulated it with our 2.5-D modelling program. It failed. Then we changed it into high resistivity layer. It was successful. The model we used is shown in Figure 3.10. The modelled apparent resistivity data is displayed in Figure 3.11. This example makes us realise that the low apparent resistivity zone in survey data may not mean the presence of a low resistivity zone in the geological structure.

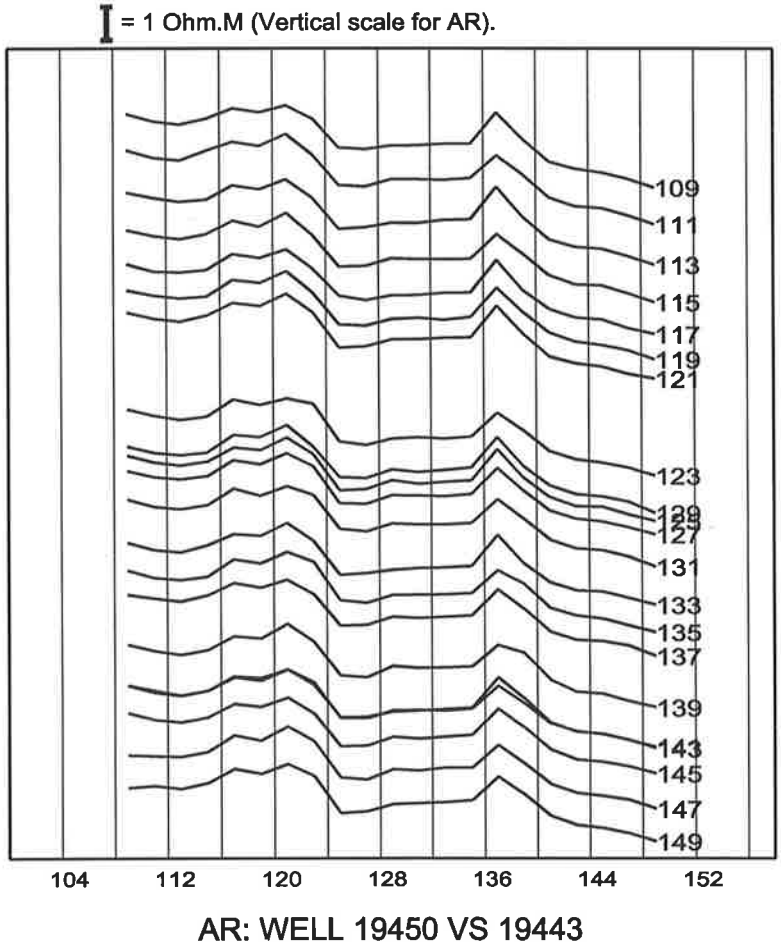

Figure 3.9 The apparant resistivity stacked profiles for one of the Bolivar cross well surveys. The numbers on the bottom and the right are the depths of the middle point of two electrodes in the same well. The adjecent profiles were separated with a fixed interval to show all profiles clearly.

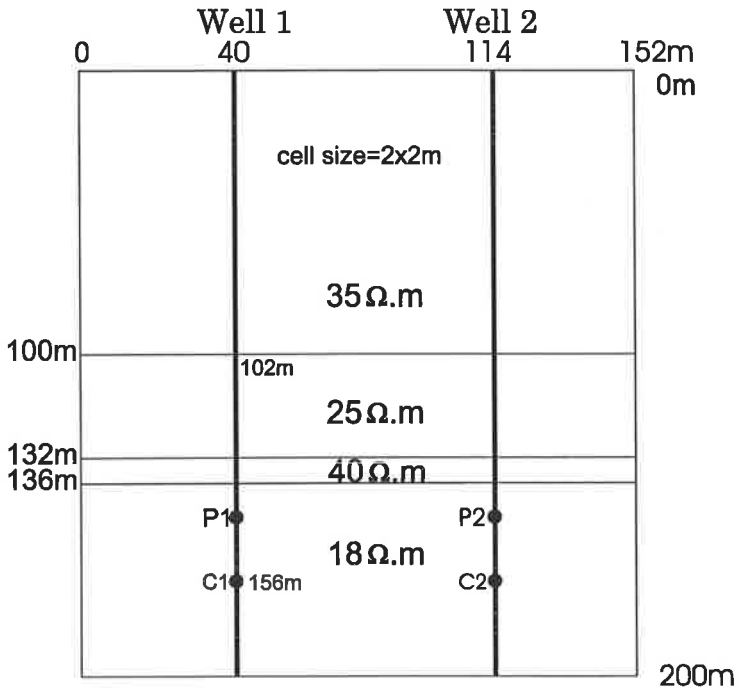

Figure 3.10 The model layout of the second 2.5-D model - model 2-1.

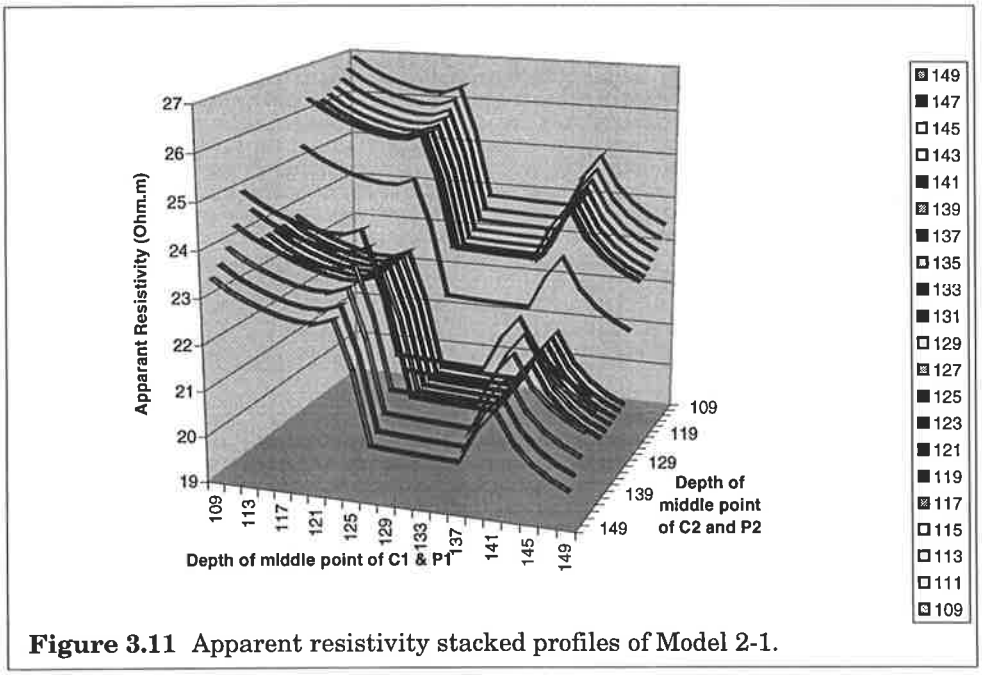

Figure 3.11 Apparent resistivity stacked profiles of Model 2-1.

3.3.5.3 Example 3 – Continuous, Discontinuous and Faulted Conductors

This set of modelling is for investigating the difference of apparent resistivity responses from the three different thin layer models, as shown in Figure 3.12. The first model is a continuous conductor model in which the layer remains connected between both boreholes (Model A). The second model is a discontinuous conductor model in which the layer is broken between the two boreholes (Model B). The last model is a faulted conductive zone, as shown in Figure 3.12 (Model C). The distance between the two boreholes in all three models is 48 metres. The resistivity contrast in all three models is 10:1, viz. 1000Ωm:100Ωm. The cell size in the forward modelling is 2 meters. There are 31 electrode positions employed in each borehole, evenly spaced 4m apart over the depth range 40m to 160m.

The 'survey' layout is shown in Figure 3.13. The bipole-bipole configuration is applied. We use the crosshole multiple scanning data acquisition procedure, which is the same as the acquisition procedure used in the last model. The difference is that three different separation intervals (8m, 16m and 32m) between the two electrodes AM or BN in each borehole were used. So these models produced a lot more data than the last model. In total there are 841 (29x29) data points obtained for the AM and BN interval of 8 metres, and 729 (27x27) and 529 (23x23) points for the intervals of 16m and 32m, respectively. This yields 2099 data points for the 3 multiple scanning runs with 3 different electrode spacings.

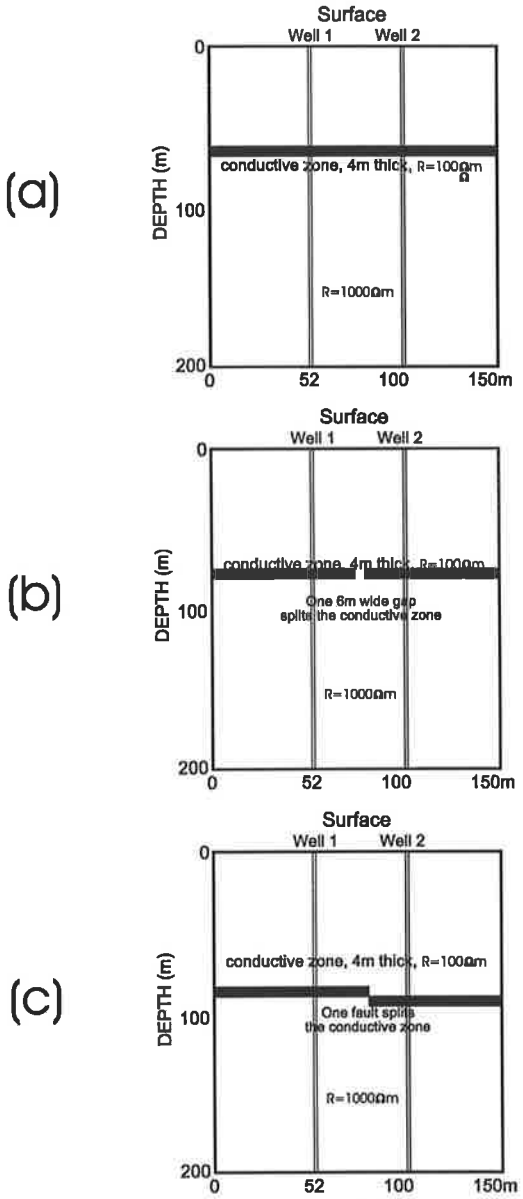

Figure 3.12 The layout of the third sets of resistivity models: (a) a model with a continuous conductive zone at depth 90m; (b) a model having a 4m wide gap splitting the conductive zone; (c) a model having a fault splitting the conductive zone.

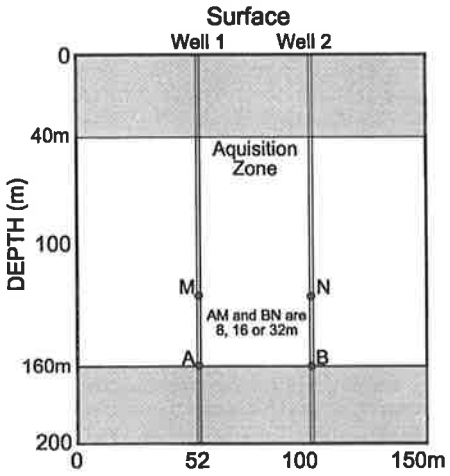

Figure 3.13 Data acquisition design. For each scanning, the distance of AM and BN is fixed to 8, 16, or 32m.

The apparent resistivity stacked profiles for the three models using an AM and BN spacing of 32m are displayed in Figure 3.14. Electrode B position is shown along the horizontal axis and electrode A position is shown along the vertical axis. It is hard to tie any point of the curves to any spatial point of the models, since both the axes are depths. It shows only the position and possible relationship between AM and BN.

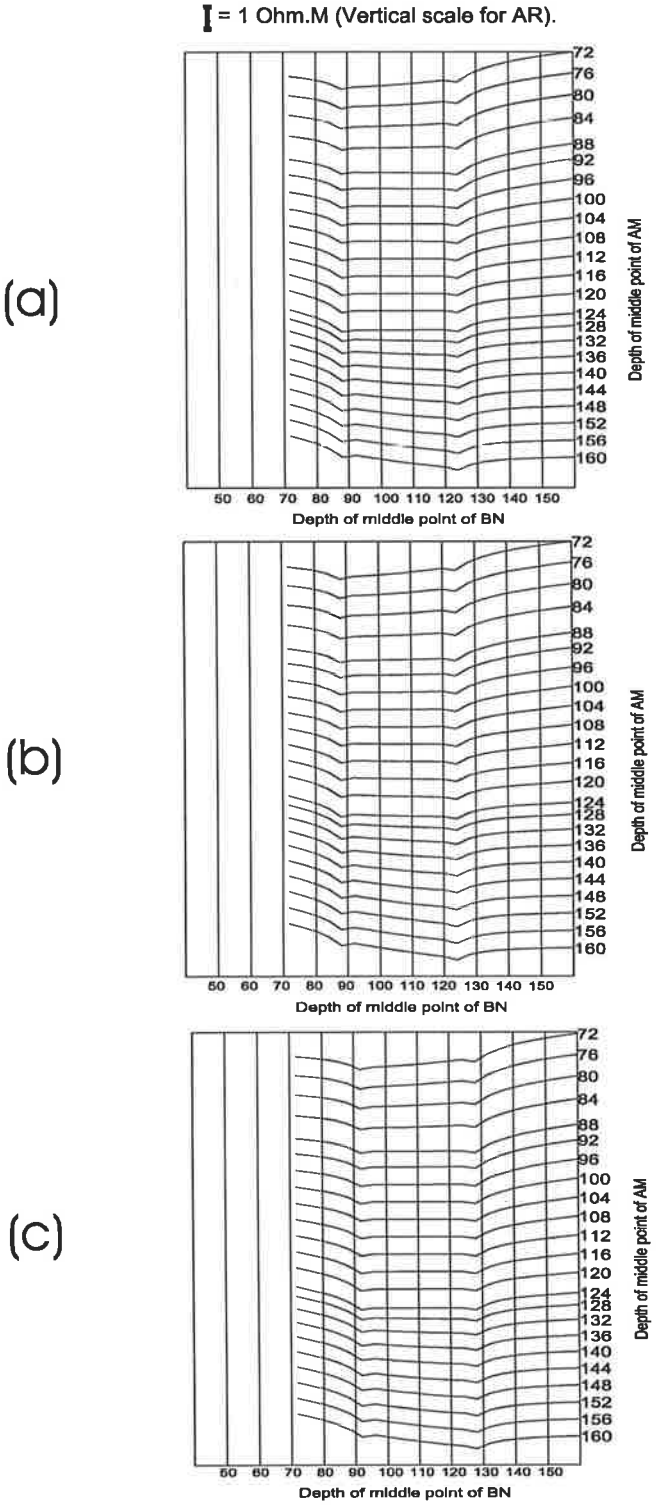

Figure 3.14 The apparent resistivity stacked profiles for the modeled scanning data for AM and BN 32 metres interval. (a) is for model 1 (continuous model), (b) is for model 2 (discontinuous model), and (c) is for model 3 (faulted model).

So from the profiles, we can see little other than the low resistivity zone in the middle of the depth range. The three profiles look almost the same when separated in position. It is too hard to interpret the profiles even with a lot of survey data because it is impossible to deduce that there is a fault or termination to the conductive zone. So a new technique has to be developed to interpret this sort of data. A resistivity inversion has been applied on all modelling data of this set of models. The result will be shown in the next chapter.

3.3.5.4 Example 4 – A square 'conductor' and a square 'resistive body' between two wells

These two models are used to investigate the sensitivity of the 2.5D resistivity inversion program to see if it can invert a square anomaly between two wells with enough data points and with the right 'survey' configuration. The modelling designs are shown in Figure 3.15.

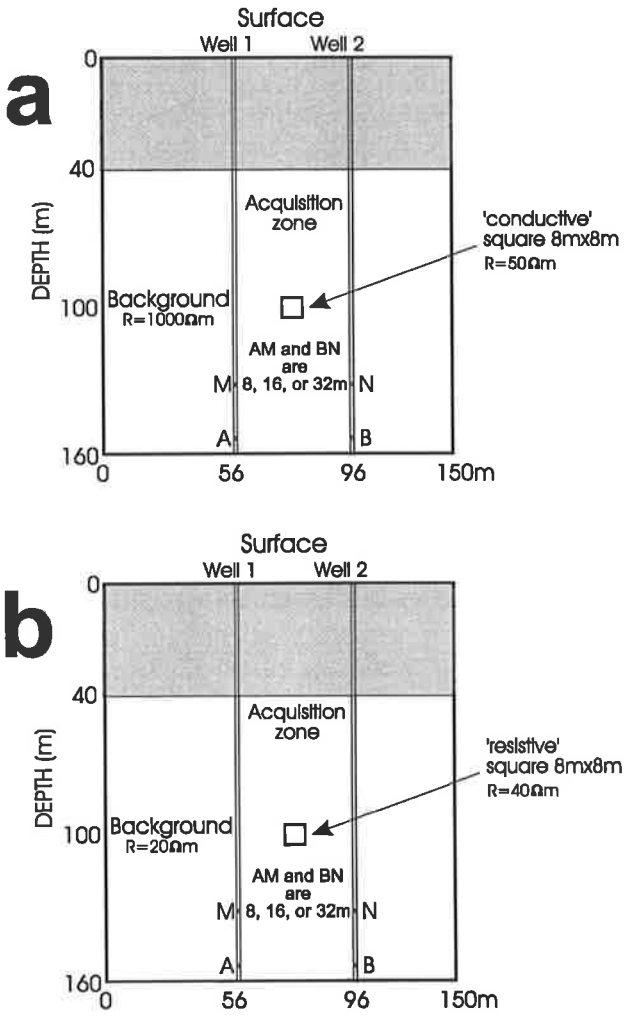

Figure 3.15 This diagram shows the two square model design layouts. Graph **a** is a 'conductor' model and graph **b** is a 'resistive body' model. The multiple spacing 'crosshole multiple scanning' is applied, with AM & BN fixed to 8, 16,or 32m.

The size of the square target is 8m x 8m. In the first model, the background resistivity is 1000Ωm and the 'conductor' resistivity is 50Ωm. In the second model, the background resistivity is 20Ωm and the 'resistive body' resistivity is 40Ωm. The distance between two

wells is 40m and the accessible range in the both boreholes is 120m (from the depth 40m to 160m). The cell size in the modelling is 2 meters. There are 31 electrode positions employed in each borehole, evenly spaced 4m apart over the depth range 40m to 160m.

The bipole-bipole configuration is applied. The multiple spacing 'crosshole multiple scanning' data acquisition procedure was used with three different spacing intervals (8m, 16m and 32m) between the two electrodes AM or BN in each borehole. So this model produces a large number of data points. In total there are 841 (29x29) data points obtained for the AM and BN interval of 8 metres, and 729 (27x27) and 529 (23x23) points for the intervals of 16m and 32m, respectively. This yields 2099 data points for the 3 multiple scanning runs with 3 different electrode spacings.

The apparent resistivity stacked profiles for the three models using an AM and BN spacing of 32m are displayed in Figure 3.16. From the profiles, we can see that all profiles are continuous and there is no turning point. This is because the background resistivity distribution is uniform and there is no resistivity interface crossed by the electrodes in the wells. However, the anomaly is clearly delineated by the 'survey' and is manifest as a decrease for the 'conductor' model and as an increase for the 'resistive body' model in the apparent resistivity profiles.

The interpretation or delineation of the feature can only be done by means of inversion. This is given in the next chapter.

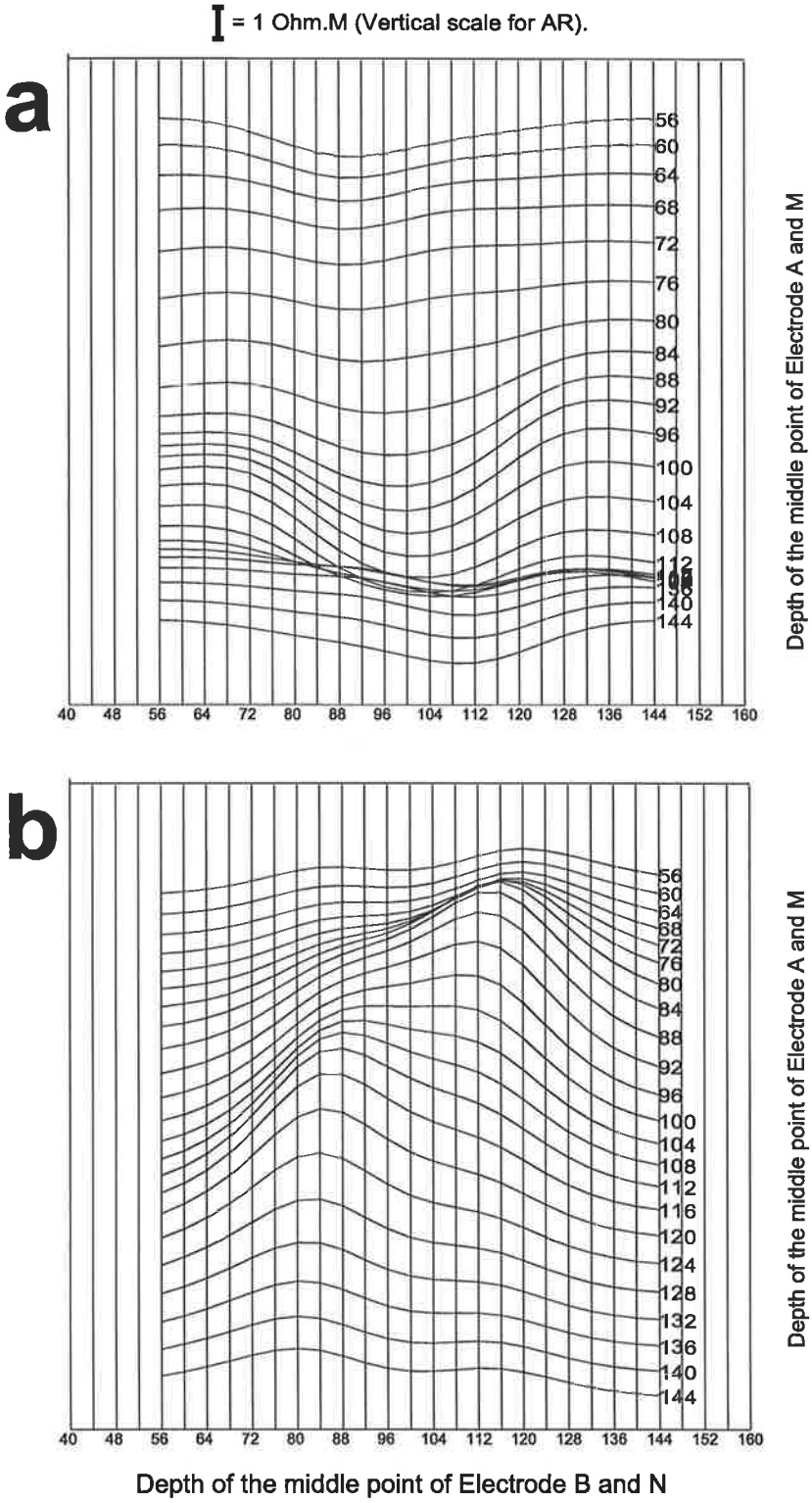

Figure 3.16 Apparent resistivity stacked profiles for the both square models (32m spacing data only). Graph **a** is of the 'conductor' model and graph **b** is of the 'resistive body' model.

3.4 3-D RESISTIVITY MODELLING

The derivation of 3-D numerical resistivity modelling formulae is similar but slightly simpler than that for 2.5-D resistivity modelling, since the forward and inverse Fourier transforms between the space domain and the wavenumber domain are not necessary in the 3-D case. The main effort is how to optimise the computer resources: CPU and memory, in order to model reasonable size grids.

3.4.1 Derivation of Formulae

The 3-D partial differential equation used to model the potential distribution with a point current source is

$$\nabla \cdot (\sigma \nabla U) = -\frac{I}{2}\delta(x-x_c)\delta(y-y_c)\delta(z-z_c) \tag{3.48}$$

where $\sigma = \sigma(x, y, z)$ stands for conductivity of the medium, $\nabla = (\partial_x, \partial_y, \partial_z)$ stands for the 3-D gradient operator in (x,y,z) space, and (x_c, y_c, z_c) is the current source position.

We set the operator L in equ (3.1) to:

$$L = \nabla \cdot (\sigma \nabla) \tag{3.49}$$

and the function f in equ (3.1) to:

$$f = -\frac{I}{2}\delta(x-x_c)\delta(y-y_c)\delta(z-z_c). \tag{3.50}$$

Substituting these quantities into equation (3.6), then integrating by parts, we obtain

$$\sum_i \{\int_\Omega [\sigma \nabla N_i \cdot \nabla N_j]dr + \int_{\partial\Omega} \sigma\ N_j B N_i d\Gamma\}\, U_i = \frac{I}{2} N_j \delta_{is} \qquad (j = 1,2,3,\ldots,m), \tag{3.51}$$

where $\delta_{is} = 1$ if $r_i = r_s$ and $\delta_{is} = 0$ if $r_i \neq r_s$.

Then the above equation can be rewritten in matrix form as follows:

$$MU = C_s \tag{3.52}$$

where

$$M = (M_{ij})_{n\times n} \quad and \quad M_{ij} = \sum_e (A_{ij}^e + T_{ij}^e) \tag{3.53}$$

$$U = \{U_i\}^T \qquad (i = 1,2,\ldots,N) \tag{3.54}$$

$$C_s = \{N_i\, \delta_{is}\}^T \qquad (i = 1,2,\ldots,N) \tag{3.55}$$

$$A_{ij}^{e} = \int_{\Omega_e} \sigma \, [\nabla N_i \cdot \nabla N_j] dr \tag{3.56}$$

$$T_{ij}^{e} = \int_{\partial\Omega} \sigma \; N_j B N_i d\Gamma \,. \tag{3.57}$$

After discretization of the integral range and suitable choice of shape functions, equation (3.51) reduces to a system of linear equations, which can be solved with the banded Cholesky decomposition ($M=LL^T$) (Zhou, 1998) for all the nodal values U_i.

3.4.2 Gridding the Model Area

First, the 3-D model volume is divided into small equal-sized 3-D cells. In order to prevent the artificial boundary reflections, the five boundaries (left, right, front, back and bottom) are extended (refer to Figure 3.17). In like fashion to the 2.5-D situation, the sizes of the 3-D cells in the modelling area are the same but the cell size is increased for the extended area.

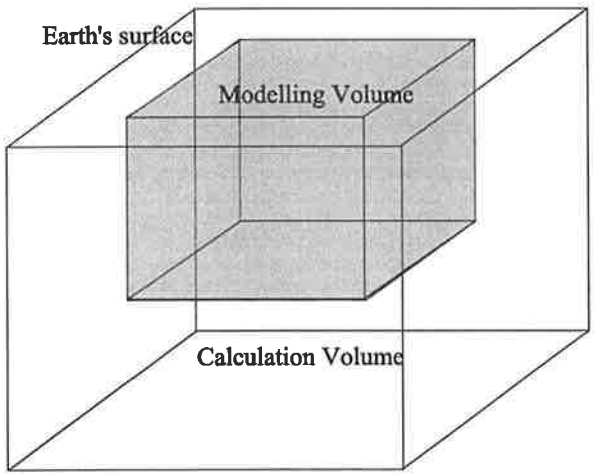

Figure 3.17 The diagram shows the relationship between modelling volume and calculation volume in 3-D forward resistivity modelling in order to reduce the artificial boundary reflections.

In the 3-D situation, the cell structure of each 3-D cell is designed as shown in Fig. 3.18. In each 3-D cell, 8 shape functions will be designed for each node in the cell as follows:

At point 1 **(x_1,y_1,z_1)**:

$$N_1 = \frac{(x-x_2)(y-y_2)(z-z_2)}{(x_1-x_2)(y_1-y_2)(z_1-z_2)} = -\frac{(x-x_2)(y-y_2)(z-z_2)}{\Delta x \cdot \Delta y \cdot \Delta z}. \tag{3.58}$$

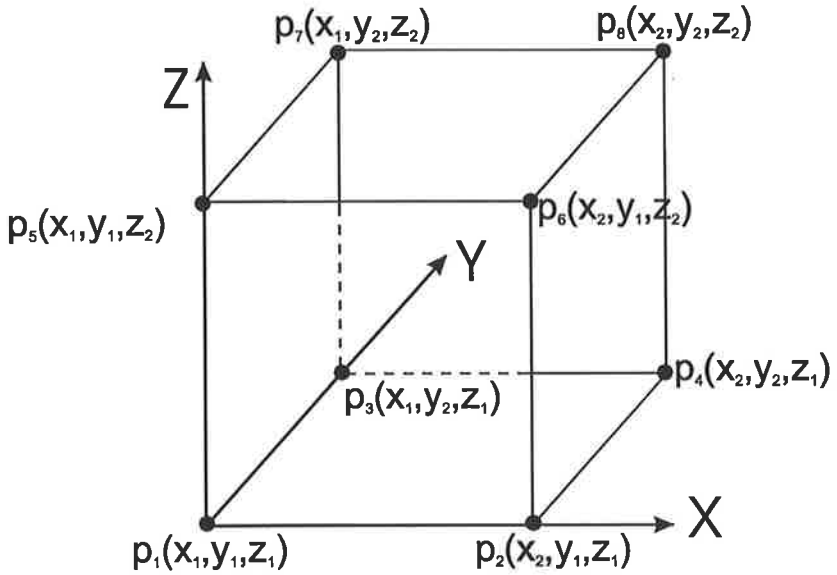

Figure 3.18 The cell structure for 3-D resistivity modelling and shape function design.

At point 2 **(x_2,y_1,z_1)**:

$$N_2 = \frac{(x-x_1)(y-y_2)(z-z_2)}{(x_2-x_1)(y_1-y_2)(z_1-z_2)} = +\frac{(x-x_1)(y-y_2)(z-z_2)}{\Delta x \cdot \Delta y \cdot \Delta z}. \tag{3.59}$$

At point 3 **(x_1,y_2,z_1)**:

$$N_3 = \frac{(x-x_2)(y-y_1)(z-z_2)}{(x_1-x_2)(y_2-y_1)(z_1-z_2)} = +\frac{(x-x_2)(y-y_1)(z-z_2)}{\Delta x \cdot \Delta y \cdot \Delta z}. \tag{3.60}$$

At point 4 **(x_2,y_2,z_1)**:

$$N_4 = \frac{(x-x_1)(y-y_1)(z-z_2)}{(x_2-x_1)(y_2-y_1)(z_1-z_2)} = -\frac{(x-x_1)(y-y_1)(z-z_2)}{\Delta x \cdot \Delta y \cdot \Delta z}. \tag{3.61}$$

At point 5 **(x_1,y_1,z_2)**:

$$N_5 = \frac{(x-x_2)(y-y_2)(z-z_1)}{(x_1-x_2)(y_1-y_2)(z_2-z_1)} = +\frac{(x-x_2)(y-y_2)(z-z_1)}{\Delta x \cdot \Delta y \cdot \Delta z}. \tag{3.62}$$

At point 6 **(x_2,y_1,z_2)**:

$$N_6 = \frac{(x-x_1)(y-y_2)(z-z_1)}{(x_2-x_1)(y_1-y_2)(z_2-z_1)} = -\frac{(x-x_1)(y-y_2)(z-z_1)}{\Delta x \cdot \Delta y \cdot \Delta z}. \tag{3.63}$$

At point 7 **(x_1,y_2,z_2)**:

$$N_7 = \frac{(x-x_2)(y-y_1)(z-z_1)}{(x_1-x_2)(y_2-y_1)(z_2-z_1)} = -\frac{(x-x_2)(y-y_1)(z-z_1)}{\Delta x \cdot \Delta y \cdot \Delta z}. \quad (3.64)$$

At point 8 **(x_2,y_2,z_2)**:

$$N_8 = \frac{(x-x_1)(y-y_1)(z-z_1)}{(x_2-x_1)(y_2-y_1)(z_2-z_1)} = +\frac{(x-x_1)(y-y_1)(z-z_1)}{\Delta x \cdot \Delta y \cdot \Delta z}. \quad (3.65)$$

The above eight shape functions can be summarised into a general shape function for simplicity:

$$N_i = k_i \cdot \frac{(x-a_i)(y-b_i)(z-c_i)}{\Delta x \cdot \Delta y \cdot \Delta z} \quad (3.66)$$

where

$$a_i = \begin{cases} x_1 \\ x_1 + \Delta x \end{cases} \quad (3.67)$$

$$b_i = \begin{cases} y_1 \\ y_1 + \Delta y \end{cases} \quad (3.68)$$

$$c_i = \begin{cases} z_1 \\ z_1 + \Delta z \end{cases}. \quad (3.69)$$

No.	Position	K_I	a_i -x_1	b_i -y_1	c_i -z_1
1	x_1,y_1,z_1	-1	dx	dy	dz
2	x_2,y_1,z_1	+1	0	dy	dz
3	x_1,y_2,z_1	+1	dx	0	dz
4	x_2,y_2,z_1	-1	0	0	dz
5	x_1,y_1,z_2	+1	dx	dy	0
6	x_2,y_1,z_2	-1	0	dy	0
7	x_1,y_2,z_2	-1	dx	0	0
8	x_2,y_2,z_2	+1	0	0	0

The gradient of the general shape function is:

$$\nabla N_i = \frac{Ki}{\Delta x \cdot \Delta y \cdot \Delta z}((y-b_i)(z-c_i),(x-a_i)(z-c_i),(x-a_i)(y-b_i)). \quad (3.70)$$

The product of two gradients is:

$$\nabla N_i \bullet \nabla N_j = \frac{K_i \cdot K_j}{(\Delta x \cdot \Delta y \cdot \Delta z)^2}(g_1(y,z) + g_2(x,z) + g_3(x,y)) \quad (3.71)$$

where

$$g_1=(y-b_i)(z-c_i)(y-b_j)(z-c_j) \tag{3.72}$$

$$g_2=(x-a_i)(z-c_i)(x-a_j)(z-c_j) \tag{3.73}$$

$$g_3=(x-a_i)(y-b_i)(x-a_j)(y-b_j). \tag{3.73}$$

The integral range for x is from x_1 to x_2. We transform variable x into x' by using the following formula in order to make integration easier:

$$x'=(x-x_1)/\Delta x \quad \text{or} \quad x=\Delta x\, x'+x_1 \quad \text{where} \quad \Delta x=x_2-x_1. \tag{3.74}$$

So the integral range for x is changed and it is now from 0 to 1.

As such

$$x-a_i=\Delta x\, x'+x_1-a_i=\Delta x(x'-l_i) \tag{3.75}$$

where

$$l_i=\begin{cases}0 & a_i=x_1\\ 1 & a_i=x_1+\Delta x\end{cases} \quad \text{or} \quad l_i=\frac{a_i-x_1}{\Delta x}. \tag{3.76}$$

Similarly,

$$y-b_i=\Delta y\, y'+y_1-b_i=\Delta y(y'-m_i) \tag{3.77}$$

$$z-c_i=\Delta z\, z'+z_1-c_i=\Delta z(z'-n_i) \tag{3.78}$$

where

$$m_i=\begin{cases}0 & b_i=y_1\\ 1 & b_i=y_1+\Delta y\end{cases} \quad \text{or} \quad m_i=\frac{b_i-y_1}{\Delta y} \tag{3.79}$$

$$n_i=\begin{cases}0 & c_i=z_1\\ 1 & c_i=z_1+\Delta z\end{cases} \quad \text{or} \quad n_i=\frac{c_i-z_1}{\Delta z}. \tag{3.80}$$

Now we try to complete the following volume integral:

$$\begin{aligned}\int_{z1}^{z2}\int_{y1}^{y2}\int_{x1}^{x2} g_1(y,z)\,dxdydz &= \int_{z1}^{z2}\int_{y1}^{y2}\int_{x1}^{x2}(y-b_i)(y-b_j)(z-c_i)(z-c_j)\,dxdydz\\ &= \Delta x\int_0^1\int_0^1 \Delta y^2\,(y'-m_i)(y'-m_j)\,\Delta z^2(z'-n_i)(z'-n_j)\,dydz\\ &= \Delta x\int_0^1\int_0^1 \Delta y^3\,(y'-m_i)(y'-m_j)\,\Delta z^3(z'-n_i)(z'-n_j)\,dy'dz'\\ &= \Delta x\Delta y^3\Delta z^3\left(\frac{1}{3}-\frac{m_i+m_j}{2}+m_im_j\right)\left(\frac{1}{3}-\frac{n_i+n_j}{2}+n_in_j\right)\end{aligned} \tag{3.81}$$

where m_i, m_j, n_i and n_j are either 0 or 1.

Similarly we can obtain:

$$\int_{z1}^{z2}\int_{y1}^{y2}\int_{x1}^{x2} g_2(x,z)dxdydz = \int_{z1}^{z2}\int_{y1}^{y2}\int_{x1}^{x2}(x-a_i)(x-a_j)(z-c_i)(z-c_j)dxdydz$$
$$= \Delta y\Delta x^3\Delta z^3(\frac{1}{3}-\frac{l_i+l_j}{2}+l_il_j)(\frac{1}{3}-\frac{n_i+n_j}{2}+n_in_j) \quad (3.82)$$

and

$$\int_{z1}^{z2}\int_{y1}^{y2}\int_{x1}^{x2} g_3(x,y)dxdydz = \int_{z1}^{z2}\int_{y1}^{y2}\int_{x1}^{x2}(y-b_i)(y-b_j)(x-a_i)(x-a_j)dxdydz$$
$$= \Delta z\Delta y^3\Delta x^3(\frac{1}{3}-\frac{m_i+m_j}{2}+m_im_j)(\frac{1}{3}-\frac{l_i+l_j}{2}+l_il_j) \quad (3.83)$$

Therefore, we can obtain the following equation under the assumption that σ is constant in each cell e:

$$A_{ij}^e = \int_{\Omega_e}\sigma\,\nabla N_i\cdot\nabla N_j]dr$$
$$= \sigma\int_{z1}^{z2}\int_{y1}^{y2}\int_{x1}^{x2}\nabla N_i\cdot\nabla N_j dxdydz$$
$$= \int_{z1}^{z2}\int_{y1}^{y2}\int_{x1}^{x2}\frac{K_i\cdot K_j}{(\Delta x\cdot\Delta y\cdot\Delta z)^2}(g_1(y,z)+g_2(x,z)+g_3(x,y))dxdydz \quad (3.84)$$
$$= K_i\cdot K_j(\frac{\Delta y\Delta z P_yP_z}{\Delta x}+\frac{\Delta x\Delta z P_xP_z}{\Delta y}+\frac{\Delta x\Delta y P_xP_y}{\Delta z})$$

where

$$P_x = (\frac{1}{3}-\frac{l_i+l_j}{2}+l_il_j)$$
$$P_y = (\frac{1}{3}-\frac{m_i+m_j}{2}+m_im_j)\,. \quad (3.85)$$
$$P_z = (\frac{1}{3}-\frac{n_i+n_j}{2}+n_in_j)$$

For the boundary condition, B_e=0 is chosen for the top free-surface boundary, and

$$B_e = \frac{r'^2\cos\theta_1 + r^2\cos\theta_2}{rr'(r+r')} \quad (3.86)$$

for the other five boundaries (bottom, left, right, front and back), where r is the distance from the source to a boundary point, r' is the distance from the image current source (reflected in the top boundary) to a boundary point, θ_1 and θ_2 are the angles between the artificial current flow directions (straight line from current source point or image current source via the top boundary to the cell) and the normal to the artificial boundary respectively, as shown in Fig 3.19.

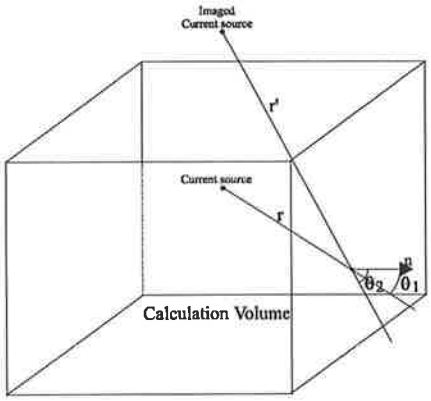

Figure 3.19 The diagram shows how the artificial boundary is handled in 3-D resistivity modelling.

The boundaries for the 3D resistivity modelling are in two dimensions. So each rectangular area in each boundary side is divided into 4 equal size triangles as was done in 2.5-D resistivity modelling. So there are 5 nodes and 4 separated triangles in each cell, after the cell is sliced. It is the same as the situation in 2.5-D gridding. As such, the same calculation method is used for deriving the following 3-D boundary handling formulas:

$$T_{ij}^{e} = \sigma_e B_e \left(E_{ij}^{e} - \frac{E_{ic}^{e} E_{jc}^{e}}{E_{cc}^{e}} \right) \qquad \text{(i,j=k,l,m,n)} \tag{3.87}$$

where

$$E_{ij}^{e} = \frac{\Delta_e}{12}(1+\delta_{ij}) \qquad \text{(i,j=k,l,m,n,c)} \tag{3.88}$$

except

$$E_{kn}^{e} = E_{nk} = E_{ml}^{e} = E_{lm}^{e} = 0 \tag{3.89}$$

since

$$\int_{S_e} N_i N_j ds = \frac{\Delta_e}{12}(1+\delta_{ij}) . \tag{3.90}$$

After A^{e}_{ij} and T_{ij}^{e} are calculated, M_{ij} is known and a linear equation system (3.52) is formed. Then by solving the linear equation system with a standard algorithm, the potential U distribution in the 3-D volume with one electric current source is obtained. One can then use the principle of superposition to obtain the response for any number of current sources and sinks by adding up the potentials algebraically for each source point. In our modelling, we use just two current electrodes – a positive source and a negative sink.

3.4.3 3-D Resistivity Modelling Examples

3.4.3.1 Comparison of the modelling calculation results with analytic solutions

To verify the both 2.5-D and 3-D resistivity modelling program, the analytic potential responses of a two-horizontal-layer model were calculated and were compared with the results from both modelling programs. The layout of the model is shown in Figure 3.20. From the figure, one can see that all 16 potential electrodes and one source electrode are on the surface and the thickness of the first layer is 5 metres. The resistivity of the first layer is 30Ωm and the second one is 100Ωm.

The analytic potential responses of the model were calculated with the following formula (Telford, 1990):

$$V = \frac{I\rho_1}{2\pi}\left[\frac{1}{r} + 2\sum_{m=1}^{1000}\frac{k^m}{\left\{r^2 + (2mz)^2\right\}^{1/2}}\right] \quad \text{and} \quad k = \frac{\rho_2 - \rho_1}{\rho_2 + \rho_1} \tag{3.91}$$

with m=1, 2, ..., 1000. The analytic data and numerical modelling data from both the 2.5-D and the 3-D modelling program are shown in Figure 3.21. The relative errors are calculated with the following formula

$$relative\_error = \frac{\text{mod}elling\_data - analytic\_data}{analytic\_data} \times 100 \tag{3.92}$$

and shown in Figure 3.22. From the figure, it can be seen that the maximum relative error is about 1.5% for the 2.5-D modelling program (with 12 wave number values) and 1.3% for the 3-D modelling program. The average relative errors are about 0.6% and 0.4% for 2.5-D and 3-D modelling programs, respectively. So both programs produce acceptable calculation accuracy.

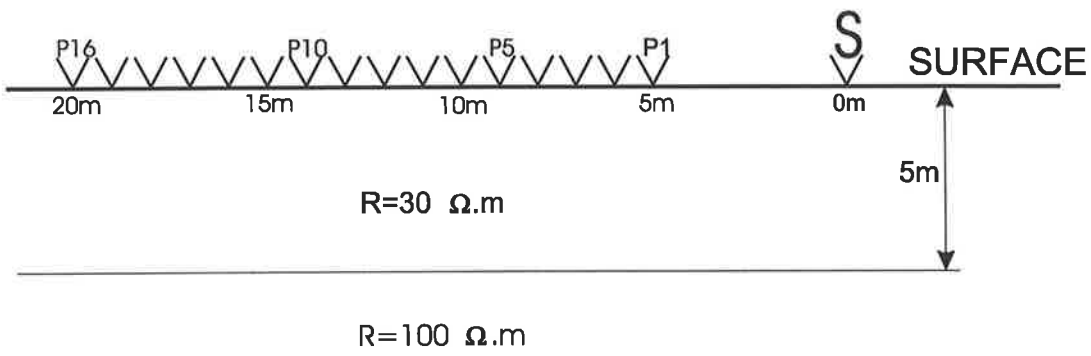

Figure 3.20 This two-layer model is used to compare the modelling results from the 2.5-D and 3-D modelling programs with the analytic results. S is the source electrode and P1 to P16 are potential electrodes.

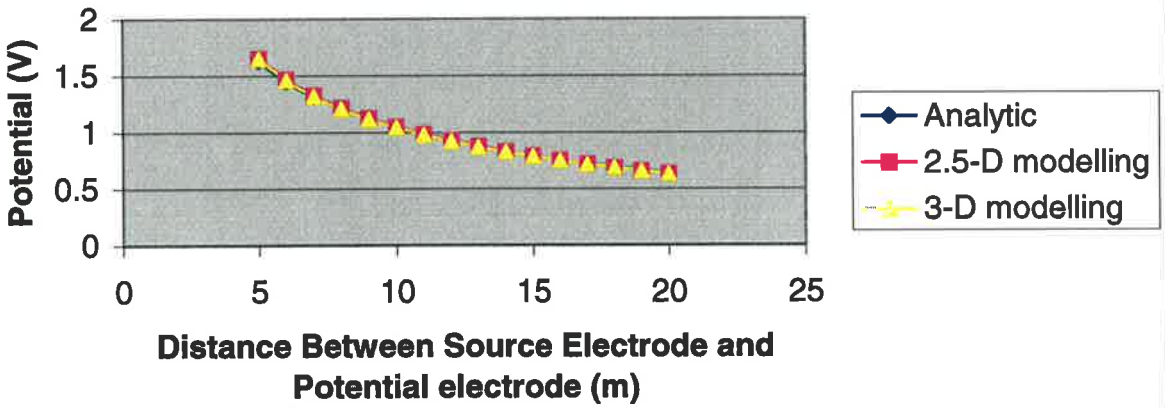

Figure 3.21 The graph shows the voltage differences between the calculated modelling results and the analytical results.

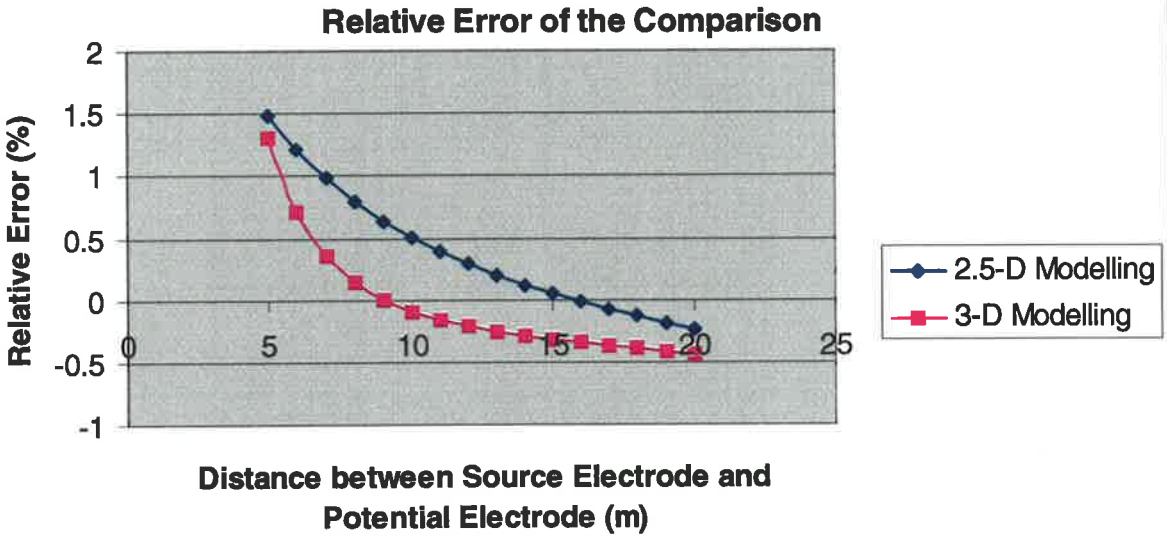

Figure 3.22 The graph shows the relative errors of the comparison displayed in Figure 3.21.

The analytic potential responses of a 3-D model, a buried sphere, were also calculated to verify the 3-D resistivity modelling program. The layout of the model is shown in Figure 3.23. The sphere, buried at a depth of 1m, has the lower resistivity (1Ω.m) than the host rock. The radius of the sphere is 2m. The background resistivity is 30Ω.m, yielding a contrast of 30:1. The layout for the one current and 16 potential electrodes is the same as in the above two-layer model.

The analytic potential response of the model was calculated with the following modified formula (Liang, 1979):

$$V = \frac{I\rho_1}{2\pi}\left[\frac{1}{r} - \left(\frac{1}{\rho_2} - \frac{1}{\rho_1}\right) \times \sum_{l=0}^{1000}\left[\frac{la^{2l+1}}{\left[\left(\frac{1}{\rho_2} + \frac{1}{\rho_1}\right) * l + 1\right] d^{l+1}} \frac{1}{b^{l+1}} P_l(\cos\theta)\right]\right] \qquad (3.93)$$

with l=1, 2, …, 1000, where r stands for the distance between the current electrode and the potential electrode, d stands for the distance between the current electrode and the centre of the sphere, b stands for the distance between the potential electrode and the centre of the sphere, a is the radius of the sphere, and θ is an angle (refer to Figure 3.23).

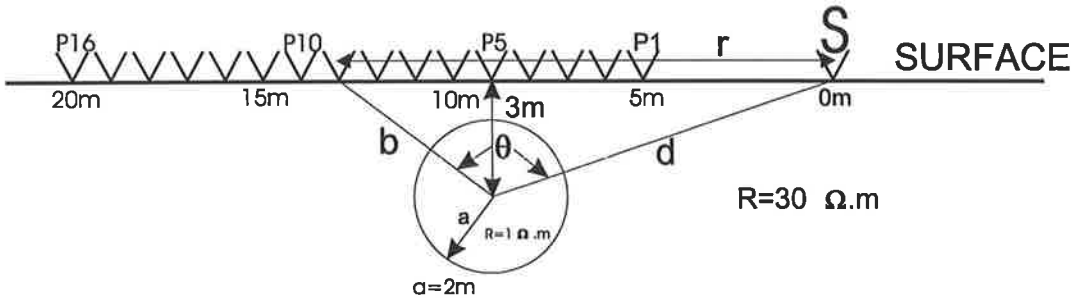

Figure 3.23 This 3-D sphere model is used to verify the 3-D resistivity modelling program. Both the modelling and analytic values were calculated and compared. S is the source electrode and P1 to P16 are potential electrodes.

Both the analytic solution and the numerical modelling data from 3-D modelling program are shown in Figure 3.24. The relative errors are calculated with the same formula as above and are shown in Figure 3.25. From the figure, it can be seen that the maximum relative error is less than 2.5% and the average relative errors are less than about 1%. The accuracy is acceptable. These errors mainly arise for two reasons. One is that the sphere can only be simulated roughly with the algorithm based on cubic griding. The second one is that the accuracy of the parallelepiped element schemes, which was used in this 3-D modelling program, is not as good as the one for the tetrahedron element schemes (refer to Zhou and Greenhalgh, 2001).

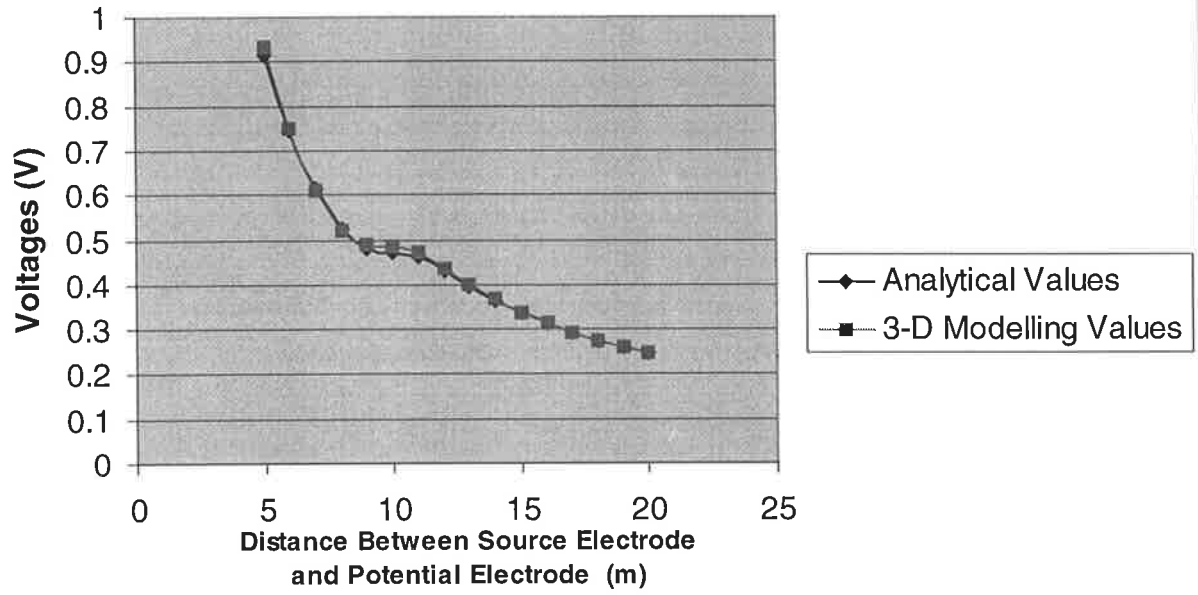

Figure 3.24 The graph shows the voltage differences between the modelling results with the 3-D resistivity modelling program and the analytical results.

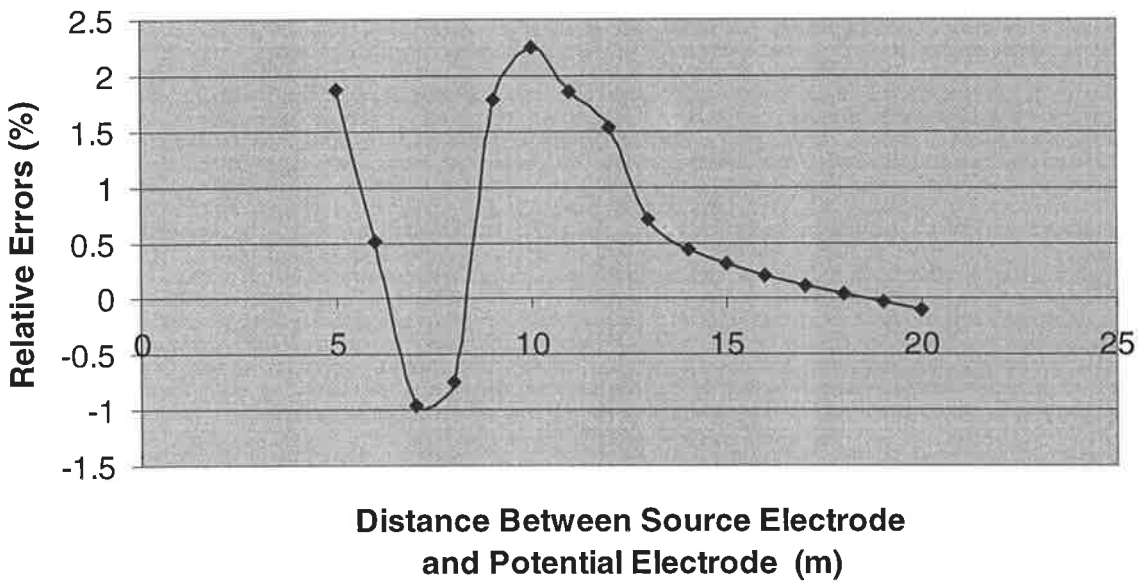

Figure 3.25 This graph shows the voltage differences among the calculated modelling results and the analytical results.

3.4.3.2 Example 1 – Comparison with the 2.5-D modelling program for a single horizontal interface

This model is exactly the same as the 2.5-D model 2-1 presented in Section 3.3.5.2, except this is a 3-D model instead of 2-D model. The purpose of this modelling is to compare the results from the 2.5-D modelling program with the 3-D program.

Only one profile has been extracted from the crosshole multiple scanning data of model 2-1. Then this profile is compared with the result from the 3-D modelling program. Figure 3.26 shows both profiles on the same graph. From the figure, it can be seen that the result is almost the same in shape and values. But the voltage values from the 3-D modelling program are slightly larger than the ones from the 2.5-D modelling program. This may be a result of using only a very limited range of wavenumber values k_y in 2.5-D resistivity modelling.

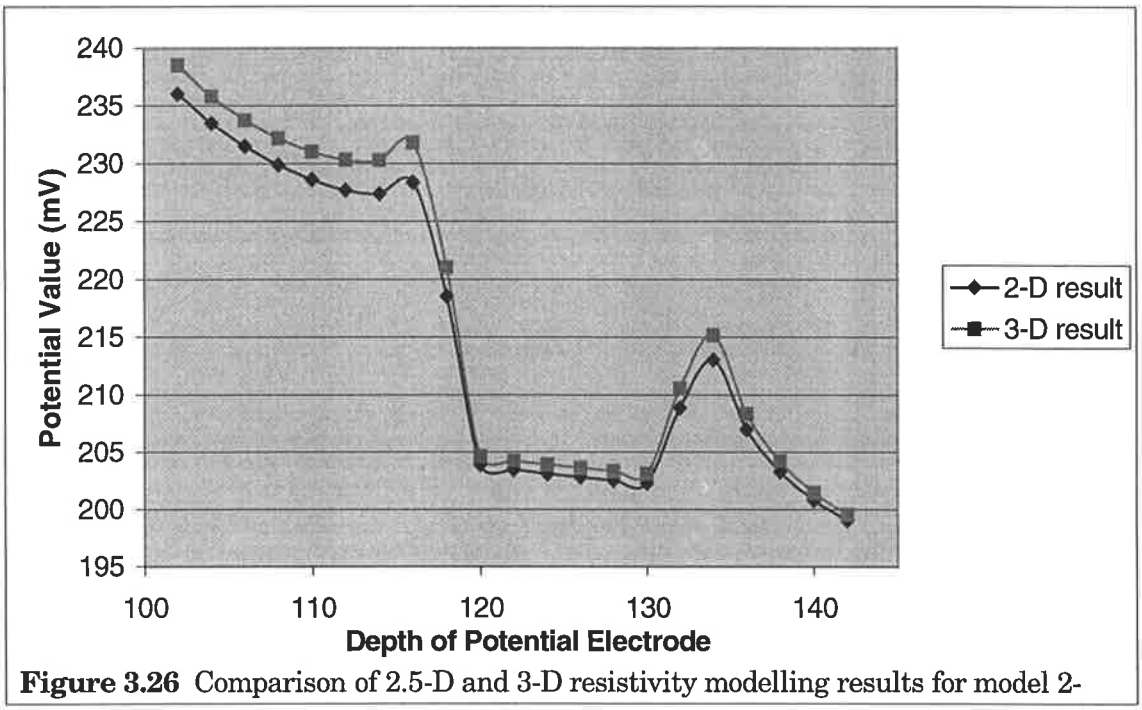

Figure 3.26 Comparison of 2.5-D and 3-D resistivity modelling results for model 2-

3.4.3.3 Example 2 – Effect of borehole water on crosshole resistivity surveys

This set of models is to examine the influence of the borehole and its contained fluid (resistivity contrast) on tomography profiles and scans.

Cross well electric imaging is a new method used in mineral and environmental exploration. In general, the wells used for this kind of surveys are filled with water. The water may be of similar or different resistivity to the formation water contained in the rock pore space. The rock will always have a higher resistivity than its contained fluid (the formation factor effect).

The borehole water normally is more conductive than fresh water because it contains dissolved mineral salts. This helps pass the electricity between the electrodes and borehole side. However when the survey data is interpreted, the borehole water effect is never considered. The following tests were designed to investigate how serious the borehole water effect is.

For this investigation, we have to use a full 3-D resistivity modelling program to simulate the borehole water effect. In 2.5-D resistivity modelling, the resistivity can only be changed in the X and Z directions, not in the Y direction, so we cannot use a 2.5-D resistivity modelling program for this situation.

The layout of the 3-D model used for this investigation is shown in Figure 3.27. It is a uniform cube with two drill holes in it. I have to assume that the wells are of a square shape (0.2m x 0.2m) in the X-Y section, in order to consider them in 3-D modelling. The distance between the two wells is 14m. There are 4 electrodes in the two boreholes. A and B are the two current electrodes and M and N are two potential electrodes. In this modelling, A and B remain towards the bottom (at a depth of 20m) of the two wells respectively. M and N are moved up simultaneously at 2-metre intervals in the two boreholes over the depth range 18m to 2m. We can obtain 12 potential values during the movements for each resistivity model. The cell size for all the models is 0.2m. So the mesh size is 100X40X125.

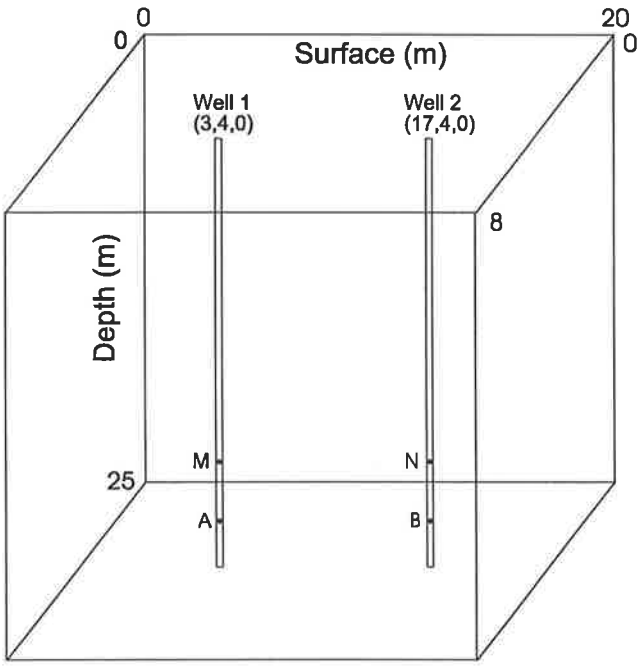

Figure 3.27 The model layout of the third set of model experiments.

With the same configuration, four sets of potential values are calculated for four different resistivity models. The first two resistivity models ignore the borehole/water effect and have constant background rock resistivity values of 200 Ω.m and 600 Ω.m, respectively. The next two models simulate the borehole water effect by changing the resistivity in the two borehole to 20 Ω.m with the background resistivity set to 200 Ω.m and 600 Ω.m, respectively.

The four groups of the calculated potentials are displayed in graphic format in Figure 3.28. Obviously, the larger the background resistivity, the larger the voltages. But one can see from the figure that the water in the boreholes indeed affects the potential values and makes the voltages higher. Apparent resistivities have been calculated from the voltages, currents and geometric factors and are shown in Figure 3.29.

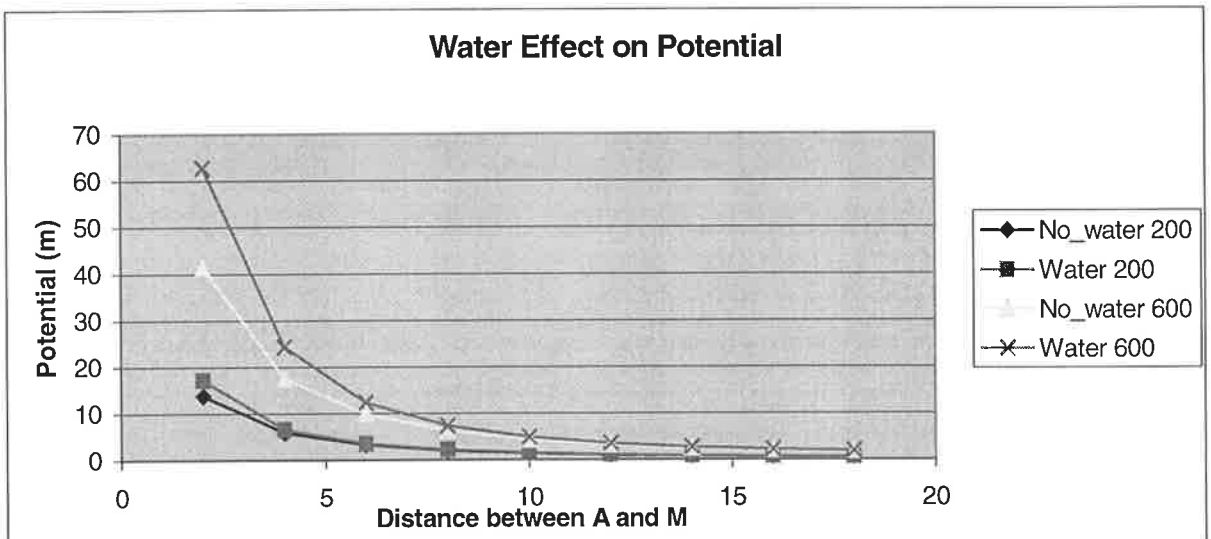

Figure 3.28 The comparison of the potential responces from four different models.

From the figure, it can be seen that the calculated apparent resistivity curves are flat lines at the correct true model resistivity (200 Ω.m and 600 Ω.m respectively) for the two uniform models. However, the water in the two boreholes changes the two apparent resistivity curves as shown in the figure, pulling the line up for the smaller AM values. It is very interesting that the low resistivity water makes the apparent resistivity higher.

The relative percentage errors were calculated by the following formula and are displayed in graphic format in Figure 3.30.

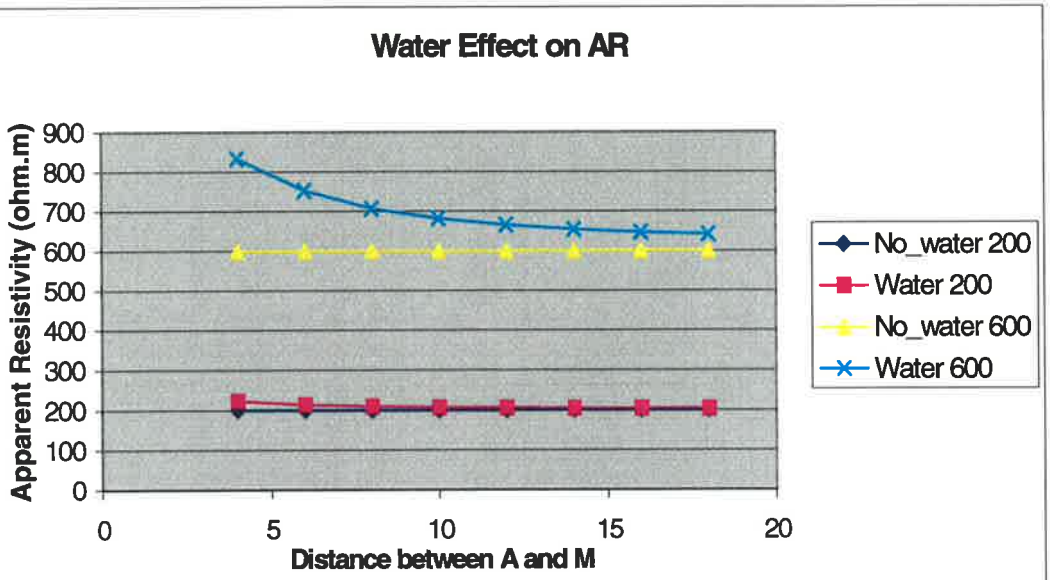

Figure 3.29 Comparison of the apparent resistivity of four different models.

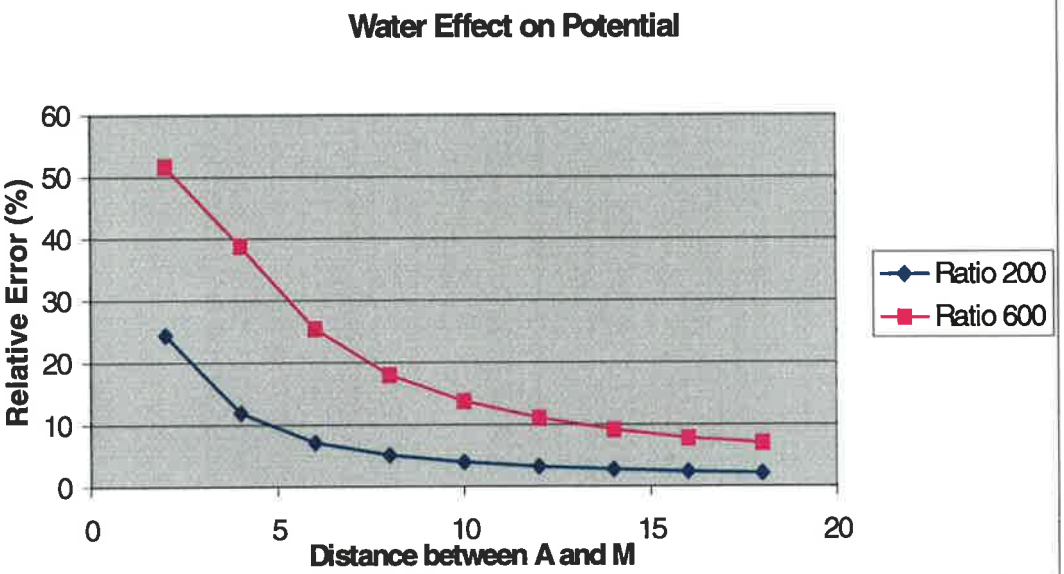

Figure 3.30 The comparison of the relative errors produced from borehole water .

Relative error = $(V_{water} - V_{no\_water}) / V_{no\_water} * 100$

where V_{water} and V_{no_water} are the voltage values for models with water and without water, respectively. The relative errors calculated from potential values are the same as those calculated from the apparent resistivities. From Figure 3.30, it is clear that the errors are mainly due to two factors. The first one is the contrast of the background resistivity and the water resistivity. The higher the contrast, the higher the error. The second factor is the distance between two electrodes AM and BN in the same borehole. The shorter the distance, the higher the errors.

From the four model tests, we know that the only thing we can do to reduce the borehole water effect is to make the distance between the two electrodes in the same borehole large, because we can not change the contrast of the background resistivity and borehole water resistivity.

In all our cross well resistivity surveys, the minimum distance between two electrodes in the same borehole is 14 metres and the contrast between the background resistivity (about 18Ω.M) and the water resistivity (about 4.5Ω.M) is not very large, So the borehole water should not produce significant distortion in any of our field surveys.

Chapter 4

INVERSION OF RESISTIVITY DATA

4.1 INTRODUCTION

Forward modelling and inversion are two basic and very important components in geophysical data processing and interpretation. Forward modelling produces the theoretical response (synthetic data) from the assumed physical properties of subsurface. For example, if the resistivity distribution in an area is given, the electric potential response from one or more current sources can be calculated with the numerical modelling technique discussed in the previous chapter. Inversion accomplishes the opposite task, and tries to find the physical property distribution (subsurface structure) from the observations. For example, after the voltages from the current sources are collected, inversion determines the actual resistivity model which best matches the observed electric potentials.

The relationships between forward modelling and inversion are illustrated schematically in Figure 4.1. From the figure, it is clear that inversion is used in geophysical interpretation to provide the best subsurface picture (physical properties) from geophysical measurements. The forward problem has to be solved first, to simulate the earth response. Only then can the inversion problem be solved with different optimisation algorithms, which try to find the optimum model, which matches observed data, with the aid of forward modelling methods. The direct, automatic adjustment of the model properties to achieve this is the essence of geophysical inversion.

Inverse theory is an organised set of mathematical techniques for reducing data to obtain useful information about the physical world on the basis of inferences drawn from observations. In other words, inversion tries to find one model from many possible models, which is the "best fit" to the observations and is stable. Regularisation and model smoothness are the other two key factors in geophysical inversion. There is no simple prescription of how to weight these three factors: data fit, regularisation (to control convergence) and degree of model complexity, in performing an inversion. All inversion results are dependent on four things: (1) the accuracy and convergence properties of the inversion algorithm, (2)

completeness of the observations, (3) presence of noise, and (4) the sensitivity of the actual measurements to the model parameters being sought.

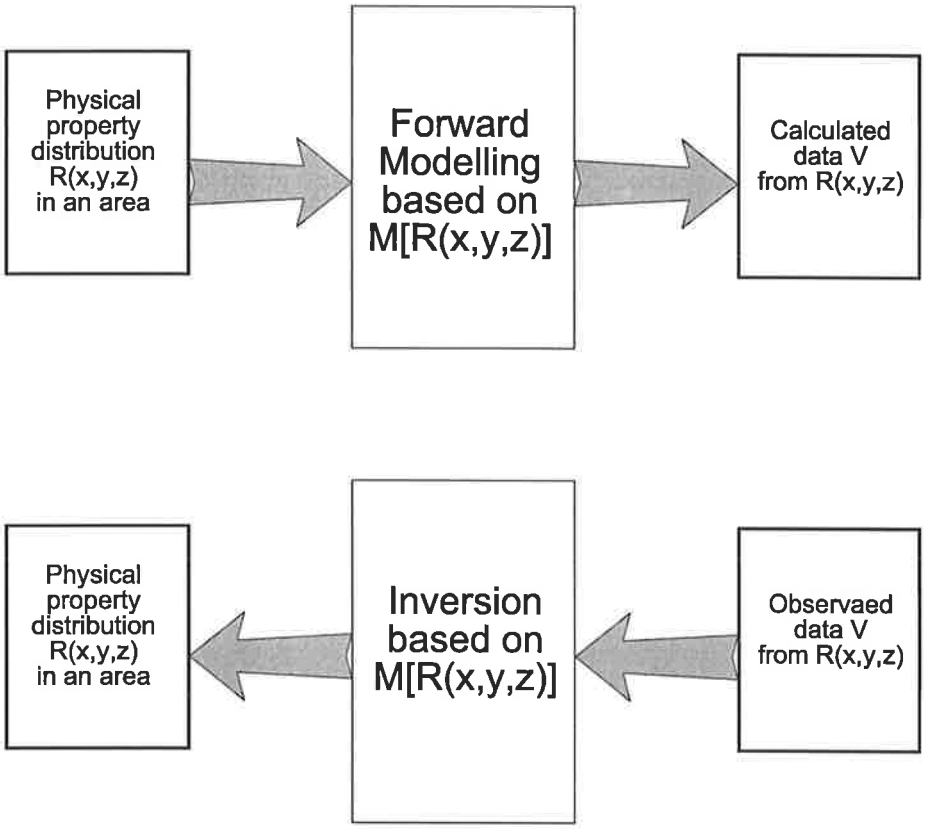

Figure 4.1 The relation among physical property distribution, observed data, forward modelling and inversion.

If the function M[R(x,y,z)] in Figure 4.1 is linear, the inversion will not be too difficult. Since we can express the problem for digital data in matrix form as

$$MR = V\,, \tag{4.1}$$

then by solving the above linear equation system with the least squares criterion, we can obtain:

$$R = (M^T M)^{-1} M^T V\,. \tag{4.2}$$

This kind of inversion is called linear inversion. The stability depends on the form of the inverse matrix $(M^T M)^{-1}$, i.e. the condition number, or ratio of largest to smallest eigenvalues of the matrix, and sparsity.

If function M[P(x,y,z)] in Figure 4.1 is non-linear, the solution of the inversion will be much more complicated. Normally, an iterative algorithm is needed to find an approximate solution

from some starting model. The resistivity inverse problem in geophysical exploration is in general non-linear. It is discussed in detail in the following sections.

Generally speaking, the forward modelling function M depends on the physics of the problem and the physical property being investigated. Different problems involve different governing equations. So the inversion function will be different as well. However, all inversion methods consist of the following three basic parts: forward modelling, setting the inversion objective function, and minimisation of the objective function.

4.2 FORWARD MODELLING

Forward modelling is a very important and necessary part of the inversion technique. It produces the synthetic earth response data from a given physical property model. The term d(m) is used to stand for the theoretical response data of forward modelling where m is the model parameters. Then the calculated response data d(m) can be used to compare with the observed data.

Modelling is related to the physical property to be inverted. So for different physical properties (eg. velocity, resistivity and magnetic susceptibility), different forward modelling functions (or different governing equations) will be used to obtain the corresponding values.

The 2.5-D and 3-D numerical resistivity forward modelling technique, as discussed in the previous chapter, will be used to produce the corresponding electric potential data for 2.5-D and 3-D resistivity inversion.

4.3 INVERSION OBJECTIVE FUNCTIONS

The second part of inversion, setting the inversion objective function, is to formulate an equation that describes what cost function we wish to minimise. The L2 norm misfit function

$$\| e \|_2 = [\sum_i | e_i |^2]^{1/2} \tag{4.3}$$

is often used as the inversion objective function in geophysical inversion. Here e_i is the error of the data fit. The L1 norm misfit function

$$\| e \|_2 = \sum_i | e_i | \tag{4.3a}$$

is another inversion objective function, which is more robust than the L2 norm misfit function if the noise in the data is not Gaussian, since it treats all errors with the same weighting function, instead of treating the larger error with the greater weights as in the L2 norm misfit

function. Since the L1 norm misfit function is not derivable at the origin, some modifications are required to find a minimum of the function (Claerbout and Muir, 1973; Wolke and Schwetlick, 1988; Madsen and Nielsen, 1993). Due to the easy implementation of the optimisation, the L2 norm inversion is more popular in geophysical inversion.

There are a few commonly used L2 inversion objective functions. The simplest one is

$$\Phi(m) = \| d_0 - d(m) \|^2 \tag{4.4}$$

where $m=\{m_1, m_2, \ldots m_n\}$ are physical property parameters, d_0 is the observed data and d(m) is the modelled data. By finding the minimum of $\Phi(m)$, we can obtain m, which will produce the best response data to fit the observed data. However, such an inversion is often ill-posed or ill-conditioned, especially in those areas of the subsurface not well constrained (perhaps through lack of coverage) and it is necessary to introduce an additional damping term to the objective function.

A more general and popular inversion objective function is

$$\Phi(m) = \Phi_d(m) + \lambda \Phi_m(m) = \| W_d(d_0 - d(m)) \|^2 + \lambda \| W_m(m - m_0) \|^2 \tag{4.5}$$

where λ is a regularisation parameter that is given before calculation, W_d and W_m are two symmetric weighting matrices of the data set and the model parameters respectively, m_0 is the initial model parameters and m is the inverted parameters. Equation (4.5) is normally called the Tikhonov function.

Similarly, by finding the minimum of $\Phi(m)$ or solving the following optimisation problem with a given λ

$$\min[\Phi(m)] = \min[\Phi_d(m) + \lambda \Phi_m(m)] \tag{4.6}$$

we can obtain the "best" model m that will be the inversion result.

Generally speaking, this part of geophysical inversion is independent of which physical property is being inverted.

4.4 SOLUTIONS OF THE OBJECTIVE FUNCTIONS

The most difficult part of inversion is to find a correct solution for an objective function. In the general case, the forward modelling function d(m) is non-linear. So it is very hard to obtain an analytical solution for equation (4.6) directly.

Mathematically, the inversion problem can be viewed as an optimisation problem. Most optimisation algorithms can be applied to solve equation (4.6), ie. a global optimisation method, such as the Monte Carlo method of exhaustive solution model space search, Simulated Annealing and Genetic algorithms. These optimisation techniques find the global minimum of the objective function in the whole model space. They do not need an initial guess model, although often restrictions will be placed on allowable parameter bounds. But for the large scale inverse problems (large number of data points and model parameters), they are very time consuming. So these global optimisation methods are often only applied to the middle scale of inversion. The popular inversion algorithms used in geophysics are the local optimisation techniques, such as the steepest descent method, conjugate gradient method, Gaussian-Newton method, all of which need an initial model and calculation of the Frechet derivatives of the data response to the model. A good starting model will aid the convergence of the inversion. The main advantages of these methods are efficiency and effectiveness in yielding a solution to equation (4.6) with a good initial guess, which may be obtained from other geological survey information.

In other words, because equation (4.6) is non-linear, you may find only one smallest misfit solution for equation (4.6). But there are many local minima solutions for equation (4.6), i.e., the topography of the solution space contains many hills and valleys. The method used to find the smallest solution is the global minimum method and the method used to find a local minimum solution is the local minimum method. Because there may be a few local minimum solutions for equation (4.6), the initial point for searching a local minimum will be critical. This is why the initial model is very important for a local minimum method. Inversion algorithms can get easily trapped in the wrong local minimum, if the initial solution is far removed from the absolute minimum.

To obtain a local minimum of $\Phi(m)$, we can differentiate equation (4.6) and set the result to zero:

$$\frac{\partial \Phi(m)}{\partial m} = \frac{\partial \Phi_d(m)}{\partial m} + \lambda \frac{\partial \Phi_m(m)}{\partial m} = 0 \ . \tag{4.7}$$

By substituting equation (4.5) into (4.7), we obtain

$$-(\frac{\partial d(m)}{\partial m})^T W_d[d_0 - d(m)] + \lambda W_m(m - m_0) = 0 \tag{4.8}$$

where $\frac{\partial d(m)}{\partial m}$ is the sensitivity (Jacobian) matrix formed by the Frechet derivatives of the synthetic data d(m). Because d(m) is non-linear, it is still very difficult to obtain a solution for equation (4.8) directly.

W_d and W_m are à priori information or weighting matrices of the observed data and model parameters, respectively. Generally W_d and W_m are set to unitary matrices since it is hard to obtain reliable statistical information about the observed data and the model parameters. So equation (4.8) becomes:

$$\lambda I (m - m_0) = (\frac{\partial d(m)}{\partial m})^T [d_0 - d(m)] \tag{4.9}$$

where I is the unit matrix.

Then an iterative approach to the solution of equation (4.6) can be constructed in the following way (Zhou, 1998). Firstly, by simultaneously adding the term $(\frac{\partial d(m)}{\partial m})^T (\frac{\partial d(m)}{\partial m})(m - m_0)$ to both sides of equation (4.9), it follows that

$$\begin{aligned} &[(\frac{\partial d(m)}{\partial m})^T (\frac{\partial d(m)}{\partial m}) + \lambda I](m - m_0) \\ &\quad = (\frac{\partial d(m)}{\partial m})^T \{[d_0 - d(m)] + (\frac{\partial d(m)}{\partial m})(m - m_0)\} \end{aligned} \tag{4.10}$$

Next, considering the matrix $[(\frac{\partial d(m)}{\partial m})^T (\frac{\partial d(m)}{\partial m}) + \lambda I]$ to be generally invertible (so long as an appropriate positive value is chosen for the parameter λ), equation (4.10) can be rewritten as follows:

$$\begin{aligned} m = m_0 + &[(\frac{\partial d(m)}{\partial m})^T (\frac{\partial d(m)}{\partial m}) + \lambda I]^{-g} \\ &(\frac{\partial d(m)}{\partial m})^T \{[d_0 - d(m)] + (\frac{\partial d(m)}{\partial m})(m - m_0)\} \end{aligned} \tag{4.11}$$

Finally, an iterative approach to solving equation (4.6) is suggested:

$$\begin{aligned} m_{k+1} = m_0 + &[(\frac{\partial d(m_k)}{\partial m})_k^T (\frac{\partial d(m_k)}{\partial m})_k + \lambda I]^{-g} \\ &(\frac{\partial d(m_k)}{\partial m})_k^T \{[d_0 - d(m_k)] + (\frac{\partial d(m_k)}{\partial m})_k (m_k - m_0)\}, \\ &(k = 0,1,2,3,....). \end{aligned} \tag{4.12}$$

where the superscript -*g* denotes the general inverse matrix. By subtracting m_k from both sides of the above equation then combining the terms of $(m_k - m_0)$, an alternative form for the solution is obtained:

$$m_{k+1} = m_k + [(\frac{\partial d(m_k)}{\partial m})_k^T (\frac{\partial d(m_k)}{\partial m})_k + \lambda I]^{-g}$$
$$(\frac{\partial d(m_k)}{\partial m})_k^T \{[d_0 - d(m_k)] - \lambda(m_k - m_0)\}, \qquad (4.13)$$
$$(k = 0,1,2,3,.....).$$

Equation (4.13) is the generalised iterative solution for equation (4.6). For further details, the reader is referred to Zhou (1998).

4.5 CALCULATION OF THE FRECHET DERIVATIVES

Before using formula (4.13) to calculate the solution for equation (4.6), one must obtain the Frechet derivative of the synthetic data d(m_k): $(\frac{\partial d(m_k)}{\partial m})$. In this section I will discuss how this is done.

To date, many researchers have introduced various methods to calculate the Fréchet derivative, such as McGillivray and Oldenburg (1990), Boerner and Holladay (1990) and, Park and Van (1991). Zhou and Greenhalgh (1995,1998) developed a new method to compute the relevant derivatives for crosshole resistivity imaging and seismic full-waveform inversion in the frequency-domain. The computations are based on the numerical solution of the 2.5-D Helmholtz equation and are implemented with nearly the same scheme for both 2.5-D resistivity and acoustic problems. Firstly, by performing some differential calculus and applying the 2.5-D Green's functions, the general expressions for these derivatives are explicitly obtained for any configuration in DC surveying (four kinds of electrode arrays: pole-pole, pole-bipole, bipole-pole and bipole-bipole).

A calculation formula for apparent resistivity using all four kinds of electrode arrays was derived by Zhou (1998). It operates in the k_y frequency domain and is given by:

$$\frac{\partial \rho_a}{\partial \sigma_i} = -\frac{K}{2} F_c^{-1}[\nabla \delta\overline{G}_{AB}(r_i) \cdot \nabla \delta\overline{G}_{MN}(r_i) + k_y^2 \delta\overline{G}_{AB}(r_i)\delta\overline{G}_{MN}(r_i)] \qquad (4.14)$$

where $\delta\overline{G}_{LJ}(r_i) = \overline{G}(r_i, r_L) - \overline{G}(r_i, r_J)$, L=A or M and J=B or N, $\overline{G}(r_i, r_J)$ is the Greens function in the k_y domain, F_c^{-1} stands for inverse Fourier transform, K is the electrode geometry factor, and ρ_a is apparent resistivity.

With the aid of this formula, it is straightforward to obtain the solution of equation (4.6).

4.6 A FAST 3-D RESISTIVITY IMAGING METHOD

From Section 4.4, we know that an initial model is very important and sensitive for a local minimum inversion solution. So a good method to choose the right initial model is needed. Zhou and Greenhalgh (2002) developed a new scheme for 2-D/3-D crosshole resistivity imaging for all measurements configurations. The scheme consists of two steps: building up a crosshole approximate resistivity image as an initial image; (2) implementing tomographical inversion with the initial image as the starting model and obtaining the final image subject to geophysical logging and geological constraints. For completeness, I will give a brief review of the first part of the scheme.

The resistivity anomaly image is calculated by the following equation:

$$\tilde{\rho}^*(r) = \tilde{\rho}_{ref}(r) + D(r)\{(\frac{\partial\tilde{\rho}_a(\tilde{\rho}_{ref})}{\partial\rho(r)})^T_{ref}[\tilde{\rho}_a^{ob} - \tilde{\rho}_a(\tilde{\rho}_{ref})]\} \tag{4.15}$$

where $\tilde{\rho}_a^{ob}$ and $\tilde{\rho}_a(\tilde{\rho}_{ref})$ are the observed and synthetic apparent resistivity; $\tilde{\rho}_{ref}$ denotes a reference model; $\frac{\partial\tilde{\rho}_a(\tilde{\rho}_{ref})}{\partial\rho(r)}$ is the sensitivity function of electrical measurements from the reference model (Zhou and Greenhalgh 1999); *D(r)* is the normalised matrix operator defined by

$$D(r) = diag\{\delta\rho_{\max}\left[\left\|\tilde{\rho}_a^{ob} - \tilde{\rho}_a(\tilde{\rho}_{ref})\right\|\left\|\frac{\partial\tilde{\rho}_a}{\partial\rho(r)}\right\|\right]^{-1}\} \tag{4.15A}$$

so that the calculated values do not exceed the bound of the resistivity variation $\delta\rho_{\max}$. Considering the reference model $\tilde{\rho}_{ref}$ to be uniform, eg an average of the observed apparent resistivities $\tilde{\rho}_a$, or a kind of the average value of the weighted apparent resistivities, the calculation of $\tilde{\rho}^*(r)$ becomes very simple because the synthetic response $\tilde{\rho}_a(\tilde{\rho}_{ref})$ is constant and the sensitivity function $\frac{\partial\tilde{\rho}_a}{\partial\rho(r)}$ can be obtained by using the analytic expressions of Zhou and Greenhalgh (1999). Equation (4.15) does not involve any inversion or data-fit to

find the real model, but implies that the relative apparent resistivity anomaly $[\tilde{\rho}_a^{ob} - \tilde{\rho}_a(\tilde{\rho}_{ref})]$ is migrated to the spatial points in the model domain in terms of the different values of the sensitivity function $\frac{\partial \tilde{\rho}_a}{\partial \rho(r)}$. So, it is called approximate resistivity imaging. Synthetic experiments show that the resistivity anomaly image may give a good match to the 2-D/3-D real model with any crosshole electrode configuration (Zhou & Greenhalgh, 2002) and it can be used as an initial model for a further inversion.

4.7 APPROXIMATE NUMERICAL RESISTIVITY IMAGING EXPERIMENTS

According to the principle described in the above section, a 2-D/3-D imaging program was developed to produce resistivity images from the 'survey data' by a simple calculation (see equation (4.15)). A few sets of model data produced in Chapter 3 for the modelling experiments are used for the imaging experiments in this chapter as well. In the following subsections I will present and discuss the imaging results from the synthetic examples (modelling data). Later, in chapters 8 and 9, more imaging results will be produced as an integral part of the field data interpretation.

To speed up the imaging process, a smaller grid mesh size (large grid cell size) was used in all synthetic examples. So all imaging results are a little smaller in size than the original models, which can be seen from the next few figures. But this did not affect the imaging results.

4.7.1 Horizontal and Vertical Interface Models

The input data for this set of imaging is from the synthetic modelling data of Chapter 3. Two 3-D images have been produced from the two 2.5-D modelling results for a horizontal interface model (Fig. 3.7) and a vertical interface model (Fig. 3.8). The 2-D approximate images obtained at Y=0 are displayed in Figures 4.2 and 4.3 with all survey layout and model parameters superimposed. From Figure 4.2, it can be seen that the two horizontal layers are shown at the correct position, with the interface at a depth of approximately 130m. The average resistivity of the top layer is about 37 Ω.m and that of the bottom layer is about 80 Ω.m. Both numbers are not exactly the same as the true model resistivities, of 30 Ω.m and 100 Ω.m. According to our imaging and inversion experience, it is impossible to obtain the precise resistivity distribution with spatially limited data. The result from the approximate imaging program for the horizontal interface model is very good, because it shows the two-layer structure at the right position and in the right resistivity order.

The imaging result for the vertical interface model synthetic data is shown in Figure 4.3. The result is confusing at first glance because it shows not only a contrast in the horizontal direction, but also in the vertical direction. Then after examining the colour index bar more closely, we can see the range of resistivity variation is only about 1 Ω.m. This is very small, almost at the noise level. So this imaging result does not yield much useful information. We will later examine the full inversion result of the model to see if it can give a better result.

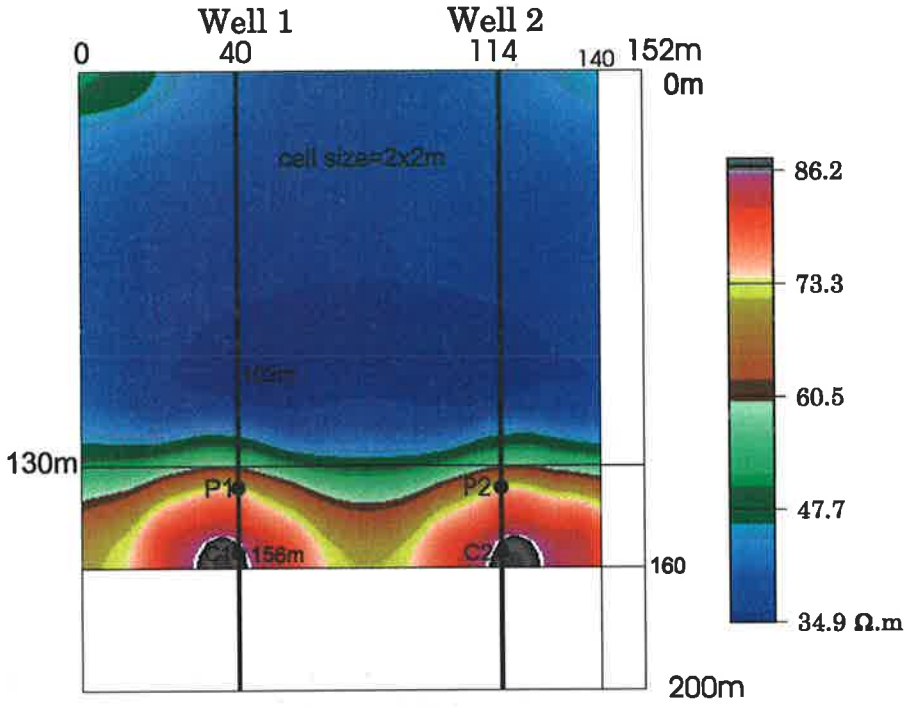

Figure 4.2 The approximate image results for the horizontal interface model.

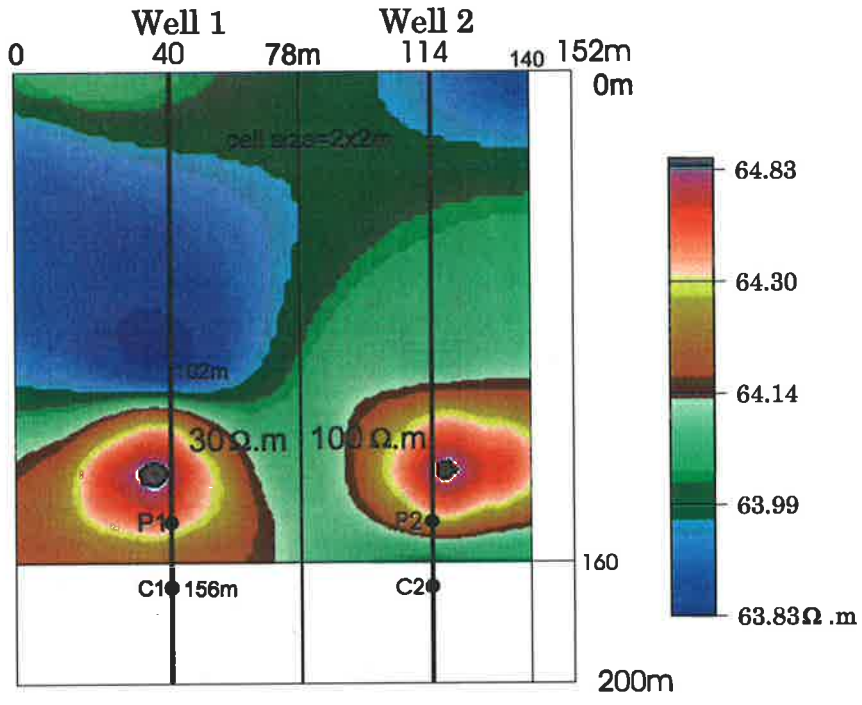

Figure 4.3 The approximate image result for the vertical interface model.

4.7.2 Discontinuous Conductor Models

The three approximate imaging results for the continuous, discontinuous and faulted conductor models are shown in Figure 4.4, with the recording geometry and true model superimposed. From the figure, we can see that the imaged results are very good because they show the conductive zones at the right position. However, there is not a great deal of difference between diagrams (a) and (b) in Figure 4.4, for continuous and discontinuous conductor models. The reason is that the conductor is quite thin, the gap in the middle for the broken conductor is small, and the crosshole measurements are not very sensitive to the horizontal resistivity variation. Diagram (c) in Figure 4.4 shows the slope from left to right, which roughly matches with downthrow of the fault. For the same reason, it is impossible to image the small gap in the middle of the conductor.

4.7.3 Approximate Imaging Conclusions

From the above experiments, we can see that the quick imaging procedure works well because it gives a preliminary resistivity distribution map from the 'survey' data. It gives the main structure of the original models. Because the imaging method is only an approximate resistivity recovery technique, not like inversion, one can not expect it to give a very good result which can match with the original model.

From the discussion in Section 4.4, we know that a good initial model is needed for all local inversion solutions and the initial model is also very important for a correct inversion result. Because the imaging program can produce a reasonable resistivity distribution image, such an image may be used as an initial model for further investigation with the full inversion program. This is demonstrated below.

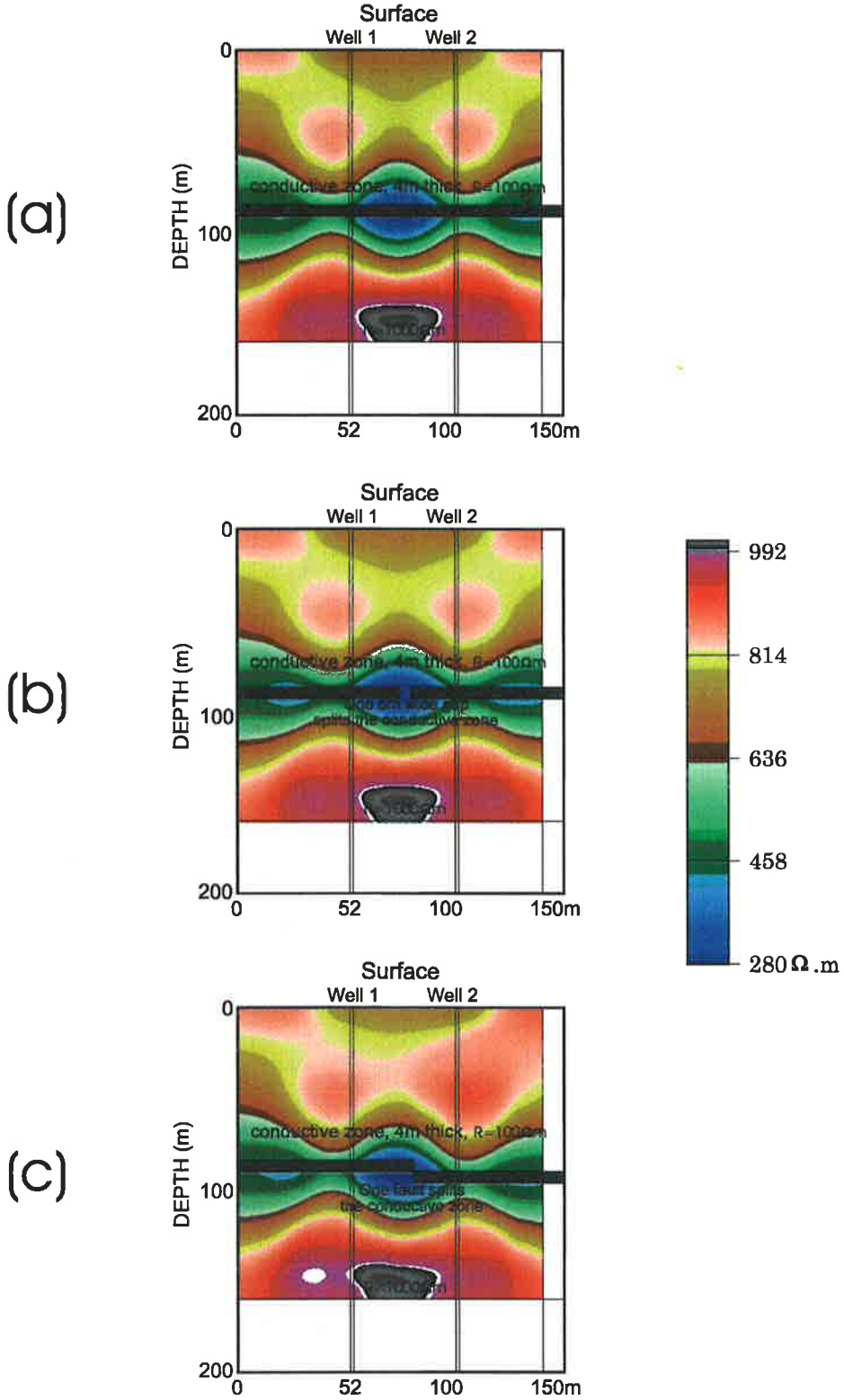

Figure 4.4 The imaging results of the second set of resistivity models: (a) a model with a continous conductive zone at depth 90m; (b) a model having a 4m wide gap within the conductive zone; (c) a model having a fault disrupting the conductive zone.

4.8 NUMERICAL RESISTIVITY INVERSION EXPERIMENTS

Six full inversions have been performed for the six models described in the previous section. They are displayed in Figures 4.5 to 4.8.

The image in Figure 4.5 is the inversion result for the two horizontal layer model. It is better than the preliminary (approximate) image and gives a clear two-layer structure picture. However, in the middle part between two wells, the interface between two layers is not very clear. This is because only 14m and 28m spacing scanning data was produced from the forward modelling and was used here for this inversion. The 14m and 28m spacing scanning data are not very sensitive to the resistivity in the middle part between two wells when the distance between two wells is much larger than 28 m.

Figure 4.6 shows the inversion result of the model with a vertical interface in the middle. From the color bar, one can see that the variation of the resistivity in the whole range is only 1 Ω.m. This means that the whole area is almost uniform. By analysing this model, I realise that there is no problem in the inversion program. The problem is that one can obtain the same voltage response after swapping the resistivities between two sides, i.e. changing the resistivity of the left side from 30 Ω.m to 100 Ω.m, and changing the resistivity of the right side form 100 Ω.m to 30 Ω.m. So it is impossible for the inversion program to recover the correct result. The problem with the vertical fault model must depend on the electrode array chosen. If for example measurements are taken with all four electrodes in one borehole at the same time, that would provide information on the difference in resistivity between the two sides. But no such information is revealed with the array used.

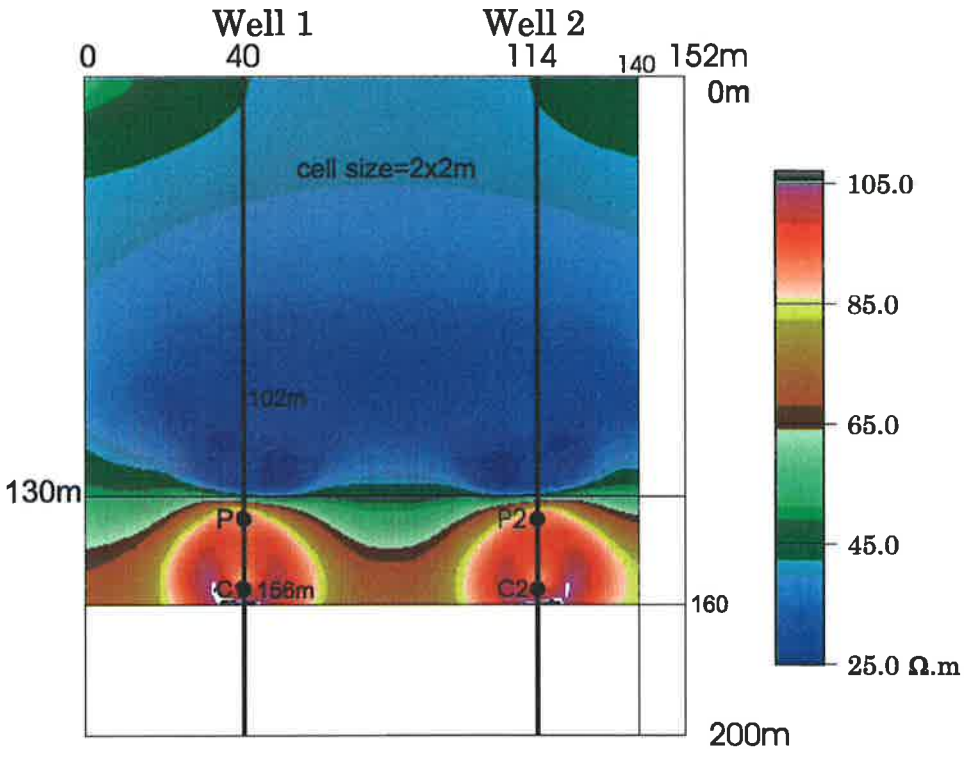

Figure 4.5 The full inversion result for the horizontal interface model.

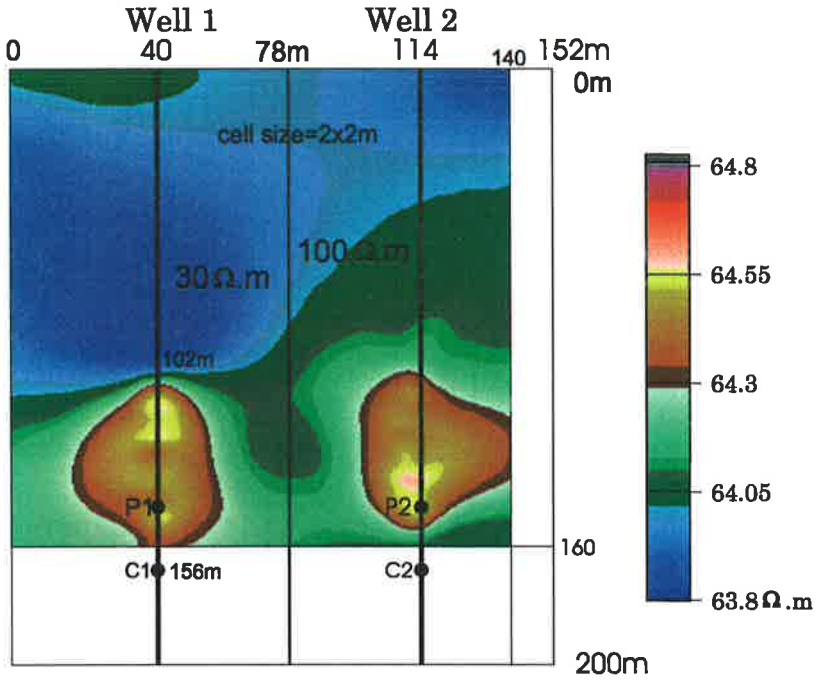

Figure 4.6 The full inversion result for the vertical interface model.

Figure 4.7 shows the inversion results for the thin conductor model experiments. The first two images match the original models pretty well except that the conductive zone is a little wider than the original model. The third image shows the slope well but it does not display the actual fault.

The last figure (Figure 4.8) shows the inversion results for the two square model experiments (refer to Section 3.3.5.4). From the figure, one can see that the two square anomalies are clearly shown in the right position, although the resistivity contrasts between the background and anomaly are not as high as the original contrast. This proves that the inversion program can produce fairly good resistivity images for the middle part of two wells, if enough data points are obtained and if the survey configuration coverage is adequate.

More inversion results of the modelling data and real surveys will be shown in the next few chapters.

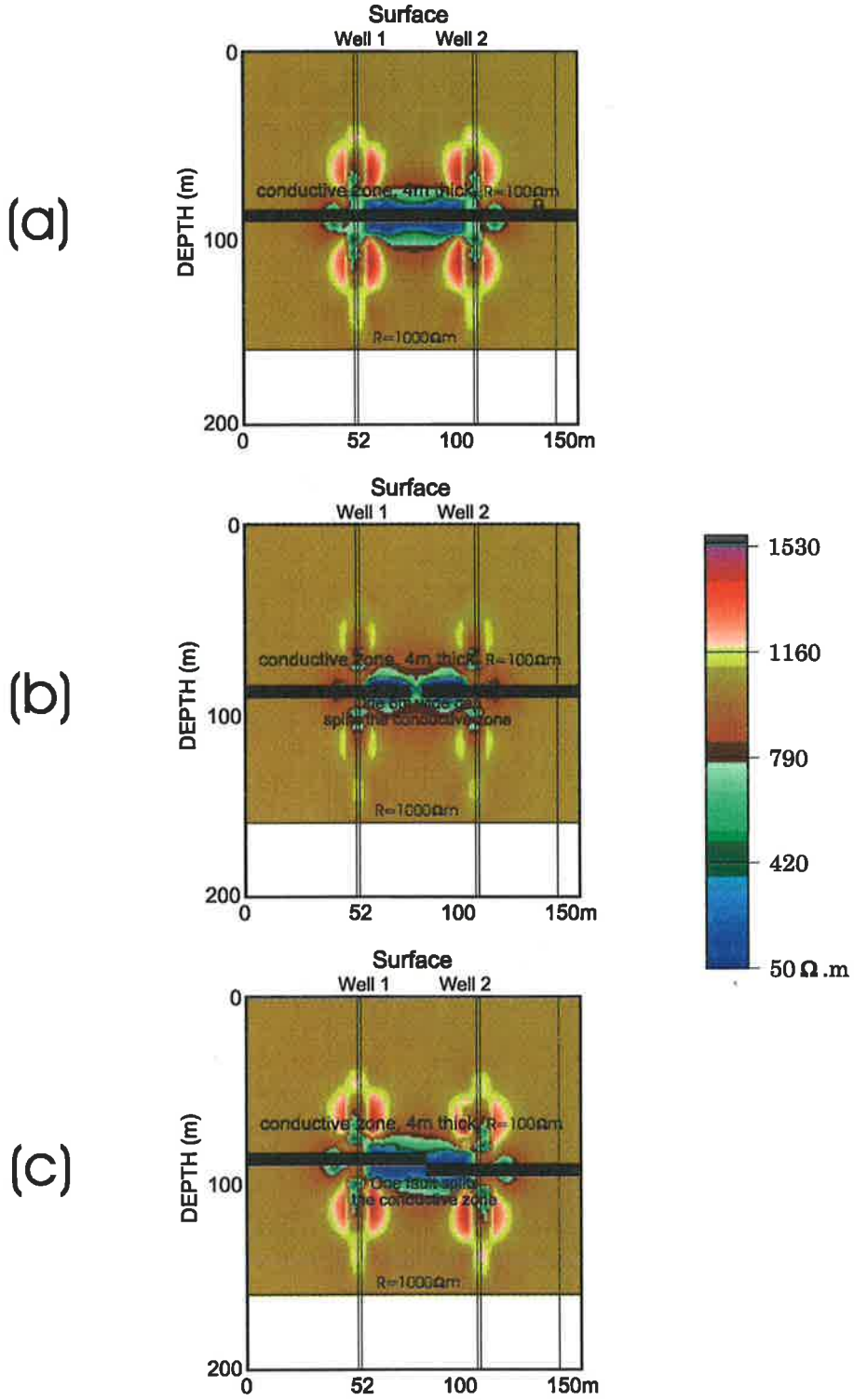

Figure 4.7 The inversion results of the second set of resistivity models: (a) a model with a continous conductive zone at depth 90m; (b) a model having a 4m wide gap spliting the conductive zone; (c) a model having a fault splitting the conductive zone.

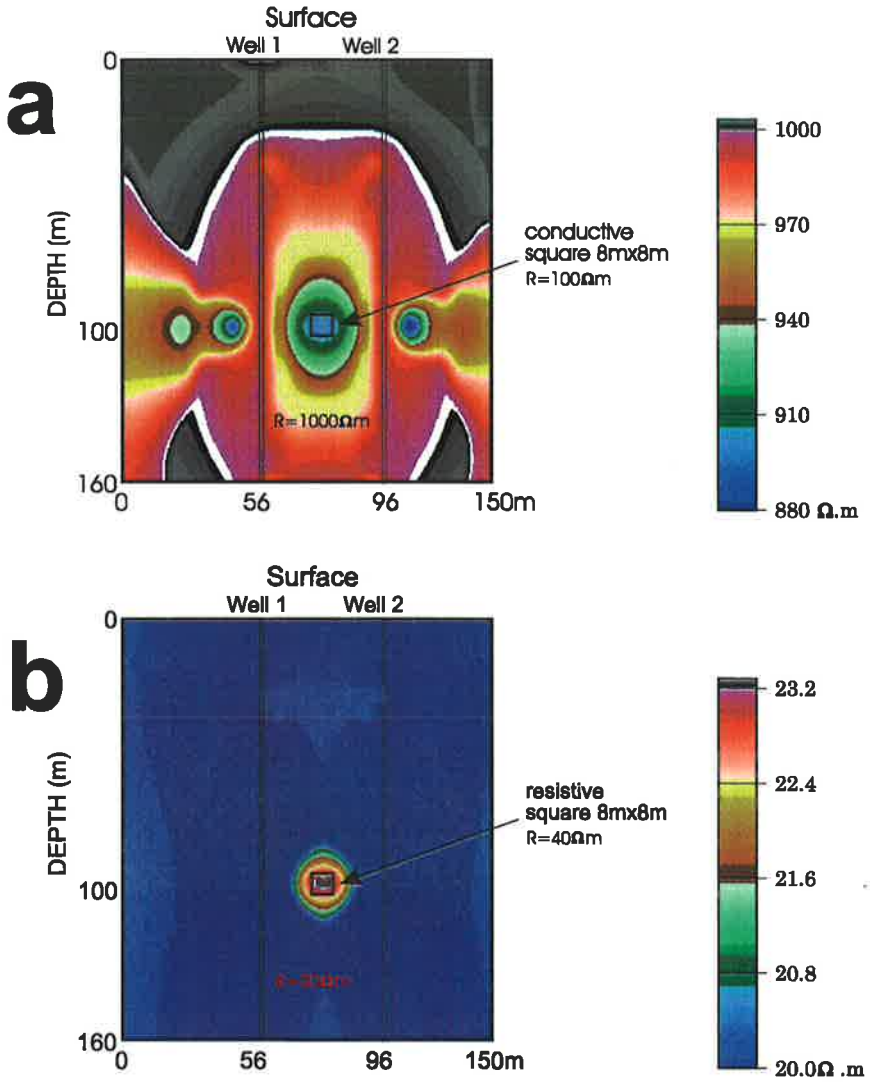

Figure 4.8 The inversion results of the two square models. Graph **a** is for the 'conductor' model and graph **b** is for the 'resistive body' model.

Chapter 5

3-D AUTOMATED LABORATORY ELECTRICAL MODELLING SYSTEM

5.1 INTRODUCTION

Electric scale modelling in the laboratory has been carried out and reported by a number of researchers (Jakosky, 1961; Goudswaad, 1957;Apparao, 1979; Apparao and Roy, 1971, 1976; Singh et al., 1971; Topfer, 1972; Karwatowski and Habberjam, 1981; Jackson, 1981; Kumata et al, 1993, 1995). The investigations have ranged from considerations of the effect of the tank wall composition on apparent resistivity determinations (Goudswaad, 1957) to resistivity tomography experiments (Kumata et al, 1995). The studies by Apparao and co-workers (1971 and 1976) were mainly concerned with questions of detection, resolution and interpretation of buried conducting dykes and other structures.

In such physical modelling, water is normally used to simulate the host rock medium. Various metals (eg. aluminium, steel, brass) and graphite are used to simulate subsurface conductors like ore bodies, while insulating rocks can be represented by plexiglass, plastic and glass. In electromagnetic modelling, one must be careful to take account not only of scaling differences for resistivity contrasts between the laboratory and the field situation, but also for length scale differences and also for frequency (or time) differences. But in DC resistivity modelling, the scaling laws (or similitude relations) are very simple (Telford et al, 1990), and involve simply the geometric factor for electrode separation or target depth. So with a scaling factor of 1000, a distance of 1 cm in the laboratory model would be equal to 10 m in the field situation. The resistivity contrast should be chosen to closely match the real (field) situation. But it is understood that the resistivity method, unlike the EM method, suffers from a saturation effect, such that beyond a certain contrast, increasing it any more does not affect the measured results. There is a substantial resistivity contrast between standard laboratory materials like fresh water

(eg. host rock) and suspended metal objects (eg. ore body) which can be reduced by increasing the salinity of the water.

My goal was to build a resistivity physical modelling system with a water tank to mainly simulate the crosshole resistivity situation with fully automatic control for moving electrodes and data acquisition. The system was designed to mainly produce bipole-bipole crosshole resistivity data and to understand the potential responses for different geologic structures. Since no one has yet developed a satisfactory method to display resistivity tomography data, it is very important to understand the response patterns of geological structures with 3-D physical resistivity modeling. Analogue models can also produce real data to test our inversion program. Because the design goal of the resistivity modelling system is to be fully automatic, it should work very efficiently. There is no mention in the literature to date of any resistivity physical model system that is fully automatic.

The design of the Adelaide University 3-D physical resistivity modelling system has been finished but the construction of the system has been only partly completed.

5.2 OBJECTIVES AND DESIGN CRITERIA FOR THE 3D PHYSICAL RESISTIVITY MODELLING SYSTEM

The main objectives in building a 3-D physical resistivity modelling system were to efficiently simulate crosshole resistivity surveys, to understand the potential distribution in some special models, and to provide real data for testing the inversion program. To obtain high efficiency for modelling, the system should be fully automated, which includes automatic positioning of electrodes, automatic current injection (on and off) and automatic data logging. The bipole-bipole configuration will mainly be used, since it is too hard to put a 'remote electrode' in the small water tank and the bipole-bipole configuration is the most effective one for crosshole resistivity imaging (Zhou 1998). Other configurations, such as the pole-pole or pole di-pole, may be simulated in the system as well, but it may produce large errors due to the very limited 'infinite distance' requirement on the current sink and/or reference potential electrode in any "pole" system. It should also be kept in mind that the tank boundary effect might be very serious when any electrode is too close to the tank edge to simulate the infinite electrode situation.

A design diagram, according to the above ideas, is presented in Figure 5.1. To simulate bipole-bipole surveying, the current electrode A and the potential electrode M are always in one 'borehole' and the distance between A and M is fixed for each scanning. So the electrodes A and M are always moved up and down simultaneously. Therefore only three stepper motors are needed to drive the pair of electrodes over the 3-D range. The same applies for current electrode B and potential electrode N. As such, two pairs of electrodes can be moved to anywhere in the water tank by two sets of three stepper motors which are controlled by a personal computer via the 'MAIN CONTROL BOX', as shown in Figure 5.1.

From Figure 5.1, one can see that all the stepper motors, the power control box, and the acquisition system are controlled by a PC via a microcontroller control board or MAIN CONTROL BOX. The normal procedure for obtaining one set of data is as follows. Firstly, the personal computer sends commands to the microcontroller to move the 2 sets of electrodes (via 6 stepper motors) to specified positions. Then the microcontroller sends a signal to the STEPPER MOTOR CONTROL BOX to drive 6 stepper motors for moving the electrodes to exact positions. After this moving task is finished, the microcontroller sends a signal to the computer to tell the computer that the job is done. Next the computer sends the acquisition parameters (for example, output current polarity change sequence and time, acquisition time interval, and so on) to the microcontroller and asks the microcontroller to start the acquisition procedure. Then the microcontroller sends the signals to the CURRENT OUTPUT CONTROL box to turn the current power on/off and change the polarity, according to the required time sequences. At the same time, the microcontroller triggers the acquisition system to start to acquire data and the computer receives digital data from the acquisition system via a fast serial port, which helps to speed the data transfer between the acquisition board and the computer. After the data acquisition is finished, the computer can start another procedure to obtain another set of data. In this way, the computer can finish the whole 'survey' without any interference. Normally the survey plan or acquisition procedures can be setup on the computer first. Then the computer completes the acquisition procedures one by one automatically. This will save an operator a lot of time and make it work very efficiently. A full survey can be programmed to run unattended and it may take only a few hours to complete the whole survey. For example, if it takes 20 seconds to shift the electrodes to the right positions and to acquire one set of data, it takes about 4.8 hours to complete a scanning procedure with 31x31=961 sets of data. This would take a few days if it was done manually.

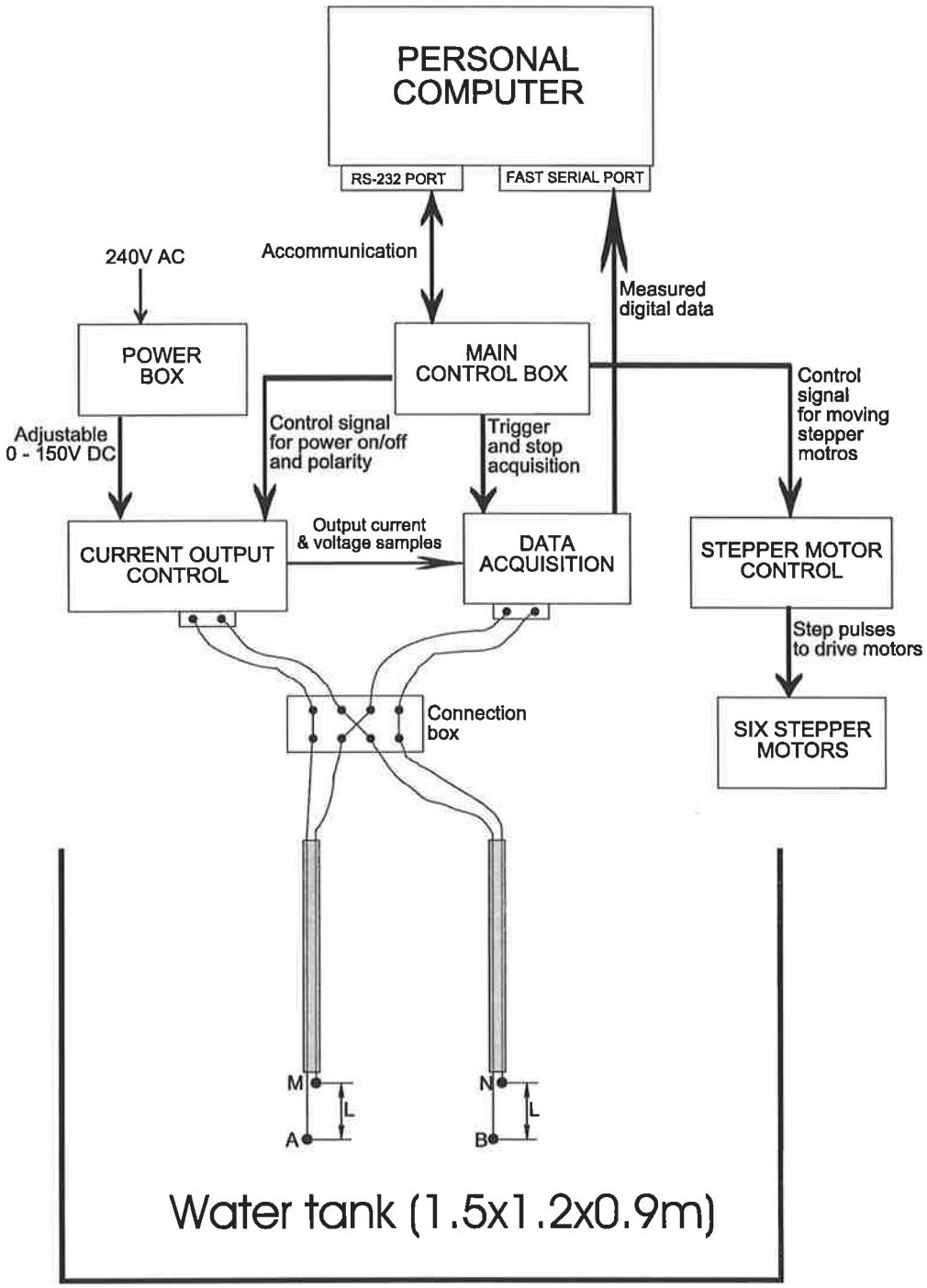

Figure 5.1 3-D physical resistivity modelling system design diagram.

In the following sections I will give a more detailed explanation about each part of the system.

5.3 MECHANICAL DESIGN

The first thing to be considered in designing the 3-D physical resistivity modelling system is the size of water tank. In theory, the larger the water tank, the better the modelling result, because a larger water tank will have less boundary effect. The plastic insulating sides prevent current from flowing outwards, forcing it to be deflected ("reflected") and to flow entirely tangentially along the boundaries of the tank. This has the effect of increasing the current density elsewhere in the volume of the tank. Due to the limitation of the available space in the lab and available plastic containers, a $1.5x1.2x0.9m^3$ plastic water tank was chosen for the 3-D physical resistivity modelling system. Even for this size of the water tank, a steel frame has to be built to support all sides of the water tank to prevent it from breaking under the water pressure, as shown in Figure 5.2. The plastic water tank can contain all sorts of liquids and solid materials for constructing different 'real' geological models.

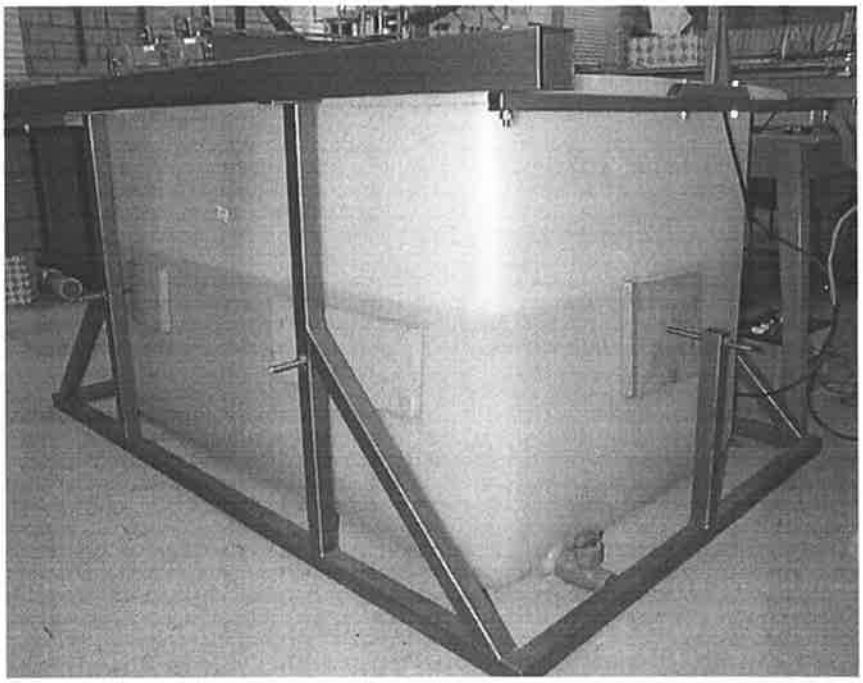

Figure 5.2 The photograph of the water tank with the steel support frame.

In order to assess how serious the water tank boundary effect is, the following analytical calculations were completed. Only the bipole-bipole configuration is considered for the boundary effect test, because this is the main electrode array used in the physical modelling system. The calculation is based on configuration shown in Figure 5.3. The four electrodes are set to the central part of the water tank, a certain distance apart as shown in Figure 5.3. Firstly, the

potentials P_{MN_1} between two potential electrodes M and N are calculated ignoring the side and bottom boundary effects (considering the top boundary effect only). Secondly, the potential P_{MN_2} is calculated again but this time taking account of the first-order reflections from all boundaries (including the top boundary effect as well). Potentials P_{MN_1} and potentials P_{MN_2} are calculated with the following analytic formulas (since the tank is made of plastic, the complete "reflection" from all boundaries is assumed):

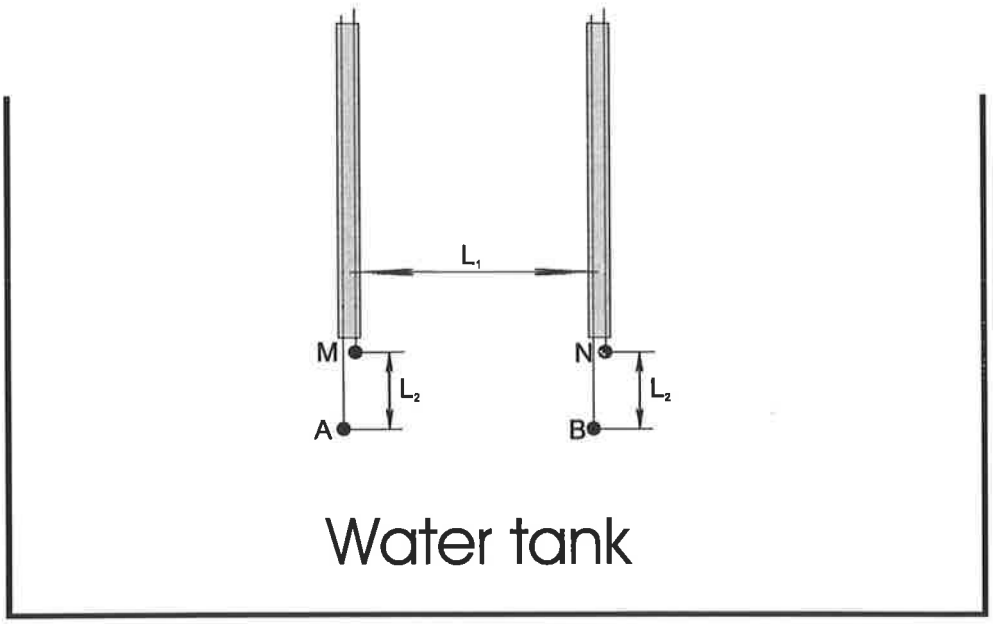

Figure 5.3 The configuration for calculating the tank boundary effects.

$$P_{MN} = \frac{I\rho}{4\pi}\left(\frac{1}{D_{AM}} - \frac{1}{D_{BM}} - \frac{1}{D_{AN}} + \frac{1}{D_{BN}}\right) \tag{5.1}$$

$$P_{MN\_top} = \frac{I\rho}{4\pi}\left(\frac{1}{D_{AtopM}} - \frac{1}{D_{BtopM}} - \frac{1}{D_{AtopN}} + \frac{1}{D_{BtopN}}\right) \tag{5.2}$$

$$P_{MN\_bottom} = \frac{I\rho}{4\pi}\left(\frac{1}{D_{AbottomM}} - \frac{1}{D_{BbottomM}} - \frac{1}{D_{AbottomN}} + \frac{1}{D_{BbottomN}}\right) \tag{5.3}$$

$$P_{MN\_left} = \frac{I\rho}{4\pi}\left(\frac{1}{D_{AleftM}} - \frac{1}{D_{BleftM}} - \frac{1}{D_{AleftN}} + \frac{1}{D_{BleftN}}\right) \tag{5.4}$$

$$P_{MN\_right} = \frac{I\rho}{4\pi}\left(\frac{1}{D_{ArightM}} - \frac{1}{D_{BrightM}} - \frac{1}{D_{ArightN}} + \frac{1}{D_{BrightN}}\right) \tag{5.5}$$

$$P_{MN\_front} = \frac{I\rho}{4\pi}\left(\frac{1}{D_{AfrontM}} - \frac{1}{D_{BfrontM}} - \frac{1}{D_{AfrontN}} + \frac{1}{D_{BfrontN}}\right) \tag{5.6}$$

$$P_{MN\_back} = \frac{I\rho}{4\pi}\left(\frac{1}{D_{AbackM}} - \frac{1}{D_{BbackM}} - \frac{1}{D_{AbackN}} + \frac{1}{D_{BbackN}}\right) \tag{5.7}$$

$$P_{MN\_1} = P_{MN} + P_{MN\_top} \tag{5.8}$$

$$P_{MN\_2} = P_{MN} + P_{MN\_top} + P_{MN\_bottom} + P_{MN\_left} + P_{MN\_right} + P_{MN\_front} + P_{MN\_back} \tag{5.9}$$

where D_{IJ} means the distance from current electrode I to potential electrode J and the subscripts on D, Ax and Bx, stand for the image current source positions.

Then the ratio Q (%) between P_{MN_2}-P_{MN_1} and P_{MN_1} is calculated as:

$$Q = \frac{P_{MN\_2} - P_{MN\_1}}{P_{MN\_1}} \times 100 \tag{5.10}$$

From the abovc formulas, we know that current I and resistivity ρ of the medium in the water tank will affect P_{mn_1} and P_{mn_2} , but not Q, since both I and ρ can be cancelled from the above formula.

As shown in Figure 5.3, we set the horizontal distance between AM and BN to L_1 and set the vertical distance between A and M to L_2 (the distance between B and N is always the same as the distance between A and M). Then $Q(L_1,L_2)$ is calculated with the current I=100mA and resistivity ρ=10Ωm, as both L_1 and L_2 are changed from 6cm to 42cm. The calculated values of $P_{MN\_1}(L_1,L_2)$ are shown in Table 5.1. The values for $P_{MN\_2}(L_1,L_2)$ are given in Table 5.2 and the values for $Q(L_1,L_2)$ are given in Table 5.3. The tabular data are also shown in graphic format from Figure 5.4 to 5.6.

Table 5.1 The calculated potential response Pmn_1(L1,L2), unit is V.

	L1 (cm)										
	0	6	10	14	18	22	26	30	34	38	42
	6	0.78	1.29	1.61	1.82	1.96	2.06	2.14	2.20	2.25	2.29
	10	0.23	0.47	0.67	0.82	0.94	1.03	1.10	1.15	1.20	1.24
	14	0.09	0.21	0.34	0.44	0.53	0.61	0.67	0.72	0.76	0.80
L2 (cm)	18	0.05	0.11	0.19	0.26	0.33	0.39	0.44	0.49	0.52	0.56
	22	0.03	0.07	0.12	0.17	0.22	0.27	0.31	0.35	0.38	0.41
	26	0.02	0.04	0.08	0.11	0.15	0.19	0.23	0.26	0.29	0.32
	30	0.01	0.03	0.05	0.08	0.11	0.14	0.17	0.20	0.23	0.25
	34	0.01	0.02	0.04	0.06	0.09	0.11	0.14	0.16	0.19	0.21
	38	0.01	0.02	0.03	0.05	0.07	0.09	0.12	0.14	0.16	0.18
	42	0.01	0.01	0.03	0.04	0.06	0.08	0.10	0.12	0.14	0.16

Table 5.2 The calculated potential response Pmn_2(L1,L2), unit is V.

	L1 (cm)										
	0	6	10	14	18	22	26	30	34	38	42
	6	0.78	1.29	1.62	1.83	1.97	2.08	2.17	2.23	2.29	2.34
	10	0.23	0.47	0.67	0.83	0.95	1.05	1.12	1.18	1.24	1.29
	14	0.09	0.22	0.34	0.45	0.54	0.62	0.69	0.75	0.80	0.84
L2 (cm)	18	0.05	0.12	0.19	0.27	0.34	0.41	0.46	0.51	0.56	0.60
	22	0.03	0.07	0.12	0.18	0.23	0.28	0.33	0.37	0.41	0.45
	26	0.02	0.04	0.08	0.12	0.16	0.21	0.25	0.29	0.32	0.36
	30	0.01	0.03	0.06	0.09	0.12	0.16	0.19	0.23	0.26	0.29
	34	0.01	0.02	0.04	0.07	0.10	0.13	0.16	0.19	0.22	0.25
	38	0.01	0.02	0.04	0.06	0.08	0.11	0.13	0.16	0.19	0.22
	42	0.01	0.02	0.03	0.05	0.07	0.09	0.12	0.14	0.17	0.19

Table 5.3 The calculated relative error Q(L1,L2) .

	L1 (cm)										
	0	6	10	14	18	22	26	30	34	38	42
	6	0.14	0.23	0.35	0.52	0.71	0.94	1.19	1.47	1.77	2.11
	10	0.44	0.59	0.81	1.08	1.40	1.78	2.19	2.66	3.16	3.70
	14	1.02	1.23	1.52	1.89	2.34	2.85	3.43	4.06	4.75	5.49
L2 (cm)	18	1.95	2.20	2.56	3.02	3.58	4.22	4.93	5.72	6.57	7.48
	22	3.25	3.54	3.96	4.49	5.13	5.87	6.70	7.61	8.60	9.65
	26	4.93	5.24	5.69	6.28	6.98	7.79	8.70	9.71	10.79	11.95
	30	6.91	7.23	7.70	8.31	9.04	9.89	10.84	11.90	13.04	14.26
	34	9.03	9.35	9.81	10.42	11.15	12.00	12.96	14.02	15.17	16.40
	38	11.05	11.35	11.79	12.36	13.06	13.88	14.81	15.84	16.96	18.17
	42	12.63	12.90	13.31	13.84	14.49	15.26	16.13	17.10	18.17	19.32

From Figure 5.4 and 5.5, one can see that there is a slight difference between the values, especially in the left part of the two figures. However, from Figure 5.6, it can be seen that the percentage error increases with the increment of L1 or L2. Specifically, the L2 increment produces a larger boundary reflection effect than L1 since there are two horizontal boundary reflections (left and right) which are affected by changing L2 and there is only one vertical boundary reflection (bottom) which is affected by changing L1. Fortunately, the normal value of L1 we choose is less than 18cm, based on experience we had with physical resistivity modelling tests in a smaller water tank. From Figure 5.6, one can see that if we keep the distance L2 smaller than 30cm, the boundary reflection error Q will be smaller than 6%, which is tolerable.

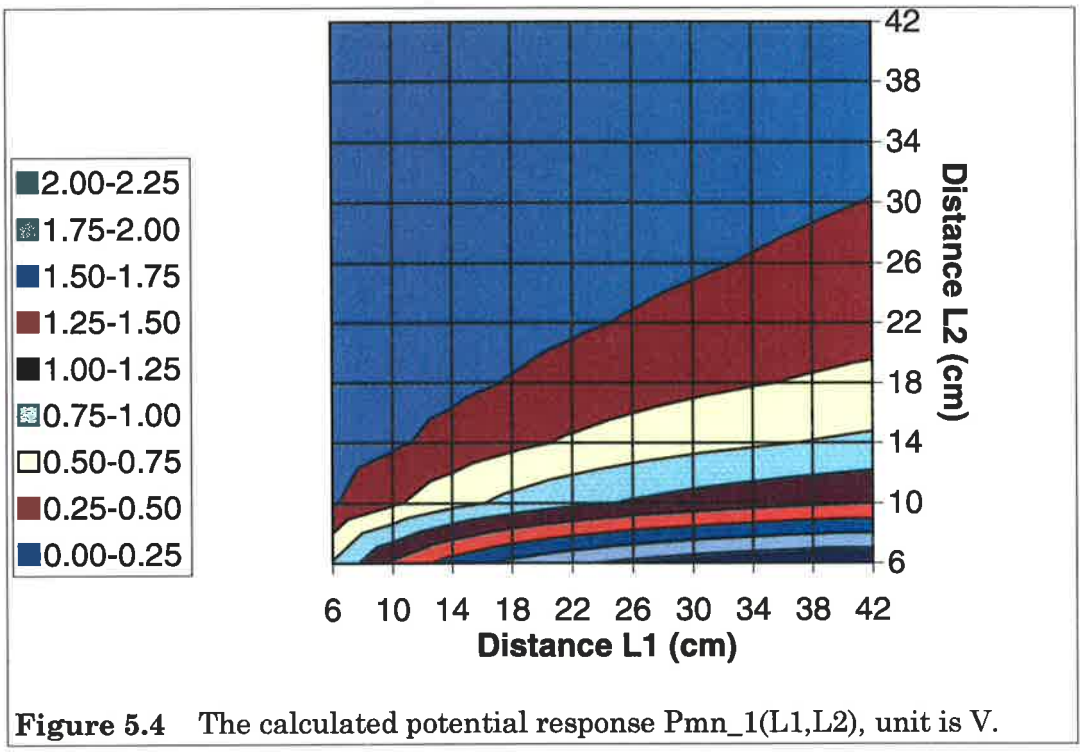

Figure 5.4 The calculated potential response Pmn_1(L1,L2), unit is V.

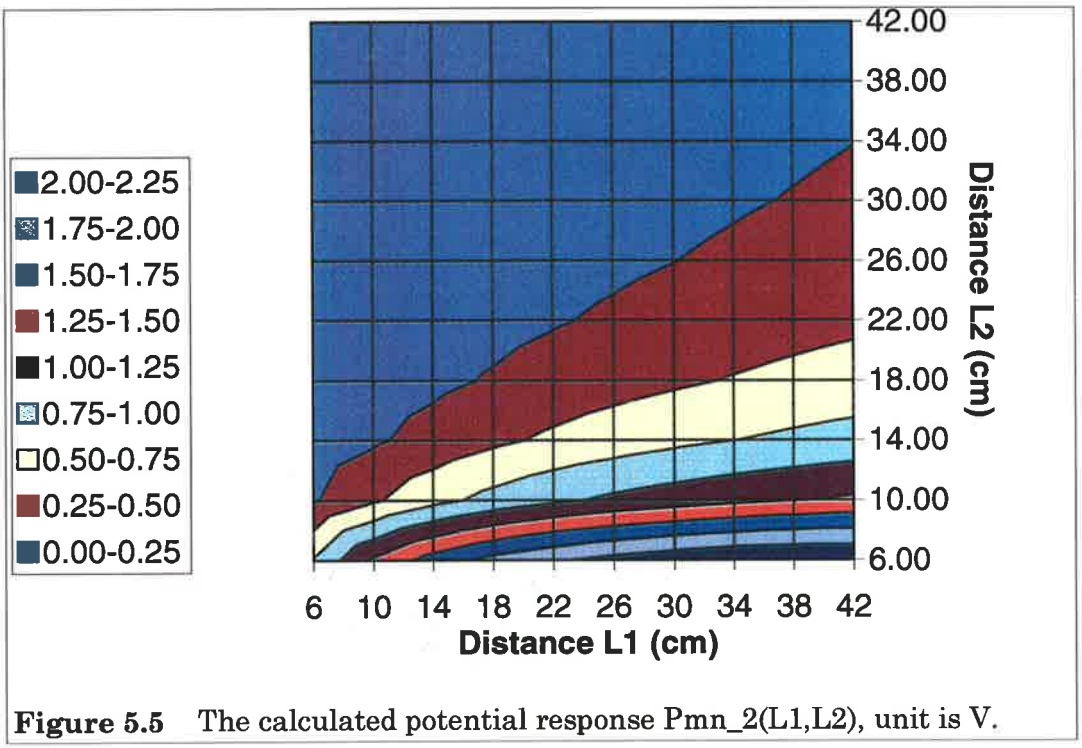

Figure 5.5 The calculated potential response Pmn_2(L1,L2), unit is V.

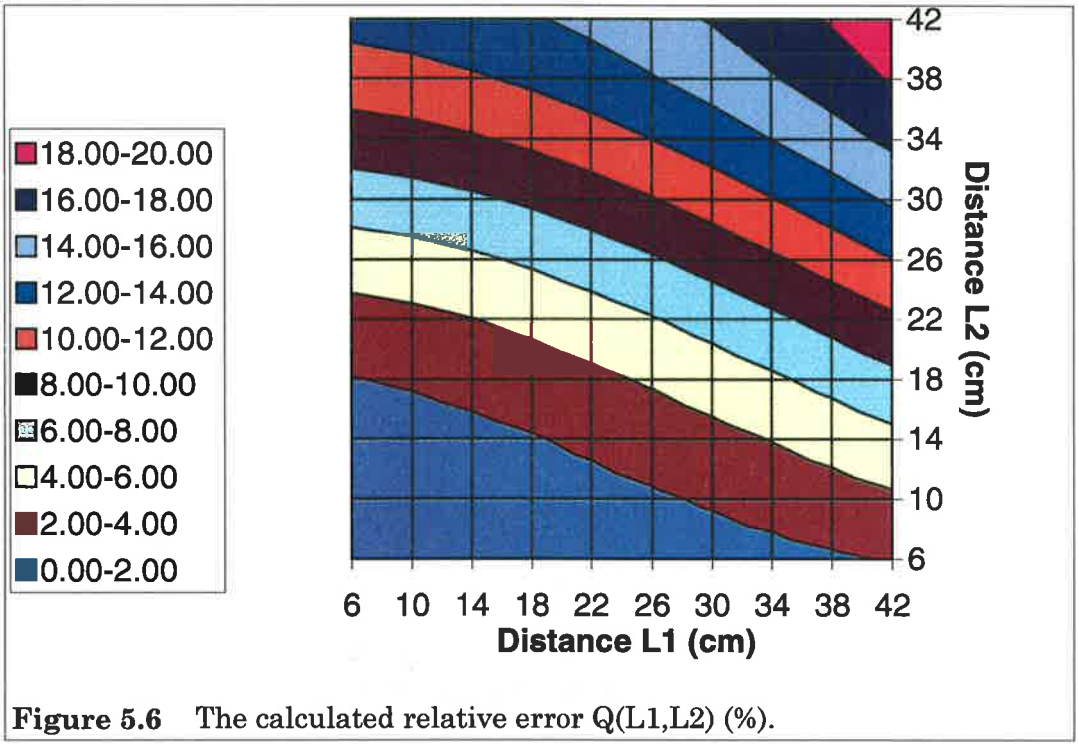

Figure 5.6 The calculated relative error Q(L1,L2) (%).

In conclusion, for the dipole dipole configuration in the 3-D physical resistivity modelling system, the boundary effect will not be significant and the error it produces on the observed data will be smaller than 6%, if the distance L1 is smaller than 18cm and L2 is smaller than 30cm.

5.4 3-D AUTOMATED MOVEMENT OF ALL FOUR ELECTRODES

To automate the whole system, computer controlled positioning of the four electrodes has to be achieved. Since the main goal of the system is to simulate crosshole resistivity surveys, the distance between two electrodes in the same borehole is fixed for each data scanning run. As such, only two pairs of electrodes need to be controlled separately. One pair of electrodes is placed in each simulated borehole (or vertical profile) and they move together, keeping a fixed distance between them during crosshole scanning. From the photograph of Figure 5.7, it can be seen that each pair of electrodes are driven by 3 step motors, one for the X direction, one for the Y and one for the Z. So the two pairs of electrodes can be fully controlled in 3 directions by a computer via the six stepper motors. The reason for using the stepper motors in this system is to guarantee the positioning accuracy. Because all six stepper motors are 1.8 degree step angles, we can be sure that the positioning error will be less than 0.1mm, which is more than adequate for this modelling system. Figure 5.7 illustrates the whole positioning system that includes six stepper motors, six driving axes and associated supports.

The six stepper motors are driven by six commercial stepper motor driving boards that are controlled by the microcontroller in the MAIN CONTROL BOX. Figure 5.8 is a photograph of one driving board.

The driving board is for a unipolar stepper motor and is in a standard Euroboard size, complete with a 32-way DIN 41612 plug connector for plugging into any Eurocard compatible racking system which we used for accommodating all six stepper motor driving boards, the power supply and the main control board.

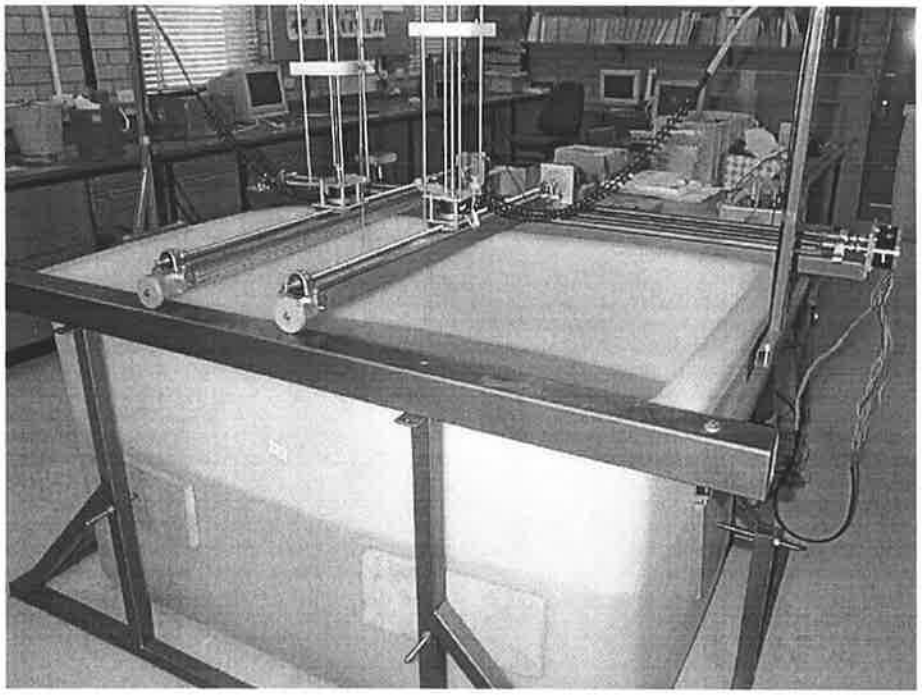

Figure 5.7 The photograph of the complete 3-D physical resistivity modelling system.

In order to drive the main shaft smoothly and accurately, high working torque and high-resolution stepper motors have to be used. Two different sizes of the stepper motors are used in this system. The four larger ones are Sanyo high torque stepper motors, whose rated current is 4A and holding torque is 2745mNm, and they are used to drive along the X and Y axes. The two smaller ones are used to drive along the Z-axis. Since the rated current of the stepper motors is too large, a separate power supply had to be built for them.

In order to test the six stepper motors and mechanical driving system, a manual controlled driving box was built, as shown in Figure 5.9. The box can be used to drive any of the six stepper motors with a variable speed in any directions. From the tests, both the stepper motors and

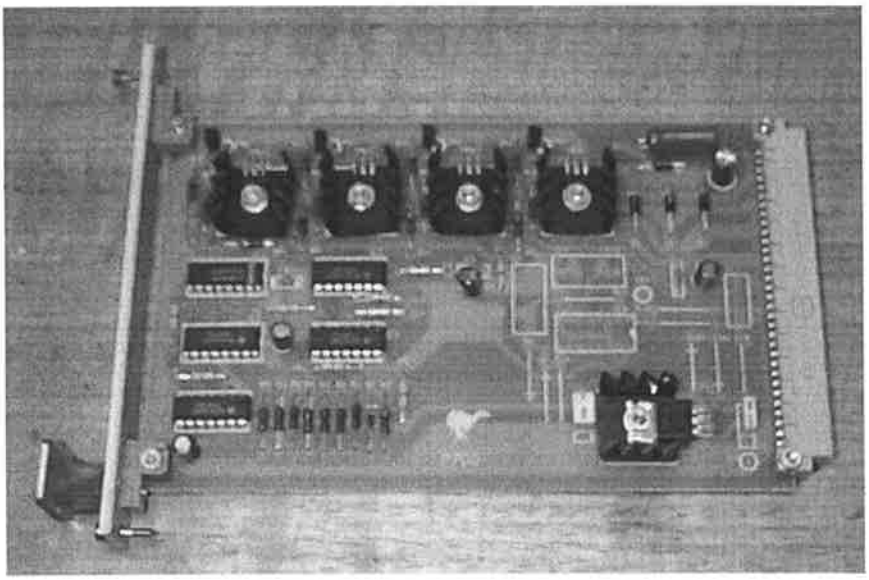

Figure 5.8 The photograph of the commmercial stepper motor driving board.

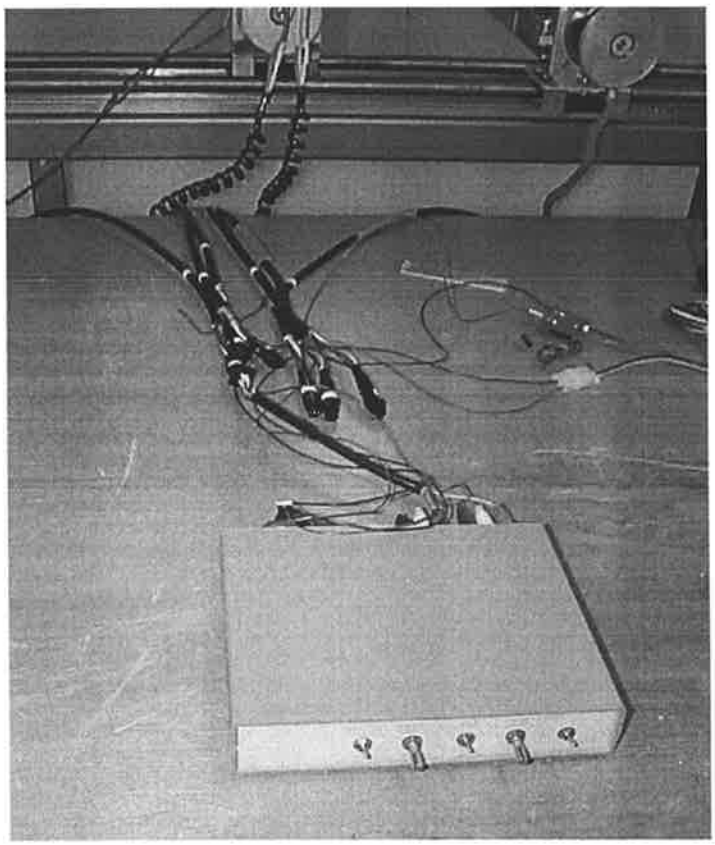

Figure 5.9 The photograph of the manually controlled driving box for testing the stepper motors and the driving system.

mechanical parts work very well. Due to the high torque needed at the start of movement, the initial speed should not be very high at the start. Since the moving speed is totally controlled by the MAIN CONTROL BOX via a microcontoller, it is very easy to control the moving speed by the software.

5.5 CURRENT SOURCE DESIGN

The commonly used current source waveform in field resistivity surveys is shown in Figure 5.10. Normally it consists of one half cycle of a positive square wave followed by a quiet (or zero current) period, then a negative square wave. The frequency of the change is about from 0.1 to 20 Hz. The reason to change between positive and negative square waveforms is to remove self-potential effects and prevent polarization occurring at the potential electrodes.

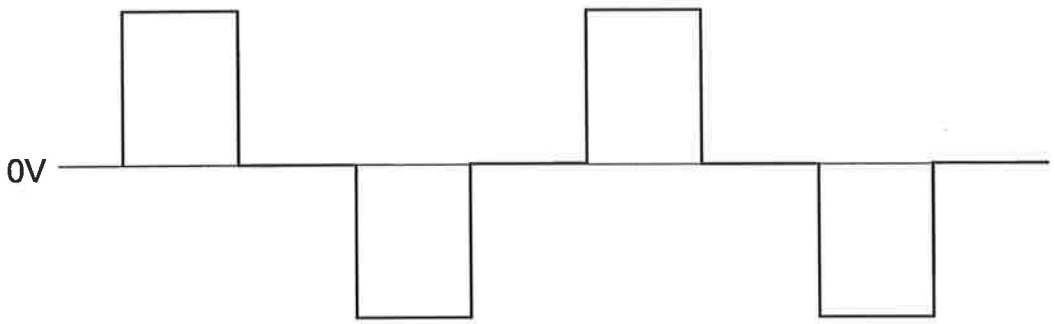

Figure 5.10 The general output voltage waveform used in resistivity survey.

There are two main parameters to consider when designing the current source. The first one is frequency of the source or the width of the square wave. The second is the amplitude of the square wave pulse. From the numerically calculated data shown in Figure 5.4 and 5.5, the potential difference between two potential electrodes becomes smaller as their separation decreases. So the main concern in setting the amplitude is if the power source can provide enough current and potential difference between two potential electrodes with the maximum voltage output of the power source. Since the output voltage of the power source is downwards adjustable from the maximum to 0V, we do not need to worry if the output voltage is too high. Therefore a few preliminary tests were undertaken before deciding on the pulse amplitude. The layout of the tests is shown in Figure 5.11. First for the extreme case: smallest L=4.5cm and the output voltage of 110VDC, the current and the measured potential difference were 77.2mA and

1870mV, respectively. The second case: L=10.5cm and an output voltage of 110VDC, the current and the potential difference were 75.1mA and 3150mV, respectively. The larger the L, the larger the potential difference. The measured current and potential difference are large enough for our modelling acquisition system. So from the two tests, we know the output voltage 110VDC is sufficient for this resistivity modelling system.

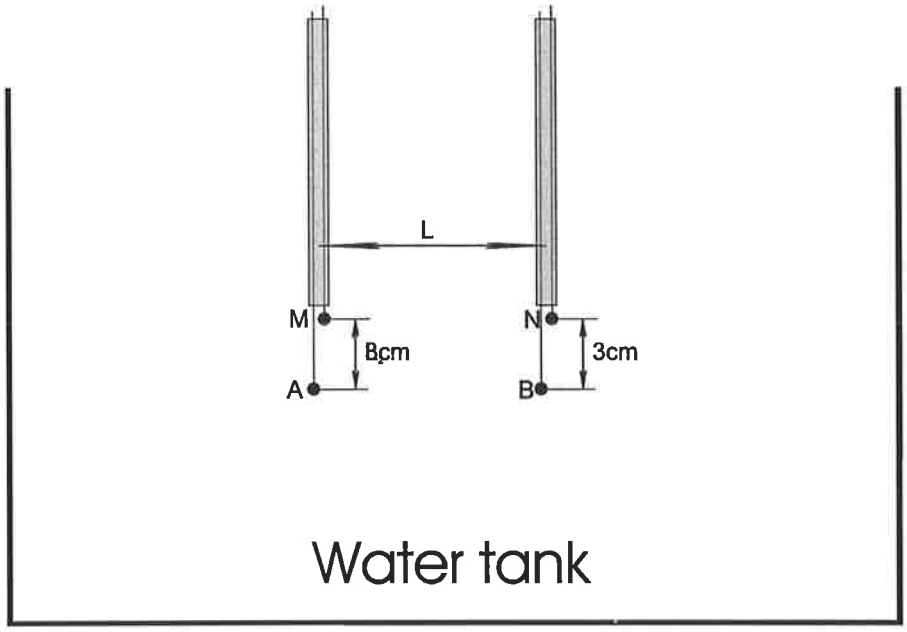

Figure 5.11 The test layout for determing the appropriate power source level for the system.

A commercial field resistivity instrument, a SYSCAL– R2 (for details refer to Chapter 6) was used for the above tests.

The current source was designed to accommodate the frequency range from 0.01 to 50 Hz. The upper frequency is mainly limited by the relays, which we use to switch on/off the current source and change the polarity. But such a frequency range is good enough for all resistivity and IP modelling. Rarely would one go above 20 Hz, to avoid skin depth and EM coupling effects.

According to the above criteria, the circuit design of the power box is shown in Figure 5.12. It is an AC to DC adjustable converter. The input to the power box is 240V AC and the output is DC adjustable from 0V to 120V DC with a variable voltage transformer. It has two pairs of output terminals with the one common output terminal S4. The two pairs of outputs are for easily

changing the polarity of the output. Figure 5.12 shows the main components of the circuit to be two transformers, two rectifiers and two filtering circuits. The DC output from this box is be connected to the POWER CONTROL BOX that controls the ON/OFF switch and changes the polarity of the current output. The main function of the power box is to provide an adjustable and stable DC source for the current injection. The power box was designed and completely constructed by myself. It was tested by qualified electricians and found to work well. Figure 5.13 shows the finished power box.

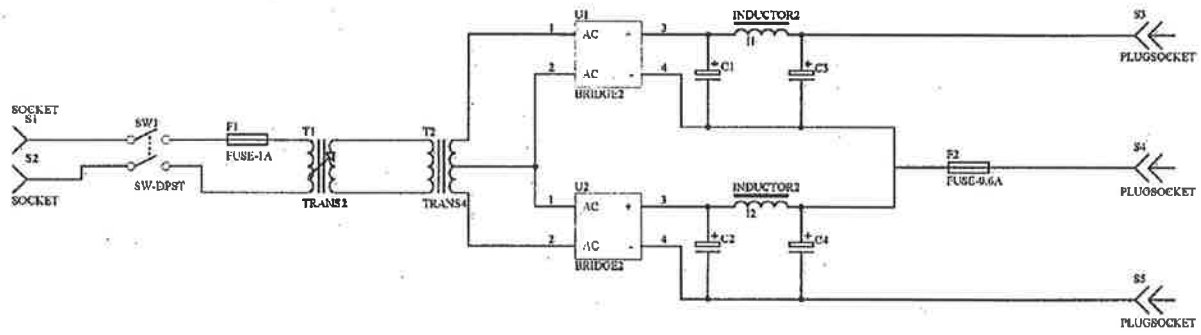

Figure 5.12 The circuit design of the power box.

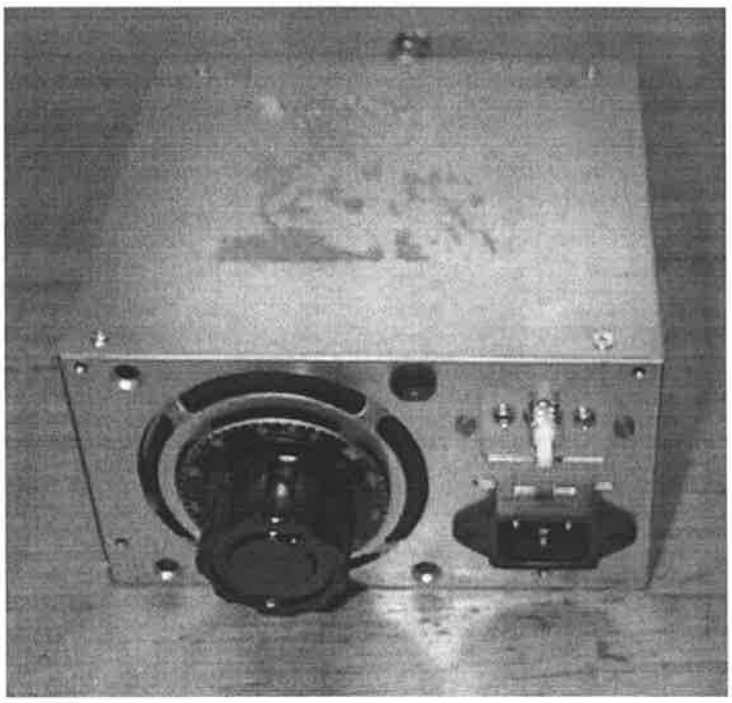

Figure 5.13 The photograph of the finished power box.

The power control box of the current power supply was designed 1) to change the output polarity; 2) to switch the power on/off; 3) to provide the output current and voltage samples to the acquisition box for the current and voltage measurements. The circuit design is shown in Figure 5.14. P1, P2, and P3 in the middle part of the figure are three power supply inputs from the power box. P4 and P5 on the right side of the figure are the current outputs to the two current electrodes. Between them are two relays for switching on/off (Relay 1) the power output and changing (Relay 2) the polarity of the output. Relays 1 and 2 are controlled by 2 wires (pin 7 and 8 of J1) from the MAIN CONTROL BOX via the relay control and drive circuit. The two relays can also be controlled by two manual switches (SW2 and SW3) for test purposes. The output voltage waveform is sampled and sent to an isolation amplifier U5 (ISO122) to enlarge it. The output current is also sampled and enlarged by an OP amplifier U7 (LM4250). Then it is sent to an isolation amplifier U6 (ISO122) for further enlargement. The output voltage and output current samples are sent to the acquisition box via pin 5 and 6 of J1. The components U2 and U3 are two isolation power supplies for the two isolation amplifiers (U5 and U6). Because the output voltage is very high (up to 110V DC), the above isolation power converters and isolation amplifiers have to be used to protect the whole system. Normally the output waveform voltage measurements are unnecessary in resistivity modelling, but they may be useful for other research purposes. Pins 1 and 2 of J1 provide power supply (12V DC) for the control circuit of the power control box.

The design of the power control box is complete and the printed circuit board has been designed and made. However, it has not been completely assembled due to lack of technical support.

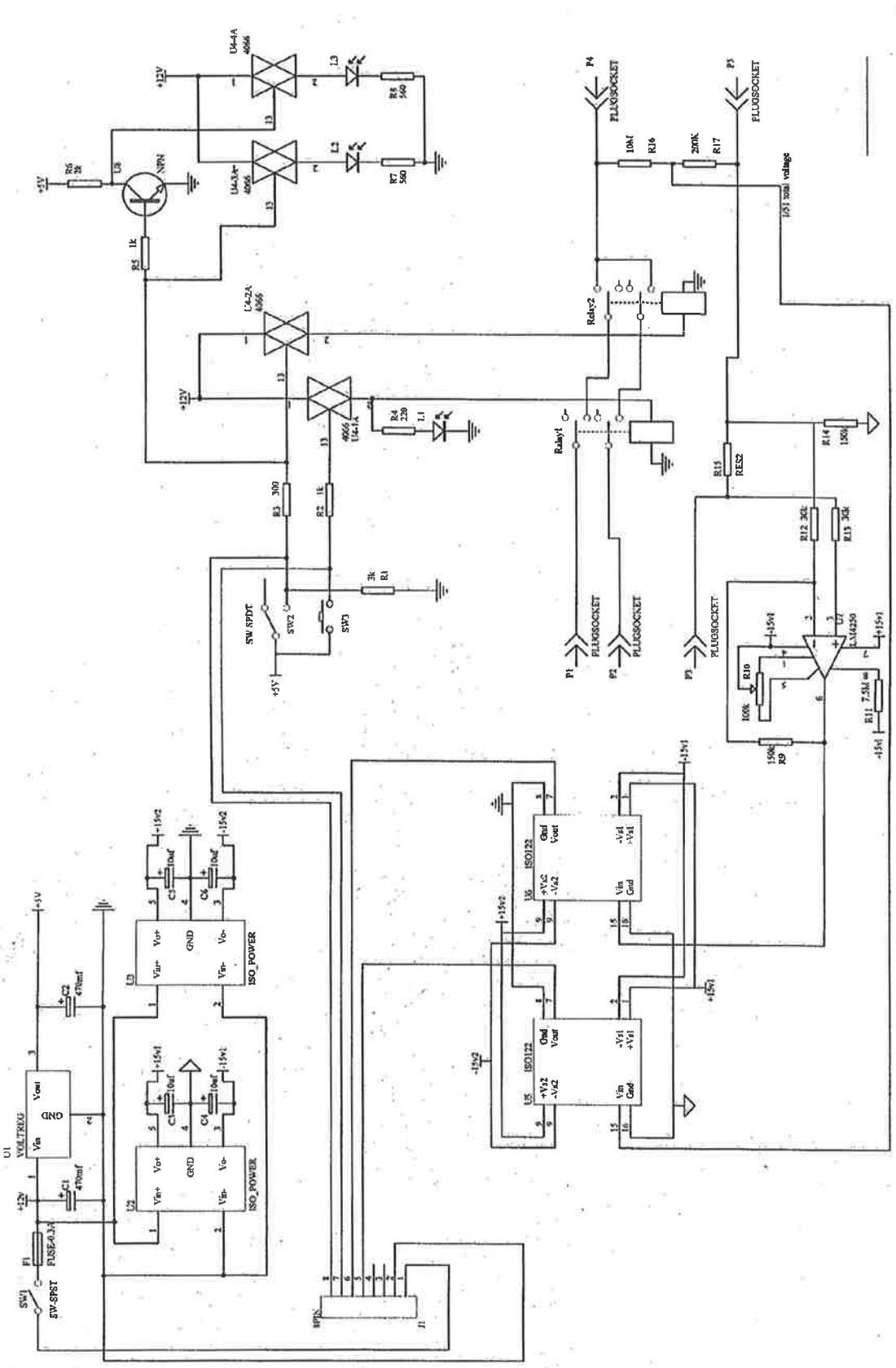

Figure 5.14 The circuit diagram of the power control box.

5.6 THE DESIGN OF THE ACQUISITION BOX

The acquisition box is a general A/D converter controlled by a microcontroller 8051 and built by technicians at Flinders University. It is triggered by the MAIN CONTROL BOX. This acquisition box can acquire 4 channel data simutaneously at a maximum speed of 4k samples per second with 16 bit resolution, yielding a voltage interval as small as 0.16mV. The acquisition input voltage range is from –5V to +5V. This is suitable for both resistivity and IP physical modelling. Presently only 3 channels are used for measuring output voltage, output current and potential difference. With this high sample rate, we can record and analyse voltage, current and potential waveform changes for the whole measurement procedure. Then the measured waveform changes can be used for more detailed resistivity and IP research.

The acquisition box is controlled and triggered by the MAIN CONTROL BOX. After it is triggered, it sends 3 channel analog/digital converted data directly to the PC via a special fast serial port. The output voltage and the output current samples come from the power control box, as shown in Fig 5.14. The potential sample is from the two potential electrodes M and N directly. The data sampling period can be from 1 second to 100 seconds at the rate of 1000 samples per second for each channel. So the acquired data are very useful for researching waveform changes in current, voltage and potential. In fact, this system is ideal for IP measurements as well.

There is no circuit of the acquisition box I can display here, since Flinders University owns the copyright of the box.

The acquisition box was connected to the personal computer and tested with driver software I developed in Microsoft Visual Basic. It works perfectly.

5.7 THE DESIGN OF THE CENTRAL CONTROL BOX

From Figure 5.1, it can be seen that there is a main control box between the PC and the other boxes. The reason for this is that a normal PC is a multitask system, but is not good for real-time control, such as controlling triggering and acquisition simultaneously. So the microcontroller box or MAIN CONTROL BOX is inserted between the PC and the other boxes. The microcontroller box obtains commands from the PC, then controls the stepper motors, the acquisition system, and the power control box simutaneously.

The circuit design of the MAIN CONTROL BOX is shown in Figure 5.15. The central part of the main control box is U1 – an 89C2051 microcontroller. It communicates with the PC via a normal RS232 serial port with the help of U5 (MAX233) which converts between the 5V TTL voltage level and 12V RS232 voltage level. The reason to use a serial port is that the communication between the PC and the main control box mainly is for passing commands only. So the slow transmission speed of the serial port is not a problem. This microcontroller is the "brain" of the box. A program has to be developed and written into the microcontroller in order to interpret and complete the commands from the PC correctly. Some of the C subroutines have been written.

Another major IC chip in the box is U2 (XC9536) – a programmable logic circuit, which replaced a lot of the logic circuits used for controlling the stepper motors, the current power supply and the waveform acquisition system. This makes the circuit look much simpler. Also this chip makes design and testing much easier since you can change the logic design and control sequence without changing any circuit design, just reprogram the programmable logic chip via an in-system connector J3.

Normally, according to the commands from the PC, the microcontroller box or the MAIN CONTROL BOX firstly moves two sets of electrodes to the exactly specified positions by sending step pulse signals to six stepper motors respectively via six stepper motor drive boards. Secondly, the box completes the following two tasks simultaneously: (1) orders the power control box to switch on or off the output power and to change the output power polarity according to the orders from PC; (2) sends a trigger signal to the acquisition box to start the AD conversions. Then the acquisition box sends the converted digital data to the PC via a fast serial port (RS458 interface) until the specified number of conversions have finished. The MAIN CONTROL BOX continues to repeat the above two tasks until all 'survey' points are finished.

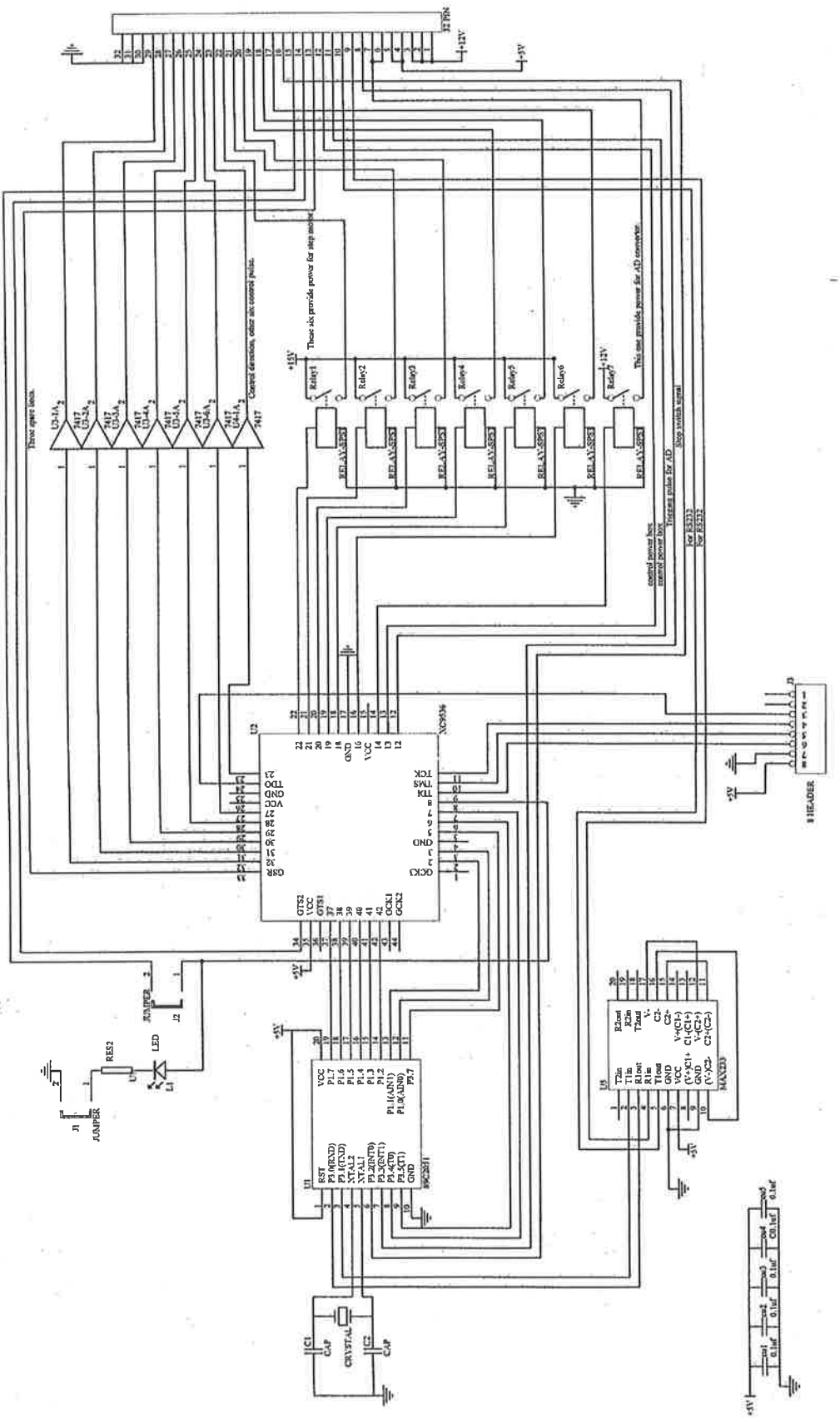

Figure 5.15 The circuit diagram of the main control box.

5.8 SUMMARY AND FURTHER WORK REQUIRED

This physical resistivity modelling system is a very advanced 3-D resistivity physical modelling system with fully automatic control from moving electrodes to acquiring full waveform electrical data. What the operator needs to do is to make a plan and enter the survey specification into the personal computer. Then the system may finish the work in a few hours without any interference. After it finishes each measurement, the data will be automatically stored in the computer. This will make physical modelling much more efficient than doing it manually. Especially since all tasks completed by the modelling system are controlled by a control file with all parameters needed, it is very easy to repeat a modelling test with or without some parameter changes. Because of the high sample rate of our acquisition box, this system can not only record all waveform changes of injected voltage, current, and potential for the full resistivity measurement, but also it can be used for IP physical modelling which needs recording all detailed waveform changes after the injected current is switched off.

The design of the whole 3-D physical resistivity system was completed by myself and partly finished.

All mechanical parts, including the water tank, 3-D electrode moving system (stepper motors, steel axes and mechanical support) and position measurements, are completely finished and tested with a manual control. The main mechanical work was done by Mr. Trevor McGrath of Flinders University of South Australia. I completed all the connections and satisfactorily tested it.

The four electrode connections were tested with a SYSCAL-R2 – a resistivity acquisition system (for details refer to Chapter 6), and found to work fine.

The power box was completed by myself and tested by an electronics technician in the Department of Physics, University of Adelaide. It passed all tests.

The design of the power control box, stepper motor control box and the main control box are finished and all printed circuit boards have been made. The next step is to construct them and test them. Unfortunately, this will involve a lot of time and high fidelity electronics work that is beyond my time limits and current ability. At the start, one technician helped me on this project.

But later, he left the university, placing completion of the 3-D physical resistivity modelling system in jeopardy. Fortunately, our 2.5-D and 3-D resistivity numerical modelling and inversion system helped me a lot in the interpretation and processing of the Bolivar ASR resistivity data without 3-D physical modeling system support.

Nevertheless, I plan to finish building the laboratory electrical system as a later (post-doctoral) project.

Chapter 6

BOLIVAR ASR EXPERIMENT

6.1 INTRODUCTION

The saving and reuse of water has become a very important consideration worldwide with water shortage more serious than at any time before. Aquifer storage and recovery (ASR), which is a form of artificial recharge of groundwater that makes use of a single well to inject and recover water, was the motivation for the present study. A common way to store water is to build a dam on the Earth's surface. However this is expensive and suffers from the added problem of significant evaporation in hot climates like South Australia.

Storing water underground in an aquifer and recovering it later was first raised by Pyne (1995). This technique has the potential to substantially reduce the cost for storing water in comparison to the construction and maintenance of above ground storage facilities. However it is still in the experimental stage. ASR is especially useful in regions where there is a seasonal shortfall between water availability and supply. The principle is illustrated in Figure 6.1.

An ASR research project (Gerges 1996) commenced in July 1997 at the Bolivar site on the Northern Adelaide Plains in South Australia (see Figure 6.2). This trial was undertaken to help develop and demonstrate the ASR technique. The intention was to examine the feasibility of injecting the winter excess of reclaimed water into the aquifers beneath the North Adelaide Plains and recovering the water in summer for use in irrigating the crops grown in the Virginia Horticultural area to the immediate north. A parallel aim was to examine the quality change of the injected water and its effect on the current water resources.

Adelaide receives most of its precipitation in the winter months. The ASR project was designed to take the winter excess of reclaimed water from the Bolivar Wastewater Treatment Plant near the site and inject it into the T2-aquifer. This aquifer lies about 100 m below the surface. The Bolivar plant currently processes 40000 ML/year of effluent and is therefore a suitable source of water for pumping. The benefits of this project include: protecting

groundwater supplies against further salinization, enhancing groundwater supplies, reducing nutrient-rich discharge to the sea, and more efficiently using water resources in an area where water has been a limited factor to economic growth. If successful, this pilot project will enable the design of a large scale ASR scheme in the area.

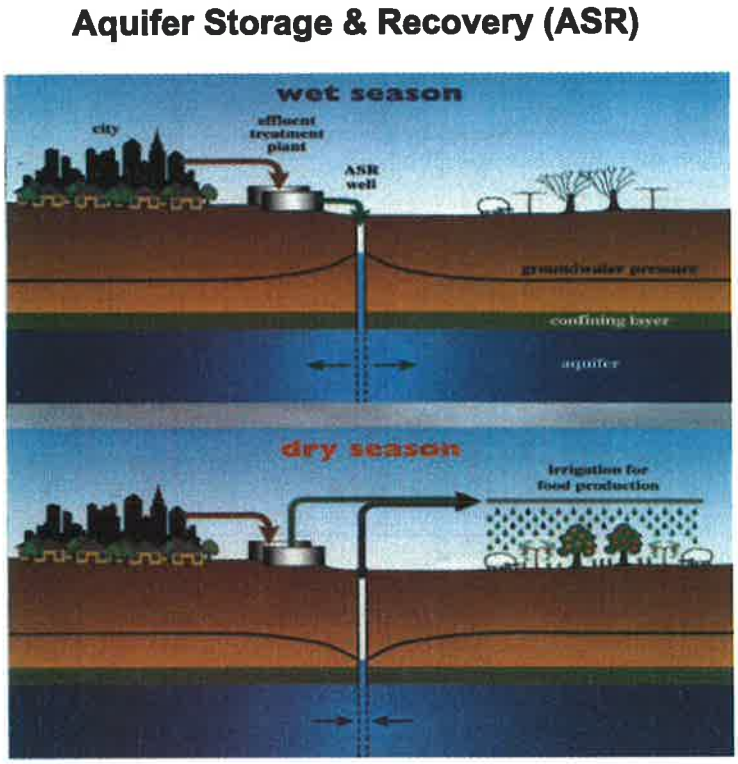

Figure 6.1 Illustration of the principle of Aquifer Storage & Recovery (ASR).

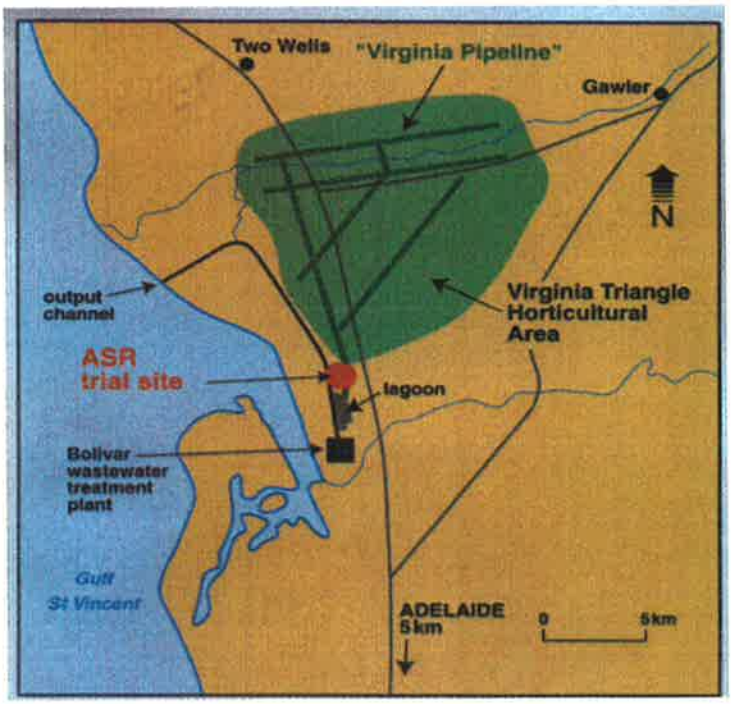

Figure 6.2 Location of the ASR trial site. Bolivar wastewater treatment plant is only about 1km away.

6.2 GEOLOGY AND WELL-LOG INFORMATION AT THE ASR TEST SITE

The ASR test site at Bolivar lies within the Northern Adelaide Plains (NAP). A representative east-west geological cross section of the NAP is shown in Figure 6.3.

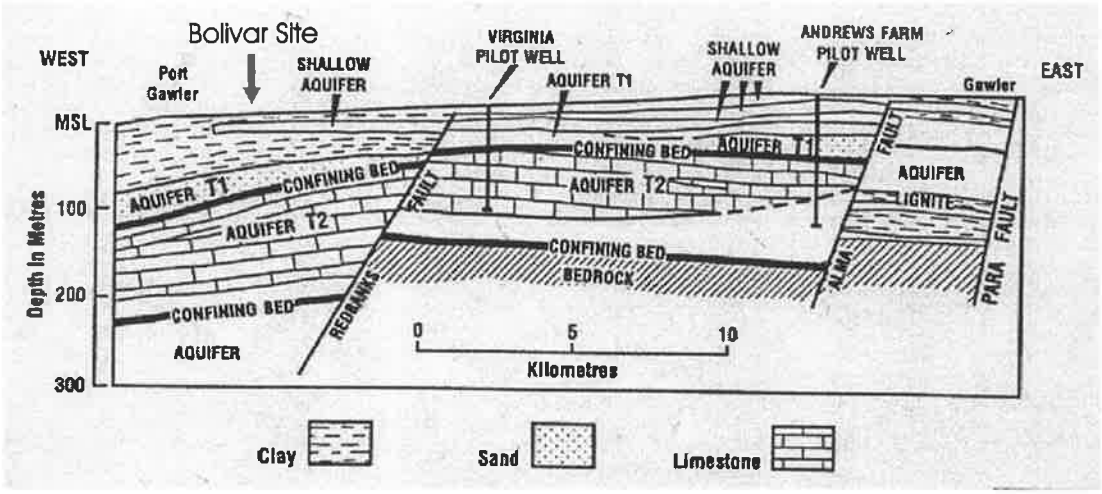

Figure 6.3 The geological cross section of the Northern Adelaide Plains.

The diagram also shows the approximate location of the Bolivar test site on this section. Good quality ground water is available beneath the NAP from aquifers T1 and T2 of Tertiary age. Deeper and more saline aquifers lie below the T2-aquifer. In addition to the Tertiary aquifers, there are a number of shallower aquifers composed mainly of clay and silt with thin layers of sand; these aquifers are of Quaternary age. The T1-aquifer comprises sand and limestone and, in cross-section, is 'wedge'-shaped with an average thickness of 30 m in the west but thins to the east. Salinity in the T1-aquifer ranges from 600 mg/L to 2000 mg/L. The underlying T2-aquifer, targeted for the ASR experiment and separated from the T1-aquifer by a thick layer of impermeable clay (Munno Para Clay), consists of variably cemented fine carbonate (calcarenite) and sand material (sandstone). It covers a relatively large area and has an average thickness of 80 m. Salinity in this aquifer ranges from 600 to greater than 3000 mg/L. Figure 6.4, which is a contour map of T2 aquifer salinity variation in the area, shows the gradient zone of salinity change of the underground water in the NAP.

From Figure 6.4, we see that the Bolivar site is located in the gradient zone of 1000~2000 mg/L where the western part is expected to have lower electrical conductivity than the eastern part due to the higher salinity concentration in the west. This means that the resistivity (inverse of conductivity) of the T2-aquifer may exhibit a certain variation, due to the different salinity levels. The T2-aquifer at the site occupies the depth range 90m-170 m.

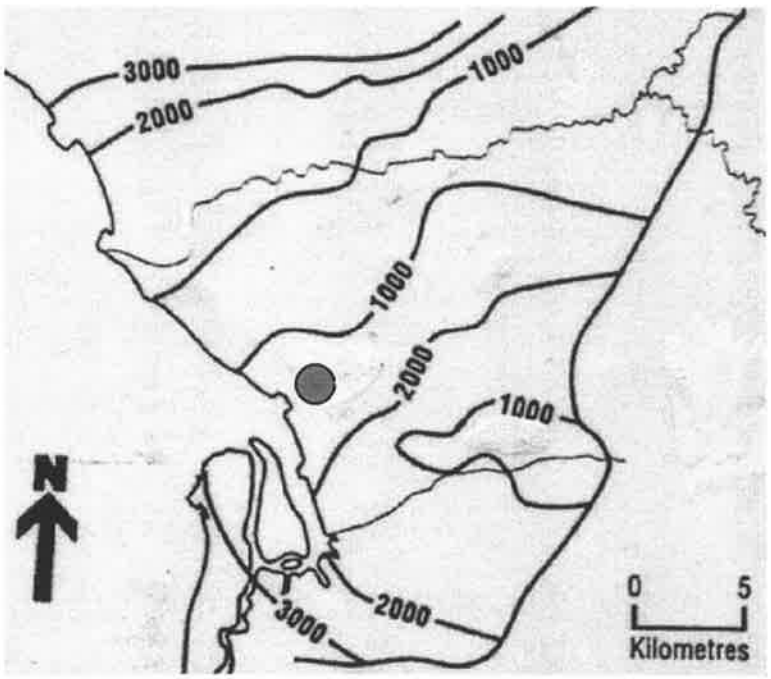

Figure 6.4 The salinity contour in Northern Adelaide plains.

The ASR project encompasses a wide variety of hydrologic research topics and measurements, including water quality change, water flow direction, salinity concentration change, the effect on the top T1 aquifer, and so on. More than 16 wells were drilled at the site for the different research purposes (refer to Figure 6.5).

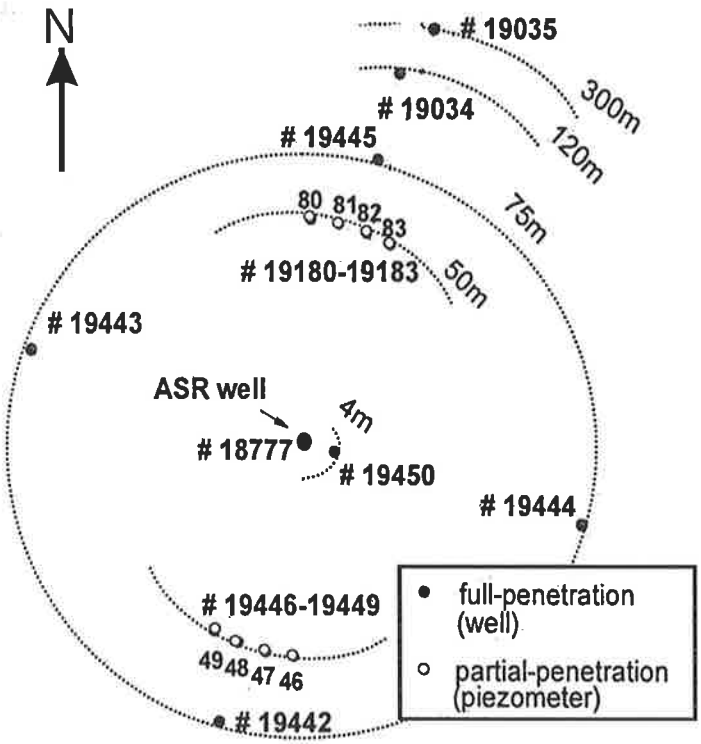

Figure 6.5 Location of wells at the Bolivar ASR test site.

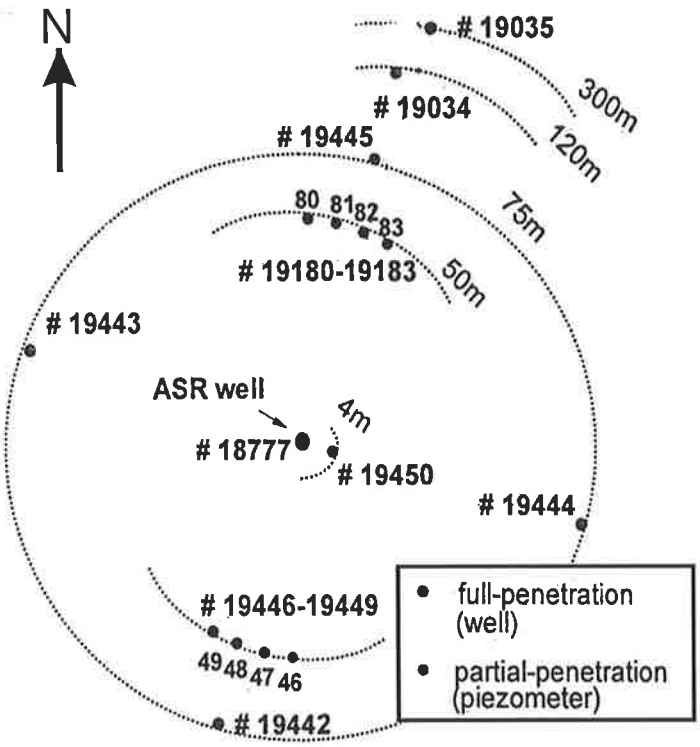

Figure 6.5 Location of wells at the Bolivar ASR test site.

All wells have been geologically and geophysically logged. Figure 6.6 shows the relative positions of the three wells, the injection well, Wells 19035 and 19134 (located 120 m and 300 m east from the injection well), and the extracted geophysical well logging profiles: the Laterolog, self potential log and Deep induction Log. The logging profiles show the very similar geology beneath the site and indicate the obvious property change in the vertical direction and only mild change in the horizontal direction. A few prominent interfaces are evident from the logs (in the figure) at depths of 110m, 130m and 146m, dividing up the aquifer into distinct layers. These layers are very important in the interpretation of our resistivity survey data.

6.3 WHY USE ELECTRICAL IMAGING?

Monitoring the advance and flow directions of the injected water are key elements of the ASR project. Eight wells (19180 to 19183 and 19446 to 19449) (refer to Figure 6.5), drilled on the circumference of a circle of radius 50 metres, were used to directly monitor the reach of the injected water from the different layers through installation of piezometers and other regular geochemical and physical monitoring. Wells 19180 to 19183 are in the north direction and all wells 19446 to 19449 are in the south. Therefore before the injected water reaches the 50 metre circle, or if the injected water preferentially flows towards the east or west, it is difficult to know where it is without some remote sensing means.

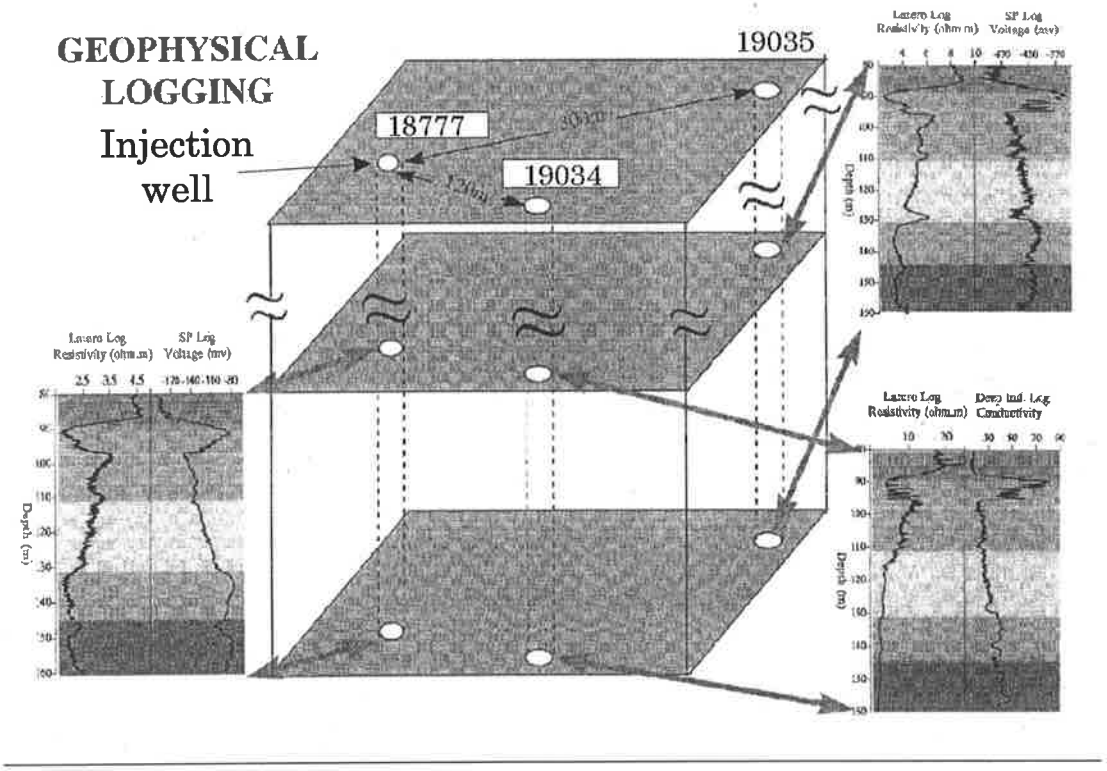

Figure 6.6 The relative positions of the three wells and their extracted logging profiles to show the similarity of the three logging data.

The injected water, which is the reclaimed water from the Bolivar Wastewater Treatment Plant, has a salinity much less than that of the groundwater in the T2 aquifer. The resistivity of the fresh reclaimed water (4.6 Ω.m) is higher than the more saline groundwater(2.7 Ω.m) in the aquifer. So this suggests using the resistivity method as the remote sensing tool. It is very good at detecting resistivity contrasts that are caused by the salinity differences of the different waters. Since the T2 aquifer lies 100m below the surface, it is too hard to use normal surface resistivity profiling and sounding methods to obtain information on resistivity change at depth. Surface resistivity methods lack the requisite resolution to map aquifer properties and flow paths on such a scale Therefore a resistivity tomography method is the best choice for imaging the resistivity variation associated with fresh water intrusion.

Changes of resistivity due to the migration of groundwater have been observed commonly and form the basis of electrical monitoring techniques in applied geophysics. Both surface and downhole arrays have been employed, the latter having a greater sensitivity to movement of fluids (Asch and Morrison 1989, Bevc and Morrison 1991). Crosshole resistivity tomography or imaging is a newly developed technique in geophysical exploration (Daily and Owen 1991, Shima 1992). It makes use of variations in electrical properties of the subsurface to image targets between boreholes. Recently, the Adelaide University Geophysics group has

developed the technique for general practical application (Zhou and Greenhalgh 2000). We showed that some specified three- and four-electrode crosshole configurations can be employed and have significant merits in field measurement over the pole-pole configuration for crosshole resistivity imaging. With these configurations, a rapid 2-D/3-D crosshole imaging scheme was developed and examined by synthetic experiments. The experimental results show that it may be applied to monitoring the underground water injection by imaging the plume of the injected water and the water-flow paths.

6.4 ELECTRICAL MONITORING STRATEGY

To electrically image the water flow paths, four monitor wells (19442 to 19445, refer to Figure 6.7) were drilled on the circumference of a circle of radius 75 meters, centered on the injection well. They were used for acquiring crosshole resistivity data.

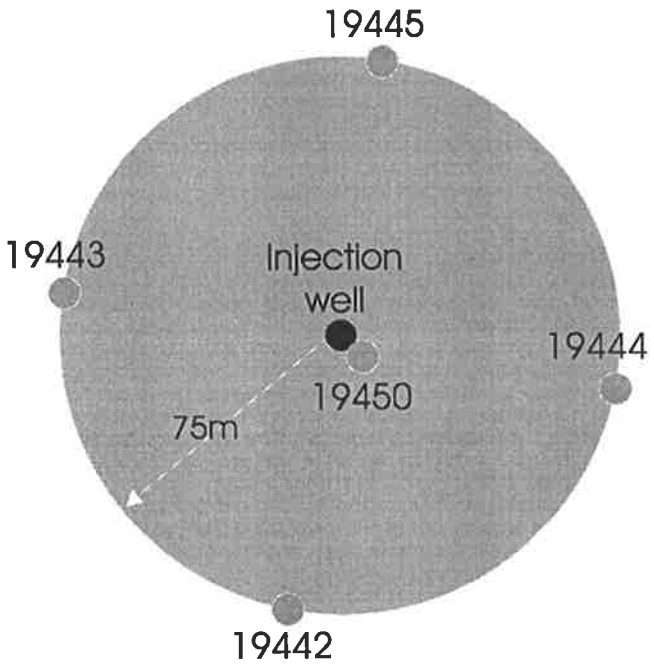

Figure 6.7 The relative location of the observation wells used in resistivity tomography surveys during the water injection period.

Well 19450, four metres away from the injection well (18777), was also used for acquiring resistivity data. Before the above five wells were drilled and water injection started, some preliminary surface, surface-to-borehole and borehole-to-borehole (using additional wells) resistivity surveys were undertaken to understand the resistivity distribution at the site, and to compare the electrical responses with the known geologic and well log information (see Chapter 7).

2-D/3-D resistivity modelling, imaging and inversion techniques were employed to obtain the basic resistivity structure from the crosshole data. 3-D resistivity experiments were repeated at different times after injection began to obtain the time-lapse tomography images of the aquifer from the acquired data.

6.5 OTHER TIME-LAPSE MEASUREMENTS

Apart from the resistivity tomographic surveying, some other physical and chemical quantities, such as pH, dissolved oxygen, electrical conductivity, temperature, and pressure, were also monitored frequently in the set of boreholes drilled on the circle of radius 50 m from the injection well. The profiles of these physical quantities are very helpful in interpreting our processed resistivity data. Figure 6.8 shows some of the profiles used. For example, graph (b) in the figure shows the electrical conductivity versus depth in Well 19445 at different times. This graph demonstrates how the conductivity changes during that period.

I will give a more detailed explanation in the next few chapters about how to use these measurements to help interpret the crosshole resistivity data.

6.6 PUMPING OPERATIONS

The first water injection started in October, 1999 and the final water injection stopped in April, 2001. During this period, a range of hydrological, geochemical and geophysical experiments were conducted. The water injections (pumping operations) were interrupted on several occasions. Table 6.1 summarises the main events during the period of pumping. A cumulative plot of volume of the injected water in the period is given in Figure 6.9. At the time of writing, the water injection phase had completely finished but the water recovery phase is yet to start.

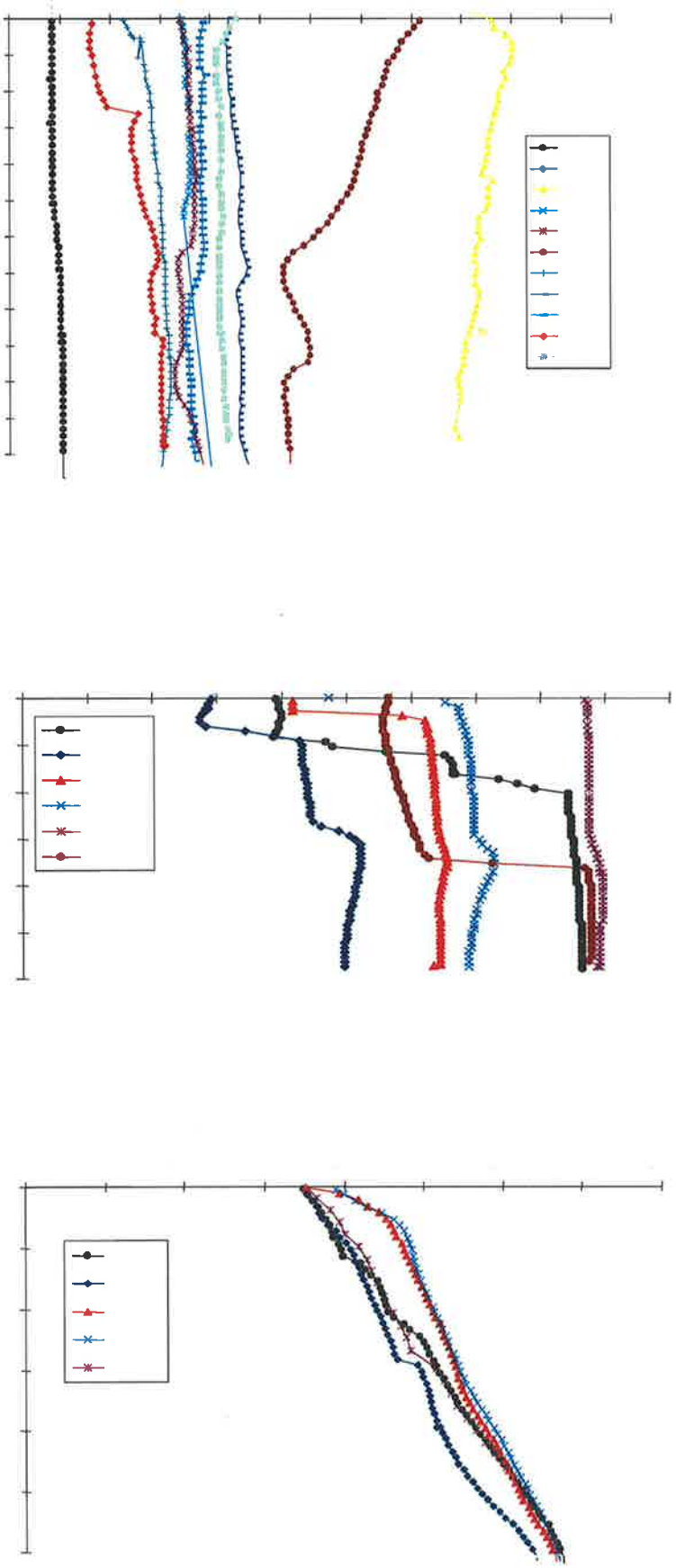

Figure 6.8 Some other time-lapse physical log data profiles: a) dissolved oxygen (DO, mg/l) logging data in well 19450; b) Electric conductivity (EC) logging data in well 19445; c) temperature logging data in well 19444.

Table 6.1 Summary of the main events during the whole ASR test period (from June, 1998 to April, 2001).

DATE	Description
Jun., 1998 – Sep., 1999	Preparing for water injection and conducted many preliminary resistivity surveys (surface, surface to borehole, borehole to borehole).
Oct., 1999 – Nov., 1999	The first water injection period (30ML). Three time-lapse resistivity tomographic surveys (each used 4 pairs of boreholes in chord configuration) were finished.
Dec., 1999 – Mar., 2000	Injection well redevelopment.
Apr., 2000	5 ML water injection test. One resistivity tomographic survey was finished with 4 pairs of different boreholes (in radial configuration).
May., 2000 – Jul., 2000	Some other tests and well redevelopment.
Aug., 2000 – Apr., 2001	The second water injection period. A total of about 220ML water was injected. Three time-lapse resistivity tomographic surveys were completed with 4 pairs of different boreholes (in radial configuration).

According to the work we have done and the summary of the main events in Table 6.1, we divided our resistivity research work into 3 periods. In the first period (from June, 1998 to September, 1999), many preliminary surface, surface-to-borehole and borehole-to-borehole surveys were conducted in order to understand the main subsurface resistivity characteristics at the ASR test site. A detailed explanation of the survey work in the period is given in Chapter 7.

Period 2 started in October, 1999 and ended in March, 2000. Three sets of time-lapse tomographic surveys were completed with four pairs of boreholes forming chords on the circular monitoring layout (#19442 & #19443, #19443 & #19445, #19445 & #19444, and #19444 & #19442). The configuration is illustrated in Figure 6.10. Then the survey data were processed, imaged and inverted to detect the water flow path with other available information. The data processing and interpretation details for this period are discussed in Chapter 10.

The last period started in April, 2000 and ended in April, 2001. In this period, four time-lapse tomographic surveys were done with four different pairs of boreholes (#19450 & #19442, #19450 & #19443, #19450 & #19444, and #19450 & #19445) in a radial configuration (see Figure 6.11) using the common borehole # 19450 close to the injection well. The data processing and interpretation details for this period are discussed in Chapter 11.

Figure 6.9 The water injection progress chart for the ASR trial.

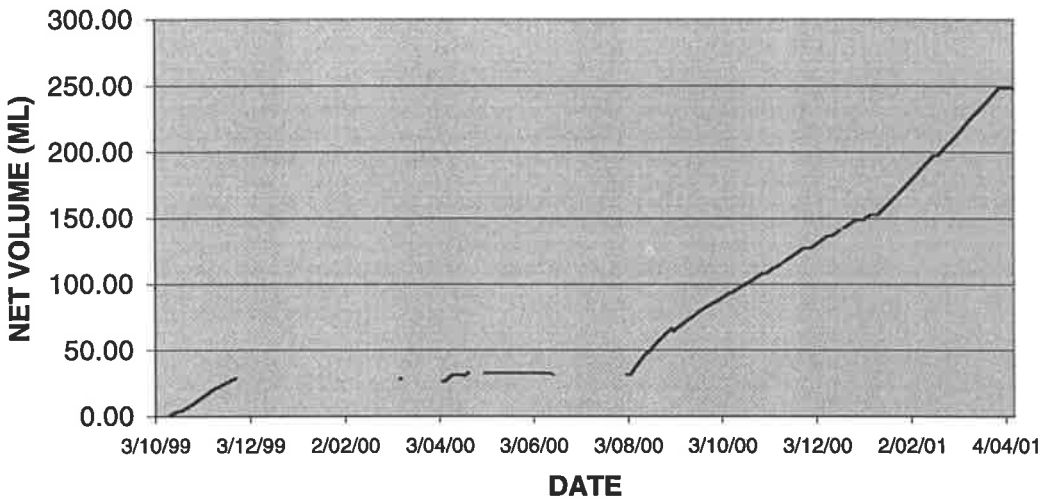

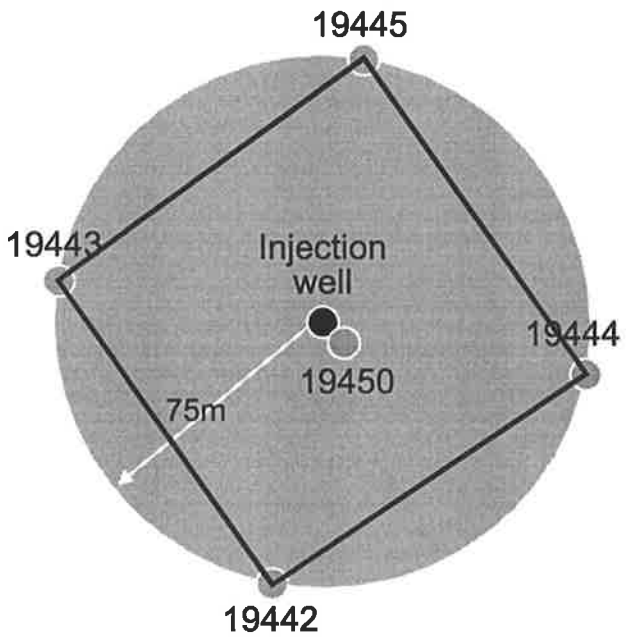

Figure 6.10 The survey layout in the second resistivity survey period.

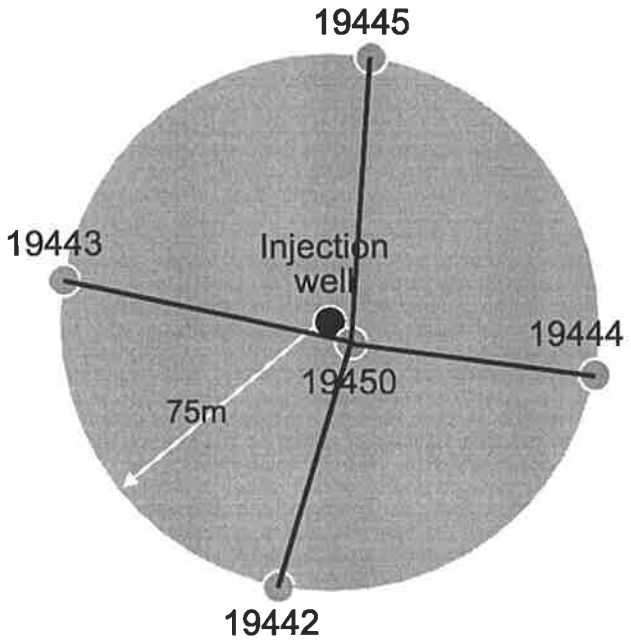

Figure 6.11 The survey layout in the third resistivity survey period.

6.7 RESISTIVITY INSTRUMENTATION USED IN ALL TESTS

The instrument used for collecting the resistivity survey data in all experiments was a SYSCAL-R2 from BRGM Instruments. A photograph is given in Figure 6.12.

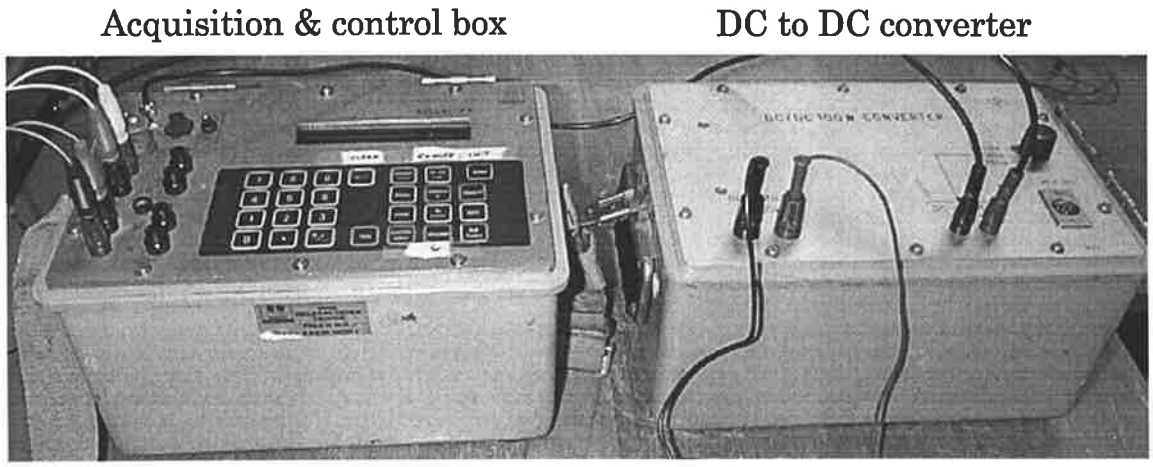

Figure 6.12 The photograph of resistivity instruments used for all resistivity surveys. They are SYSCAL-R2 resistivity meter and 100W DC to DC converter.

The SYSCAL-R2 unit consists of three components; the combined transmitter/receiver unit; a DC to DC converter; and a power source, 12V battery. The SYSCAL-R2 resistivity transmitter/receiver is a low power (110w) DC resistivity system that is powered by 6 D-size 1.5V battery. It is portable and easy to operate. It has two input channels that permit

simultaneous measurement of both voltage and current. It measures the self potential (SP) value as well, just before injecting the current into ground. This SP value is also stored with each reading and is used for SP bucking automatically. SP is also cancelled by periodically reversing the direction of current flow and adding the potentials. Up to 390 readings can be stored in the instrument's memory. The data is then transferred to a computer by a serial link. The input voltage range of the SYSCAL is - 5V to + 5V. The system can compute and display apparent resistivity for the main electrode arrays: Schlumberger, Wenner, Gradient, and dipole-dipole.

The second component of the SYSCAL-R2 electrical resistivity system is a 110W DC to DC power converter, powered by an external 12V or 24V battery. It has three different output options: 110DCV, 220DCV and 330DCV. Its maximum output current is 1A when the 110DCV option is used.

We built our own switch and cable system, which is connected to the SYSCAL-R2 resistivity meter. It was designed especially for tomographic measurements. Figure 6.13 shows the principal connection between the SYSCAL-R2 system and our switch and cables. We made two sets of cables, one for each borehole. They are 3 core cables with one conductor in each cable for the 28 meter spacing (AM2 and BN2) bipole potential measurements, one for the 14 meter spacing bipole measurements (AM1 and BN1), and one for current injection, as shown in Figure 6.13. Since the SYSCAL-R2 can measure only one set of data each time, a switch was made to change between the 14 metre spacing bipole reading and the 28 metre bipole reading (refer to Figure 6.13).

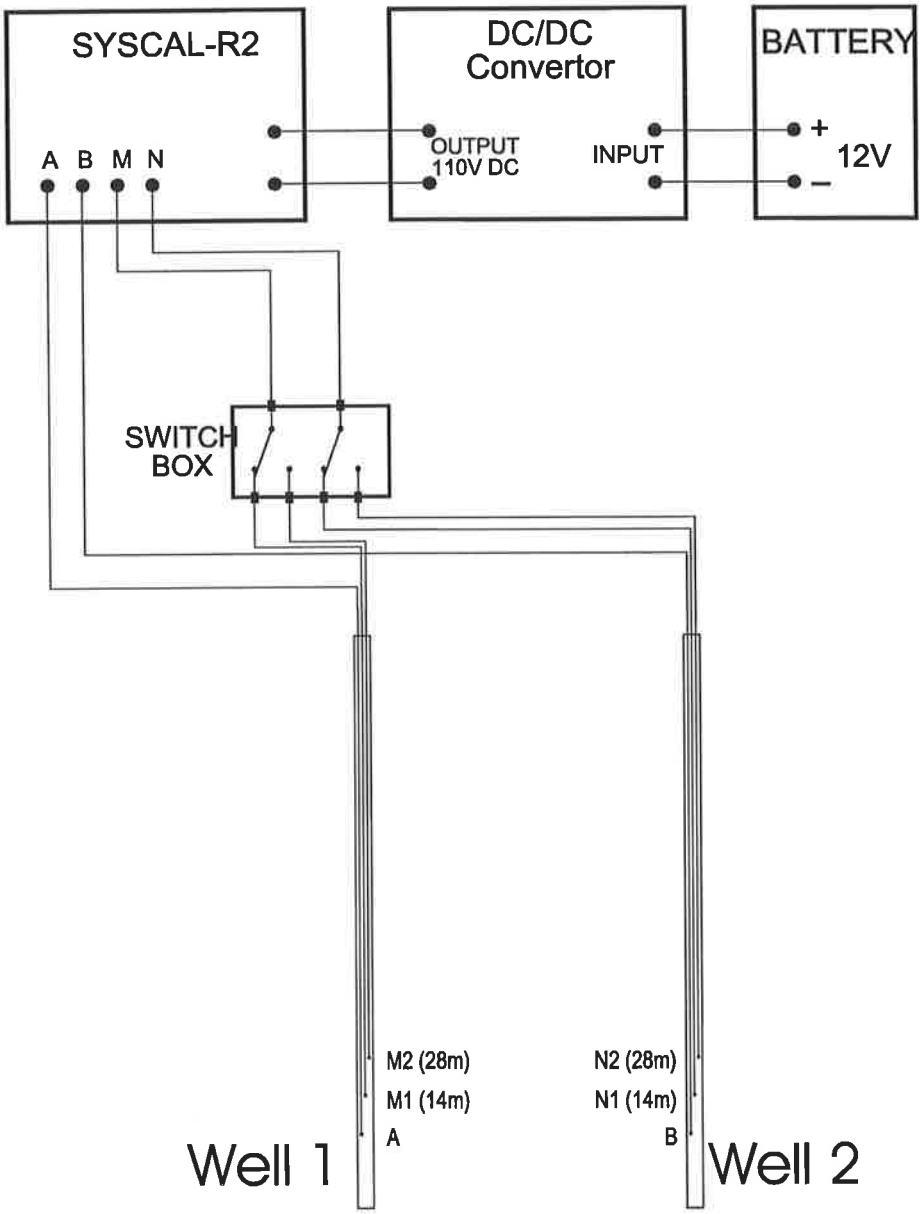

Figure 6.13 Diagram showing the resistivity instrument connections and switch box for all resistivity tomographic surveys.

Chapter 7

PRELIMINARY RESISTIVITY EXPERIMENTS BEFORE WATER INJECTION

7.1 INTRODUCTION

Before the water injection commenced, numerous surface, surface-to-borehole and borehole-to-borehole electrical resistivity experiments were conducted at the Bolivar ASR trial site. The borehole surveys utilised just three wells: the injection well (#18777), Well 19035 (120m away from the injection well) and Well 19134 (300m away from the injection well), since the five resistivity observation boreholes (19450, 19442, 19443, 19444 and 19445) had not been drilled at that time (refer to Figure 6.5 for well location details). The aim of these preliminary surveys was to obtain basic knowledge on the subsurface resistivity distribution at the ASR trial site and to test the different resistivity surveying configurations.

In total, 11 experiments were conducted in the period. These experiments can be classified into 3 groups: surface surveys, surface-to-borehole surveys, and cross-borehole surveys. All of the measured current and voltage data were converted into apparent resistivity and displayed in a graphic format. The approximate 2-D or 3-D resistivity images extracted from these surveys were produced using our 2-D/3-D resistivity imaging program (refer to Chapter 4). Since the number of data points in these surveys is very limited, full resistivity inversion is not possible. In this chapter I describe the experiments and present the results obtained in 3 groups: surface sounding, surface-to-borehole resistivity surveys and crosshole resistivity surveys.

7.2 SURFACE SOUNDINGS

The first resistivity survey we performed at the Bolivar ASR trial site entailed two Schlumberger vertical electrical soundings. The layout of the first sounding line is shown in Figure 7.1. The central point O was located about 6 meters away from the injection well (18777). The line was expanded in an east-west direction.

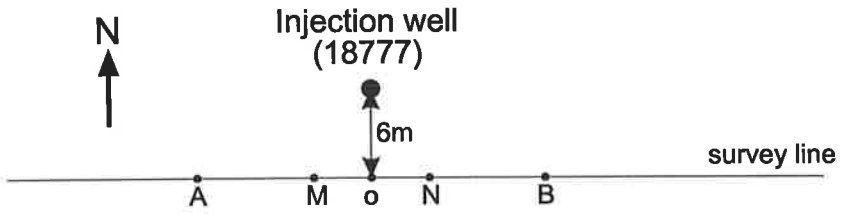

Figure 7.1 The layout of the first survey line in the surface resistivity survey.

The raw survey data and calculated apparent resistivity values (using equation (2.24)) are listed in Table 7.1.

Table 7.1 The survey data of the first line in the surface survey.

No.	A (m)	M (m)	B (m)	N (m)	V (mV)	I (mA)	AR (Ω.m)
1	1	0.15	-1	-0.15	688	1017	6.92
2	1.47	0.15	-1.47	-0.15	235.5	902.5	5.84
3	2.15	0.15	-2.15	-0.15	80	799.4	4.82
4	3.16	0.15	-3.16	-0.15	37.4	970.4	4.02
5	4.64	0.15	-4.64	-0.15	14.5	950.3	3.43
6	6.81	0.15	-6.81	-0.15	6.33	969.3	3.17
7	6.81	1	-6.81	-1	34.9	965.2	2.57
8	10	1	-10	-1	14.1	898.2	2.44
9	14.7	1	-14.7	-1	4.92	684.7	2.42
10	21.5	1	-21.5	-1	3.05	874.8	2.52
11	31.6	1	-31.6	-1	1.67	960.9	2.72
12	31.6	1.5	-31.6	-1.5	2.57	962.7	2.78
13	46.4	1.5	-46.4	-1.5	1.42	983.4	3.25
14	46.4	5	-46.4	-5	4.87	971.7	3.35
15	68.1	5	-68.1	-5	2.83	944.2	4.34
16	100	5	-100	-5	0.55	291.5	5.91
17	100	15	-100	-15	1.98	293.5	6.90

The second sounding line was expanded in a north-south direction l, as shown in Figure 7.2. The central point O was located about 20 meters south of the injection well.

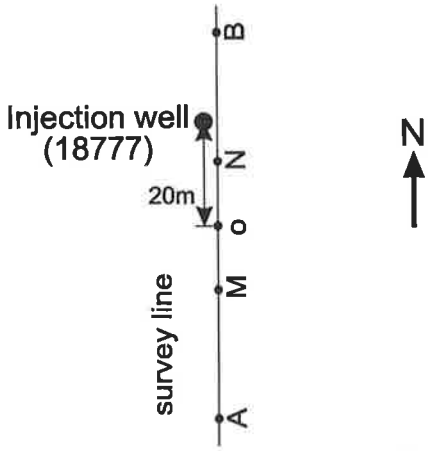

Figure 7.2 The layout of the second survey line in the surface resistivity survey.

The survey data and calculated apparent resistivity values are listed in Table 7.2.

Table 7.2 The survey data of the second line in the surface survey.

No.	A (m)	M (m)	B (m)	N (m)	V (mV)	I (mA)	AR (Ω.m)
1	1	0.15	-1	-0.15	512.8	863.5	6.07
2	1.47	0.15	-1.47	-0.15	173.8	855.1	4.55
3	2.15	0.15	-2.15	-0.15	69.5	914	3.66
4	3.16	0.15	-3.16	-0.15	26.6	920.5	3.01
5	4.64	0.15	-4.64	-0.15	12.1	942.9	2.89
6	6.81	0.15	-6.81	-0.15	5.54	921.8	2.91
7	10	0.15	-10	-0.15	2.75	929.2	3.09
8	10	0.5	-10	-0.5	9.1	942.8	3.02
9	14.7	0.5	-14.7	-0.5	4.21	1053	2.71
10	21.5	0.5	-21.5	-0.5	1.87	954.5	2.84
11	21.5	1.5	-21.5	-1.5	5.03	950.7	2.54
12	31.6	1.5	-31.6	-1.5	2.52	954.7	2.75
13	46.4	1.5	-46.4	-1.5	1.37	949.9	3.24
14	46.4	5	-46.4	-5	4.47	959	3.11
15	68.1	5	-68.1	-5	2.66	942.7	4.08
16	68.1	15	-68.1	-15	7.77	935.5	3.8
17	100	15	-100	-15	1.17	220.8	5.42

From the data in the above two tables, it can be seen that most of the potential differences between M and N are too small (less than 10mV) to be reliable when the distance between current electrode A and B exceeds 10 meters. So the calculated apparent resistivities beyond data point 10 are not reliable. The injected currents are not very small and they almost reached the limit (about 1A) of the DC/DC converter. The small voltages are a result of the low surface resistivity value and the small potential electrode separation.

The survey data were imaged using our 3-D imaging program. Figures 7.3 and 7.4 show the imaged results from the two survey lines respectively. Both figures are very similar and show that there are three layers, high (3.5Ω.m), low (2.5Ω.m) and high (5.0Ω.m). But the resistivity differences between the layers are small, only about 2Ω.m. Because these are vertical sounding profiles, only the middle part of the image is reliable.

From the above data and the imaged results, one can see that the near surface resistivity is about 3-5 Ω.m. We also realise that the power source (110W DC to DC converter) is not sufficient to conduct surface soundings or profiles and obtain information about the resistivity distribution below a few tens of metres. The T2 aquifer, the target of interest, is about 100 m below the surface. Since we are not so concerned about the resistivity distribution above the T2 aquifer, we did not conduct any more surface resistivity surveys.

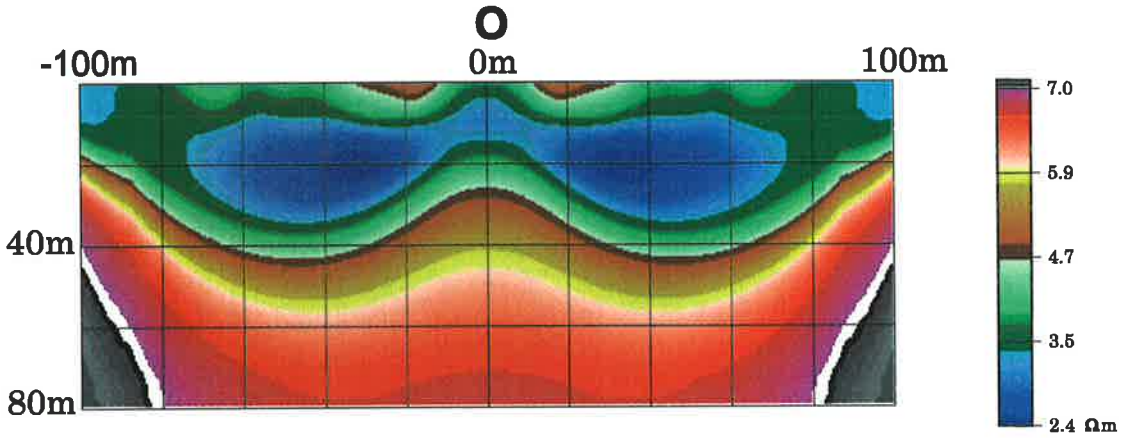

Figure 7.3 The imaged result from the data of the East-West line of the surface survey.

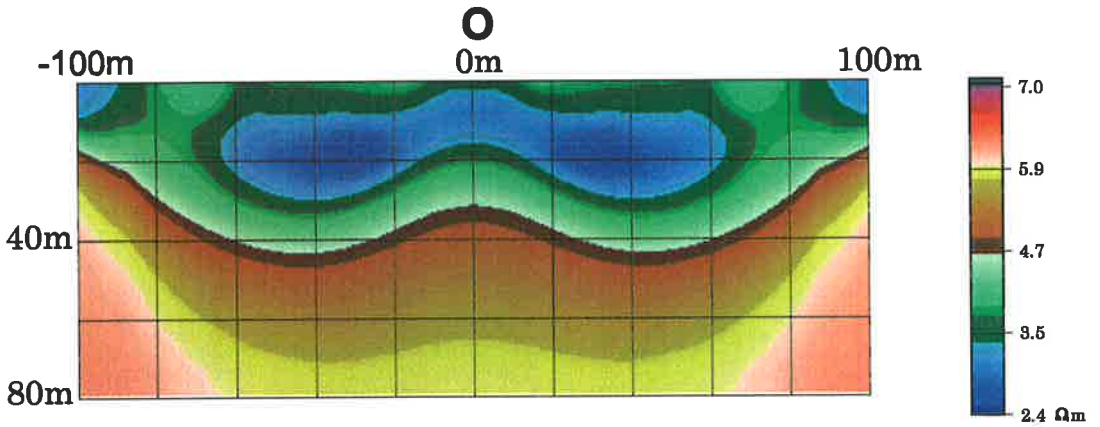

Figure 7.4 The imaged result from the data of the South-North line of the surface survey.

7.3 SURFACE-TO-BOREHOLE RESISTIVITY SURVEYS

Two different configurations are possible for surface-to-borehole resistivity survey. The first one entails having both current electrodes C1 and C2 on the surface and the other bipole (potential electrodes P1 and P2) in the borehole, or vice versa. If the distance between the current electrode bipole and the potential electrode bipole is large in such a configuration, then the measured potential values normally are very small. So reliability of potential measurements is a problem. The second configuration is to place one current electrode C1 and one potential electrode P1 (one bipole) on the surface and the other two electrodes C2 and P2 (another bipole) in the borehole. The potential measurements in this configuration are reasonable large and reliable. So this was the configuration adopted in all our surface-to-borehole resistivity surveys.

After the potential and current values were measured in the surface-to-borehole surveys, the apparent resistivities were calculated using formula (2.45).

There are two different ways – vertical profiling and horizontal profiling - to conduct the surface-to-borehole survey. The first one is to fix the electrodes C2 and P2 in a borehole and move the electrodes C1 and P1 on the surface (refer to Figure 7.5). This scheme will mainly reveal the resistivity changes in the area close to the surface and in the horizontal direction, as shown in Figure 7.5. The earth resistivity in the light shadowed area of Fig. 7.5 will mainly influence the apparent resistivity change when the surface electrodes C1 and P1 are moved to the position C1' and P1'. So we call this surface-to-borehole horizontal profiling. The second scheme is to fix the electrodes C1 and P1 on the surface and move C2 and P2 along the borehole vertically (refer to Figure 7.6). This configuration will mainly reveal the resistivity changes in the area close to the borehole (C2 and P2) and in the vertical direction, as shown in Figure 7.6. The earth resistivity in the light shadowed area of Fig. 7.6 will mainly influence the apparent resistivity change when the electrodes C2 and P2 are moved downwards in the borehole. So we can call this surface-to-borehole vertical profiling.

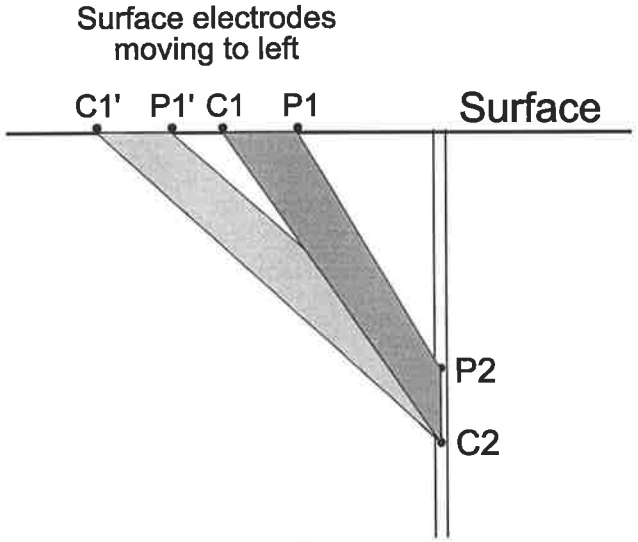

Figure 7.5 The configuration for moving C1 and P1 on the surface in surface to borehole survey.

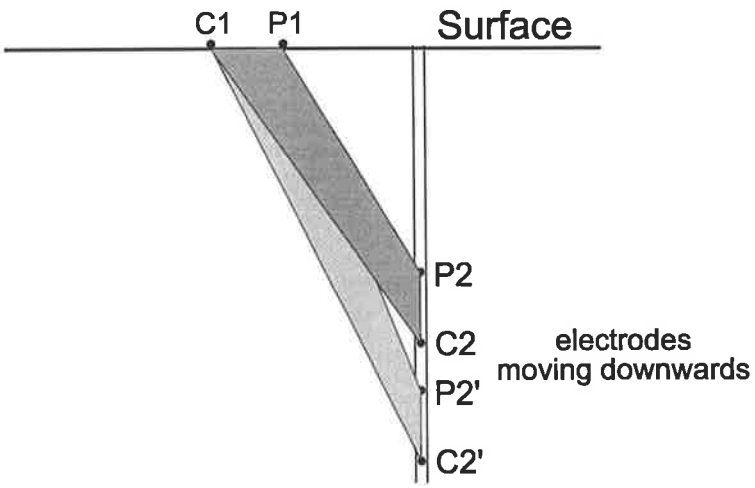

Figure 7.6 The configuration for moving C2 and P2 in the borehole in surface to borehole survey.

7.3.1 Survey 1 – Surface-to-Borehole Horizontal Profiling

Three survey lines were run along the surface at different azimuths, as shown in Figure 7.7. The bipole-bipole electrode array was used for all three lines. The cross-sectional configuration of the experiment is depicted in Figure 7.8. The distances of the four electrodes were measured from the centre point O at the well head. The current electrode C1 and the potential electrode P1 were fixed at depths of 135m and 150m respectively, within the T2 aquifer in the injection well 18777. Current electrode C2 and potential electrode P2 were placed on the surface at a fixed separation of 15m and moved progressively together radially outward at an incremental spacing of 15m, as far as 150 m either side of the well. The layout of the three survey lines is shown in Figure 7.7.

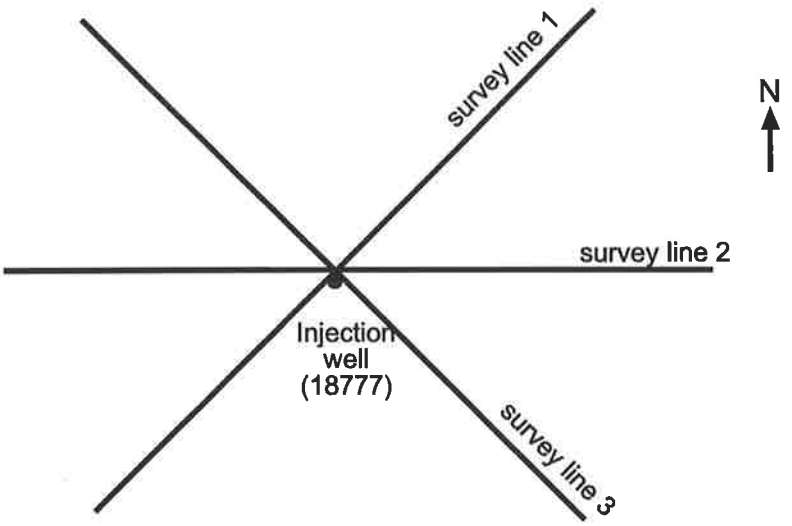

Figure 7.7 The relationship of three survey lines on the surface in the first surface-to-borehole survey.

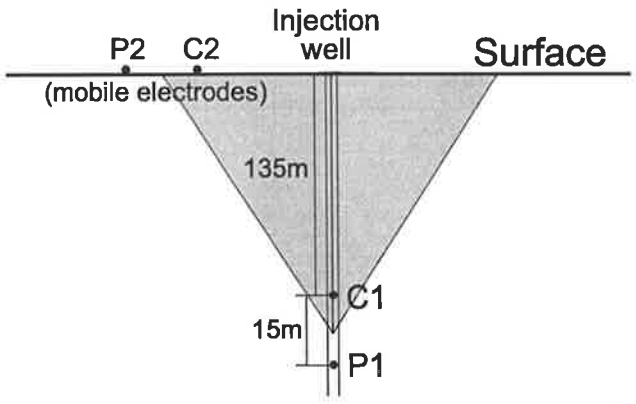

Figure 7.8 The configuration of the four electrodes in the first surface-to-borehole survey.

Referring to Figure 7.7, Line 1 starts from the southwest of the injection well and runs towards the northeast. Line 2 is a west-east line and Line 3 runs from northwest to southeast. The survey data and the calculated apparent resistivities (with formula 2.45) for Line 1 only are given in Table 7.3 for illustrative purposes.

Table 7.3 The survey data and calculated apparent resistivity of survey line 1.

No.	P2 (m)	C2 (m)	Potential(mV)	Current I(mA)	Apparent Resistivity (Ω.m)
1	135	120	110.4	1147.4	6.62
2	120	105	60.00	638. 30	6.51
3	105	90	15.00	166.20	6.29
4	90	75	71.10	771.60	6.46
5	75	60	88.60	980.60	6.37
6	60	45	82.60	908.30	6.45
7	45	30	71.40	787. 10	6.46
8	30	15	31.70	352.80	6.42
9	15	0	97.00	1071. 10	6.49
10	0	-15	96.40	1071.30	6.45
11	-15	-30	97.50	I 071.00	6.51
12	-30	-45	96.80	1071.30	6.44
13	-45	-60	96.70	I 071.20	6.41
14	-60	-75	84.00	916.70	6.47
15	-75	-90	84.70	927.20	6.41
16	-90	-105	84.80	9 I 4.10	6.47
17	-105	-120	84.80	904.60	6.49
18	-120	-135	84.20	894.30	6.48
19	-135	-150	85.30	906.10	6.44

A question which immediately arises with such a configuration is how to display the apparent resistivity data. So far no one has suggested a proper way to present the apparent resistivities in 3-D space. With the aid of our 3-D imaging program, this problem is resolved because it can produce an approximate resistivity distribution map from the observed data directly. The data from all three lines have been analysed simultaneously to produce the horizontal slices through the resistivity volume at depths of z =0, 70, 140m respectively, as shown in Figure 7.9.

The purpose of the survey is to detect the lateral variability of the resistivity above 100m depth. Since the two electrodes in the borehole were fixed at depths of 135m and 150 m and only two surface electrodes were moved from one side to the other, the variation in the measurements mainly reflects the resistivity change above 70 meters depth. From Figure 7.9, it can be seen that the resistivity distribution is nearly 'uniform' in all horizontal directions. Note that the resistivity variation across the whole area is only about 1 Ω.m. Although it is little lower in the northeast corner, the difference is very small. The mean of the apparent resistivity of the survey is about 6.45 Ω.m. Because of the salt water effect in the well, the

real (true formation) resistivity will be higher than the computed resistivity (refer to section 3.5).

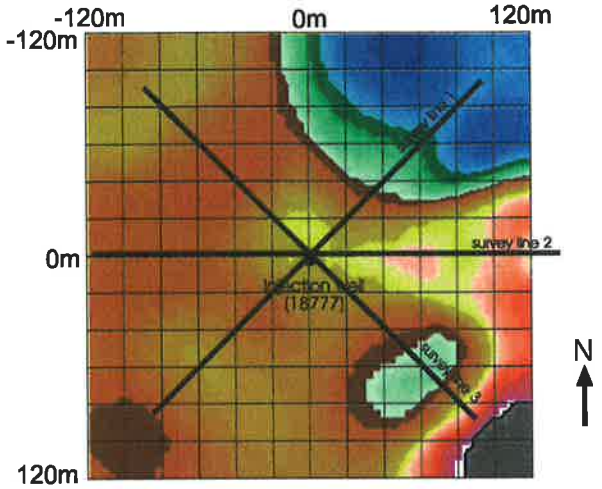

(a) Apparent resistivity distribution on X-Y plane at z=0m

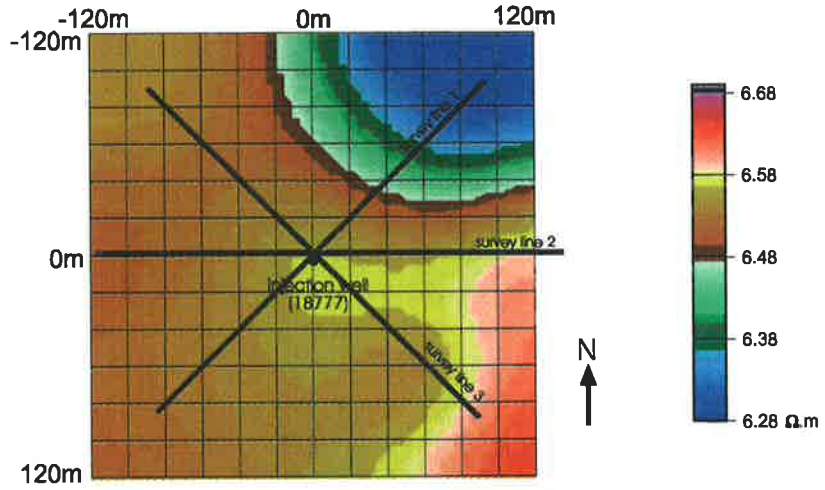

(a) Apparent resistivity distribution on X-Y plane at z=70m

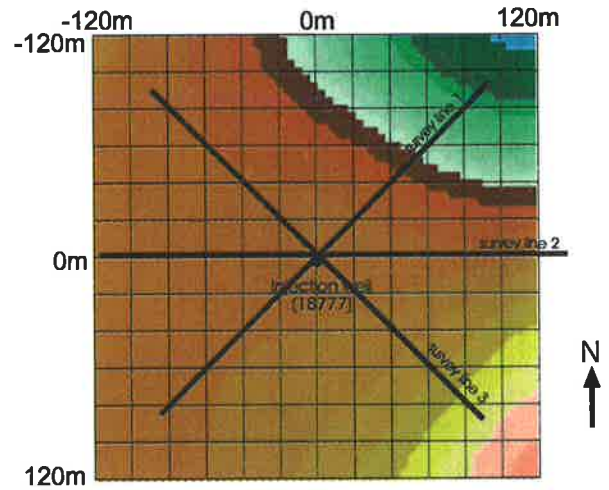

(a) Apparent resistivity distribution on X-Y plane at z=140m

Figure 7.9 The imaged results from the survey data of the three lines in the first surface-to-borehole survey.

7.3.2 Survey 2 – Surface-to-Borehole Vertical Profiling

This survey is different from the last one, although they look similar. The cross section layout of the survey is shown in Figure 7.10. This time, two surface electrodes C2 and P2 are initially fixed at 20m and 35m east of the injection well (refer to Figure 7.10). Then the two borehole electrodes C1 and P1 (still 15m apart) in the injection well are moved progressively downwards over the depth range 105m to 170m (C1 from 105m to 155m and P1 from 120m to 170m). The procedure is then repeated for a different fixed position of C2 and P2 in 15m intervals (C2 from 20m to 110m, 7 points). In total, seven sets of data were collected for seven different positions of C2 and P2. The apparent resistivities are calculated and are graphed in Figure 7.11. The survey data are also imaged using our approximate 3-D imaging procedure. The imaged result for the vertical plane is shown in Figure 7.12.

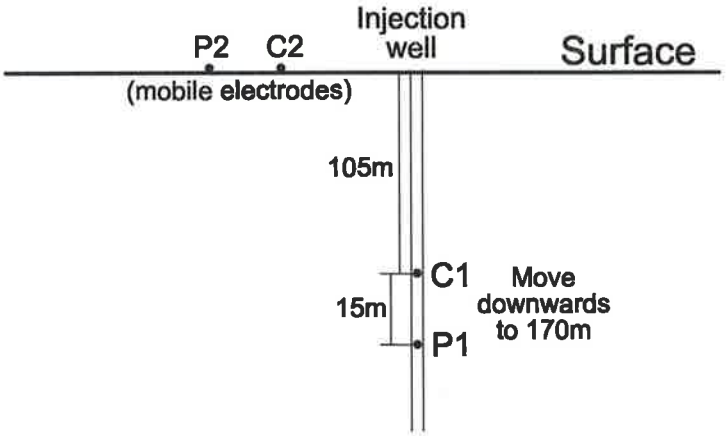

Figure 7.10 The cross section of the second surface-to-borehole survey.

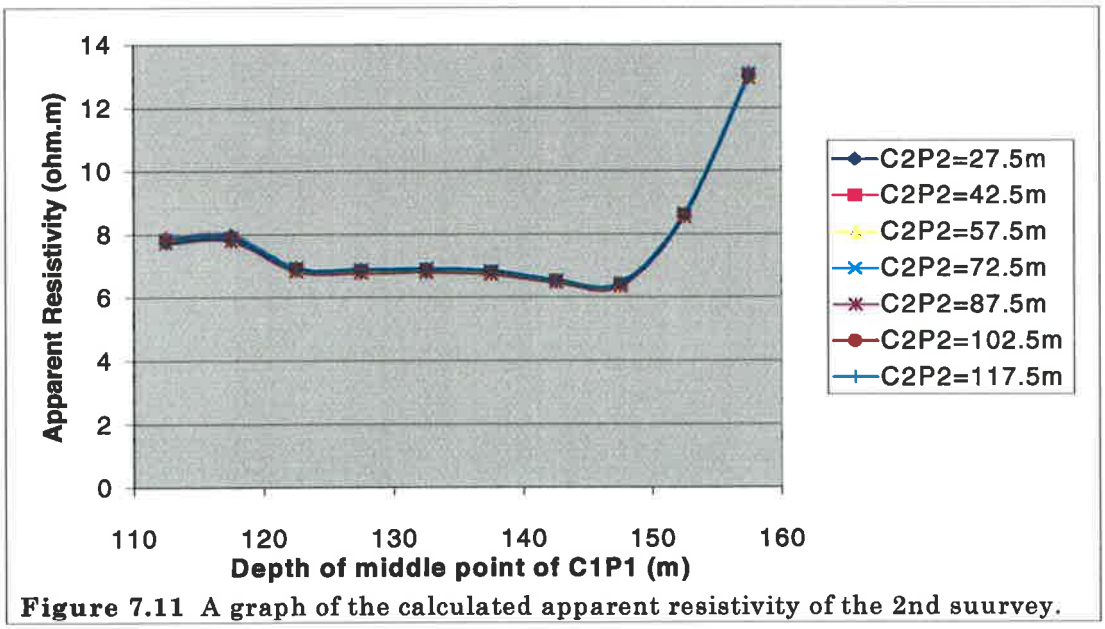

Figure 7.11 A graph of the calculated apparent resistivity of the 2nd suurvey.

The purpose of such a survey is mainly to detect the vertical resistivity changes. The vertical movement of C1 and P1 over the depth range 105m to 170m will reveal resistivity changes in this depth range.

From the raw apparent resistivity data in Figure 7.11, one can see that the horizontal movements of the electrodes C2 and P2 did not affect the apparent resistivity values much since the seven curves are all very similar (almost superimposed). This means the resistivity changes in the horizontal direction are very small, which is consistent with the findings of the first surface-to-borehole horizontal profiling survey. But the apparent resistivity graph shows changes when electrodes C1 and P1 are moved from depth 105m to depth 170m. The final resistivity image (Figure 7.12) shows the pattern, high, low and high. This indicates that there is distinct resistivity layering over this depth range. It can be seen from Figure 7.11 that the apparent resistivity suddenly increases below a depth of 147.5m. This was because the electrode C1 reached the bottom of the borehole, which made the distance between C1 and P1 much smaller and the potential on electrode P1 much higher. So we ignored the data below a depth of 147.5m.

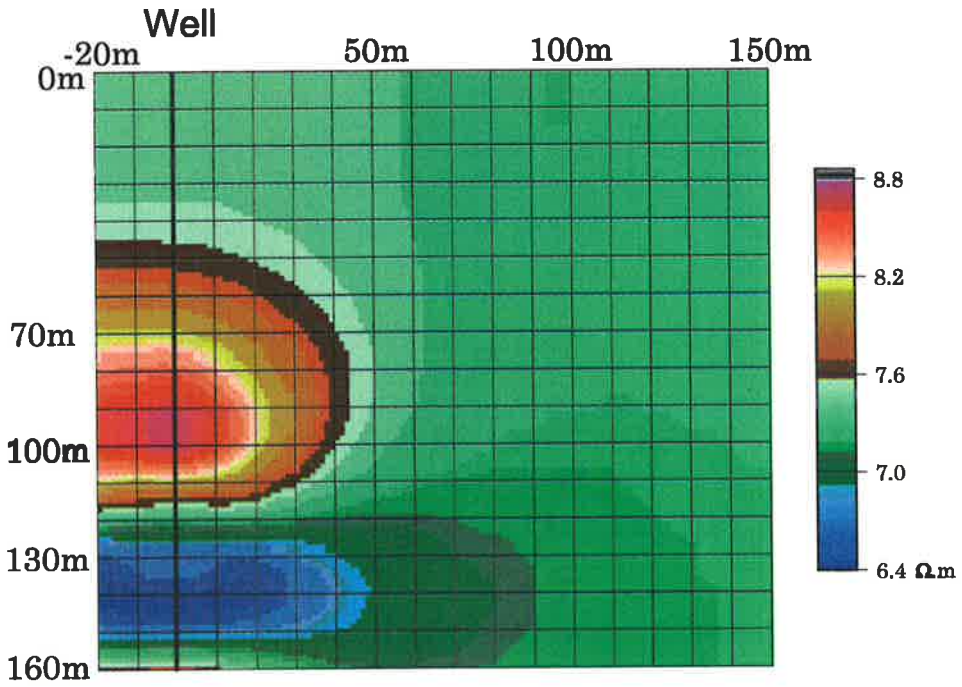

Figure 7.12 The imaged result from the survey data of the surface to borehole vertical profiling.

From the image shown in Figure 7.12, one can see that the resistivity distribution in the survey range (from depth 105m to 160m) is decreasing with depth and there are two main

layers in the range separated at the depth about 125m. From the later crosshole resistivity surveys, we know that these two resistivity distribution characteristics are correct.

7.4 THE CROSS-BOREHOLE RESISTIVITY SURVEYS

The crosshole surveys entailed placing two electrodes (C1 and P1) in one borehole and the other two electrodes (C2 and P2) in the other borehole. All voltage and current measurements for each observation point in the crosshole resistivity surveys are converted into the apparent resistivity by the formula (2.45).

Crosshole resistivity surveys can be classified into three different classes, depending on the electrode moving pattern. The first pattern involves moving four electrodes up or down simultaneously, maintaining the spacing between C1 and P1, and between C2 and P2, as shown in Figure 7.13. We call it 'crosshole screening'. This moving pattern will mainly yield apparent resistivity changes with depth.

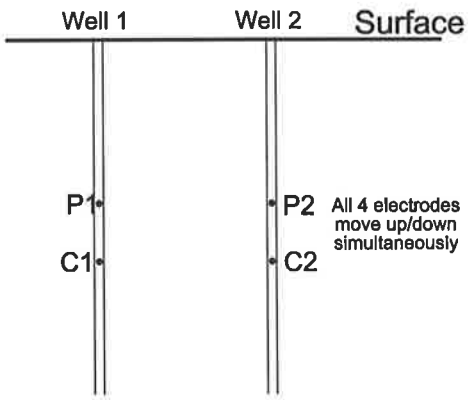

Figure 7.13 The cross section of the first moving pattern of the borehole-to-borehole survey - crosshole screening.

The second moving pattern is when C1 and P1 are fixed in one borehole and C2 and P2 are moved up or down in the another borehole, maintaining the same spacing between C1 and P1, and between C2 and P2, as shown in Figure 7.14. We call this 'crosshole scanning'. This moving pattern will mainly yield the apparent resistivity change with depth near the second borehole containing the mobile electrodes C2 and P2. The reason is that the main effective area (the shadowed area in Fig. 7.14) due to the movement of C2 and P2 is closer to the borehole where C2 and P2 are placed.

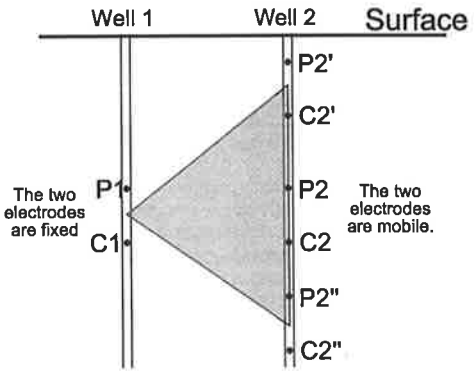

Figure 7.14 The cross section of the second moving pattern of the borehole-to-borehole survey - cross hole scanning.

Both screening and scanning configurations are simple and useful for preliminary surveys. But for detailed tomographic style surveys, the following moving pattern is the best since a lot of data can be acquired and detailed information on the inter-well medium obtained by inverting the survey data.

The last moving pattern of electrodes is the main configuration we used in our resistivity crosshole tomographic surveys. We call it 'crosshole multiple scanning'. The configuration of the 'crosshole multiple scanning' is shown in Figure 7.15. The bipole spacing (distance between the current electrode and potential electrode, C1P1 or C2P2) is fixed during the scanning. Normally, we start with the two pairs of electrode at the bottom of the each well. One pair of electrodes (C1 and P1) is kept stable in well 1 and the other pair of electrodes (C2 and P2) in well 2 is moved upwards at a fixed interval (for example, 2 meters). At each position occupied in well 2, one set of current and voltage measurements are taken. As such, N sets of potential values and current values can be obtained for each scanning (the pair of electrodes in well 2 moves from the bottom of the well to the top). This is the same as the 'crosshole scanning' technique described above. Then the two electrodes C1 and P1 in well 1 are moved up by one increment of depth and remain fixed again as the other two electrodes C2 and P2 in well 2 are moved from the bottom to the top again to obtain N sets of values. The procedure is repeated until the electrodes in well 1 reach to the top. Therefore, in total NxN sets of values can be acquired for each crosshole multiple scanning survey.

We can obtain a large amount of data after each such experiment. But it is very hard to display all these data in a proper way in which each single datum can be assigned to a fixed spatial point. The only effective way to use these data is by imaging and inversion, which can

convert all survey data into the resistivities which are associated with each spatial point. This is our purpose for completing the crosshole multiple scanning.

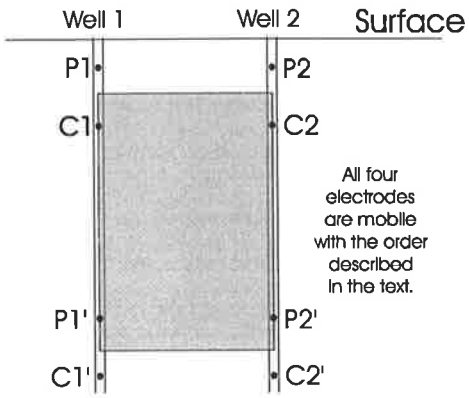

Figure 7.15 The cross section of the third moving pattern of the borehole-to-borehole survey - crosshole multiple scanning.

As stated before, in each crosshole multiple scanning, the bipole spacing (distances C1-P1 and C2-P2) in each well is fixed. So if we can complete several (not just one) crosshole multiple scannings with a few different fixed spacings of C1P1 and C2P2, we can obtain much more information from the multiple 'multiple scanning data', since the different fixed distances have different detection and penetration ranges. Certain parts of the medium can be better imaged with different spacings.

7.4.1 Crosshole Electrical Survey 1 – Configuration Experiments

As with the surface-to-borehole surveying, the crosshole resistivity survey has three different basic configuration types, as shown in Figure 7.16. The first type is when C1 and P1 are in one borehole and C2 and P2 are in the other borehole, and C1 is on the top of the potential electrode P1 and C2 is below the other potential electrode P2. The second type is when C1 and C2 are in one borehole and P1 and P2 are in the other hole. The third type is when both current electrodes C1 and C2 are on the top or the bottom of the two potential electrodes P1 and P2, as shown in diagram (c) of Figure 7.16. The equivalents are also shown.

The first crosshole survey was conducted for testing the above three different configuration types. Three sets of tests were done for the three configuration types respectively. The injection well and Well 19035, which is 120m away from the injection well, were used for these tests. The cross-section layouts of the three tests are the same as shown in Figure 7.16. The distance between two electrodes in each borehole was fixed at 15m. The 'crosshole screening' was used in these three experiments. That means that all four electrodes moved

downwards at 1m interval simultaneously from 128m to 159m depth (the bottom electrode positions). So a total of 32 data points were acquired for each configuration. The measured voltage, current, and calculated apparent resistivity of the three survey experiments are shown in Figure 7.17, Figure 7.18 and Figure 7.19, respectively.

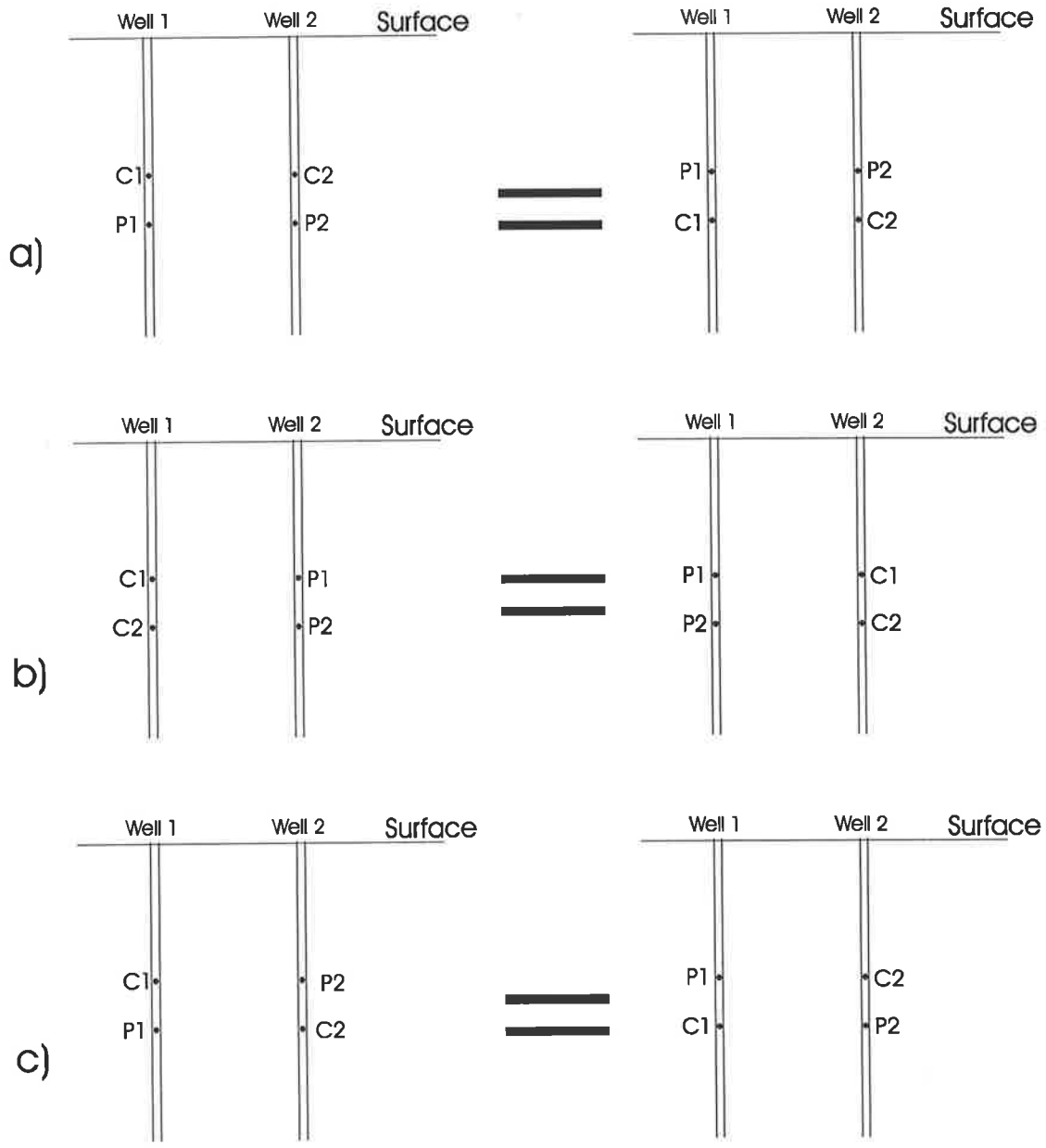

Figure 7.16 The three different configurations in borehole-to-borehole surveys.

Firstly, from these results, it can be seen that the potential values of the survey test 2 (configuration b (refer to Figure 7.16) are too small (less than 1mv) although the current values for this experiment were very large. So this configuration type is not suitable for borehole resistivity surveys. The measured potential values in the other two tests are quite reasonable and the calculated apparent resistivities are also satisfactory. From Figure 7.19,

one can see that the calculated apparent resistivities from test 1 and test 3 match very well. This means that these two configurations may work equivalently well. However, the third configuration (configuration c in Figure 7.16) may have a singularity problem in theory (Zhou, 1998). With a normal resistivity instrument, only positive potential values are recorded. But in theory, a negative potential difference between P1 and P2 is possible for configuration c. So this may produce some problem with resistivity inversion. Therefore the best configuration which can be used in normal crosshole resistivity surveys is the configuration type a, shown in a) of Figure 7.16. We used this configuration in all our later crosshole resistivity surveys.

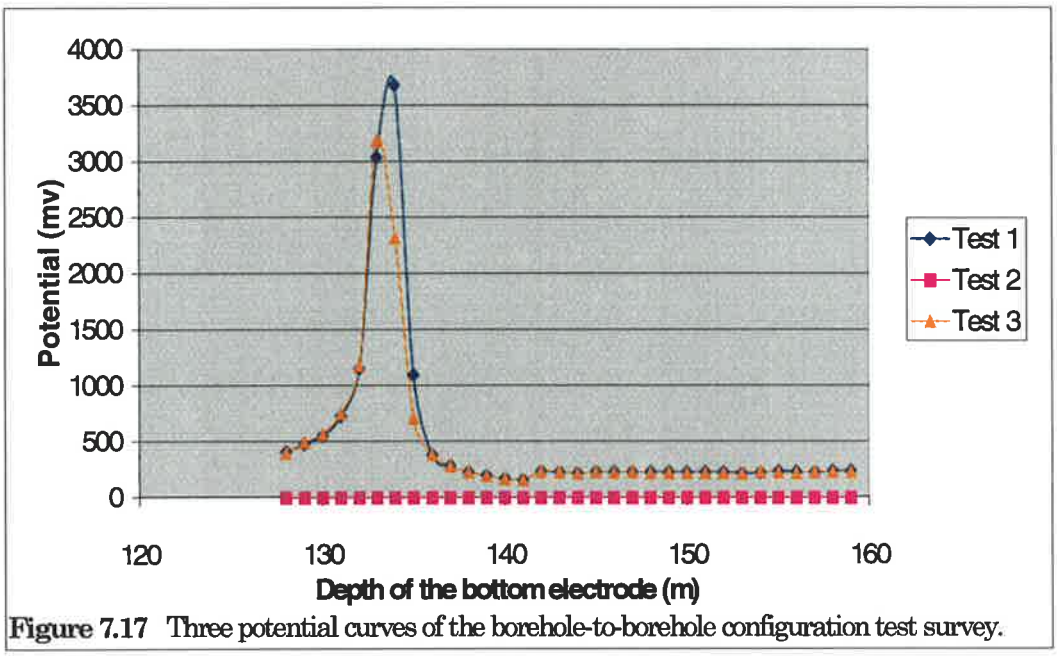

Figure 7.17 Three potential curves of the borehole-to-borehole configuration test survey.

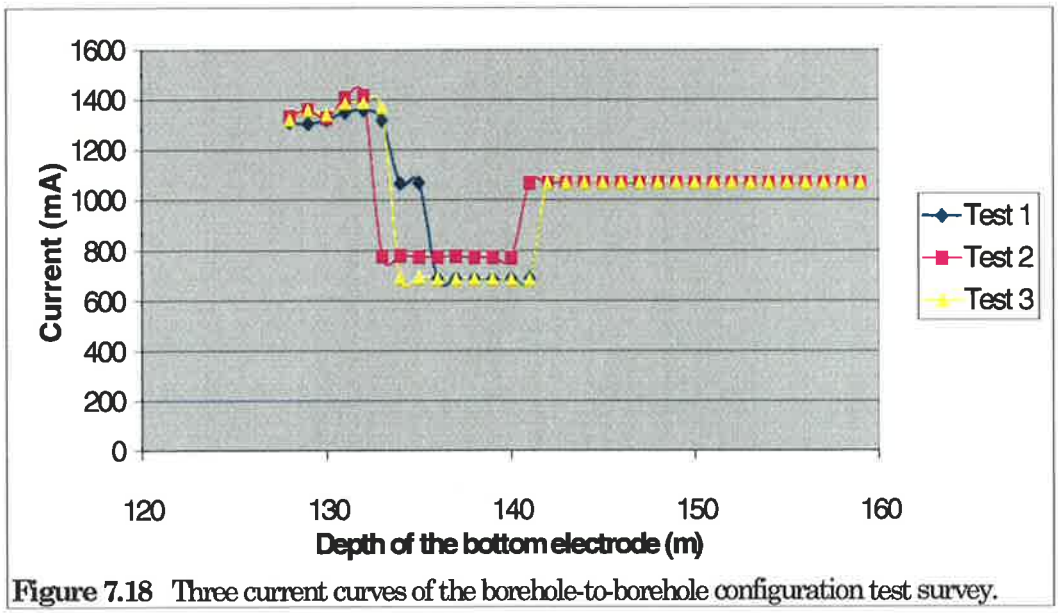

Figure 7.18 Three current curves of the borehole-to-borehole configuration test survey.

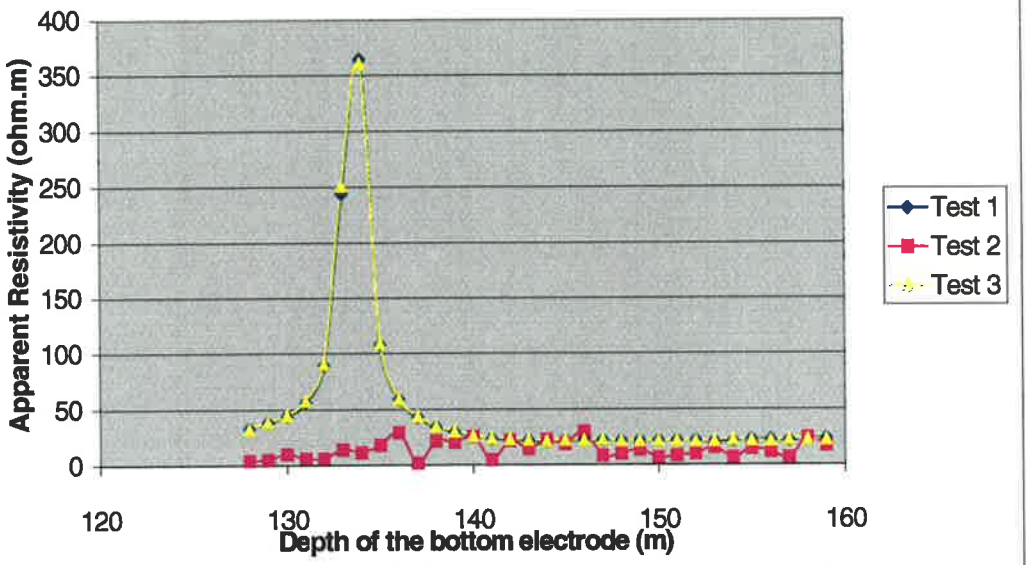

Figure 7.19 Three AR curves of the borehole-to-borehole configuration test survey.

7.4.2 Crosshole Electrical Survey 2

Two tests were done in the second crosshole resistivity experiment, again using the injection well and Well 19035. The electrode configurations of the two experiments are the same as those used in experiment 1 (a) of Figure 7.16) and experiment 3 (c) of Figure 7.16) of the above survey, except that a different electrode moving pattern was used in the two experiments. The 'crosshole scanning' moving pattern was employed in this survey, instead of 'crosshole screening'.

In both experiments, C2 and P2 were fixed at depths of 134m and 149m respectively in Well 19035, and C1 and P1 were moved over the depth ranges 134m to 151m (for C1) and 149m to 166m (for P1), respectively, in the injection well. The calculated apparent resistivities are graphed in Figure 7.20. Due to the use of 'crosshole scanning', the calculated apparent resistivities shown in Figure 7.20 will mainly reflect the resistivity change with depth near the injection well. The two resistivity curves looks very similar although they have different configuration types. Comparing these results with that obtained in survey 2 in Section 7.3.2, we find that they are similar in shape although the absolute values are different due to different background resistivities. The background range for the experiment in Section 7.3.2 is from the surface to the bottom of the injection well (in vertical direction) and the background range for this experiment is from the injection well to Well 19035 in the T2 aquifer (in the horizontal direction). Again, the measured values below the depth of 165m are suspect because the borehole is blocked at this depth and the electrode separation for subsequent measurements is no longer reliable.

Figure 7.20 Two calculated apparent resistivity curves of the second borehole to-borehole survey.

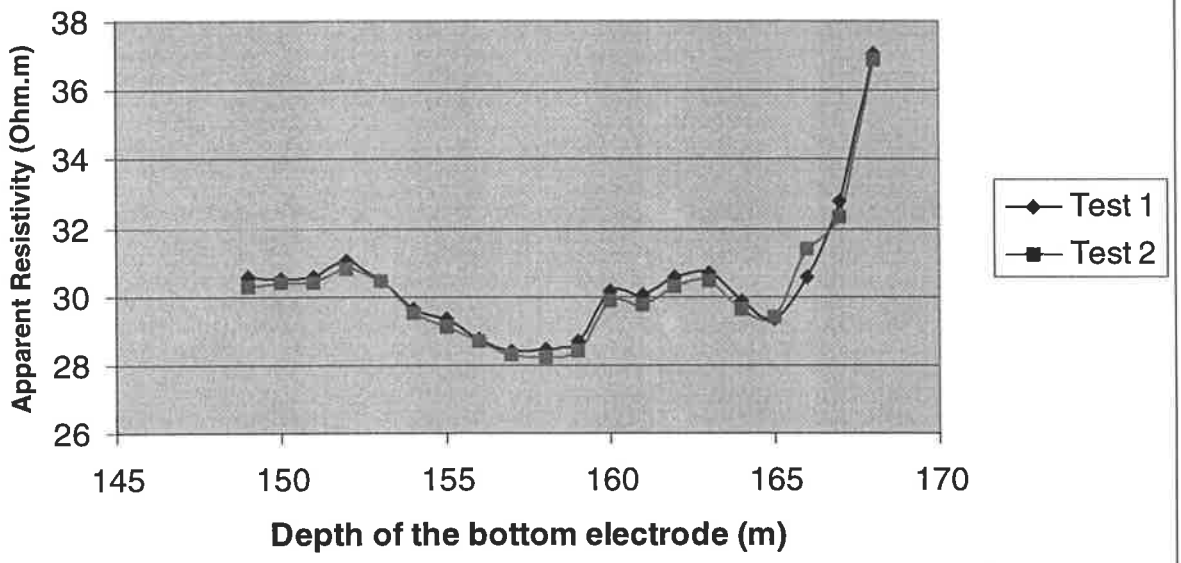

7.5 CONCLUSION

A number of preliminary resistivity surveys were carried out at Bolivar, some of which have been reported here.

The goals of the pre-water injection surveys were to 1) find a suitable resistivity surveying configuration for detecting the water flow direction in the T2 aquifer; 2) become familiar with all sorts of resistivity survey configurations; 3) obtain some basic subsurface resistivity information at the ASR site. From the surveys described, it is clear that the borehole-to-borehole configuration is the best for aquifer delineation, because the configuration will fully use the four electrodes for imaging the target area and have less effect from the region outside the area of interest. The surface configuration is definitely not suitable for this situation since the T2 aquifer is too deep. The surface-to-borehole configuration is not suitable either because it mainly responds to resistivity variations above the T2 aquifer. The 'crosshole multiple scanning' technique is the best choice since it provides enough detailed data for resistivity inversion. The use of multiple spacings in 'crosshole multiple scanning' is the preferred approach, since it yields information over different portions of the interwell medium. From all surveys we have completed, we have learnt a lot about surface-to-borehole and borehole-to-borehole resistivity exploration techniques.

According to the calculated apparent resistivities from all surveys, it can be seen that the resistivity above the T2 aquifer is lower on average than the resistivity in the T2 aquifer. So we set the resistivity above the T2 aquifer to about 10 Ohm.m when we set up the initial resistivity model in the inversion.

Chapter 8

MODELLING AND INVERSION OF WATER INJECTION: EXPECTED TIME-LAPSE RESISTIVITY RESULTS IN PHASE I

8.1 INTRODUCTION

There were two water injection phases in the Bolivar ASR trial as discussed in chapter 6. Phase 1 started in October 1999 and ended in November 1999. Phase 2 was from August 2000 to April 2001. During phase 1, three time-lapse resistivity surveys were conducted, and four pairs of crosshole resistivity multiple scannings in the chord direction were carried out, as shown in Figure 8.1. During phase 2, four time-lapse resistivity surveys were conducted, and four different pairs of crosshole resistivity multiple scannings in the radial direction were executed, as shown in Figure 8.2.

In order to understand what could be extracted and interpreted from the survey data, numerical resistivity modelling and inversion were undertaken to simulate the Bolivar ASR crosshole resistivity experiments. In this chapter we report on the results for crosshole chord-scanning synthetic measurements. In the next chapter, we report on the results for the radial scanning simulations.

From the geological cross section of the Northern Adelaide Plain (NAP) shown in Figure 6.3 and the well logs shown in Figure 6.6, one can see that the geological structure in this area is almost flat. So a simplified four horizontal layer resistivity structure, shown in Figure 8.3, is used as an initial model for numerical modelling. From the field survey data and the well log records, we also know the ground resistivity decreases with depth. So the resistivities in the initial model were set to the decrease with depth as well.

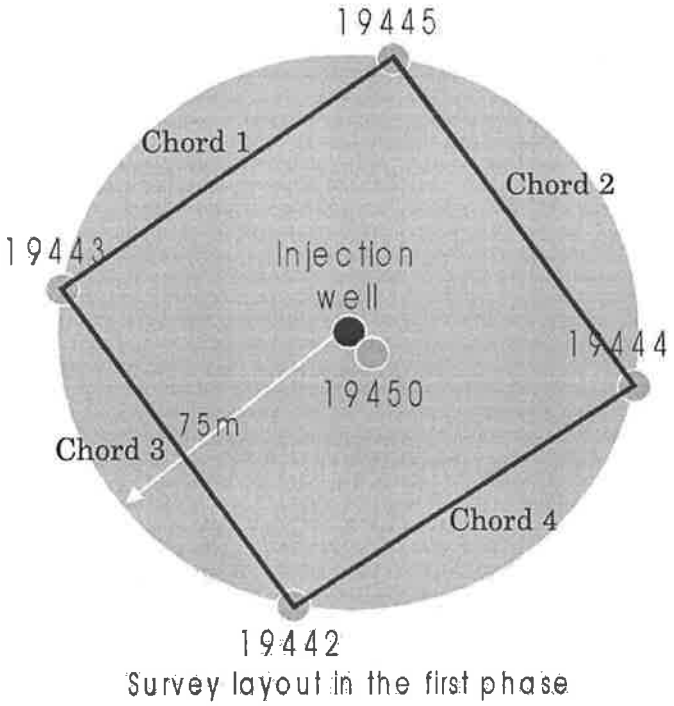

Figure 8.1 The surface layout of the cross well resistivity surveys. Four cross-hole resistivity multiple scannings, on chords 1, 2, 3 and 4, were conducted in each survey in water injection Phase I.

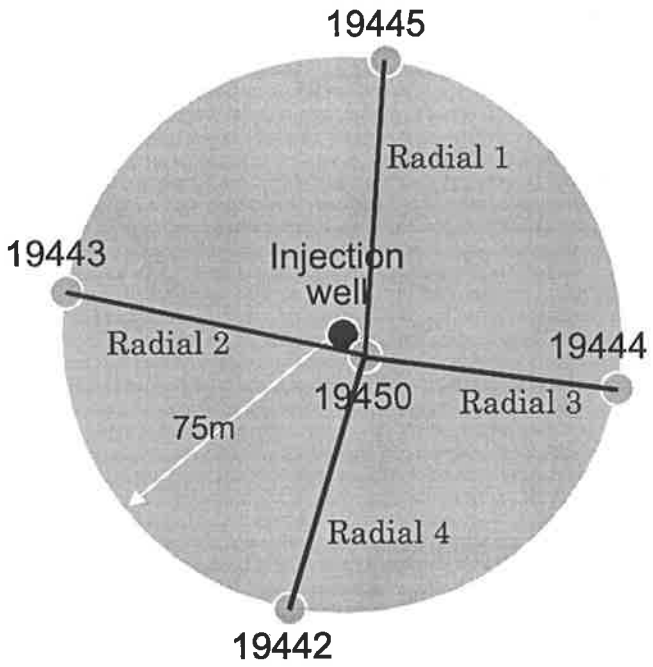

Figure 8.2 The surface layout of the crosshole resistivity surveys. Four cross-hole resistivity multiple scannings, on radii 1, 2, 3 and 4, were conducted in each survey in water injection Phase II.

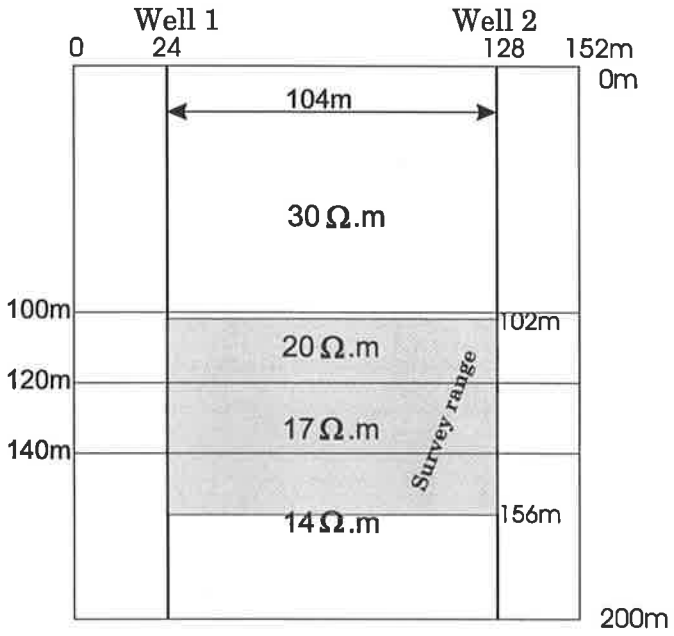

Figure 8.3 The initial model loyouts and parameters of the numerical resistivity model tests for the chord survey situation.

The same crosshole multiple scanning layout shown in Figure 8.4 was used in all field surveys in water injection Phase 1. The survey depth range in each well is from 102m to 156m. There are in total 28 (= (156-102)/2 + 1) possible electrode positions in each borehole, assuming a 2m increment. For the 14m C_1P_1 or C_2P_2 spacing, the number of computed data points is 441 (=21 x 21 voltages), while for the 28m spacing there are only 196 available data points to compute (= 14 x 14 voltages). In total, there are 637 data points in each crosshole multiple scanning.

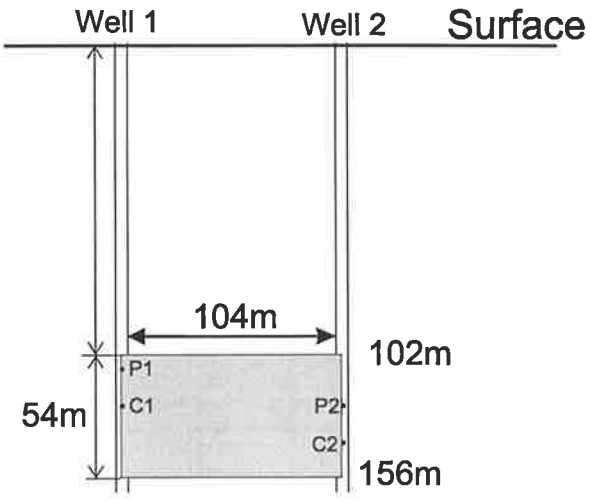

Figure 8.4 The cross section of the crosshole resistivity multiple scanning layout for all modelling in this chapter. C1 and C2 are current electrodes, and P1 and P2 are potential electrodes.

Section 8.2 provides details on the numerical resistivity modelling for simulating the surveys in Phase 1 in the chord direction. Section 8.3 gives the inversion results from the modelling data.

8.2 NUMERICAL CROSS WELL RESISTIVITY MODELLING EXPERIMENTS FOR THE CHORD CONFIGURATION

We know that the injected fresh water should flow gradually outward, as depicted in Figure 8.5. It is not easy to simulate this 3-D water flow situation in the chord well experiment with a 2.5-D electrical modelling program. Our 3-D electric modelling program can not handle such a large area with a 2m grid cell size. So we use the roughly equivalent 2-D model representation of Figure 8.6 to simulate the increase of injected water with time between any two wells forming a chord of the monitoring circle.

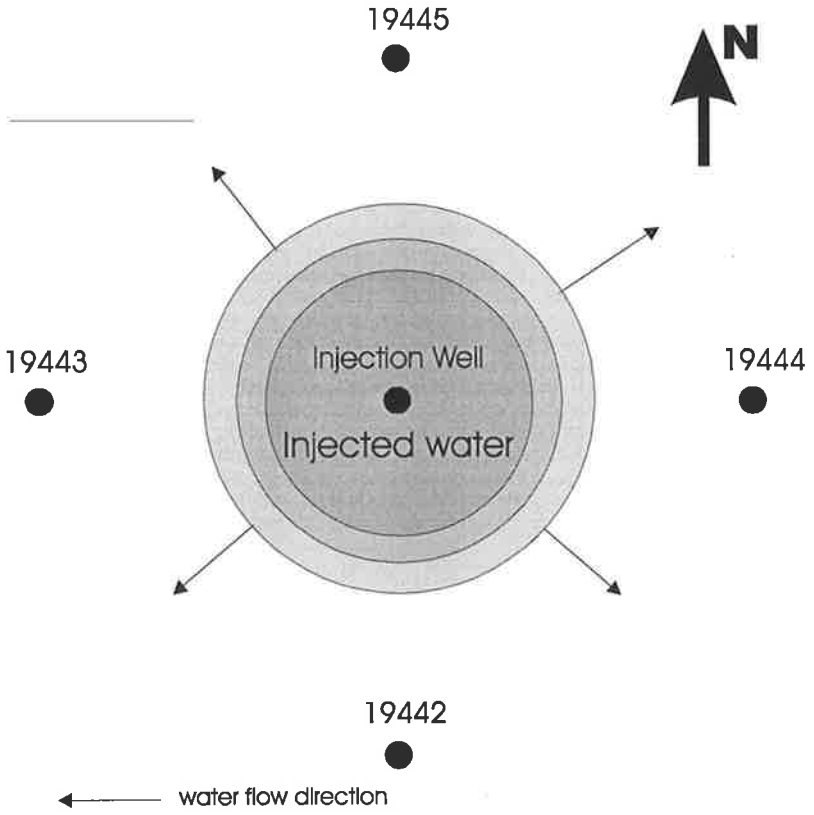

Figure 8.5 Surface view of the injected water flow trend.

The borehole layout is shown in plan view in Figure 8.1. There are four pairs of boreholes, with an average chord length of 104 m. Figure 8.4 is a summary diagram of the situation for each pair of wells. It shows in vertical section the 54m of aquifer in relation to the measurement geometry. Modelling was carried out to generate synthetic data assuming such

a crosshole multiple scanning configuration. So in total, there are 637 data points in each crosshole multiple scanning, incorporating both 14m and 28m spacings of the electrodes.

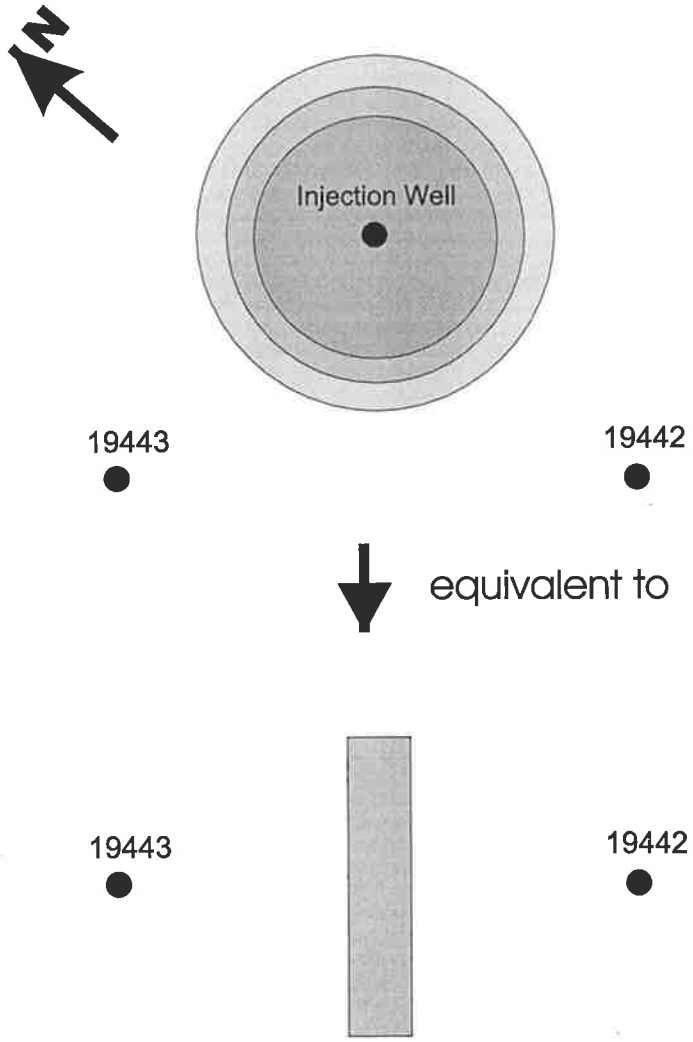

Figure 8.6 A diagram to show how to use a 2.5-D modelling program to simulate the 3-D water injection situation, depicted above.

Two different basic model sets were considered, corresponding to two different injected water flow patterns in the subsurface. The first basic model set assumes that all the layers below 100m are permeable, as shown in Figure 8.7. The second basic model set assumes that the all layers below 100m, except for the second layer, are permeable, as shown in Figure 8.8. The resistivities vary between 14 and 40 Ω.m. These values were based on electric log results, and the field apparent resistivity observations. The groundwater has a known resistivity of 2.6 Ω.m and the injected fresh water has a resistivity of 4 Ω.m. The average apparent resistivity of the survey data is about 20 Ω.m.

For each model set, four modifications are permitted as shown in Figures 8.7 and 8.8, corresponding to differing levels of (higher resistivity) fresh water infiltration. The four models in each set correspond to four separate times after pumping commences: (1)initially; (2) when the available aquifer space between the wells is 1/3 occupied by the fresh water; (3) when the available aquifer space is 2/3 occupied by fresh water, and (4) when the space between the boreholes is fully occupied. These four time-lapse scenarios are shown for both model sets in Figures 8.7 and 8.8.

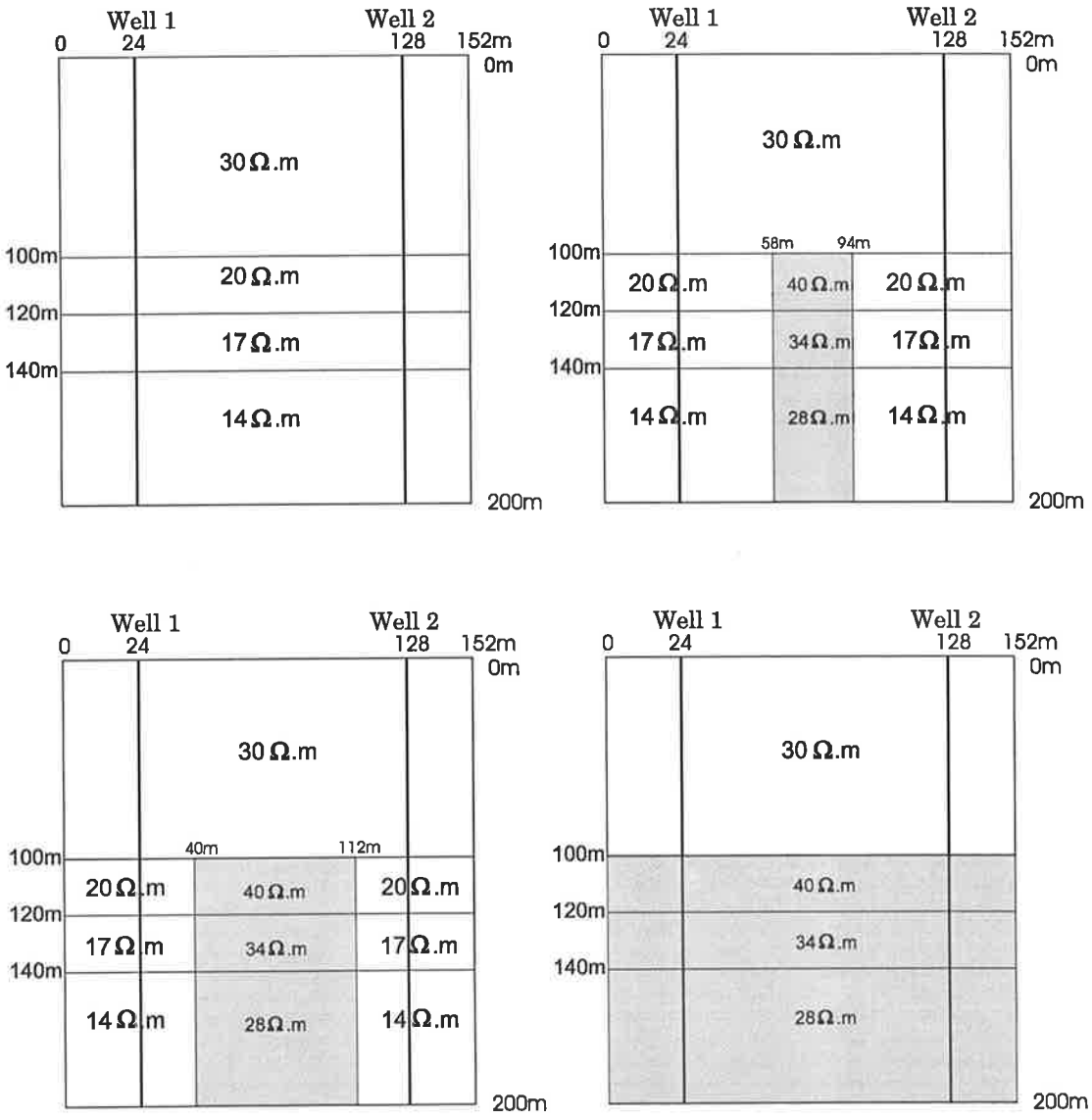

Figure 8.7 The model loyouts and parameters of the 4 numerical models of the first model set, corresponding to different stages of water injection.

The output from the 2.5-D resistivity modelling program are potential differences between the two potential electrodes P1 and P2, assuming the injection current is 1A. Then the apparent resistivity at each point is calculated. Next the average apparent resistivities, R_{14a} and R_{28a}, for the 14m and 28m spacing data are calculated for each model. Then the relative changes of

R_{14a} and R_{28a} are calculated between the four differing time stages (levels of water injection) for each model. Finally, the average apparent resistivities and their relative changes are compared among all models in each model set.

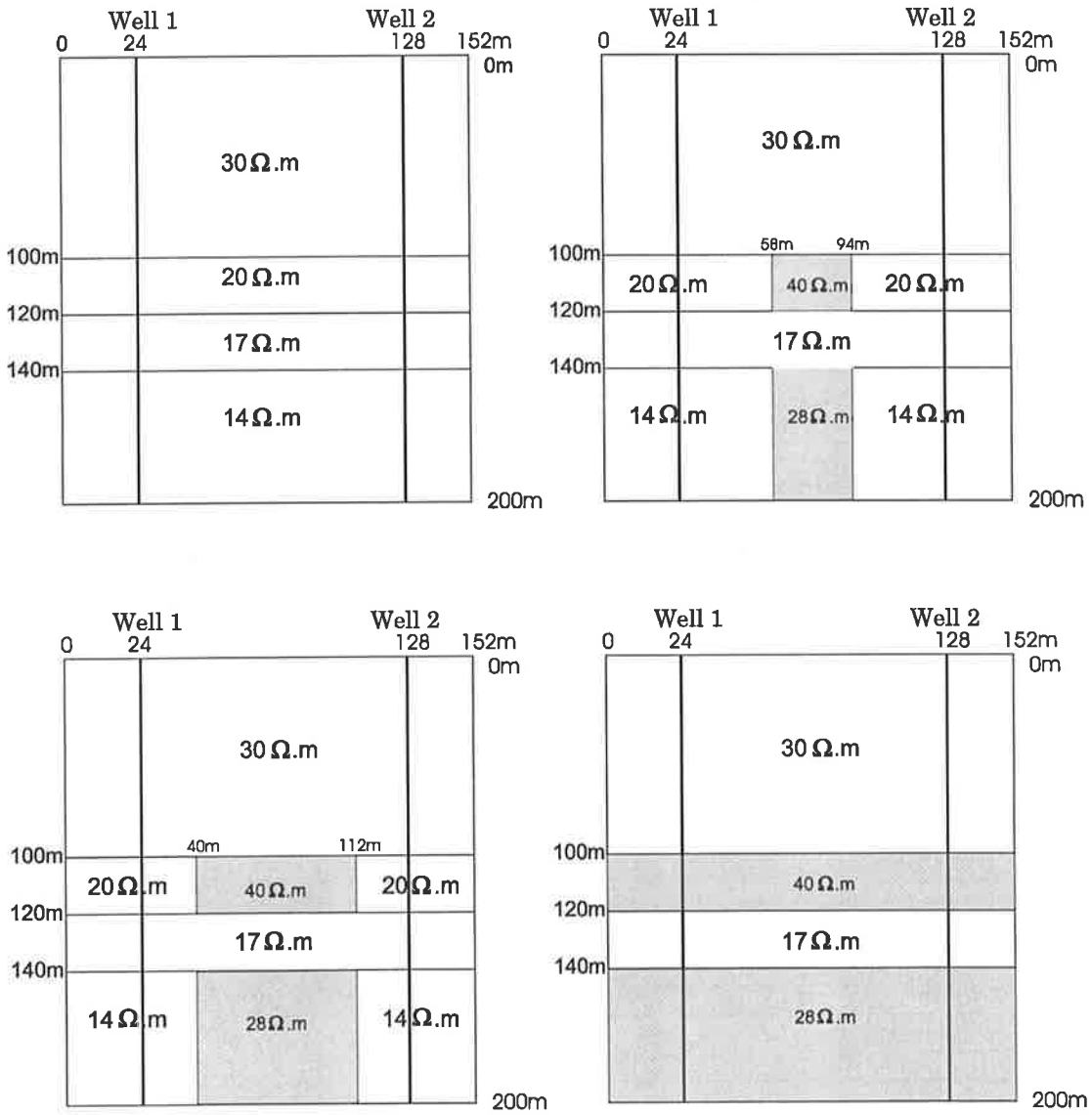

Figure 8.8 The model loyouts and parameters of the 4 numerical models of the second model set, corresponding to different stages of water injection.

8.2.1 Model Set 1 – Three Layer Aquifer, All Layers Equally Permeable

The aquifer in the first model set comprises a three layer structure (resistivities 20, 17 and 14 Ω.m) overlain by a layer of resistivity 30 Ω.m. Four numerical models have been calculated for this set, as shown in Figure 8.7. From the figure, it can be seen that the shaded area increases gradually, to simulate progressive stages of water injection. Each layer in the

aquifer is assumed to have identical hydraulic conductivity, resulting in vertical boundaries on the advancing water front, and a block like 2-D resistivity model.

The 8 stacked profiles of the modelling data of the four models for 14m and 28m electrode separation are shown in Figure 8.9 to Figure 8.16. This style of presentation is the same as that used for the field data. The different curves correspond to different midpoint depths of the bipole C2-P2. Apparent resistivity is plotted against depth of the midpoint of bipole C1-P1. The average apparent resistivity R_{14a} and R_{28a} for the 14m and the 28m spacing in the models are listed in Table 8.1. Also the relative change of the average apparent resistivity between consecutive models has been calculated and is tabulated below (Table 8.1).

Table 8.1 The minimum, maximum, average apparent resistivity and the apparent resistivity relative change of the 4 time-lapse sub-models for the first set of numerical simulations (model set 1 – 3 layer aquifer, uniform permeability).

Model Name	AR-MIN (Ω.m)	AR-MAX (Ω.m)	AR-MEAN (Ω.m)	AR Increase (%)
104m model 1-1 14m spacing	15.42	21.29	17.59	
104m model 1-2 14m spacing	16.33	22.07	18.46	5.0
104m model 1-3 14m spacing	17.86	23.54	20.01	8.4
104m model 1-4 14m spacing	30.15	34.19	32.49	62.4
104m model 1-1 28m spacing	16.50	20.07	17.85	
104m model 1-2 28m spacing	18.28	21.67	19.56	9.6
104m model 1-3 28m spacing	20.66	23.94	21.90	12.0
104m model 1-4 28m spacing	30.92	31.86	31.43	43.5

From the stacked profiles of model 1-1, model 1-2 and model 1-3, we can see that the apparent resistivity reduces with depth in each profile, which reflects the resistivity decrease with depth in the models. However the average resistivities of model 1-1, model 1-2 and model 1-3 show an increasing trend. This is because the injected fresh water causes the resistivity in the aquifer layer sequence to increase.

Figure 8.9 Apparent resistivity profiles of Model 1-1 (14m spacing).

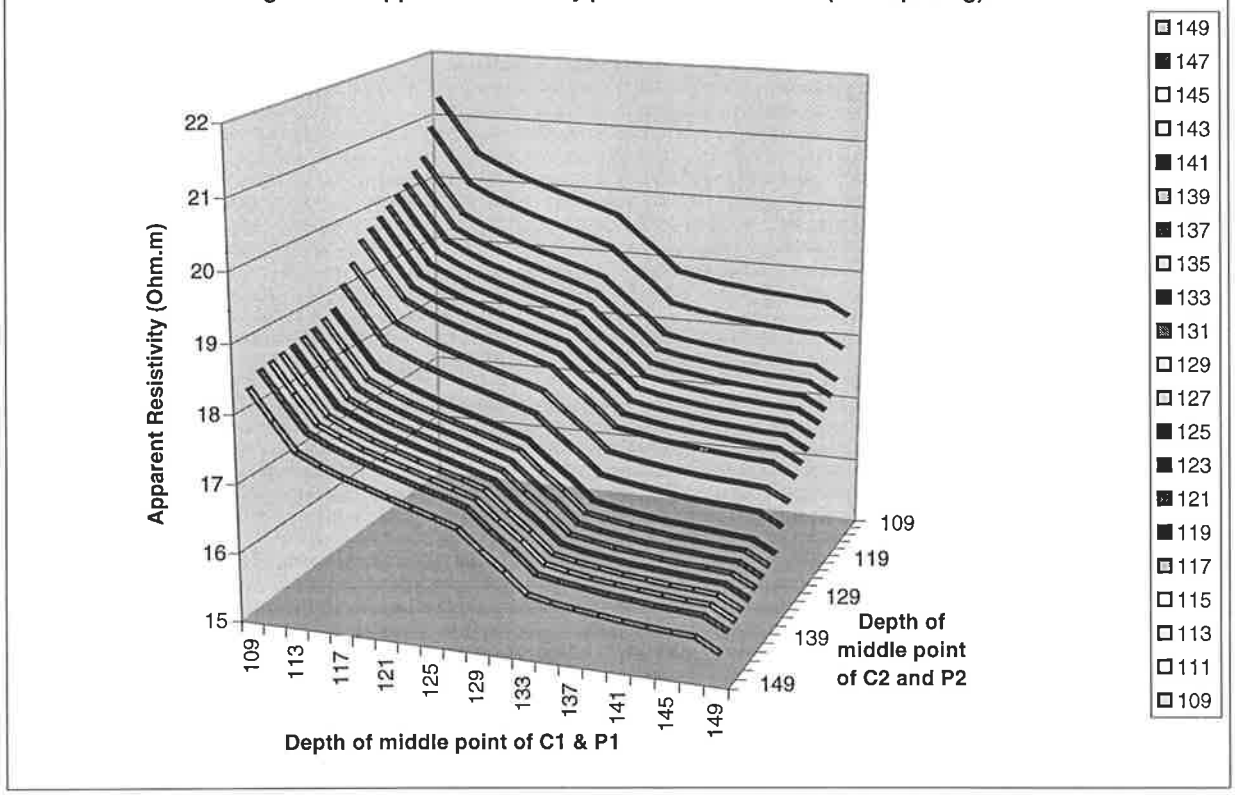

Figure 8.10 Apparent resistivity profiles of Model 1-2 (14m spacing).

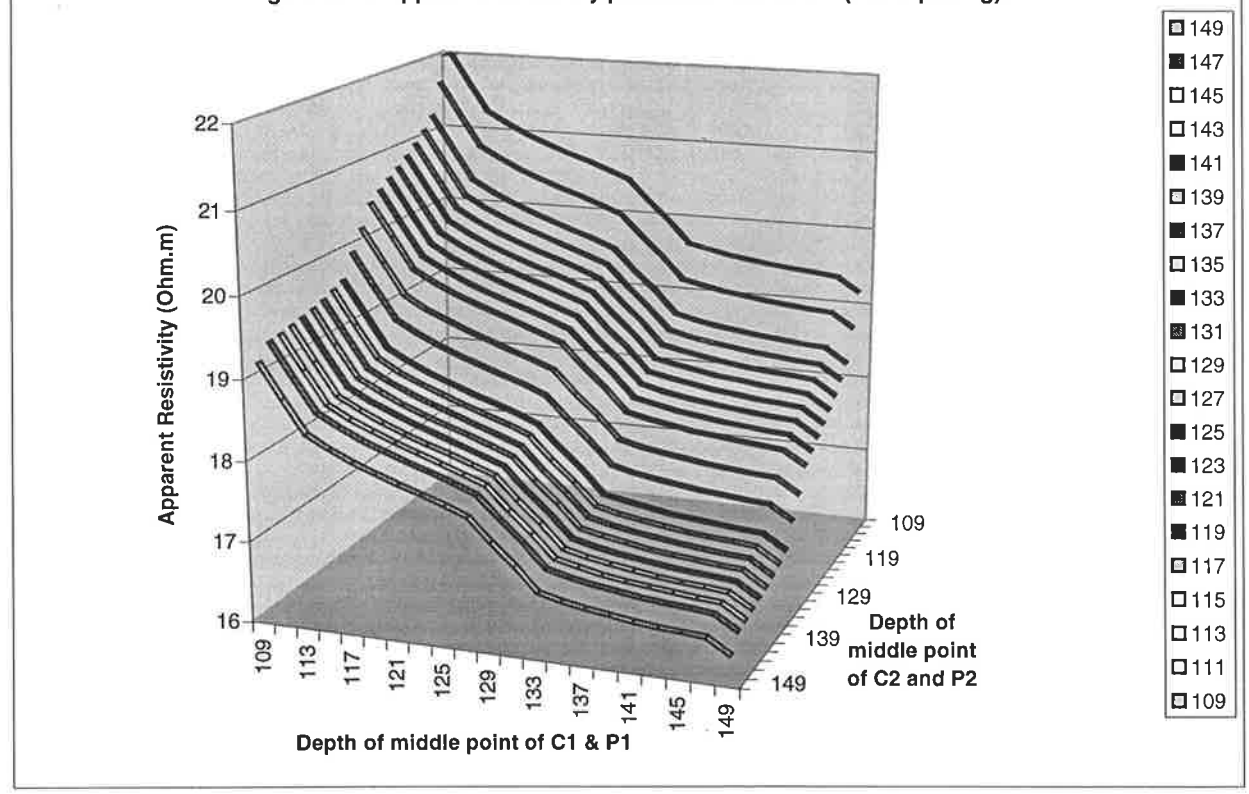

Figure 8.11 Apparent resistivity profiles of Model 1-3 (14m spacing).

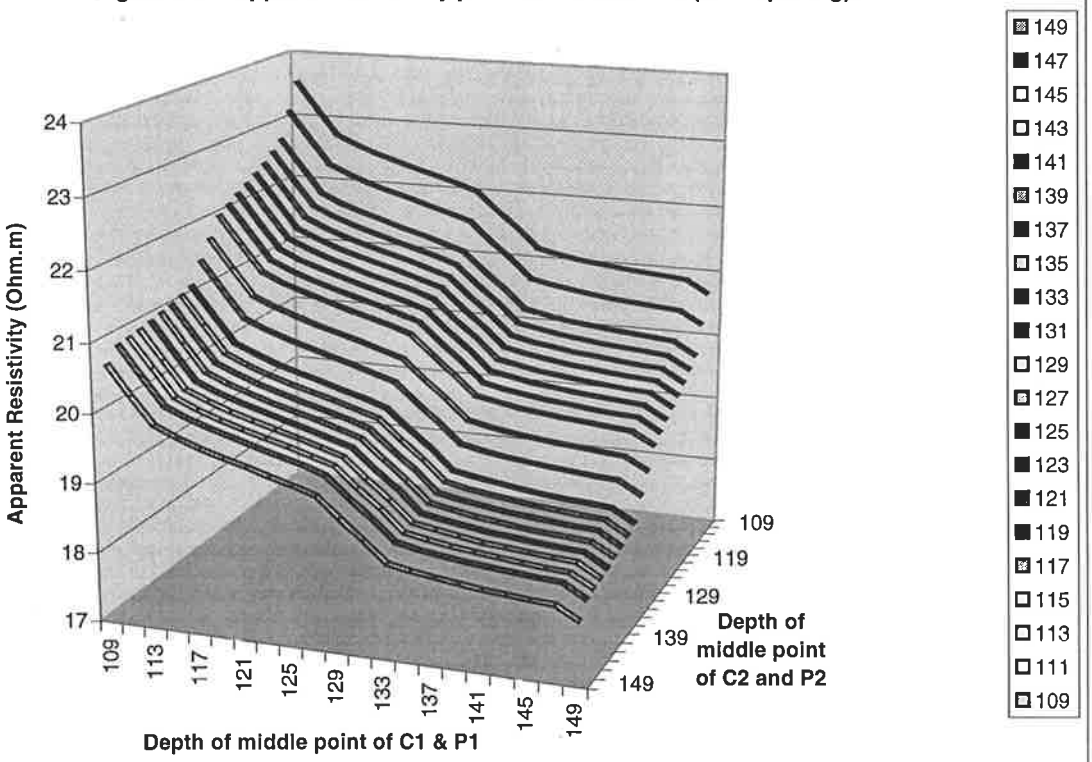

Figure 8.12 Apparent resistivity profiles of Model 1-4 (14m spacing).

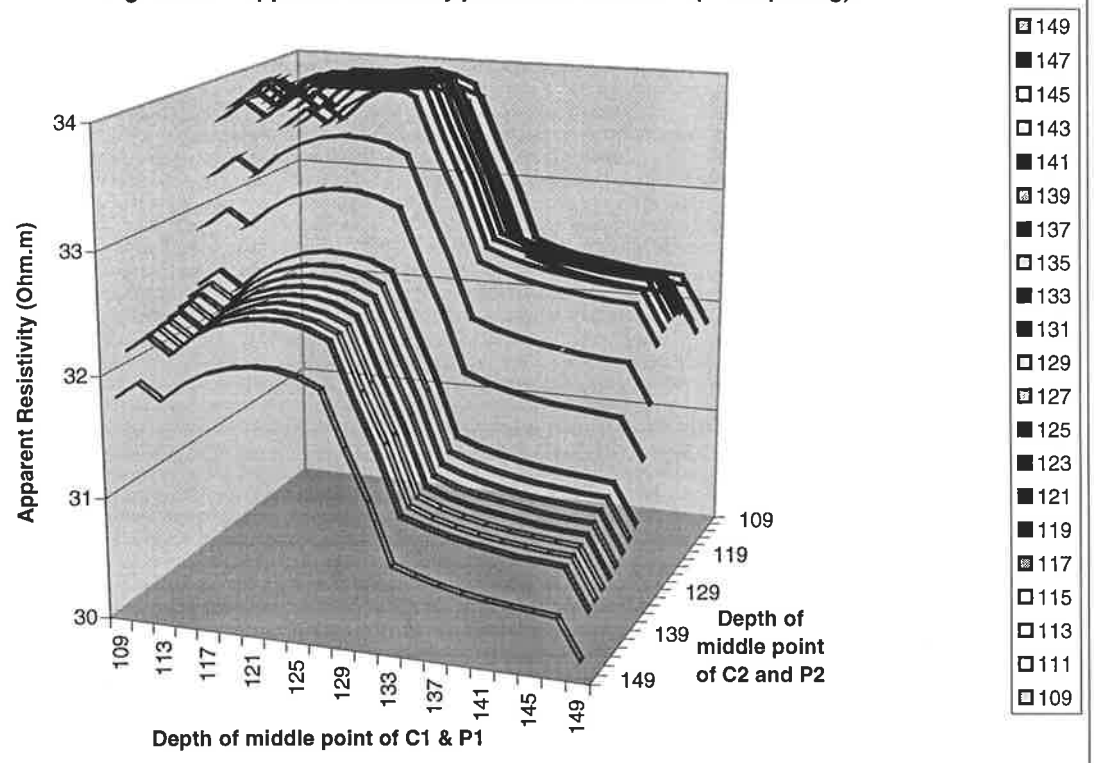

Figure 8.13 Apparent resistivity profiles of Model 1-1 (28m spacing).

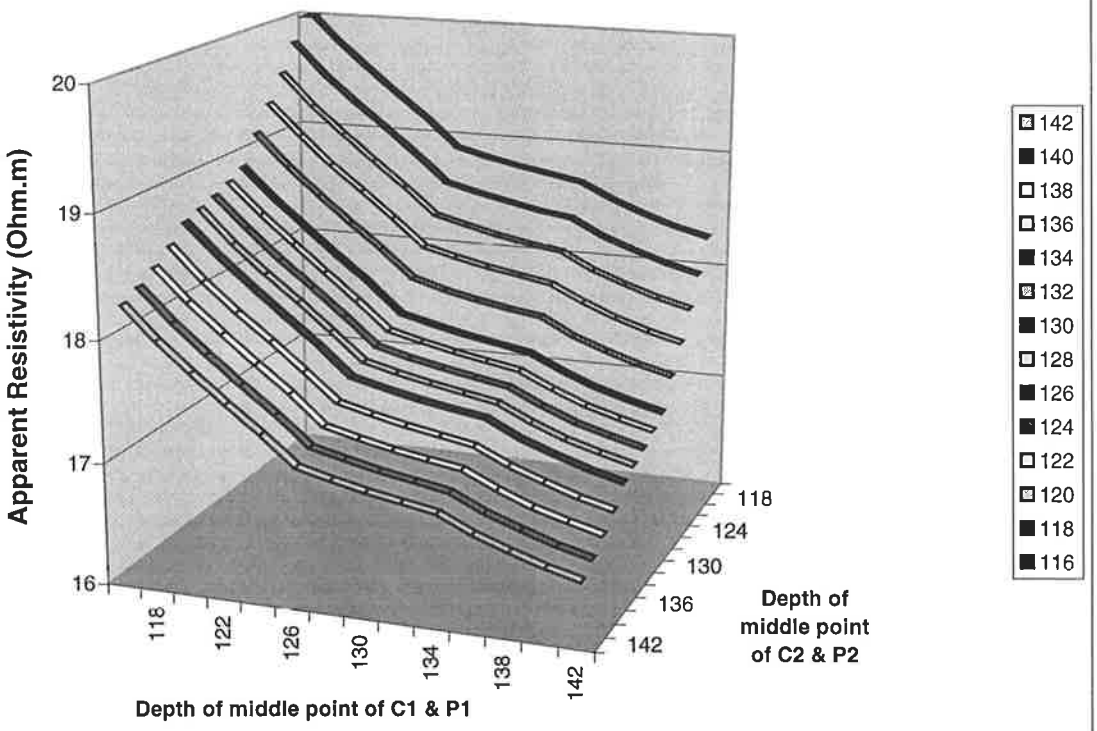

Figure 8.14 Apparent resistivity profiles of Model 1-2 (28m spacing).

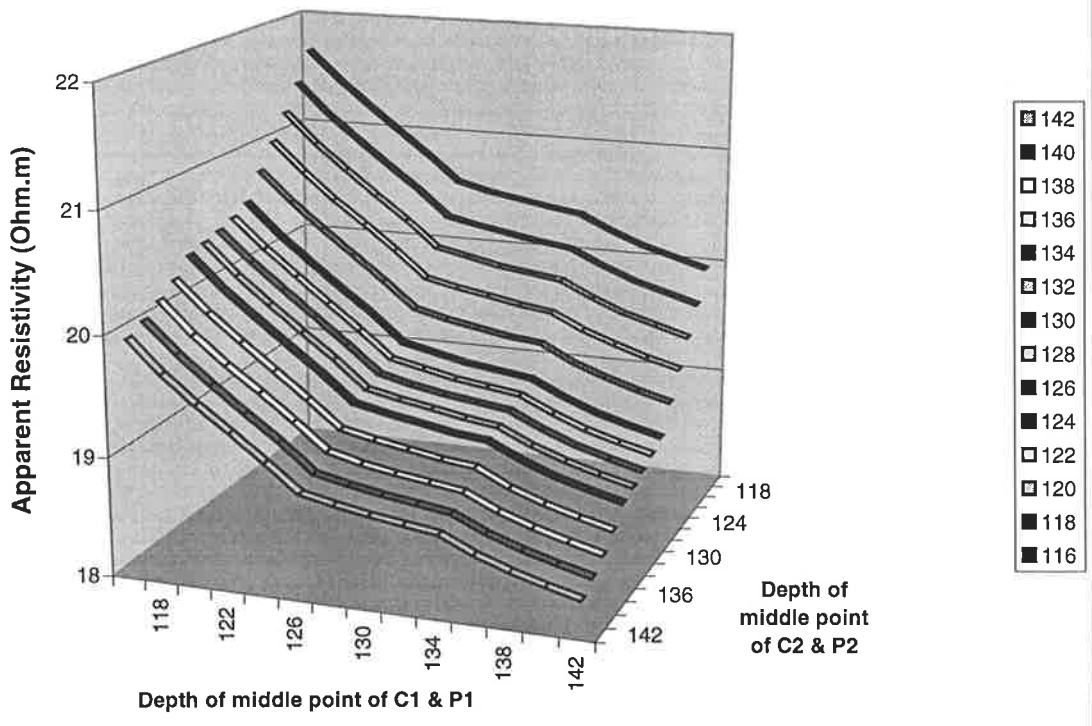

Figure 8.15 Apparent resistivity profiles of Model 1-3 (28m spacing).

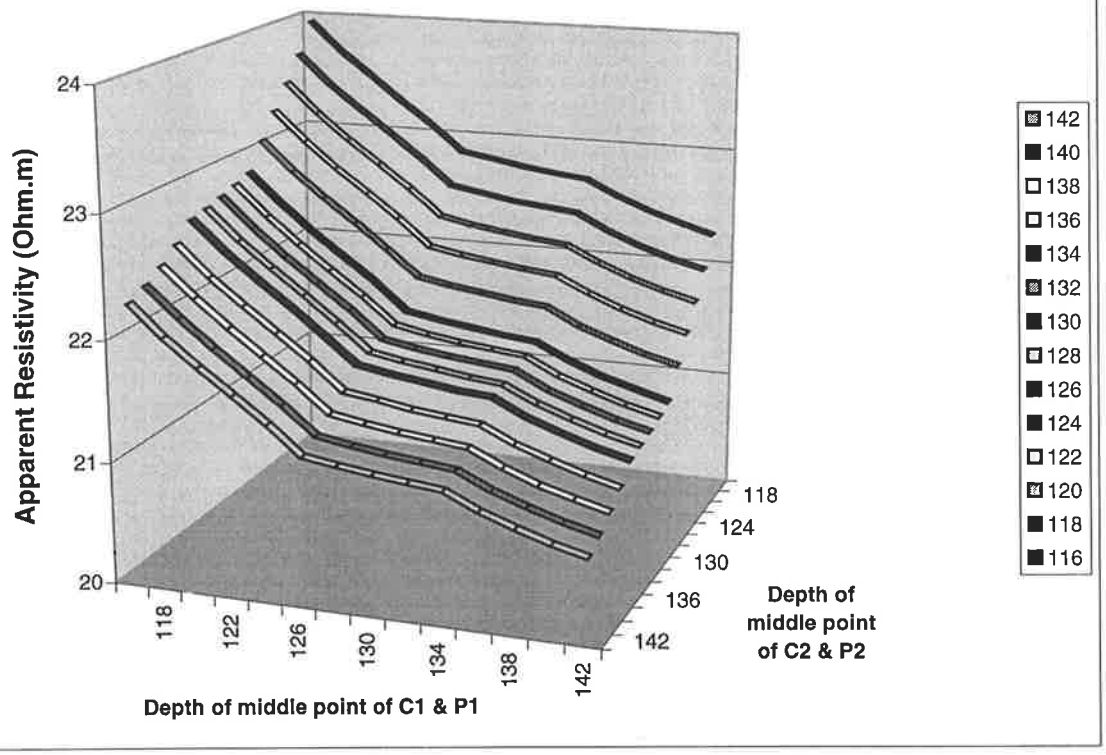

Figure 8.16 Apparent resistivity profiles of Model 1-4 (28m spacing).

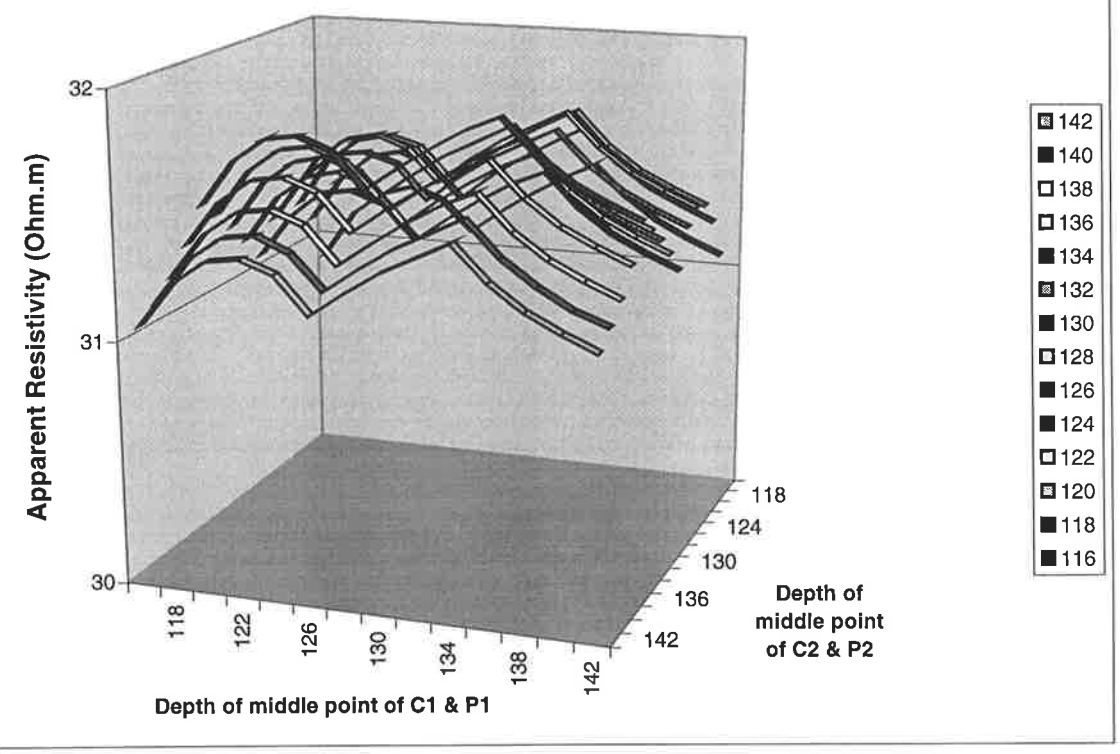

From the profiles of model 1-1, model 1-2 and model 1-3, it can also be seen that the apparent resistivity profile patterns of the three models remain the same, for both the 14m spacing and 28m spacing data. The resistivity increase in the middle part of models 1-2 and 1-3 (due to the injected fresh water) did not affect the apparent resistivity pattern (simply a DC upward shift). This is because the pattern of apparent resistivity profiles is mainly determined by the intersection points between resistivity interfaces and the borehole, and the earth resistivity near both boreholes. A turning point in the apparent resistivity profile is only produced when a potential or current electrode crosses a resistivity interface. The apparent resistivity indeed increases between model 1-1 and model 1-2, and between model 1-2 and model 1-3. The average apparent resistivity gets larger, but there are only minor changes in the apparent resistivity profile pattern.

When the 'injected water ' fills the entire inter-well space, as shown in model 1-4, the apparent resistivity pattern changes abruptly (refer to Figure 8.12 for the 14m spacing data and Figure 8.16 for the 28m spacing data). This pattern roughly shows the resistivity change pattern in model 1-4: high in the middle, lower at top and bottom.

Another very important observation with these stacked profiles is the presence of several "turning points", where the curve suddenly changes slope. For example, four turning points are clearly evident in all the stacked profiles for the 14m separation experiment. From Figure 8.4, it can be seen that there are a total of four layers and three interfaces in all four models. When an electrode (be it a current electrode or a potential electrode, it doesn't matter) crosses an interface between two different resistivity layers, the measured apparent resistivity exhibits a sharp change. This will produce a turning point. Since the first interface lies outside the range of the electrodes, there are only two interfaces, which are crossed by the electrodes, at depths of 120m and 140m in the models. For the 14m electrode separation configuration, the roving range of the current electrode C is from depth 116m to 156m, and the roving range of the potential electrode P is from depth 102m to 142m. So both current electrodes and both potential electrodes cross each interface, resulting in 4 turning points. All 14m separation stacked profiles of the four models show this to be the case. For the 28m separation configuration, the roving range of each current electrode C is from depth 130m to 156m and the roving range of each potential electrode is from depth 102m to 128m. So the current electrode crosses only one interface (depth 140m) and the potential electrode crosses only one interface (120m depth) as well, producing only two turning points in all 28m-separation stacked profiles.

It can be seen that the minimum of the apparent resistivity values shown in Table 8.1 for each model is always larger than the minimum of the actual resistivity in the model, while the maximum of the apparent resistivity in the table is always smaller than the maximum of the true (actual) resistivity in the model. This is true for all numerical modelling data. This implies that the apparent resistivity always lies between the minimum and maximum of the true resistivity.

From Table 8.1, it is clear that the apparent resistivity (AR) increases with an increasing amount of higher resistivity water injected into the subsurface. Specifically, the AR increase between model 1-3 and model 1-4 is quite high, at about 60%. This means that the injected water will greatly affect the resistivity distribution after the fresh water replaces the original salt water. However, before the injected water occupies the whole space, the increase in the AR is not very large. For example, the increase between model 1-1 and model 1-2 for the 14m separation is only about 5%, and the increase between model 1-2 and model 1-3 for the 14m separation is less than 9%. The 28m separation data exhibit a larger fractional increase than the 14m separation data, because the AR from the larger separation measurement will be affected more significantly by resistivity changes at distance from the well, than at the smaller electrodes separation. So a wide separation between two electrodes in the same borehole is very important for detecting the changes in the resistivity distance at remote locations, some distance from the borehole.

8.2.2 Model Set 2 – Three Layer Aquifer, One Layer Impermeable.

In this second model set, we consider the same three-layer aquifer, bounded on the top by an impermeable layer of resistivity 30 Ω.m. But now we assume that the intermediate aquifer layer is impermeable, so that all of the injected water is forced to flow through the layers above and below it. There is abundant evidence from both field pumping tests and laboratory measurements that the aquifer is not homogeneous. The middle section is less permeable than the rest (Dillon et al., 2001). Again we assign equal hydraulic conductivity to the layers bounding the impermeable zone, resulting in the time lapse patterns of water injection and corresponding 2-D resistivity models 2-1, 2-2, 2-3 and 2-4, as shown in Figure 8.8. The time lapse pictures correspond to fractional advances of fresh water breakthrough of 0, 1/3, 2/3 and 1, with vertical advancing plume fronts. Compared to Figure 8.7, the only difference in the actual resistivity distribution is with respect to the middle layer, which retains its constant (pre-injection) salt water value of 17 Ω.m.

The stacked profiles of the modeled apparent resistivity data of all four sub-models are shown in Figure 8.17 to Figure 8.24. The average apparent resistivity R_{14a} and R_{28a} for the 14m and the 28m separation in the models and the relative changes of the average apparent resistivity between consecutive sub-models (time lapse) are displayed in Table 8.2.

Table 8.2 The minimum, maximum, average apparent resistivity and the apparent resistivity relative change of the 4 sub models (time lapses) for numerical modelling set 2 – three layer aquifer, intermediate layer impermeable.

Model Name	AR-MIN (Ω.m)	AR-MAX (Ω.m)	AR-MEAN (Ω.m)	AR Increase (%)
104m model 2-1 14m spacing	15.42	21.29	17.59	
104m model 2-2 14m spacing	16.10	21.79	18.16	3.24
104m model 2-3 14m spacing	17.25	22.79	19.09	5.16
104m model 2-4 14m spacing	23.08	28.24	24.99	30.86
104m model 2-1 28m spacing	16.50	20.06	17.85	
104m model 2-2 28m spacing	17.74	21.08	18.96	6.23
104m model 2-3 28m spacing	19.36	22.42	20.43	7.74
104m model 2-4 28m spacing	24.52	29.56	27.49	34.56

Comparing the stacked profiles of the second modelling set with those of the first modelling set, we find that the stacked profile pattern in the first three sub-models still remains very similar. This is because the patterns of apparent resistivity profiles are mainly decided by the intersection points between the resistivity interfaces and the borehole, and the formation resistivity in the immediate vicinity of both boreholes. However the average AR in the second modelling test is lower than the average AR in the first modelling test due to the lower resistivity in the middle part of the aquifer (intermediate layer) in the second modelling test set. Comparing the AR stacked profiles (Figures 8.12, 8.16, 8.20 and 8.24) of the fourth model (Model 1-4 and Model 2-4) in both modelling sets, corresponding to complete fresh water breakthrough at the two boreholes, the results are very different. This is because the actual resistivity vs depth pattern is different. Model 1-4 is characterised by resistivity low->high->low->low (refer to (d) of Figure 8.7) whereas Model 2-4 has a resistivity depth distribution low->high->low->high (refer to (d) of Figure 8.8).

Figure 8.17 Apparent resistivity profiles of Model 2-1 (14m spacing).

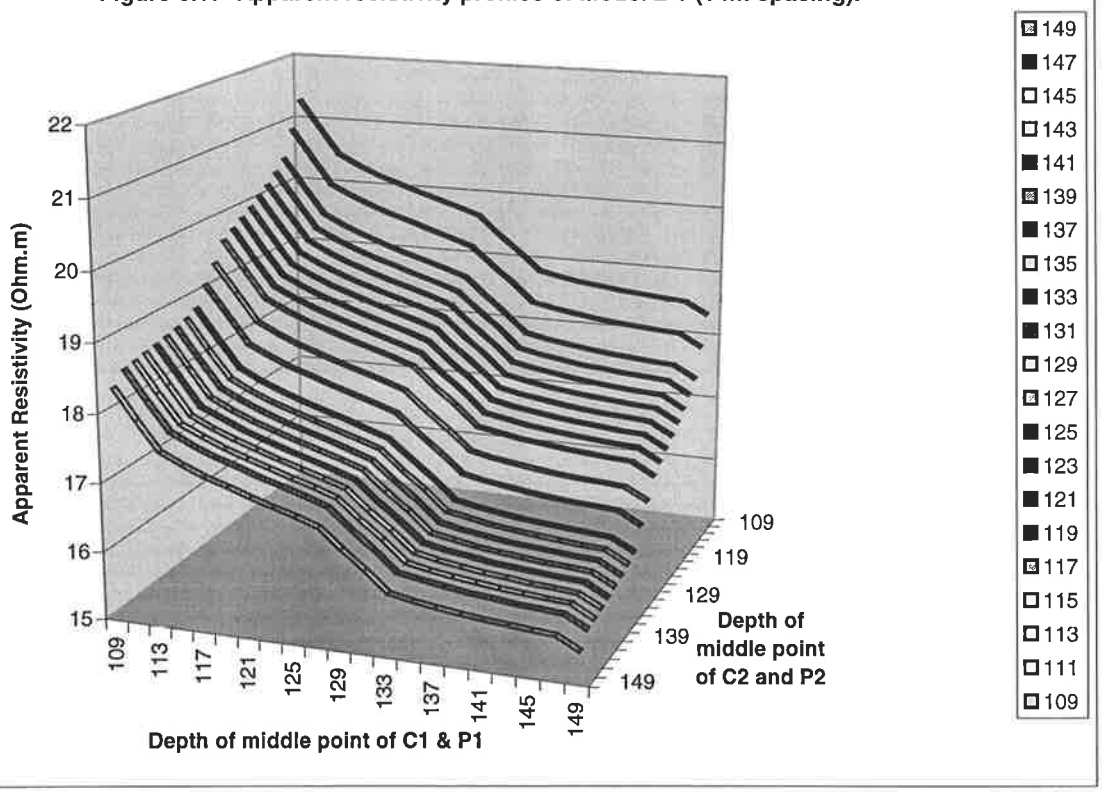

Figure 8.18 Apparent resistivity profiles of Model 2-2 (14m spacing).

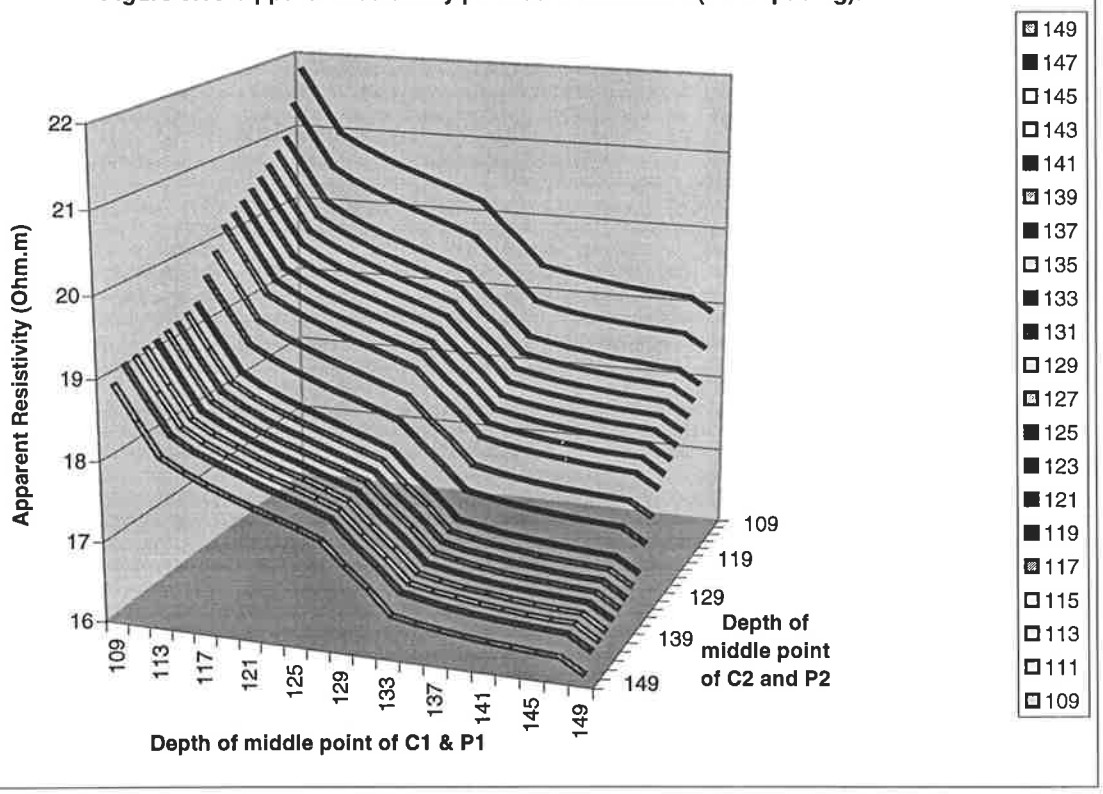

Figure 8.19 Apparent resistivity profiles of Model 2-3 (14m spacing).

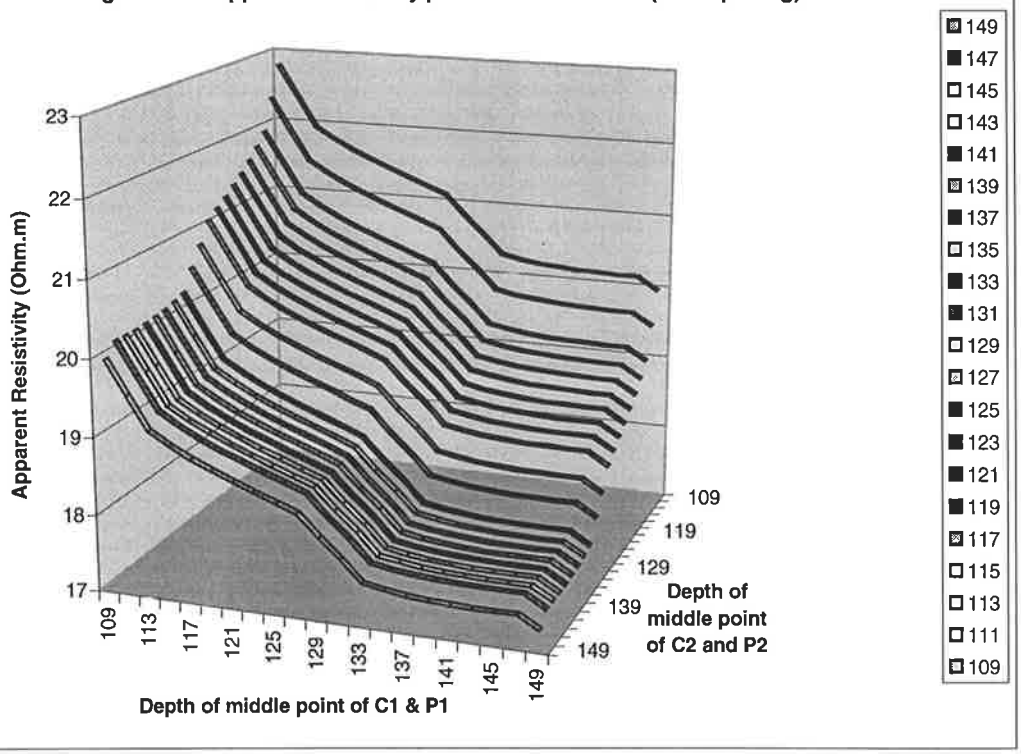

Figure 8.20 Apparent resistivity profiles of Model 2-4 (14m spacing).

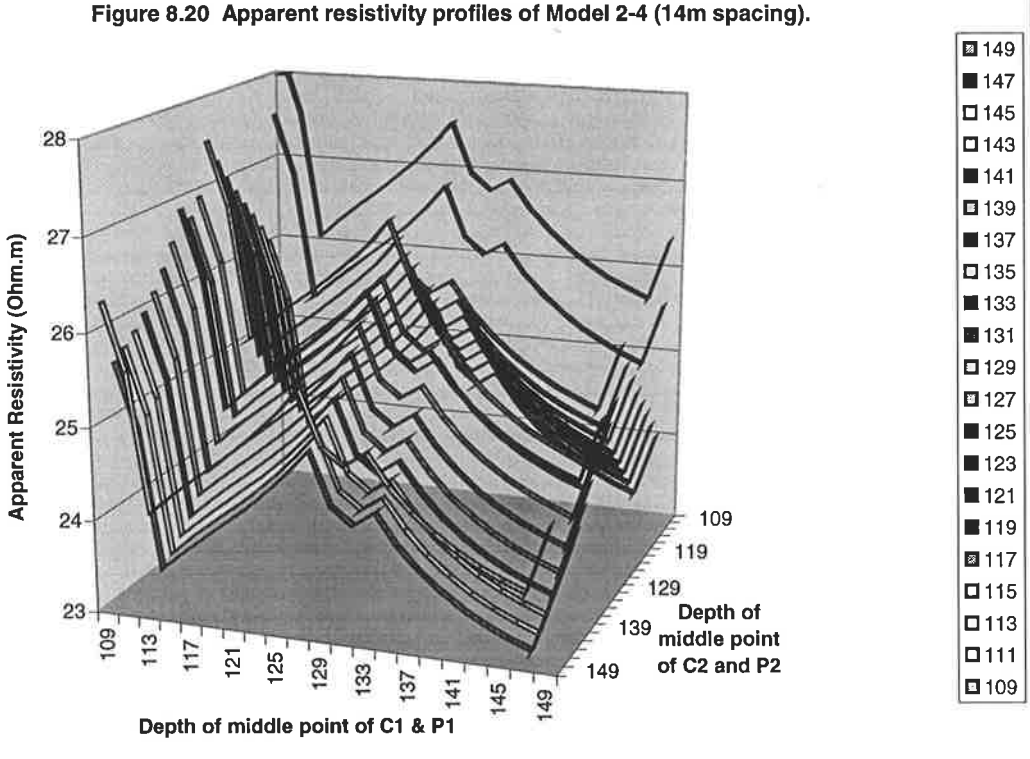

Figure 8.21 Apparent resistivity profiles of Model 2-1 (28m spacing).

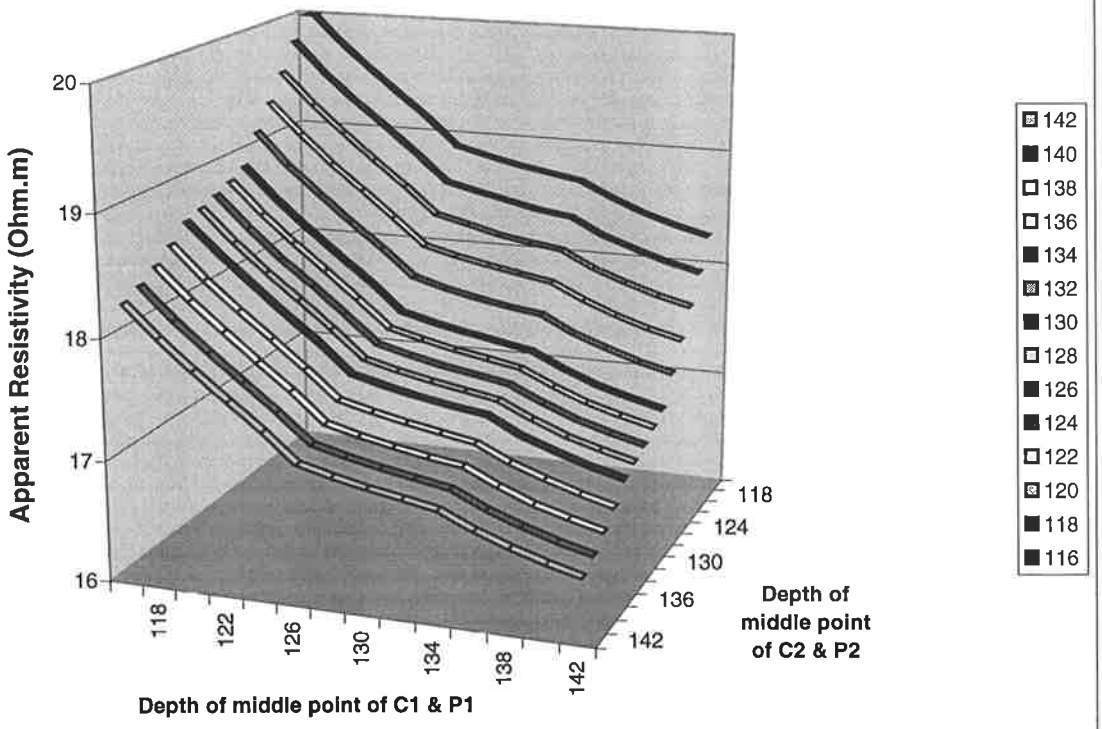

Figure 8.22 Apparent resistivity profiles of Model 2-2 (28m spacing).

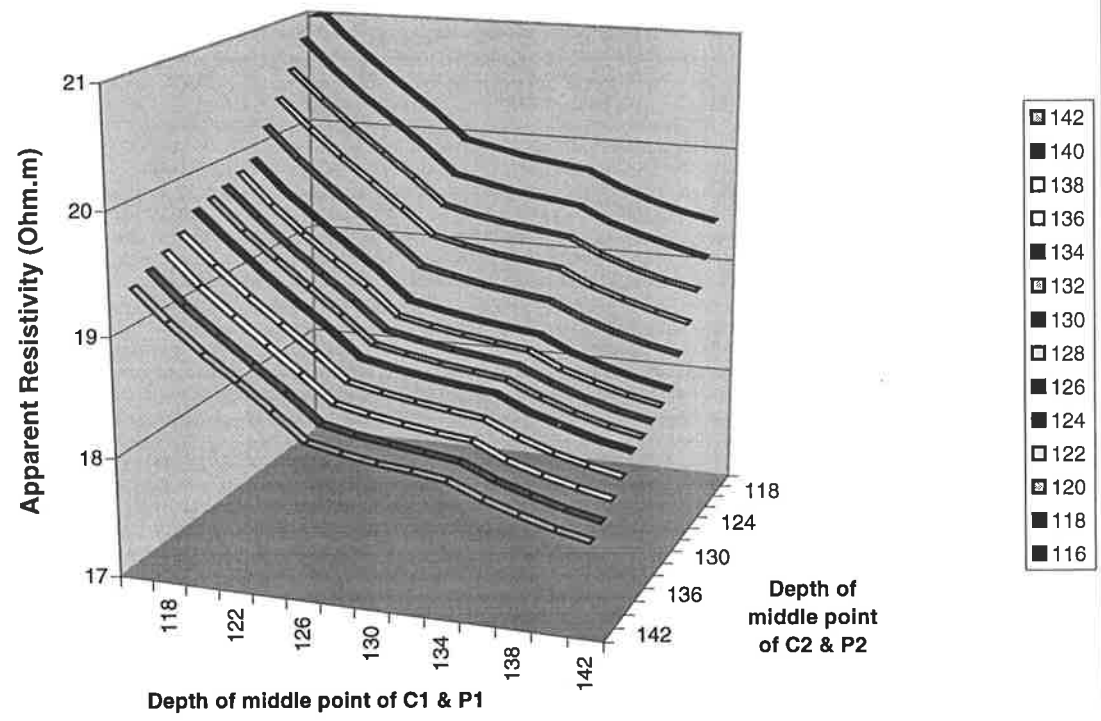

Figure 8.23 Apparent resistivity profiles of Model 2-3 (28m spacing).

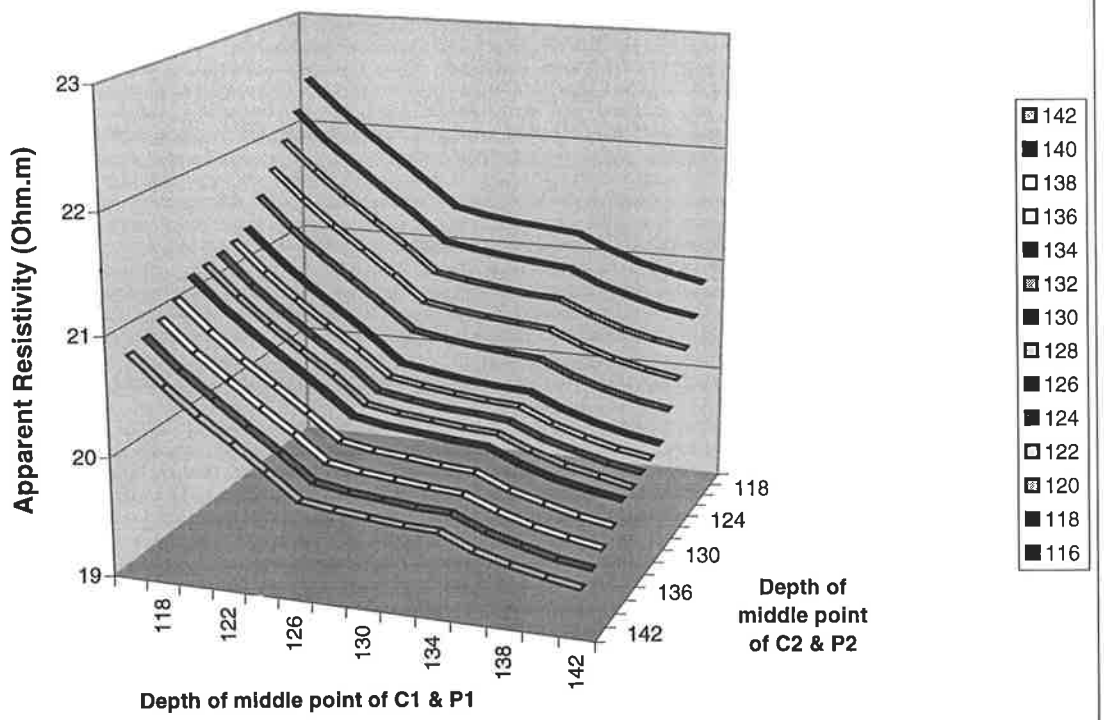

Figure 8.24 Apparent resistivity profiles of Model 2-4 (28m spacing).

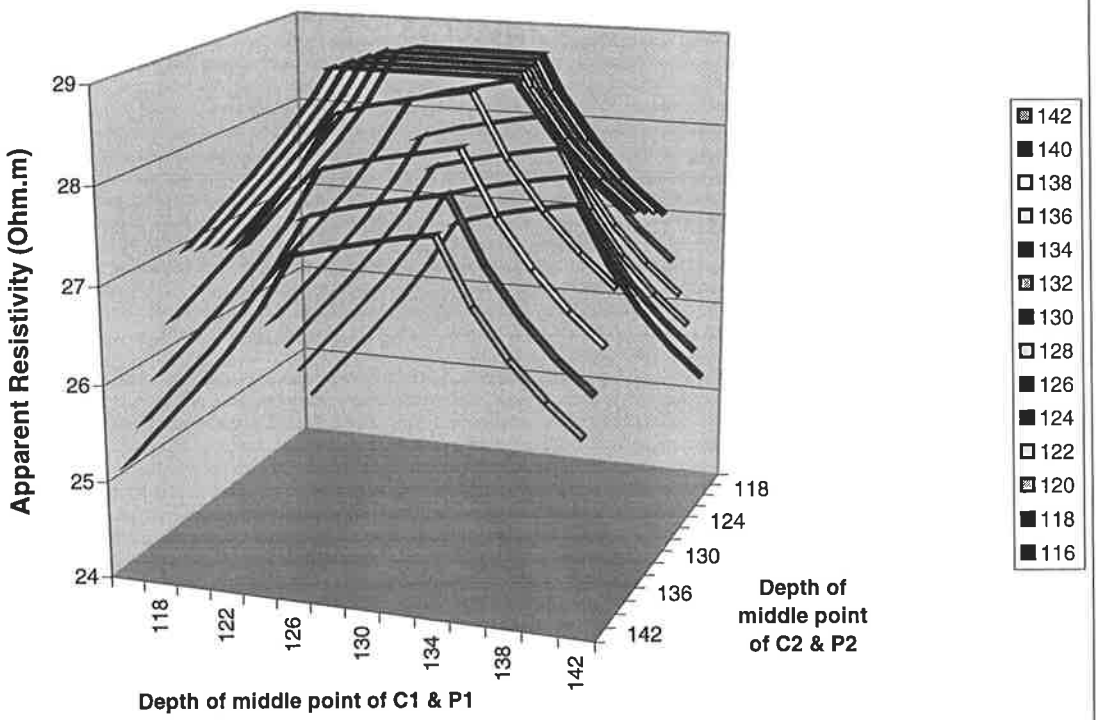

One very interesting finding is revealed in Figure 8.24. The stacked profiles in the figure show the apparent resistivity pattern low->high->low. But the actual (true) resistivity vs depth pattern of the model in the survey range is high->low->high (refer to Figure 8.8). This is just the opposite to the profile pattern. Therefore for some complicated models, the stacked profile pattern may not match with the resistivity change pattern, and could lead to false deductions. This emphasises the need for resistivity inversion as a tool of interpretation, to convert the raw AR data into an understandable resistivity distribution map.

By comparing the data in Table 8.1 and Table 8.2, it can be seen that (AR) decreases over the whole range due to the unchanged (lower) resistivity in the middle layer of the aquifer. So the relative changes given in Table 8.2 are smaller than those in Table 8.1 for the same reason.

8.3 THE SENSITIVITY DISTRIBUTIONS OF THE TWO DIFFERENT ELECTRODE SEPARATION CONFIGURATIONS

The Frechet derivatives play an important role in resistivity inversion since they determine by how much the model parameters need to be modified to match the modelling data with observed data. The Frechet derivatives show the sensitivity of the modelling data to the model parameter changes for a fixed configuration (e.g. dipole-dipole configuration) with a fixed resistivity background. The larger Frechet derivative at one spatial point means that more change for the model parameter at that position needs to be made to match the modelling data with the observed data. And the smaller the Frechet derivative at one location means a smaller change for the model parameter at that spot. So we also call the Frechet derivatives the sensitivity function (Zhou and Greenhalgh, 1999). Therefore the sensitivity distribution for an electrical configuration shows how effective the resistivity inversion method with that configuration is for any area in a model.

Before the inversion experiments of the modelling data were completed, the sensitivity distributions for the 14m and the 28m current and potential electrode separation configurations were calculated to examine how sensitive the configurations are for inversion of resistivity distribution between two wells. The background resistivity used to calculate the sensitivity distribution is 30 Ω.m. In order to compare the sensitivity distribution between the two different configurations, the calculated sensitivity distributions were normalized for each configuration respectively with the following formula

$$normalised\_sensitivity = \frac{calculated\_sensitivity}{\max(|calculated\_sensitivity|)}$$

In order to improve the resolution of the normalised sensitivity for the middle part between two wells, all negative normalised sensitivities were set to zero. Besides, there are no negative values in the middle area for this configuration. The normalised sensitivity distributions for the 14m and the 28m separations are displayed in graph (a) and (b) of Figure 8.25 respectively. For the 14m current and potential electrode separation configuration, both current electrodes are at a depth of 116m and both potential electrodes are at a depth of 102m, as shown in Figure 8.25. For the 28m separation, both current electrodes are shifted to a depth of 130m and both potential electrodes are kept at the same position.

From Figure 8.25, one can see that the normalised sensitivity in the area between two wells in graph (a) (for 14m separation) is nearly zero. However, the normalised sensitivity in the same area in graph (b) (for 28m separation) is somewhat larger, about 0.035. By comparing the positions of the dark green parts (normalised sensitivity of 0.05) in both graphs, we can see that the sensitivity contour reaches to the area only 20m away from the wells in graph (a) (14m separation) of Figure 8.25; but about 40m away from the wells in graph (b) (28m separation). So from the figure, it can be seen that the larger current and potential electrode separation in the bipole-bipole configuration will produce a larger effective depth of detectability.

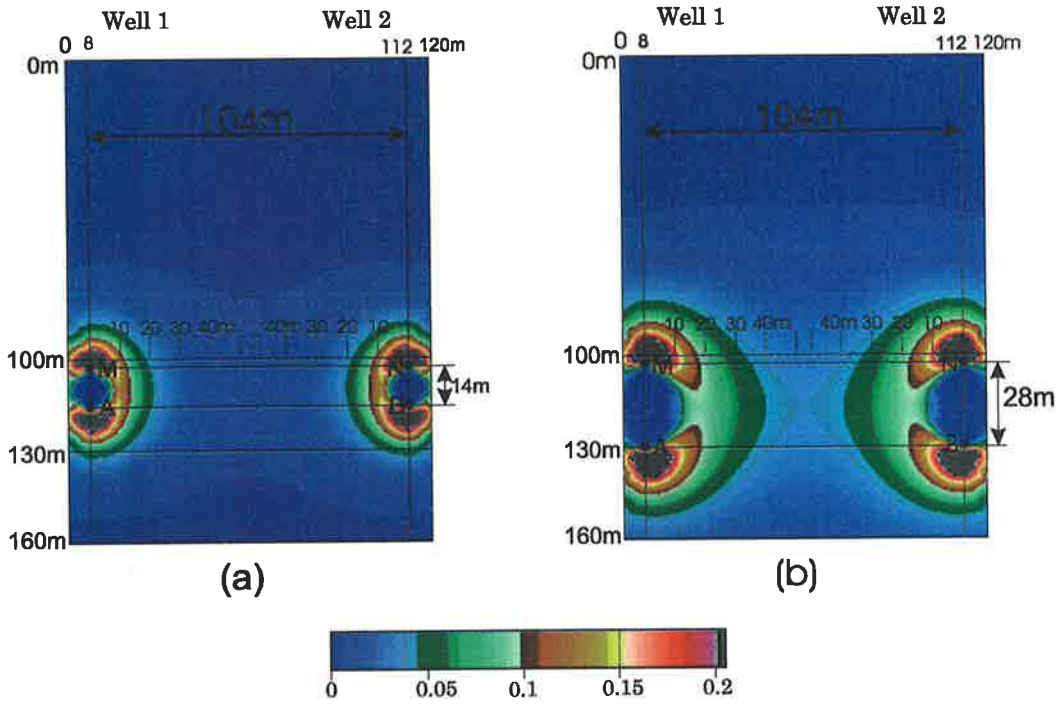

Figure 8.25 The comparison of (a) the normalized sensitivity distribution calcualted with the 14m current and potential electrode separation and (b) the normalized sensitivity distribution with the 28m separation is shown in this graph. All negative sensitivities were set to zero in order to show sensitivity contrast in the middle part..

8.4 THE INVERSION EXPERIMENTS ON THE CROSSHOLE RESISTIVITY MODELLING DATA FOR THE CHORD CONFIGURATION

All data of the two model sets were inverted with our 2.5-D resistivity inversion program. The inverted results of four models of the first modelling set are shown in Figures 8.26 and the four results of the second modelling set are shown in Figure 8.27.

For both figures, we can see that the inverted images are smaller than the original modelling area. The inversion range is from 0 to 148m in X direction and from 0 to 160m in Z direction. This can make the inversion calculation a little quicker. For the inversion area with a 2x2m grid cell size, the total number of unknowns should be 5920 (74x80). Even for the area of interest (from 24m to 128m in X direction and from 100m to 160m in Z) only, the unknowns arc 1560 (52x30). However, only 637 data points are available for each inversion. So these inversions are seriously under-determined. Besides, the accessible ranges in both boreholes are very limited (from 102m to 156m) and the distance between the two boreholes (104m) is much larger than the range. So this makes the inversions difficult.

From Figures 8.26 and 8.27, we can see that all inverted results are almost symmetric. This is because all models are symmetric. To reduce the inversion difficulty, the initial model values for the top layer (from 0m to 100m depth) were set to the original value 30 Ω.m. The initial values for the remaining layers were from the preliminary image results, which are not shown here. After inversion, all inverted images were filtered a little to remove some high frequency noise (due to instabilities) along the borehole positions. Keep in mind when analysing these results that the 14m and 28m separation between two electrodes in each borehole normally cannot produce a good inversion result for the area more than 28m away from the boreholes. So the middle part of the inversion images are just approximate and may just show some trend.

Figure 8.26 shows all the inversion results for the first model set. From the result of model 1-1 in the figure, we can see that the three-layer structure is recovered in the area near the two boreholes. But in the middle part, it is hard to see the three-layer structure due to its far distance from the boreholes. However, it can be seen that the resistivity decreases with depth in the middle part and the whole structure is almost flat. So this result basically matches with the original model, also shown in the figure.

The inverted results of model 1-2 and model 1-3 in Figure 8.26 clearly show the resistivity increase in the middle part compared with the first model, although it is impossible to see the three-layer structure in the middle part. The whole structure is not flat any more. The three-layer structures near the boreholes are still clearly shown in both results. The last inverted result in the figure shows the resistivity decease with depth in the whole area. Again the image near both boreholes is better than that in the middle part of the section.

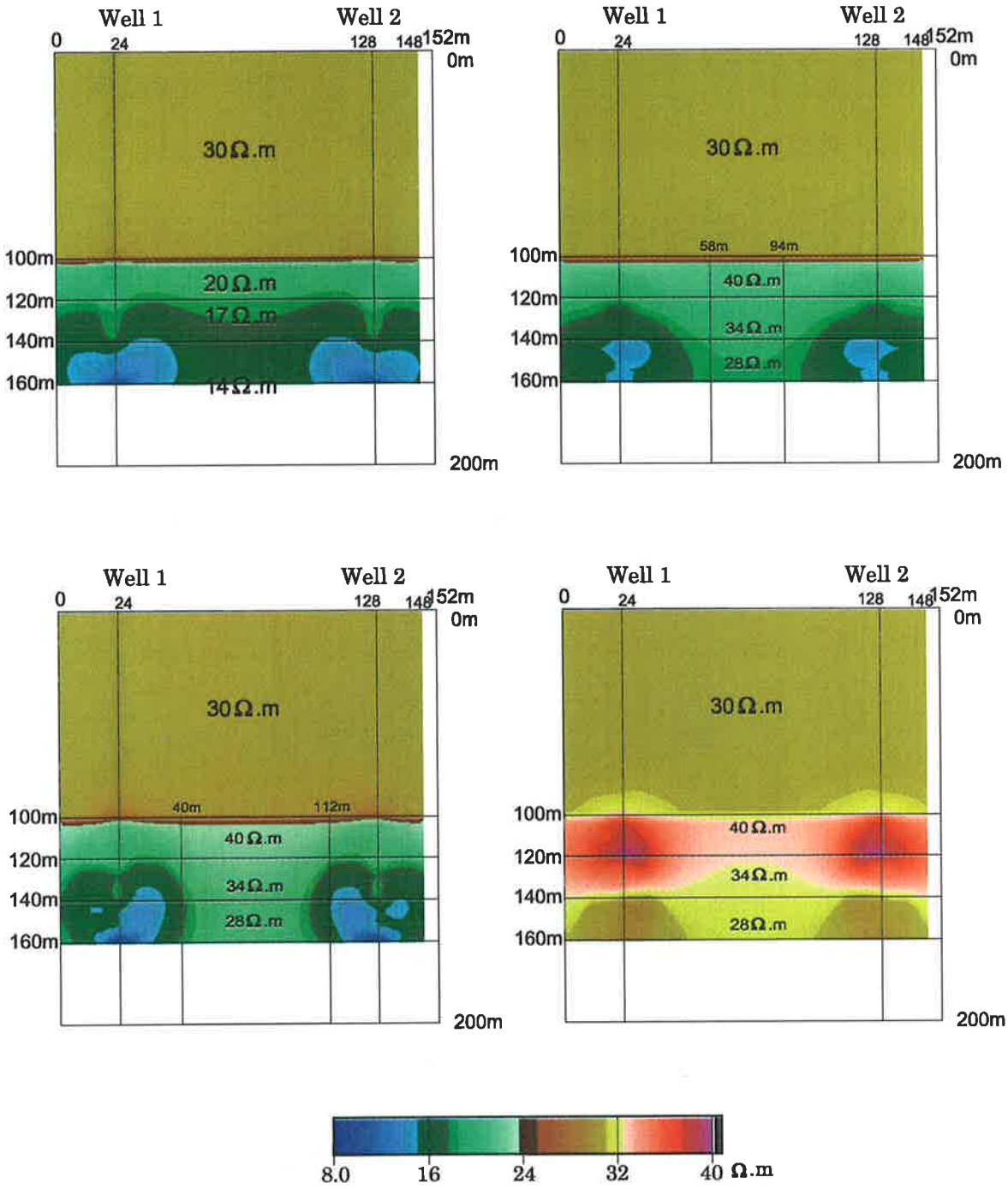

Figure 8.26 The inversion results from the modelling data with model loyouts overlain for the first model set.

Figure 8.27 shows all inversion results of the second model set. The first result is the same as the first one in Figure 8.26. The inversion results for models 2-2 and 2-3 are similar to the results of models 1-2 and 1-3 in Figure 8.26 since the resistivity distribution near the two

boreholes in all four models are almost the same. Although the different resistivity changes in the middle part may affect the inverted results, it does not produce a very large difference. These two results in the figure could not be expected to show the middle low resistivity layer in the middle region between the two wells since we used relatively small electrode separations of 14m and 28m. The inversion result for model 2-4 clearly shows the three-layer structure and the middle low resistive layer near the both boreholes. But it is hard to obtain very clear information in the middle part of the picture. Due to the low resistivity middle layer, the final result shows no hint of the middle resistivity structure.

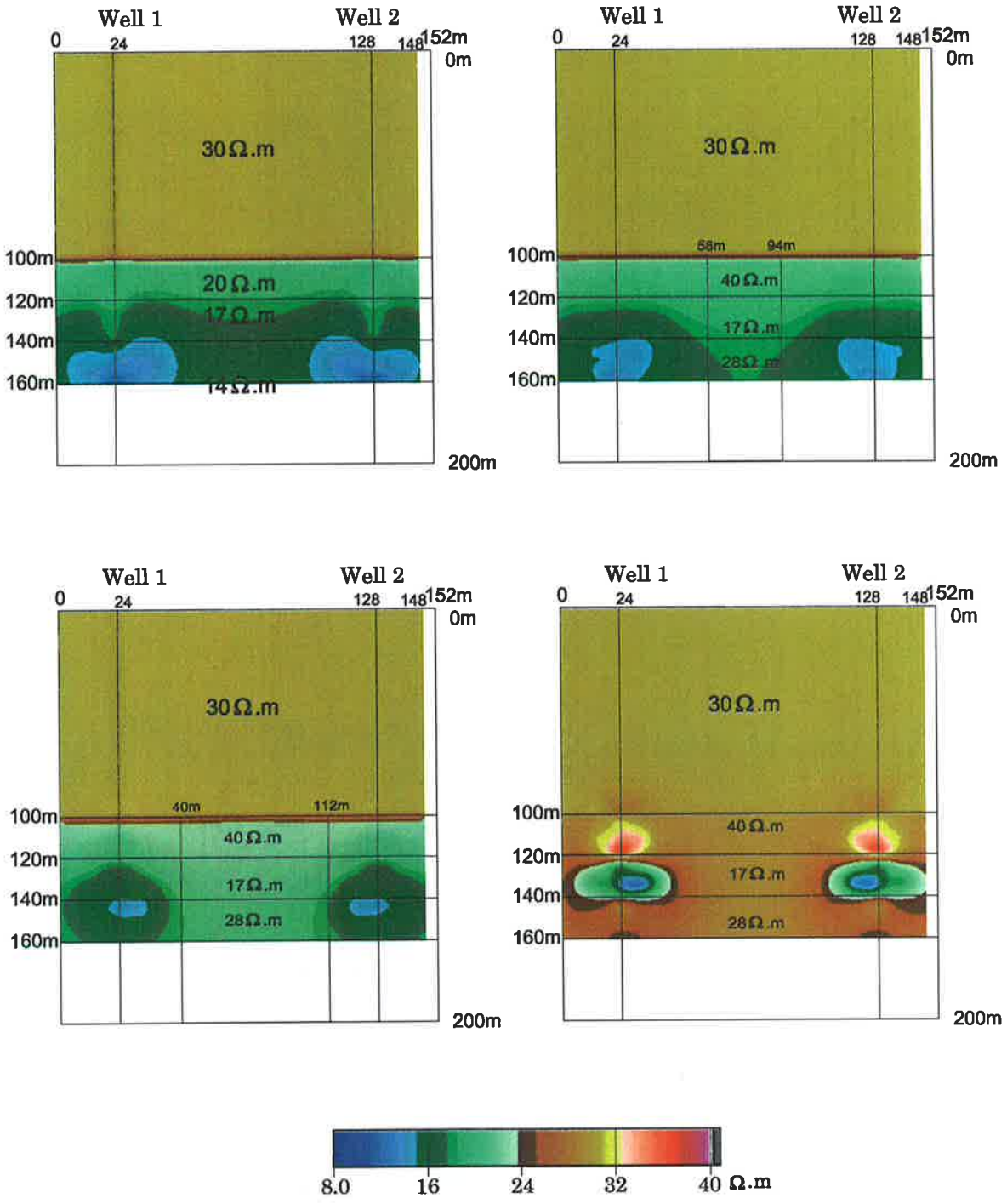

Figure 8.27 The inversion results from the modelling data with model loyouts overlain for the second model set.

From the inversion results of the above two modelling sets, two things are clear. One is that the resistivity distribution near the both boreholes can normally be imaged with the 14m and 28m configurations. The second is that the resistivity increase in the middle part can be seen in the inverted images, but not the precise detail. Moreover, these are just pure modelling experiments. There is no noise added and the resistivity of the top layer (from 0m to 100m depth) is known. For the actual field survey, the situation will be much more difficult.

8.5 CONCLUSIONS

From the above two sets of numerical modelling and inversion experiments, I offer the following conclusions:

1. The injected high resistivity water will definitely cause an observable AR increase in the resistivity crosshole multiple scanning surveys.
2. However the AR increase rate is small, less than 10% on average, until just before the injected water reaches the two survey wells. Specifically, the increase rate for the 14m separation is about 5% on average.
3. The apparent resistivity profile pattern (or shape) remains almost the same in all profiles before the injected water reaches the two survey wells. This is because the sensitivity of 14m and 28m electrode separations is not very high for the resistivity change in the middle part of the two survey wells.
4. From the stacked profiles, it can be seen that the AR decreases with increasing depth, in accordance with the actual resistivity distribution.
5. All 14m electrode separation profiles show four turning points or points of change in slope, in each profile, and all 28m electrode separation profiles show two turning points in each profile. This is caused by each electrode crossing an actual resistivity interface.
6. From the inversion results, it can be seen that the resistivity distribution near both boreholes can normally be recovered with the 14m and 28m configurations.
7. The resistivity increase in the middle part of the section between the two is recognisable, but details cannot be reliably extracted.

Chapter 9

MODELLING AND INVERSION OF WATER INJECTION: EXPECTED TIME-LAPSE RESISTIVITY RESULTS IN PHASE II

9.1 INTRODUCTION

In this chapter, I report on the resistivity numerical modelling and inversion results for simulating the water injection during Phase II of the trial. As mentioned previously, water injection Phase II of the ASR project ran from August 2000 to April 2001. In total, four time-lapse resistivity surveys were conducted over the period, and four different pairs of crosshole resistivity multiple scannings in the radial direction (between the injected well, at the centre of the circle, and the monitoring wells which surround it) in each survey were completed, as shown in Figure 9.1.

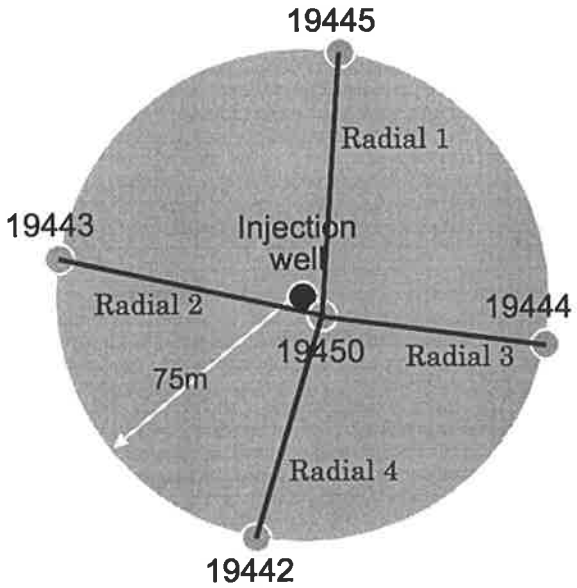

Figure 9.1 The surface layout of the crosshole resistivity surveys. Four crosshole resistivity multiscannings, on radii 1, 2, 3 and 4, were conducted in each survey in water injection Phase II.

In common with the initial model used in Chapter 8, a simplified four horizontal layer resistivity model, shown in Figure 9.2, was used as a starting model for the numerical modelling experiments. From the figure, it can be seen that the resistivities in the initial

model were set to decrease with depth. The same crosshole multiple scanning layout as used in Chapter 8, and as shown in Figure 9.3, is used for all modelling in this chapter. However, it can be noticed that the radial distance between two wells (75m) is much smaller than that used in the previous chapter for the chord configuration (104m). The survey depth range in each well is the same, from 102m to 156m. So in total, there are 637 data points in each crosshole multiple scanning.

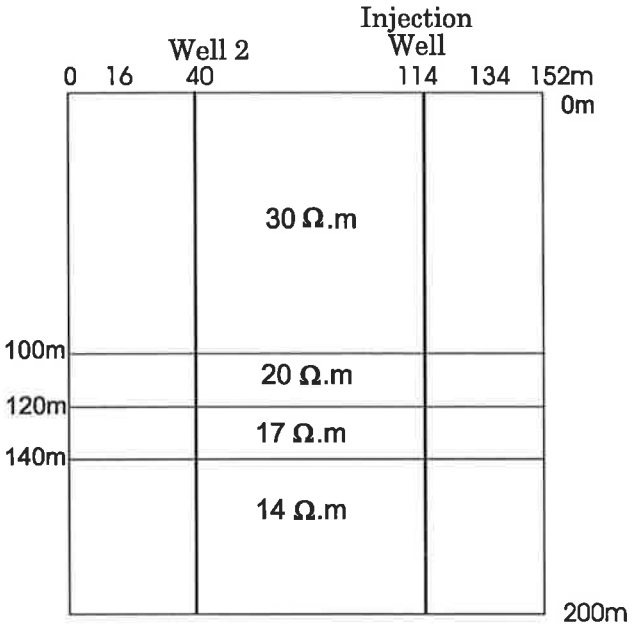

Figure 9.2 The initial model layout and parameters of the numerical resistivity model tests for the radial survey situation.

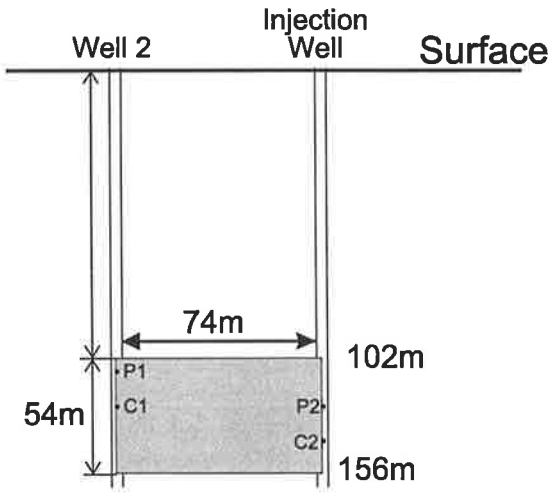

Figure 9.3 The cross section of the crosshole resistivity multiple scanning layout for all modelling in this chapter. C1 and C2 are current electrodes, and P1 and P2 are potential electrodes.

The next two sections provide details about the numerical resistivity modelling and inversion for simulating the resistivity surveys in Phase II (radial direction).

9.2 NUMERICAL CROSS WELL RESISTIVITY MODELLING EXPERIMENTS FOR THE RADIAL CONFIGURATION

Figure 9.4 is a summary diagram of the situation for each pair of wells. It shows in vertical view the 54m of aquifer in relation to the measurement geometry. Modelling was carried out to generate synthetic data assuming such a crosshole multiple scanning configuration.

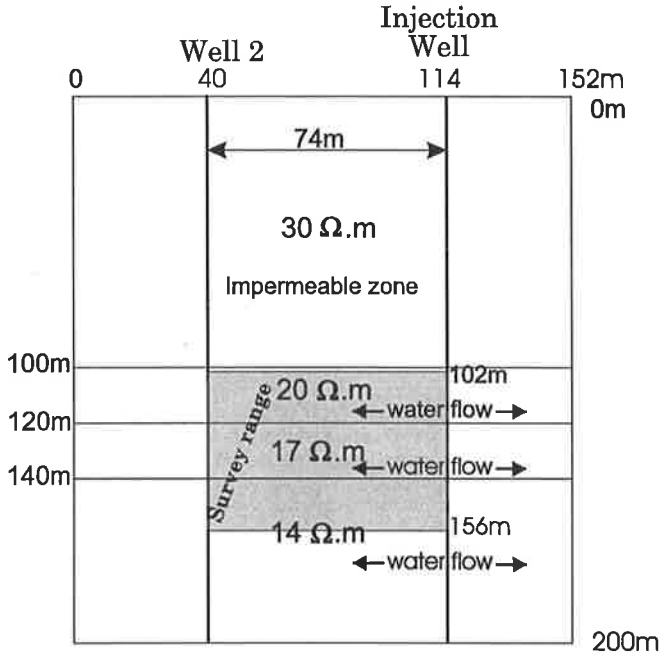

Figure 9.4 The initial model layout and parameters of the numerical resistivity model tests for the radial survey situation. The area above 100m depth is impermeable zone.

Again, two different basic model sets were considered, corresponding to two different injected water flow trends in the subsurface. The first basic model set assumes that the all layers below 100m are equally permeable, depicted in Figure 9.5. The second basic model set assumes that the all layers below 100m, except for the second layer, are permeable, as shown in Figure 9.6. The resistivities vary between 14 and 40 Ω.m.

The simulation of the water injection is easier for the radial configuration than for the chord configuration since one well must be the injection well (this is not exactly true, since the centre observation well is about 4m away from the injection well) and the injected water flows outwards from here to the other well gradually. So our 2.5-D modelling and inversion program can simulate this situation directly. For each model set, four modifications or snapshots are permitted, as shown in Figures 9.5 and 9.6. This corresponds to differing levels of (higher resistivity) fresh water infiltration. The four models in each set correspond to four

separate times after pumping commences: (1) initially; (2) when the available aquifer space between the wells is 1/3 occupied by the fresh water; (3) when the available aquifer space is 2/3 occupied by fresh water, and (4) when the space between the boreholes is fully occupied.

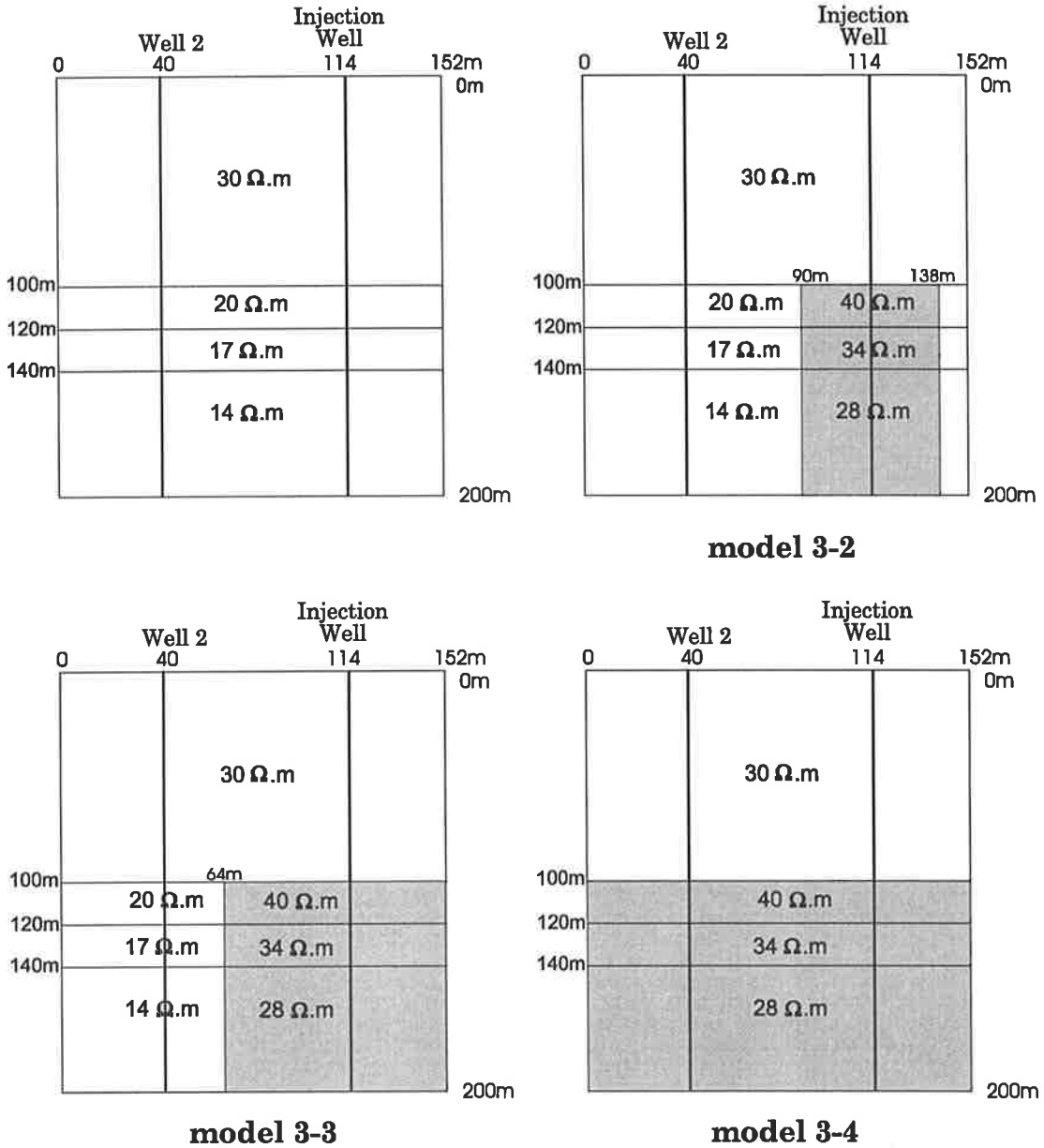

Figure 9.5 The model layouts and parameters of the 4 numerical models of the first model set, corresponding to different stages of water injection.

The output from the 2.5-D resistivity modelling program are potential differences between the two potential electrodes P1 and P2, assuming the injection current is 1A. Then the apparent resistivity at each point is calculated. Next the average apparent resistivities R_{14a} and R_{28a} for 14m and 28m spacings respectively, are calculated for each model. Then the relative changes of R14a and R28a are calculated between the four differing time stages (levels of water injection) for each model. Finally, the average apparent resistivities and their relative changes are compared among all models in each model set.

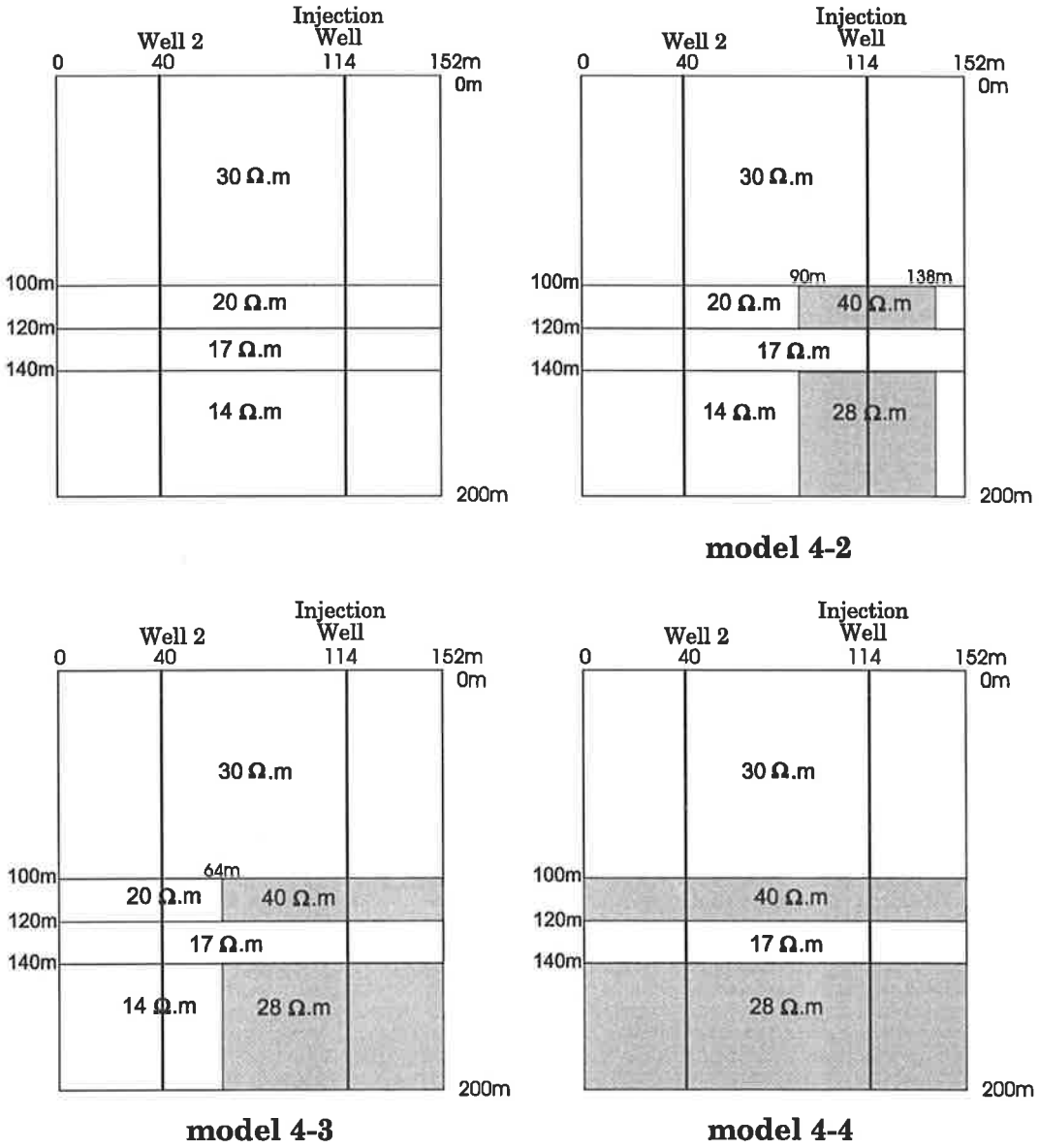

Figure 9.6 The model layouts and parameters of the 4 numerical models of the second model set, corresponding to different stages of water injection.

9.2.1 Model Set 1 – Three Layer Aquifer, All Layers Equally Permeable

The aquifer in the first model set comprises a three layer structure (resistivities 20, 17 and 14 Ω.m) overlain by a layer of resistivity 30 Ω.m. Four numerical models have been calculated for this set, as shown in Figure 9.5. From the figure, it can be seen that the shaded area (fresh water) expands from the injection well to the observation well gradually, to simulate the water flow procedure. Each layer in the aquifer is assumed to have identical hydraulic conductivity, resulting in vertical boundaries on the advancing front as shown in Figure 9.5.

The eight stacked profiles of the modelling data of the four models for 14m and 28m electrode separation are shown from Figure 9.7 to Figure 9.14. This style of presentation is the same as that used in chapter 8.

The average apparent resistivity R_{14a} and R_{28a} for the 14m and the 28m separation data in the models are displayed in Table 9.1. Also the relative change of the average apparent resistivity between consecutive models has been calculated and is shown in Table 9.1.

Table 9.1 The list of minimum, maximum, average apparent resistivity and the apparent resistivity relative change of 4 numerical models for the first set of modelling.

Model Name	AR-MIN (Ω.m)	AR-MAX (Ω.m)	AR-MEAN (Ω.m)	AR Increase (%)
74m model 3-1 14m separation	15.32	21.38	17.54	
74m model 3-2 14m separation	21.17	26.46	23.63	34.70
74m model 3-3 14m separation	23.40	28.35	25.73	8.86
74m model 3-4 14m separation	30.11	34.45	32.63	26.82
74m model 3-1 28m separation	16.36	20.16	17.78	
74m model 3-2 28m separation	21.04	23.63	22.17	24.68
74m model 3-3 28m separation	25.12	27.31	26.03	17.37
74m model 3-4 28m separation	31.12	32.05	31.62	21.46

By comparing Table 9.1 with Table 8.1, one can see that there is not much difference in the results for model 1 and model 4 between the two tables. This is because both initial models and both final models (fully filled injected water) are the same. Only the distance between two survey wells is different. So they should produce similar results. However, the results from model 2 and model 3 in the two tables have large differences since the injection well was filled with the injected water in the radial configuration. This also causes large changes in the relative increase percentage of the apparent resistivity in both tables.

Figure 9.7 Apparent resistivity profiles of Model 3-1 (14m separation).

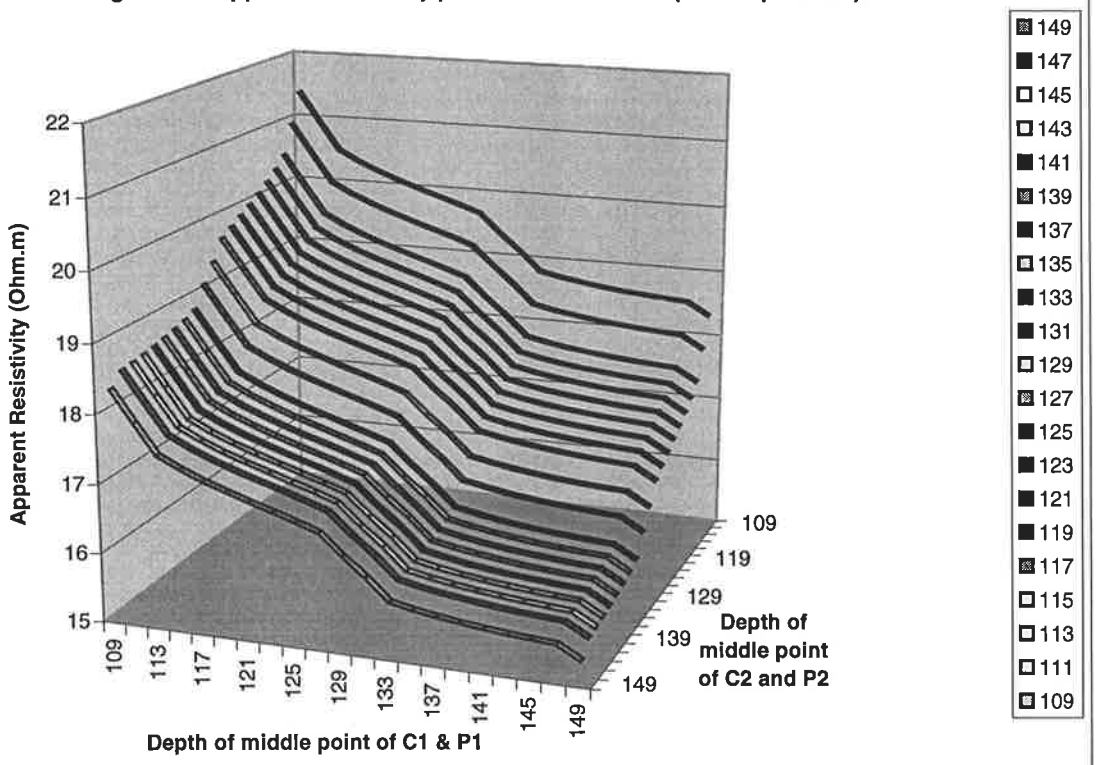

Figure 9.8 Apparent resistivity profiles of Model 3-2 (14m separation).

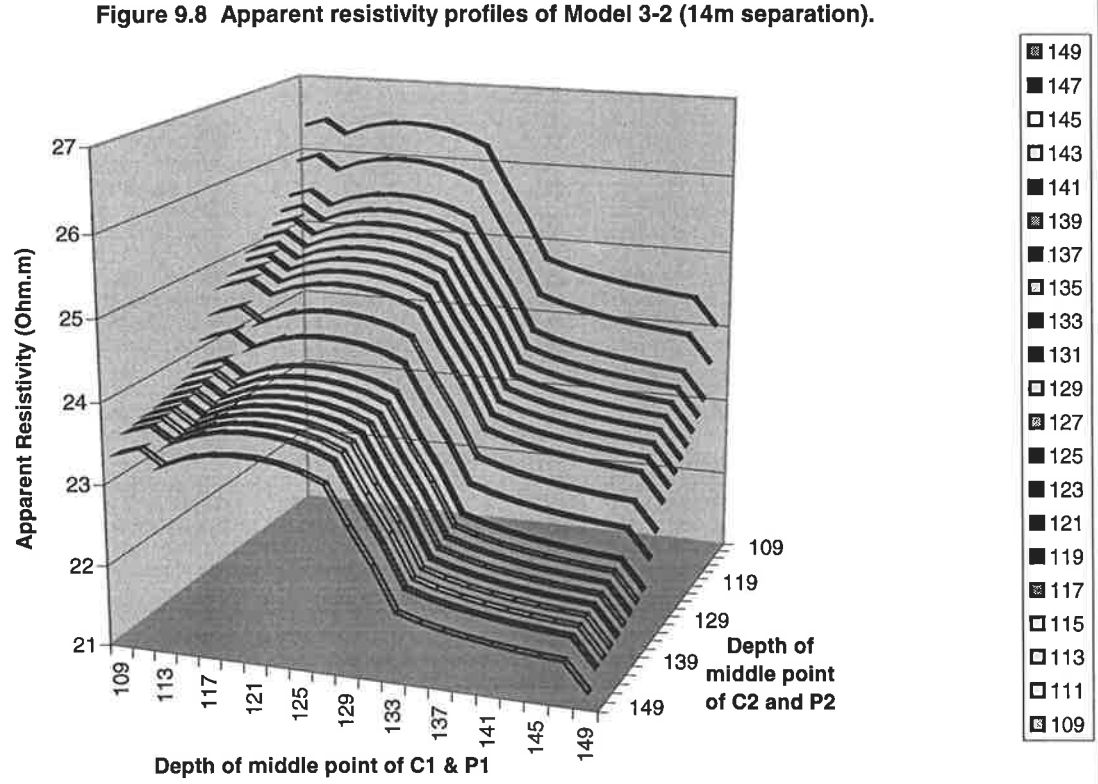

Figure 9.9 Apparent resistivity profiles of Model 3-3 (14m separation).

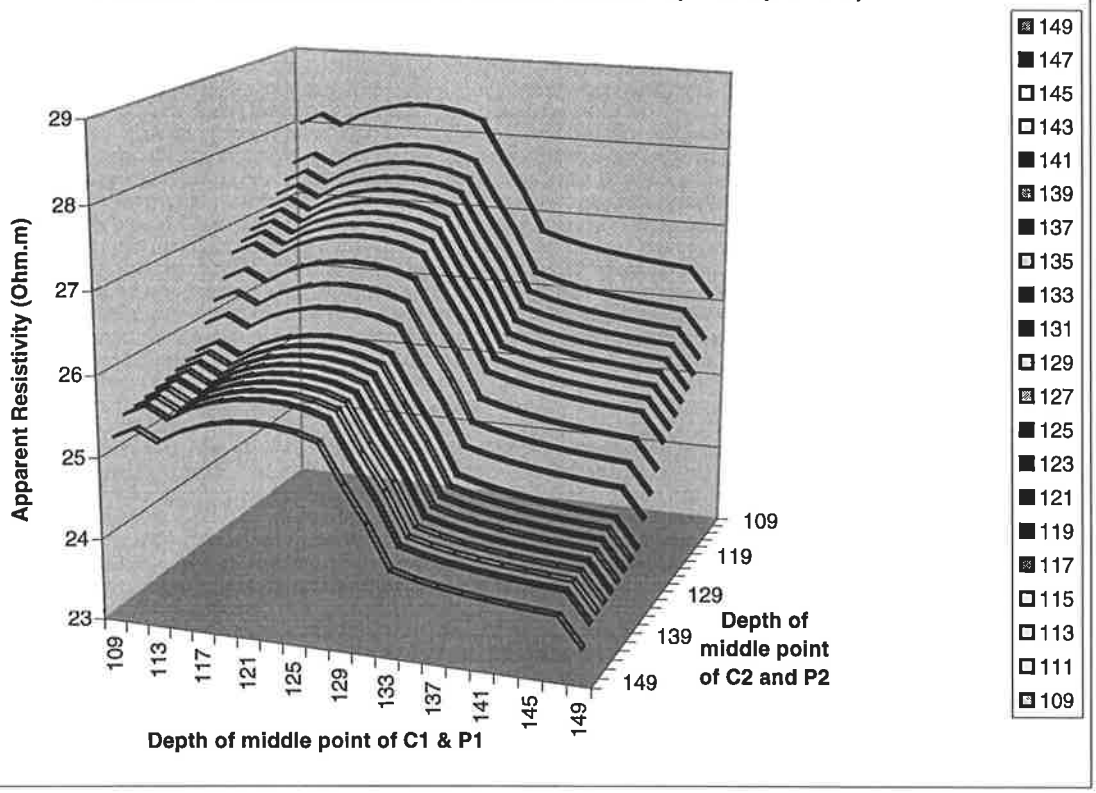

Figure 9.10 Apparent resistivity profiles of Model 3-4 (14m separation).

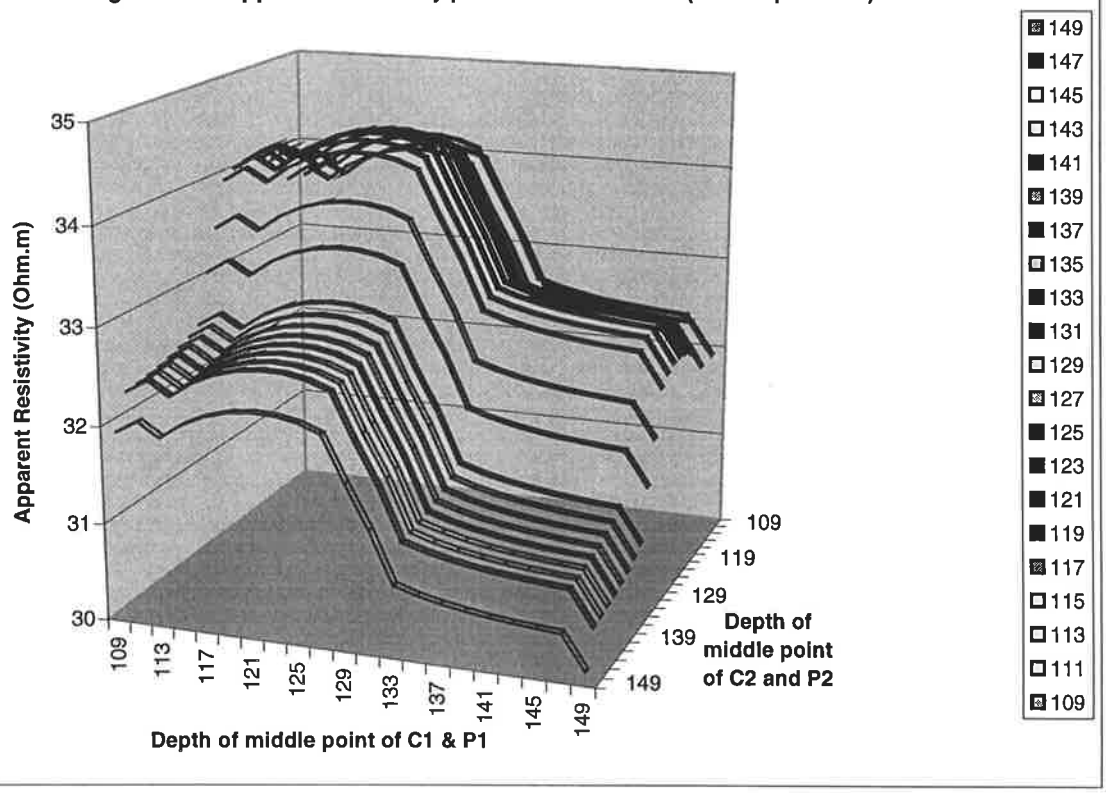

Figure 9.11 Apparent resistivity profiles of Model 3-1 (28m separation)

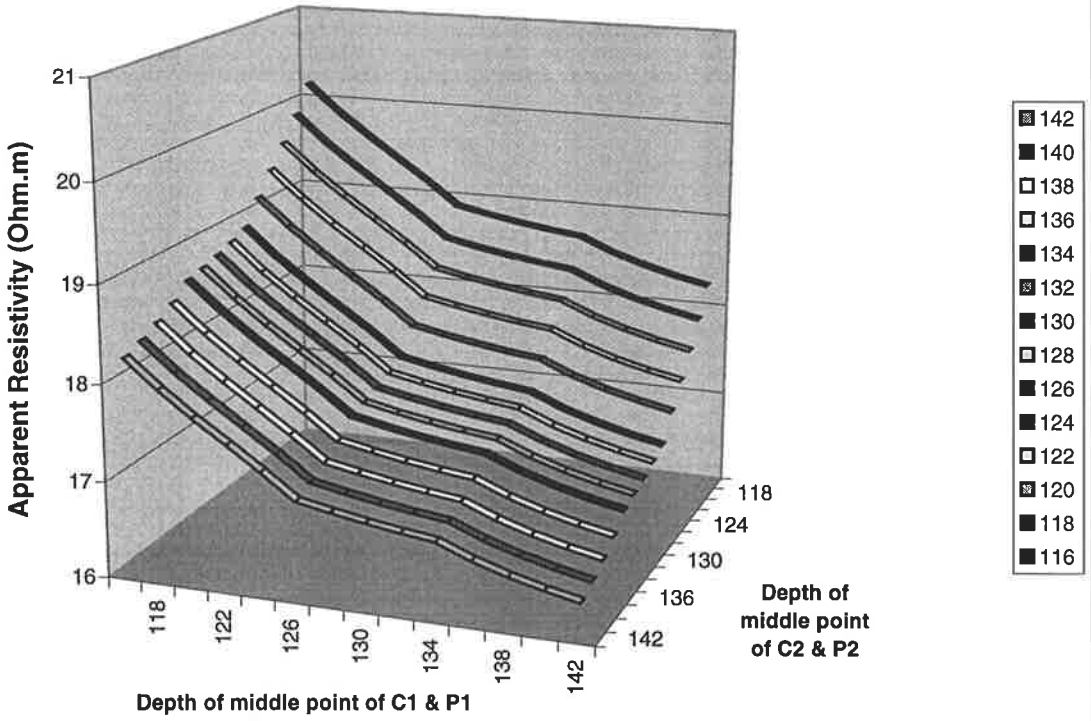

Figure 9.12 Apparent resistivity profiles of Model 3-2 (28m separation)

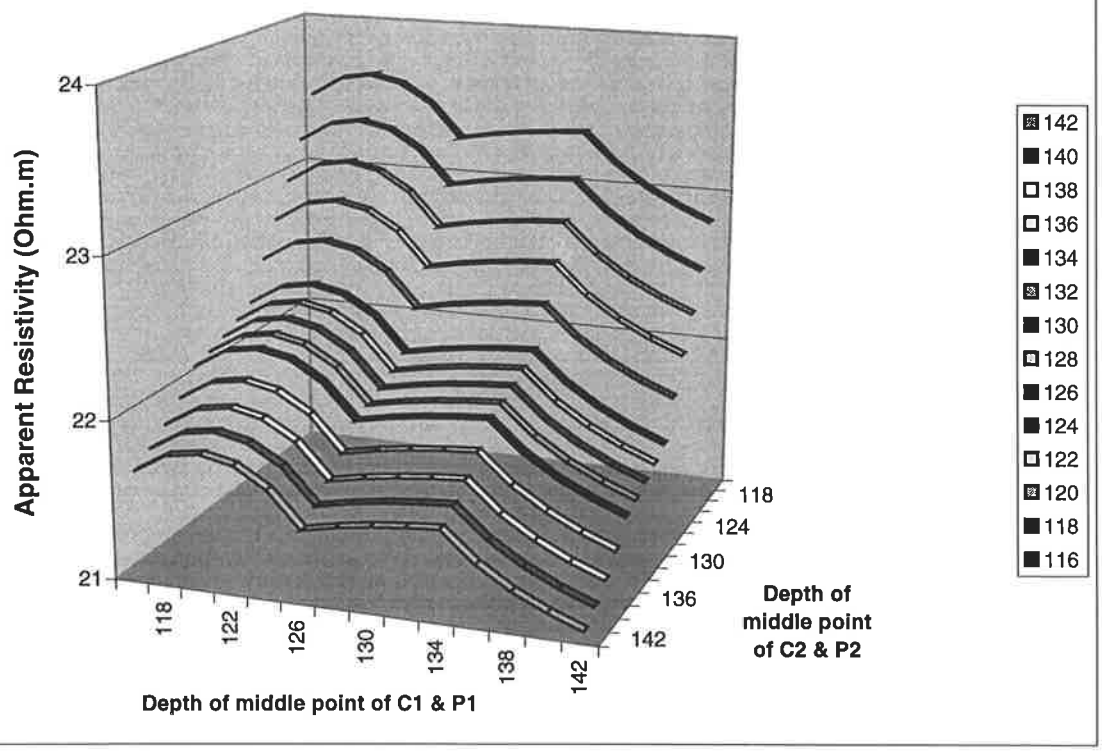

Figure 9.13 Apparent resistivity profiles of Model 3-3 (28m separation)

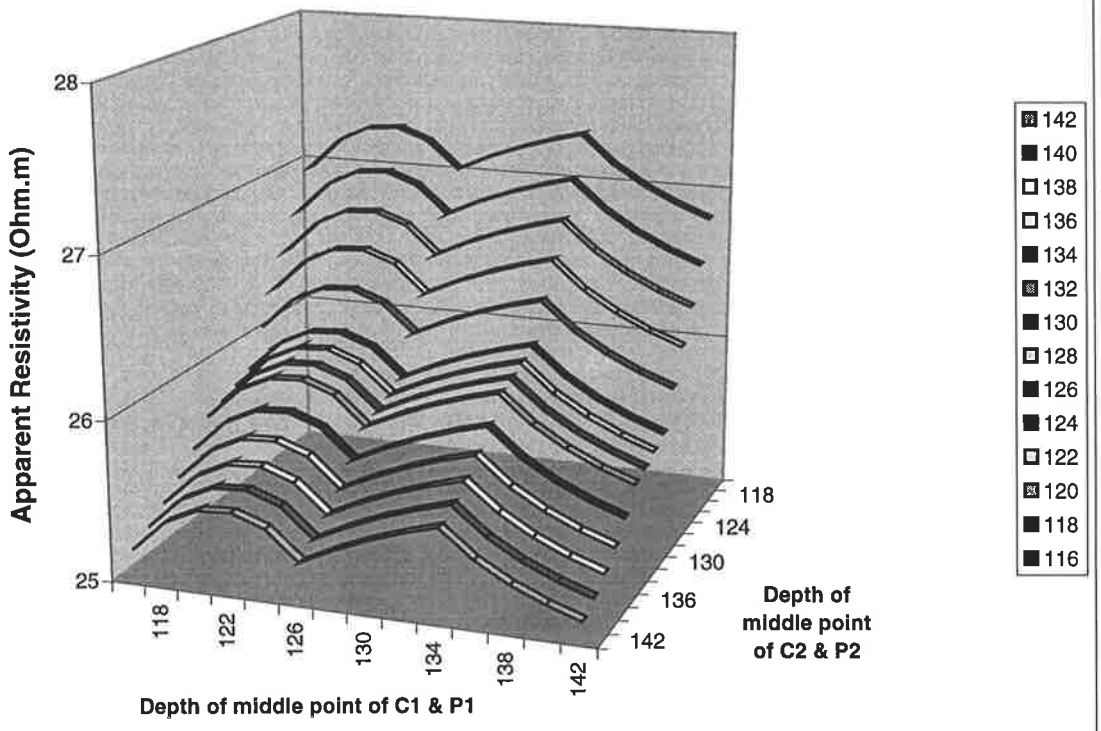

Figure 9.14 Apparent resistivity profiles of Model 3-4 (28m separation)

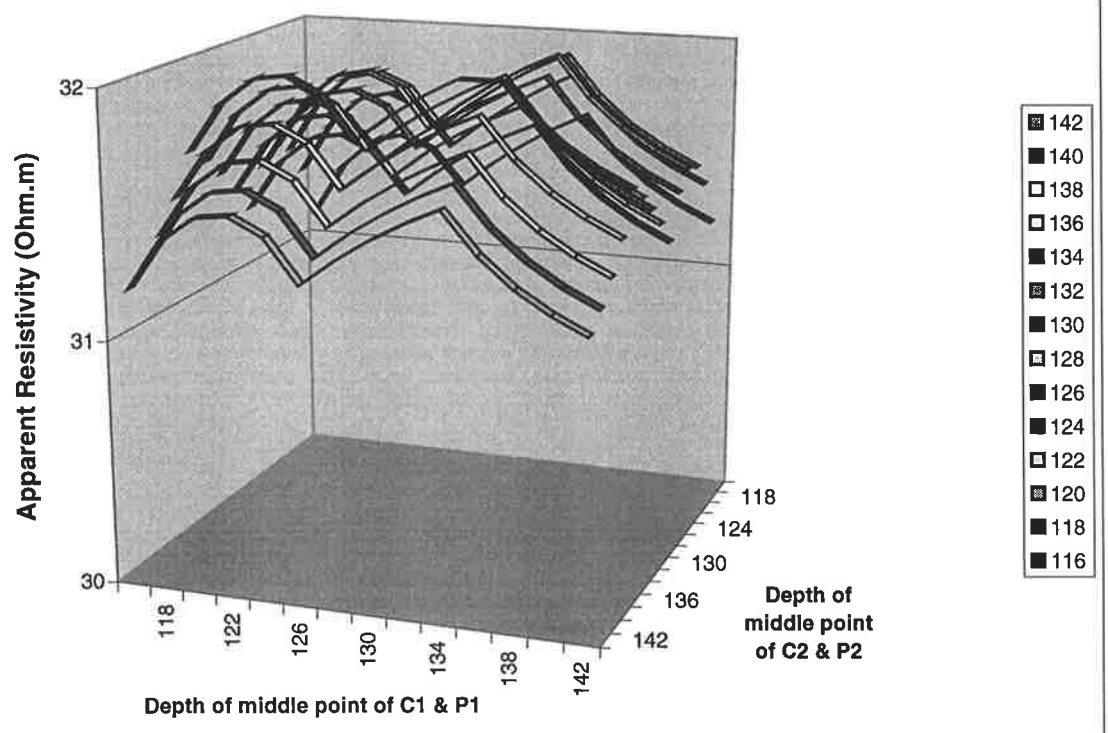

From the stacked profiles of model 3-1 (refer to Figures 9.7 and 9.11), we can see that the apparent resistivity decreases with depth in each profile, which reflects the resistivity reduction trend with depth in the model. After the water is injected and the injection well is filled with water, the model is no longer symmetric. This can be seen in Figure 9.5 and is not unlike the chord situation (chapter 8), where all 8 models are symmetric. So the profile patterns for models 3-2, 3-3 and model 3-4 exhibit some change. The profiles in Figures 9.8, 9.9 and 9.10 mainly show the resistivity trend near the injection well since the profiles are drawn versus depth in the injection well. Because the resistivity of the top layer is 30 Ω.m and smaller than the resistivity of the second layer, the left part of the profile is a little flat. If the profiles are drawn as apparent resistivity versus depth in the observation well, (see Figures 9.15 and 9.16 for model 3-2 and model 3-3), the profile patterns are different. They continue to decrease since these two profiles mainly reflect the resistivity change trend near the observation well where the injected water has not yet reached, and the resistivity decreases with depth. From Figures 9.7 to 9.16, it can be seen that the stacked profiles exhibit an apparent resistivity increase with the amount of water injected. This relates to the high resistivity fresh water. Also the average resistivities of model 3-1, model 3-2, model 3-3 and model 3-4 (refer to Table 9.1) show an increasing trend. This is because the injected high resistivity water caused an increase in the average values.

When the water fills the whole aquifer (model 3-4), the model becomes symmetric again and the stacked profiles are symmetric too. This means that the profile pattern when viewed against apparent resistivity vs the depth of BN in the observation well (WELL 2) is the same as that for depth AM in the injection well (shown in Figure 9.10).

For the same reason as given in chapter 8, four turning points are clearly shown in all four stacked profiles in Figures 9.7 to 9.10. For the 28m separation configuration, the current electrode crosses only one interface (depth 140 m) and the potential electrode crosses only one interface (120 m depth), producing only two turning points in all 28m-separation stack profiles. This is shown in Figures 9.11 to 9.14.

From Table 9.1, it is evident that the apparent resistivity (AR) increases with an increasing amount of high resistivity water injected into the subsurface. But unlike the situation in the last chapter, the AR suddenly increases between model 3-1 and model 3-2 by about 35%. This is because the injected water directly affects the current injection and the potential distribution in the injection well. In the chord measurement situation of chapter 8, the

injected water only affected the apparent resistivity indirectly in Models 1-2 and 1-3, since it did not reach either well. The AR increase between Model 3-2 and 3-3 is not very large, only about 9% for the 14m separation data and 17% for the 28m separation data.

From Table 9.1, one can also see the differing effects of water injection on the 14m and 28m bipole spacing data. For Models 3-1 to 3-2, the injected water occupies only the area near the injection well (refer to Figure 9.5). This gives a larger average AR increase (35%) for the smaller separation (14m) than the average AR increase (25%) for the larger separation (28m), since the AR of the larger separation is more influenced by the resistivity far away from the injection well. For Models 3-2 to 3-3, the situation is just the opposite. With the continuation of pumping, the injected water reaches the middle part between the two wells. This causes the resistivity to increase far away from the two wells. This change is picked up more readily by the larger separation (28m separation: 17.4%) than by the smaller separation (14m separation: 8.9%) bipoles. Therefore, different separations normally have a different detection range. This is similar to surface resistivity surveys – the larger the separation, the deeper the penetration.

9.2.2 Model Set 2 – Three Layer Aquifer, One Layer Impermeable.

In this second model set, we consider the same three-layer aquifer, bounded on the top by an impermeable layer of resistivity 30 Ω.m. But now we assume that the intermediate aquifer layer is impermeable, so that all of the injected water is forced to flow through the layers above and below it. Again we assign equal hydraulic conductivity to the layers bounding the impermeable zone, resulting in the time-lapse models 4-1, 4-2, 4-3 and 4-4, as shown in Figure 9.6. The time-lapse pictures correspond to fractional advances to fresh water breakthrough of 0, 1/3, 2/3 and 1, with vertical advancing plume fronts. Compared to Figure 9.5, the only difference in the actual resistivity distribution is with respect to the middle layer which retains its constant (pre-injection) salt water value of 17 Ω.m.

The stacked profiles of the modelled apparent resistivity data for all four sub-models are shown in Figure 9.17 to Figure 9.24. The average apparent resistivities R_{14a} and R_{28a} for the 14m and the 28m separation data, and the relative change of the average apparent resistivity between consecutive sub-models (time lapses) are displayed in Table 9.2.

Figure 9.15 Apparent resistivity profiles of Model 3-2 (14m separation).

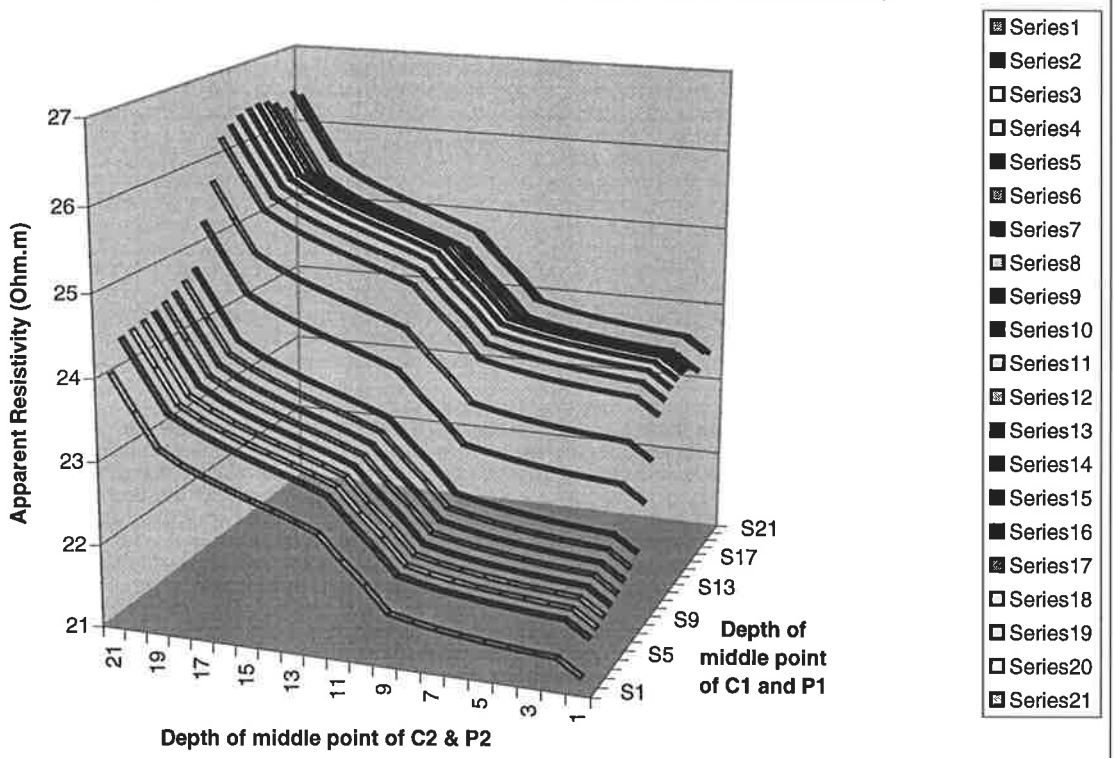

Figure 9.16 Apparent resistivity profiles of Model 3-3 (14m separation).

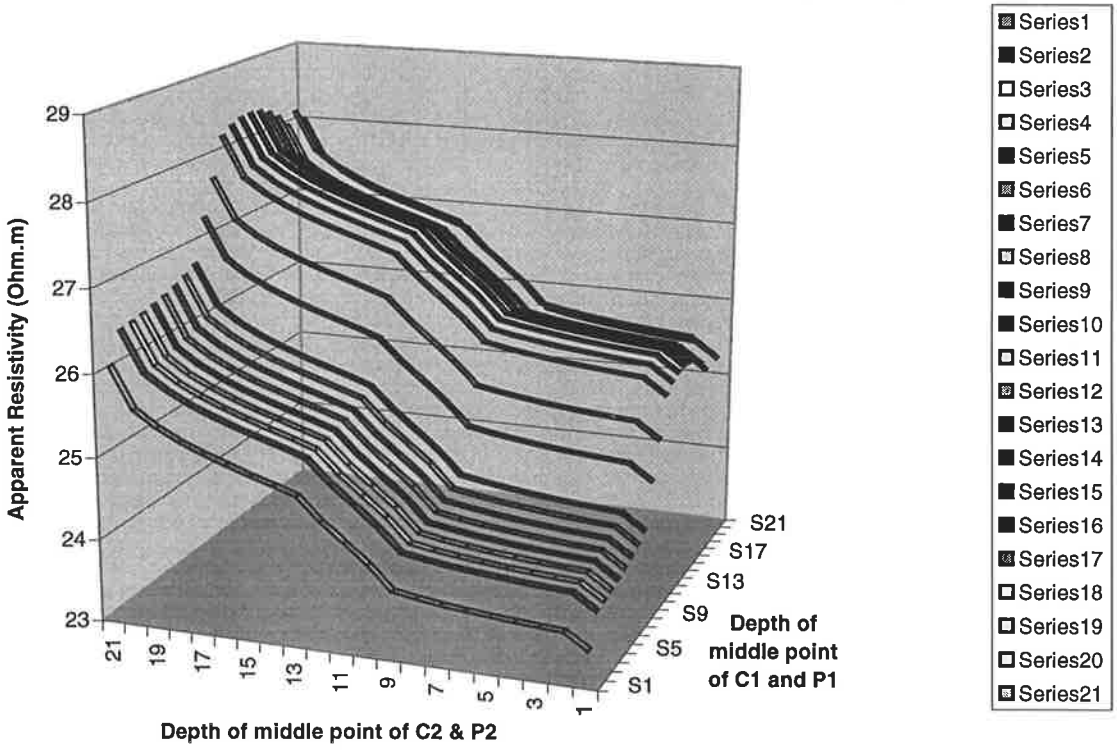

Table 9.2 The list of minimum, maximum, average apparent resistivity and the apparent resistivity relative change of 4 numerical models for the second set of modelling.

Model Name	AR-MIN (Ω.m)	AR-MAX (Ω.m)	AR-MEAN (Ω.m)	AR Increase (%)
74m model 4-1 14m separation	15.32	21.38	17.54	
74m model 4-2 14m separation	18.13	24.20	20.35	15.99
74m model 4-3 14m separation	19.57	25.14	21.53	5.77
74m model 4-4 14m separation	22.79	28.38	24.78	15.07
74m model 4-1 28m separation	16.36	20.16	17.78	
74m model 4-2 28m separation	19.12	23.13	21.05	18.38
74m model 4-3 28m separation	21.11	25.55	23.34	10.87
74m model 4-4 28m separation	24.19	29.59	27.34	17.13

From the above table, it is clear that all AR-MEANs in the table are lower than the ones in Table 9.1. This is due to the impermeability of the middle layer which causes the average apparent resistivity to drop.

The stacked profiles of the initial model, shown in Figures 9.17 and 9.21, are the same as those of the first modelling set in this chapter. They show that the apparent resistivity reduces with depth in each profile, which reflects the resistivity reduction trend with depth in model 4-1.

It is obvious that the stacked profile patterns of Models 4-2 and 4-3 for this modelling set are much different from those of the last modelling set, just because the third layer is impermeable and has lower resistivity than layers above and below it. Unlike the profile pattern of model 4-1 (continuous decease, as shown in Figure 9.17), the stacked profiles of Model 4-2 and Model 4-3 (shown in Figures 9.18 and 9.19) give a wiggle-shaped apparent resistivity pattern. This is because the actual (true) resistivity vs depth pattern of the model in the survey range is an oscillatory (wiggle) pattern as well: low->high->low->high (refer to Figure 9.6). It is not easy to interpret this kind of wiggle pattern directly. Therefore the inversion procedure may be the best and only reliable tool for the interpretation of such data.

Figure 9.17 Apparent resistivity profiles of Model 4-1 (14m separation).

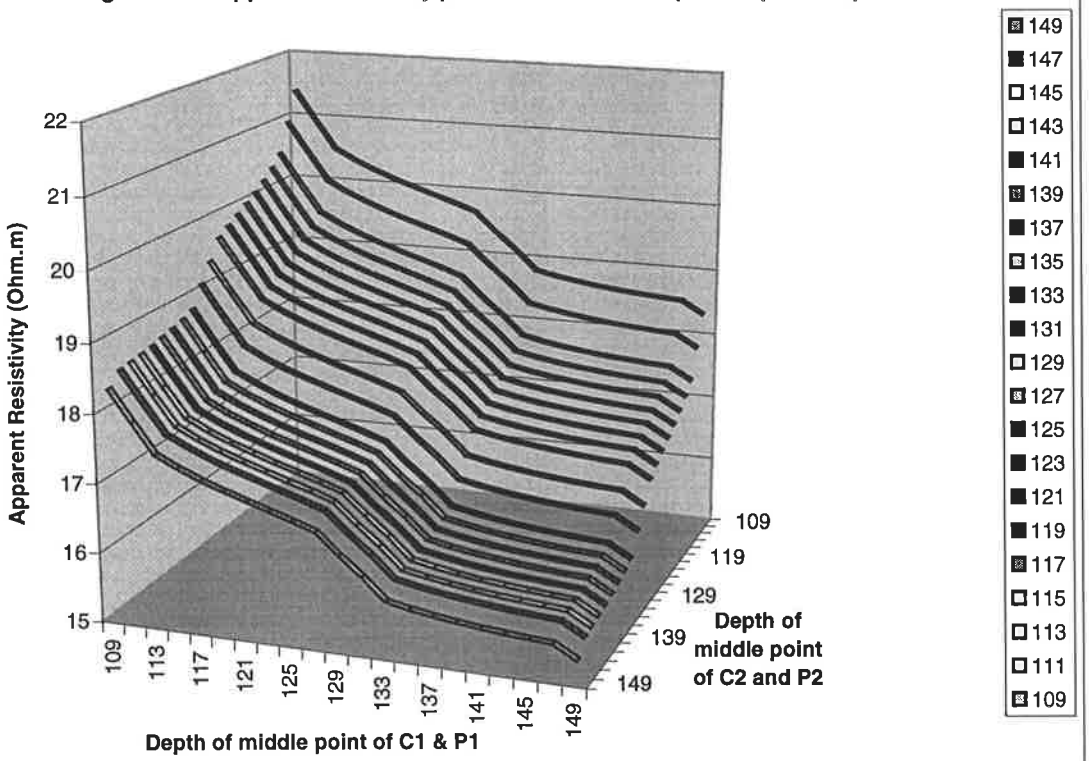

Figure 9.18 Apparent resistivity profiles of Model 4-2 (14m separation).

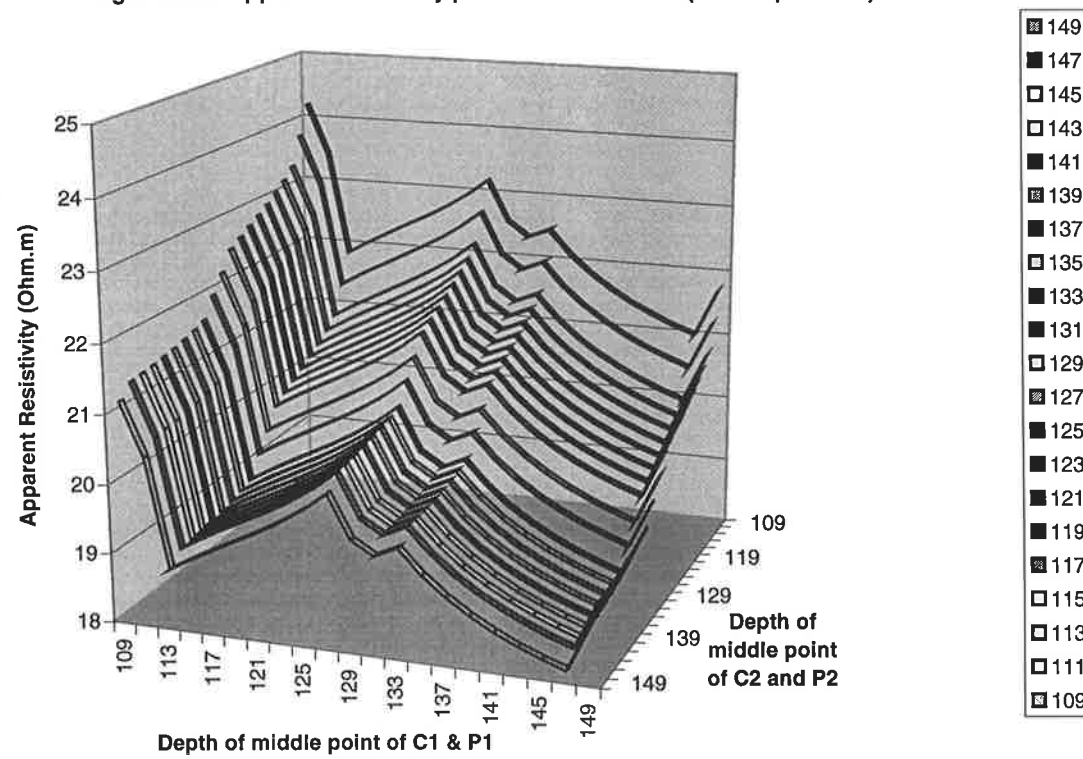

Figure 9.19 Apparent resistivity profiles of Model 4-3 (14m separation).

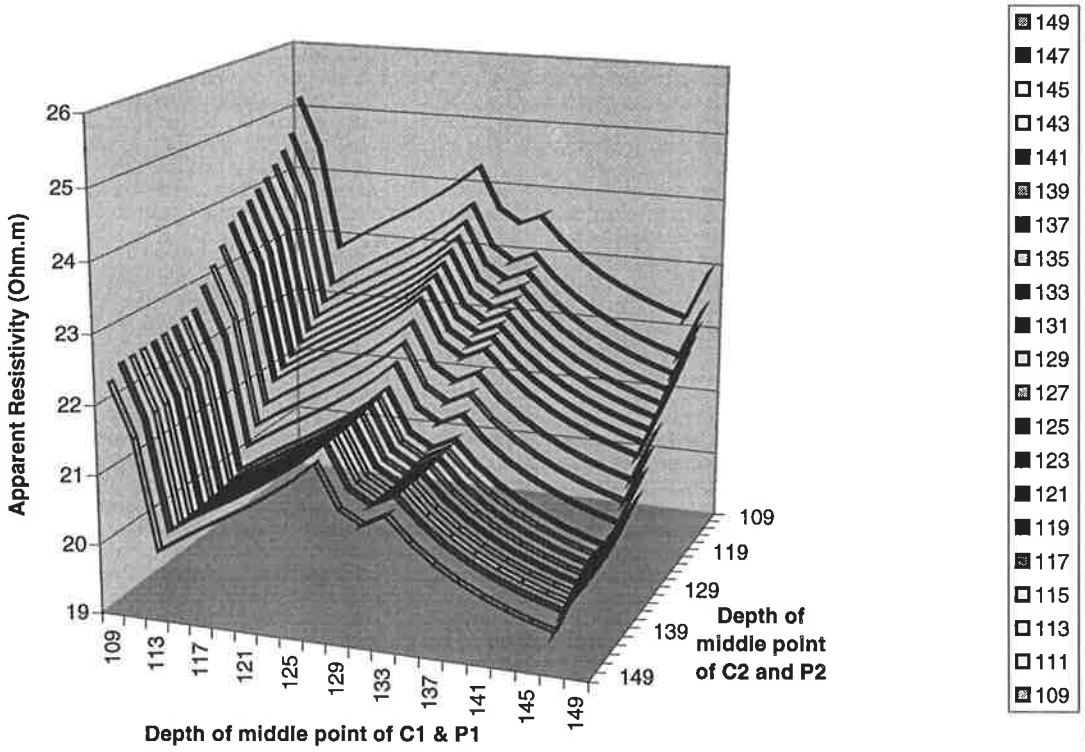

Figure 9.20 Apparent resistivity profiles of Model 4-4 (14m separation).

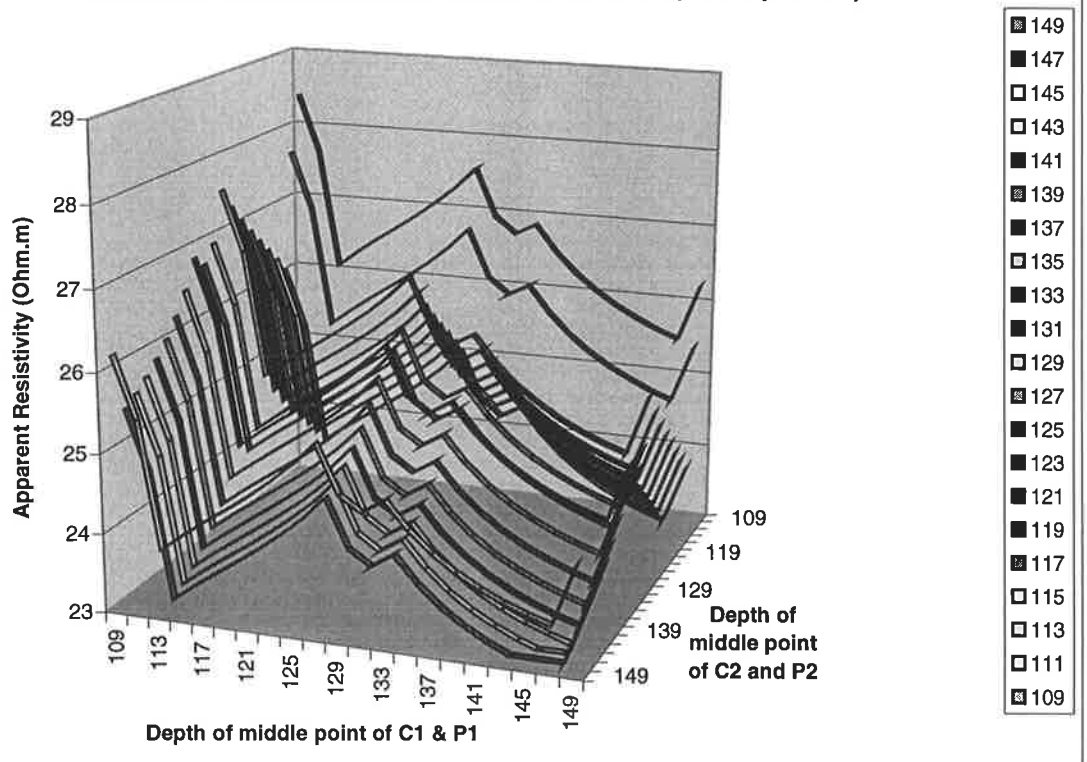

Figure 9.21 Apparent resistivity profiles of Model 4-1 (28m separation)

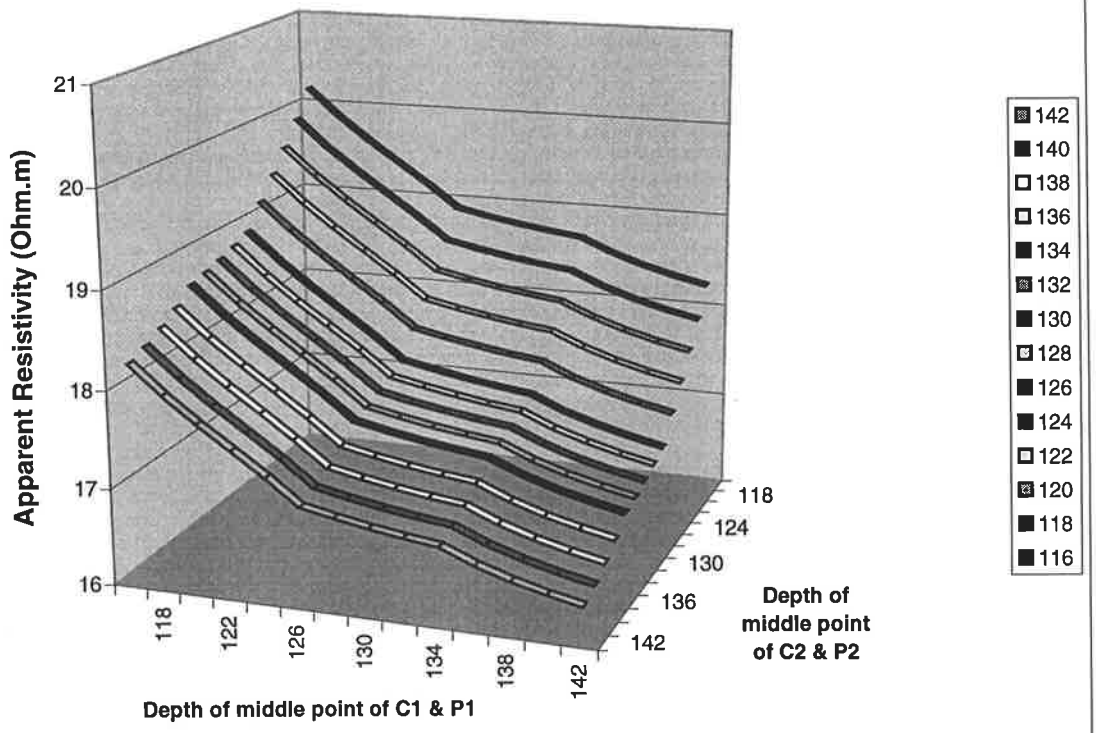

Figure 9.22 Apparent resistivity profiles of Model 4-2 (28m separation)

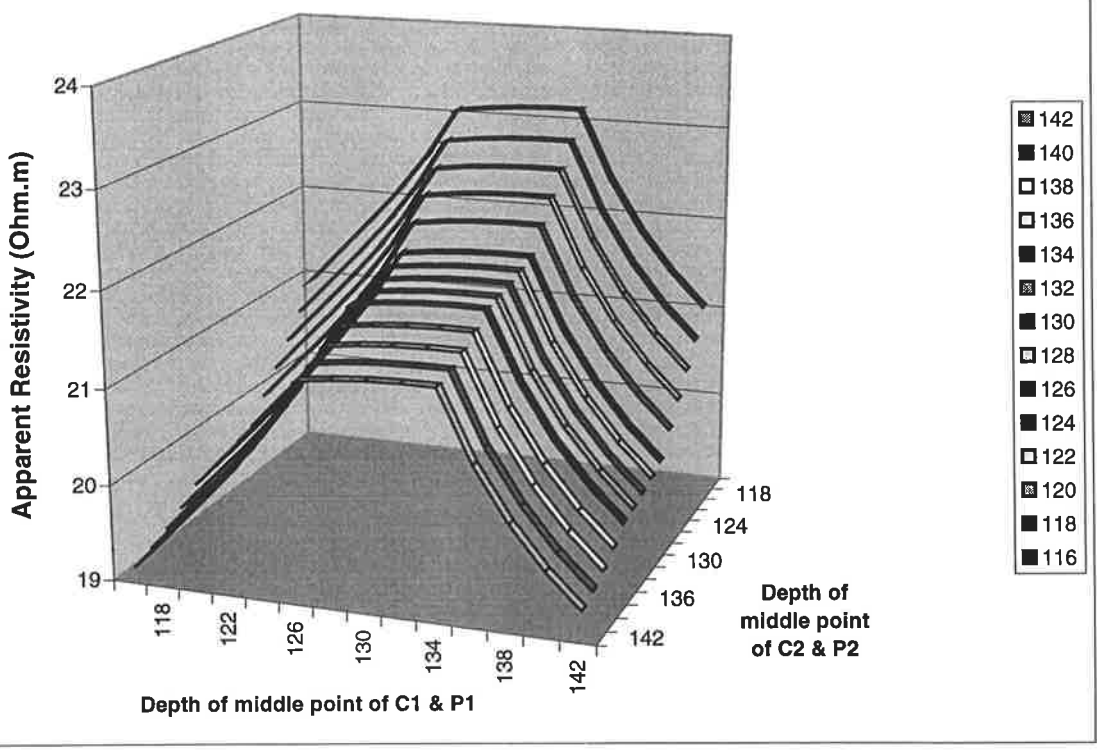

Figure 9.23 Apparent resistivity profiles of Model 4-3 (28m separation)

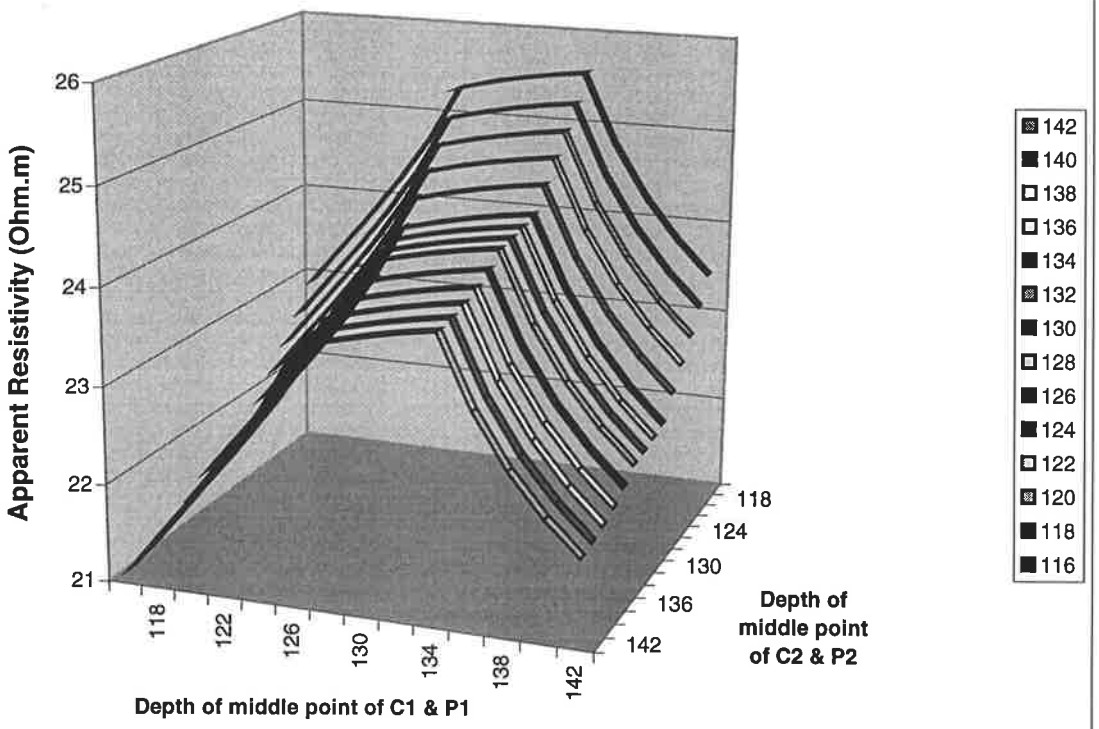

Figure 9.24 Apparent resistivity profiles of Model 4-4 (28m separation)

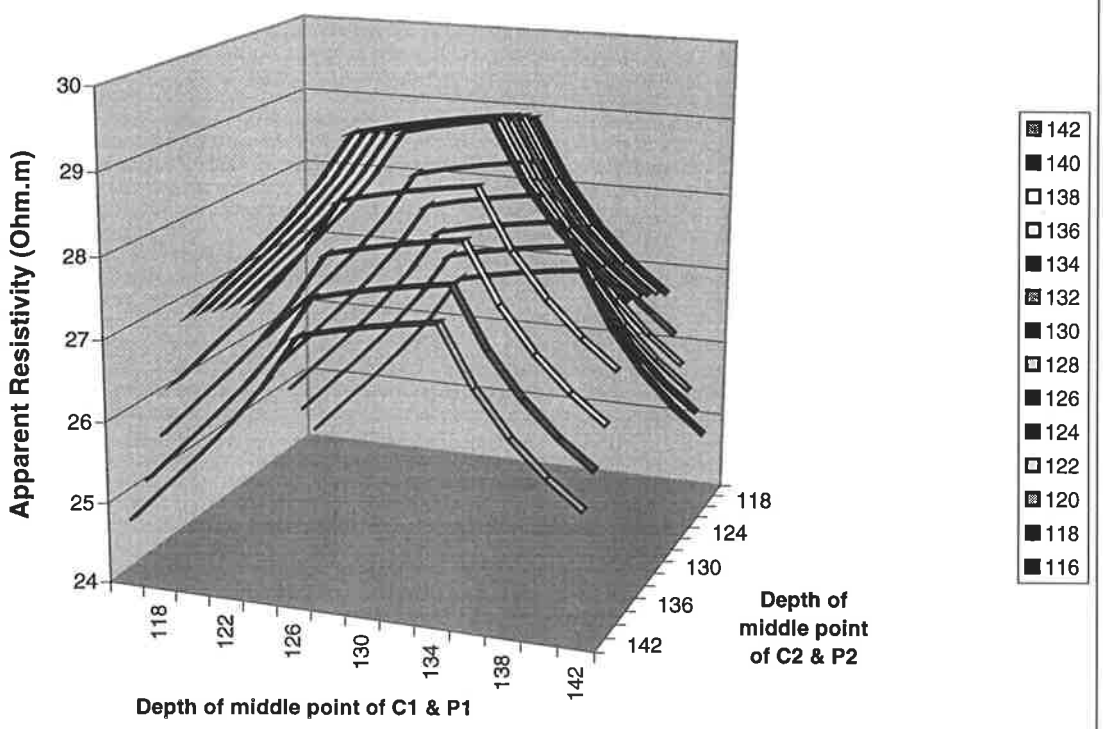

9.3 THE SENSITIVITY DISTRIBUTIONS OF THE TWO DIFFERENT ELECTRODE SEPARATION CONFIGURATIONS

In similar fashion to the chord configuration (Section 8.3), the sensitivity distributions for the 14m and the 28m current and potential electrode separation configurations were calculated and plotted before carrying out the inversion for the radial configuration. The background resistivity used to calculate the sensitivity distribution is 30 Ω.m. The calculated sensitivity distributions were normalized for each configuration as well. The normalized sensitivity distributions for the 14m and the 28m separations are shown in graph (a) and (b) of Figure 9.25, respectively. The depth positions of the current and potential electrodes in the experiment are the same as described in Section 8.3.

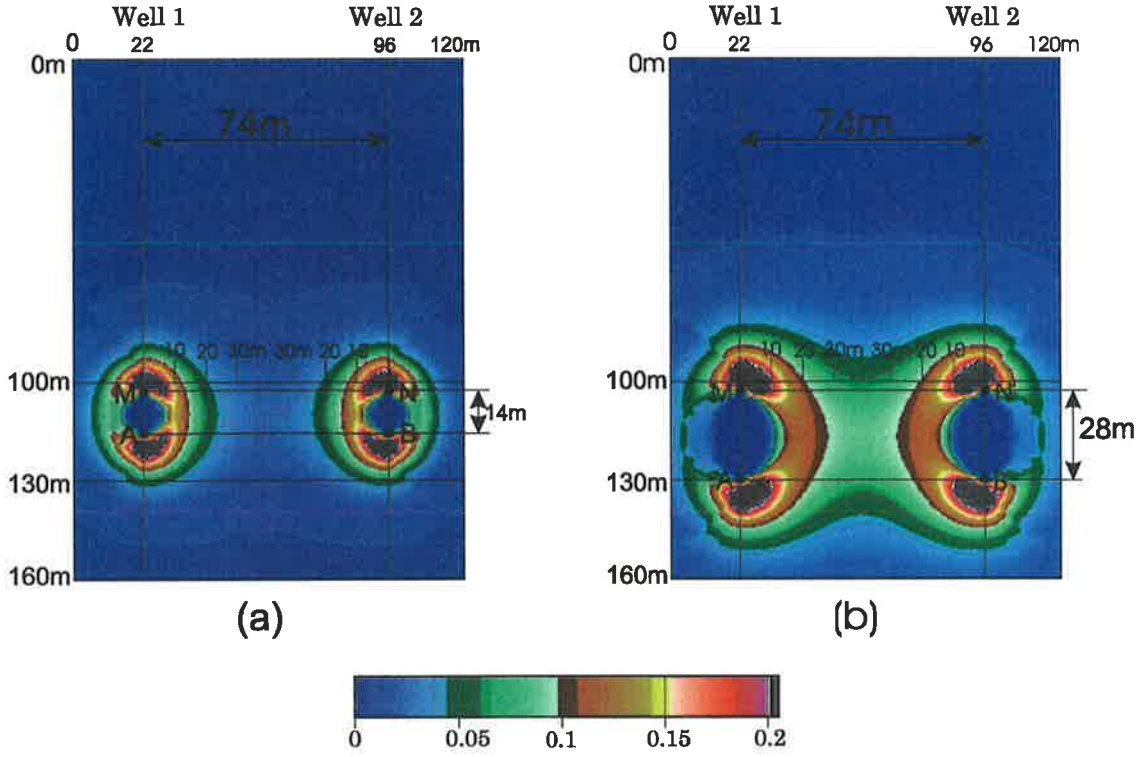

Figure 9.25 The comparison of (a) the normalized sensitivity distribution calcualted with 14m current and potential electrode separation and (b) the normalized sensitivity distribution with 28m separation is shown in this graph. All negative sensitivities were set to zero. A and B are cureent electrodes and M and N are potential electrodes.

From Figure 9.25, one can see that the normalised sensitivity in the middle area between the two wells for the 28m separation, about 0.08 shown in graph (b), is still much better than that for the 14m separation, about 0.02 as shown in graph (a). So it is still true that the larger current and potential electrode separation in the bipole-bipole configuration will produce a larger effective range of detectability.

By comparing graph (b) of Figure 9.25 with graph (b) of Figure 8.25 in Section 8.3, one can see that the normalised sensitivity in the middle area between the two wells in graph (b) of Figure 9.25 is much larger than the one in graph (b) of Figure 8.25. This is because the distance between the two wells in Figure 9.25 (74m) is smaller than the distance in Figure 8.25. This means that the inversion result for the area with a 74m well separation should be better than the result with a 104m well separation when using a 28m current and potential electrode separation.

9.4 THE INVERSION EXPERIMENTS ON THE CROSS WELL RESISTIVITY MODELLING DATA FOR THE RADIAL CONFIGURATION

All eight modelling data sets were inverted with our 2.5-D resistivity inversion program. The inversion results are shown in Figures 9.26 and 9.27.

The images are all smaller than the original modelling area, in order to make inversion calculation more efficient. Again, all inversions are seriously under-determined and the accessible ranges in both boreholes are very limited (from 102m to 156m) and the distance between the two boreholes (74m) is still larger than the range. All factors combine to make the inversion very difficult.

As mentioned earlier, four models (Model 3-1 and Model 3-4 of Figure 9.5, and Model 4-1 and Model 4-4 of Figure 9.6) of the eight are symmetric and the other four (Model 3-2 and Model 3-3 of Figure 9.5 and Model 4-2 and Model 4-3 of Figure 9.6) are asymmetric, since the injected water flows from one survey well (Injection Well) to the other (Well 2). So the four inversion results should be symmetric and the other four should be asymmetric. To reduce inversion difficulty, the initial model values of the top layer (from 0m to 100m depth) in all inversions were set to the original value 30 Ω.m. The initial values for the other layers were set from the imaging results (chapter 5), which are not shown here. After inversion, all images were filtered a little to remove the borehole positions. Again keep in mind that the 14m and 28m separations between the two electrodes in each borehole cannot normally produce a good inversion result very far away from the wells. So the middle part of the inversion images lack reliability of detail, and show only a trend.

Figure 9.26 shows all inversion results for the first model set. The results for Model 3-1 and Model 3-4 are symmetric, as predicted. Both images reveal a resistivity decrease with depth,

which matches with the original models. The three-layer structure near both boreholes can be seen from the results. But in the middle part, it is hard to see the three-layer structure due to its large distance (relative to AM & BN) from both boreholes. However, it can be seen that the resistivity decreases with depth in the middle part and the whole structure is almost flat. So this result basically matches with the original model (also shown in Figure 9.26).

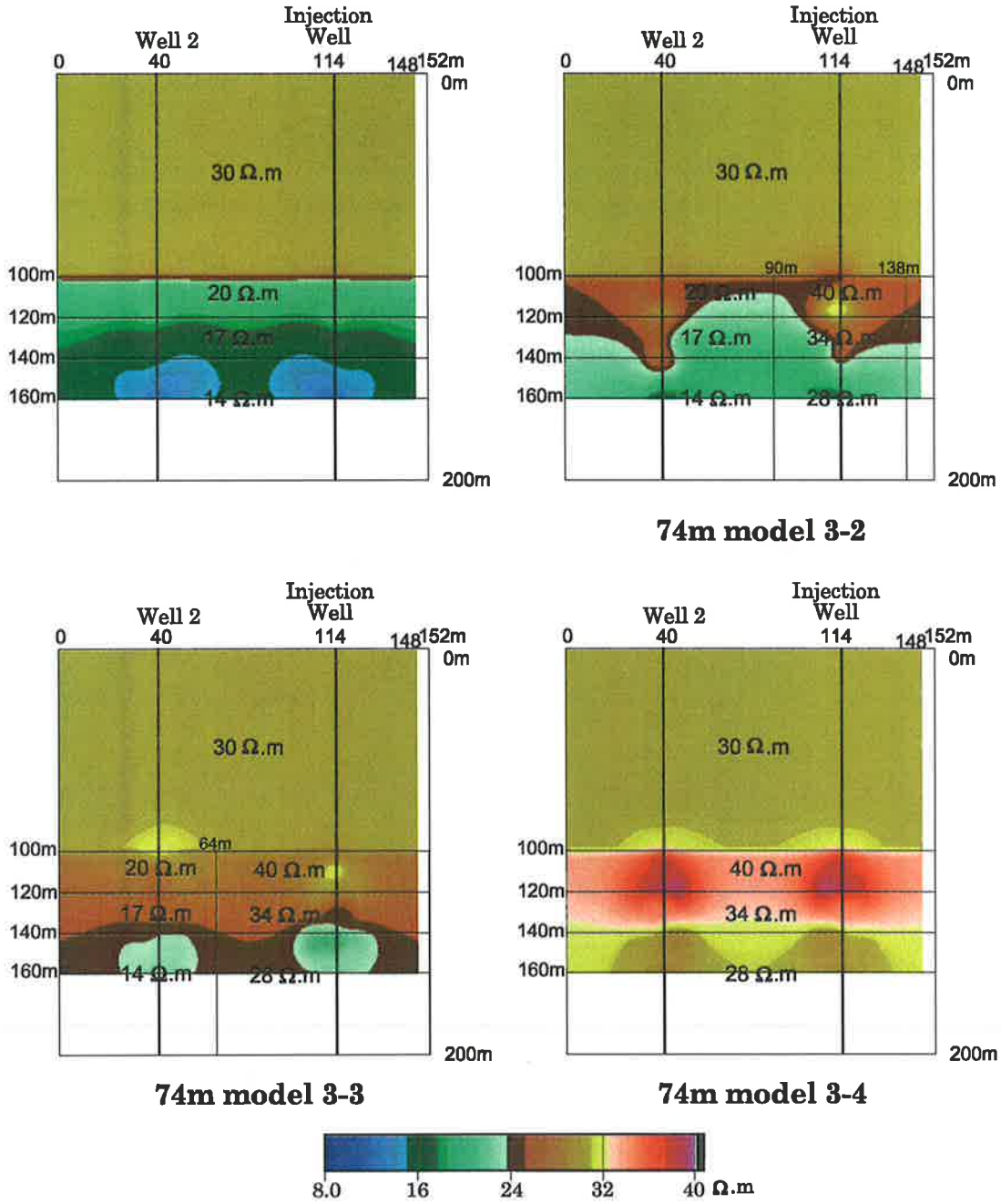

Figure 9.26 The inversion results from the modelling data with model layouts overlain for the first model set.

The inversion results for model 3-2 and model 3-3 in Figure 9.26 are asymmetric, as predicted. The resistivity decreases with depth, which is consistent with the original models. The three-layer structures near both boreholes in both images are not very clear, but still discernible. It is hard to see any structure in the middle part of the section. The resistivity near the injection well is higher than the resistivity near the other well in both inversion

results. This is as expected since the high resistivity water was injected into the injection well. However the resistivity near Well 2 should be the same as that of the background. It is too high.

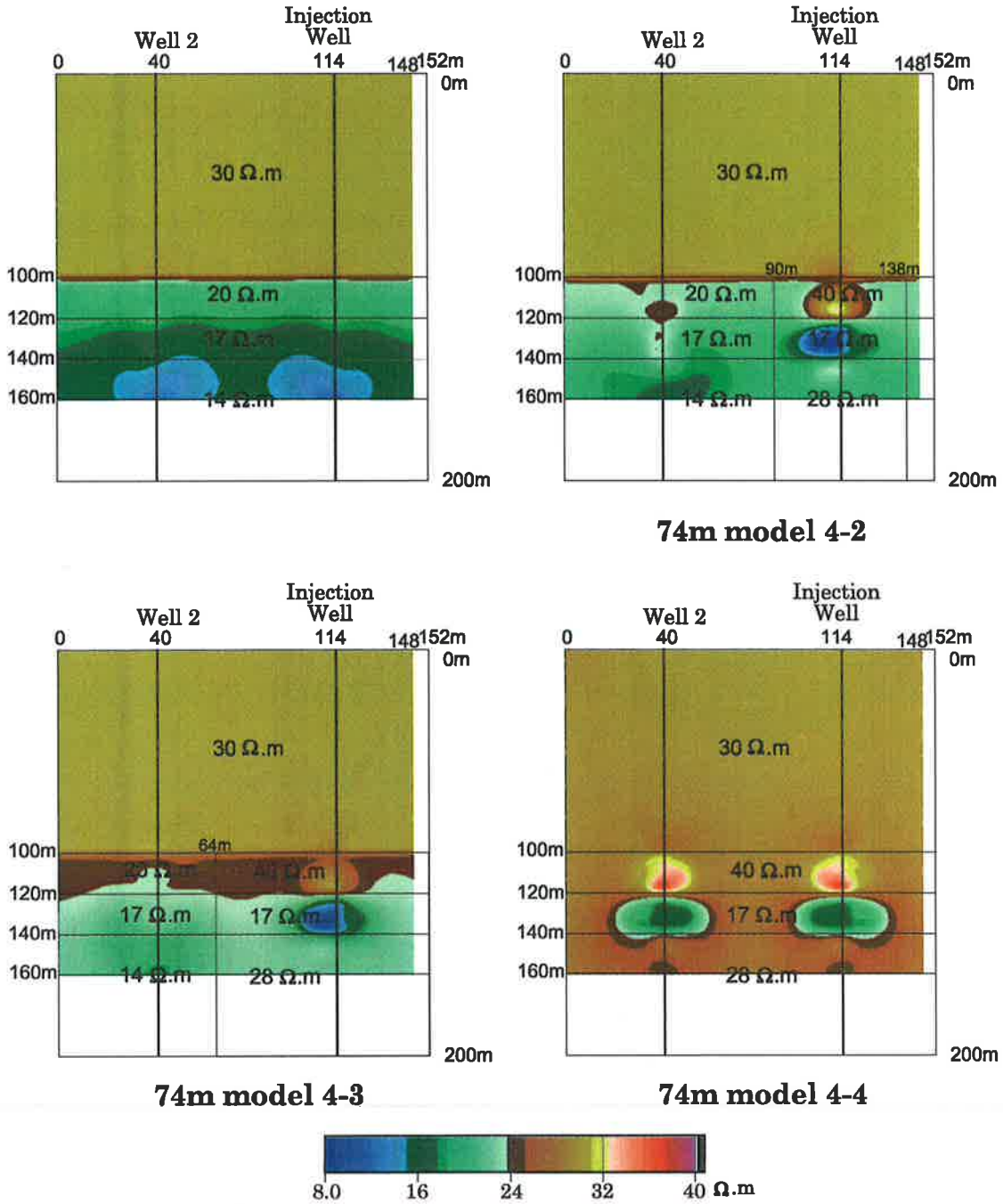

Figure 9.27 The inversion results from the modelling data with model layouts overlain for the second model set.

Figure 9.27 shows all inversion results for the second model set. The first picture is the same as the first one in Figure 9.26. All other inversion results in the figure are better than the results in Figure 9.26. The results of Model 4-2 and Model 4-3 clearly show the three-layer structure near both boreholes and the impermeable layer near the injection well. It is much clearer in the area near Well 2 compared with the results in Figure 9.26. The middle part of

both images is still not good for the reasons given earlier. The result of Model 4-4 is symmetric, as predicted, and shows the three-layer structure clearly.

From the inversion results for the above two modelling sets, two things are clear. One is that the resistivity distribution near both boreholes can normally be imaged with the 14m and 28m configurations. The second is that the resistivity increase near the injection well due to the water injection can clearly be seen in the inverted images of the second modelling set, but are not very clear in the first modelling set.

9.5 CONCLUSIONS

From the above two sets of numerical modelling and inversion experiments, I offer the following conclusions (similar to those of Chapter 8):

1. The injected high resistivity water will definitely cause an observable AR increase in the resistivity crosshole multiple scanning surveys.
2. The AR increase rate between the first model (before water injected) and the second model (after water injected) is large, from 15% to 34% on average. However the change between the second model and the third model (more water injected) drops to about 10% on average.
3. If the model is symmetric, the inversion result from the modelling data should be symmetric as well. Otherwise, the inversion result will be asymmetric.
4. From the stacked profiles, it can be seen that the AR decreases with increasing depth, in accordance with the actual resistivity distribution.
5. All 14m electrode separation profiles show four turning points (or points of change in slope), in each profile, and all 28m electrode separation profiles show two turning points in each profile.
6. From the inversion results, it can be seen that the resistivity distribution near both boreholes can normally be imaged with the 14m and 28m configurations.
7. The resistivity increase in the middle part of the inter-well medium can be imaged by inversion, but the details are fuzzy due to the small electrode spacing relative to the well separation.

Chapter 10

RESISTIVITY SURVEYS AND INTERPRETATION - PHASE I

10.1 INTRODUCTION

As mentioned in Chapter 7, the Aquifer Storage and Recover (ASR) research project (Gerges 1996, Dillon *et al* 2001) commenced in July 1997 at the Bolivar site on the Northern Adelaide Plains in South Australia. The formal water injection started on October 11,1999. Before the water injection, several surface, surface-to-borehole and borehole-to-borehole electrical surveys were undertaken in order to understand the basic resistivity distribution in this area and to find the best resistivity configuration for the crosshole tomography experiments. The details of these surveys have been discussed in Chapter 7. This chapter will mainly concentrate on the crosshole resistivity tomography surveys completed in water injection phase I and the interpretation of the survey data.

Since 1997, many boreholes for water injection or scientific monitoring of the Bolivar ASR trial have been drilled at the Bolivar test site. Six of the boreholes used in this study are shown in Figure 10.1. The central well (18777) is used for water injection and five other wells (19450, 19445, 19444, 19442, 19443) are designed for monitoring measurements. Well 19450 is only 4 meters away from the injection well and the other four wells are situated on the circumference of a circle of radius 75 meters, centered on the injection well. These boreholes penetrate the T2-aquifer to a depth of 160m. All five monitoring wells and the injection well are cased with PVC pipe from the surface down to a depth of 100 m. The depth interval from 100m to 160m is open and available for crosshole resistivity measurements and other monitoring purposes.

The water pumping progress profile (cumulative volume versus time) for the whole injection period is shown in Figure 10.2. From the figure, it can be seen that the water injection is mainly confined to only two periods: from October 1999 to February 2000 and from March 2000 to April 2001. So we split the injection period into two phases. In fact, phase I (10/99 – 2/00) is only the preliminary test (30ML injected) and phase II (3/00 – 4/01) is the main

water injection test (about 220ML of water was injected). The later is about 7 times the volume of the former.

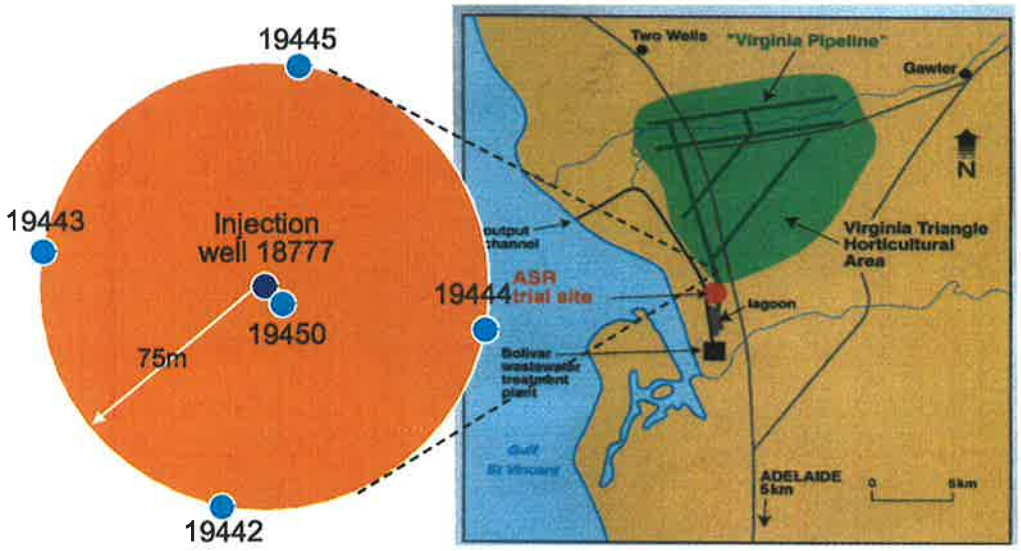

Figure 10.1 The location of the bolivar ASR trial site and the position of injection well and observation wells.

Figure 10.2 The water injection progress chart for the ASR trial.

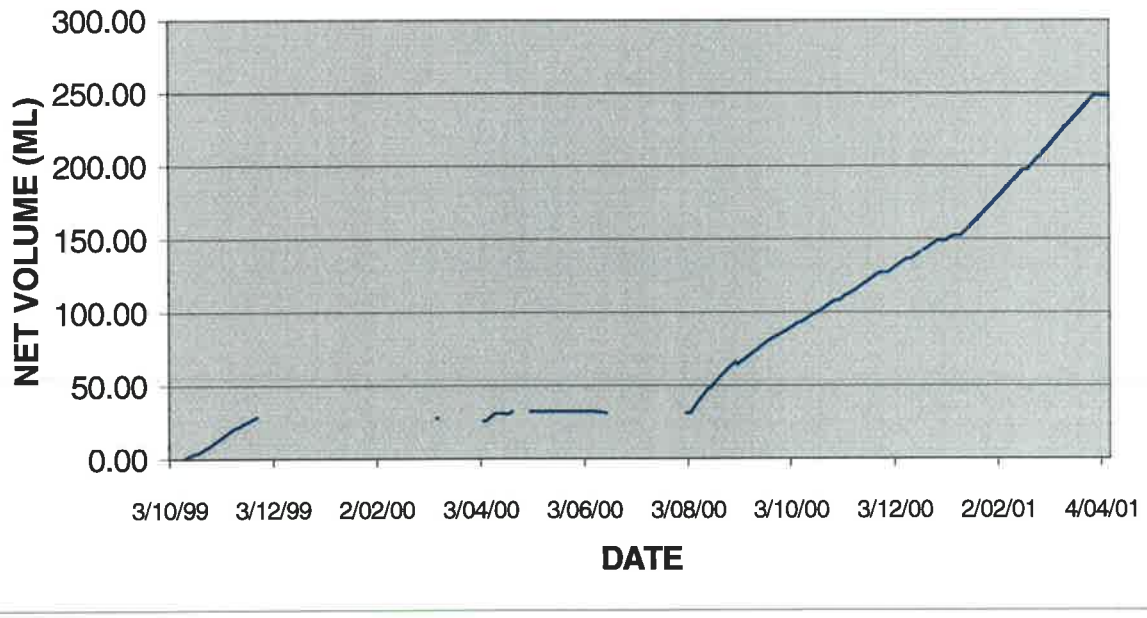

The freshwater injection at the Bolivar site in phase I commenced on October 11 and stopped on November 23, 1999. It lasted about 6 weeks.

Three crosshole tomographic surveys were done in Phase I at different stages of the water injection. Figure 10.3 shows the survey dates and water injection progress in the period. The first survey was done from 2/9/99 to 5/9/99, about 5 weeks before the water injection. The second survey was completed from 31/10/99 to 3/11/99, about three weeks after the water injection started. The last survey in this phase was done from 22/1/2000 to 25/1/2000, about 8 weeks after the water injection ceased.

Figure 10.3 Three survey dates overlain with the water injection progress graph.

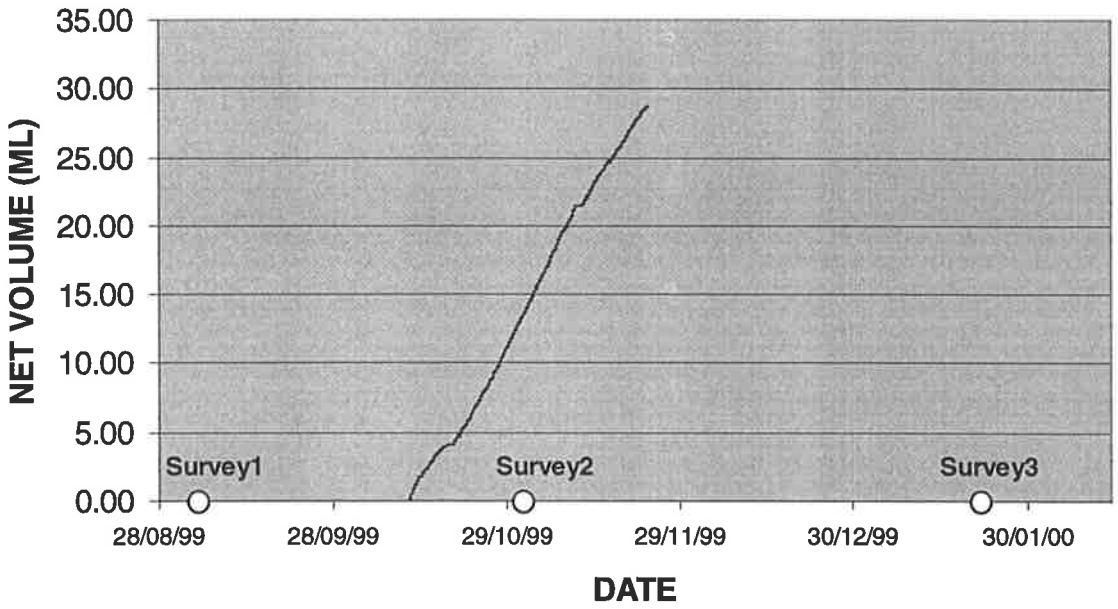

10.2 DATA ACQUISITION

10.2.1 Survey Configuration

In the first phase, we did not use the central observation well (19450) due to the occupation of another instrument in this well. We used 4 wells on the circumference of a circle of radius 75 meters. Three separate surveys were conducted in Phase I and for each survey we completed four crosshole multiple scannings involving the four chords between pairs of adjacent boreholes (19445 & 19444, 19444 & 19442, 19442 & 19443, and 19443 & 19445), as shown in Figure 10.4.

The same survey configuration and procedure was used in all three surveys in phase I. The distance between any two adjacent observation wells is 106m, as shown in Figure 10.4. The

available depth access range in all wells for the resistivity surveys is 54m, from 102m to 156m depths.

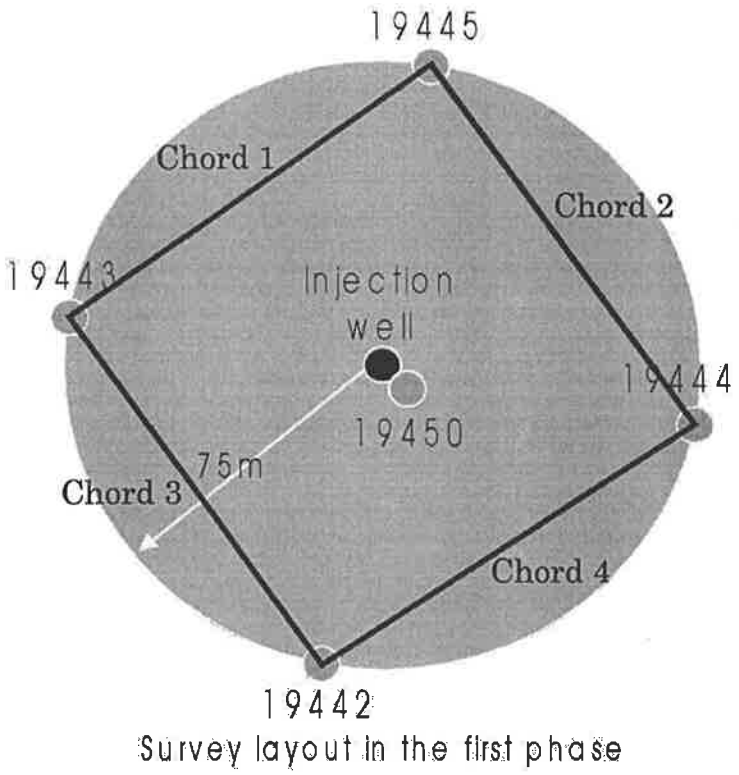

Figure 10.4 The surface layout of the cross well resistivity surveys. Four cross well resistivity multiple scannings, on chords 1, 2, 3 and 4, were conducted in each survey in Phase I.

For crosshole data acquisition, there are some specified three- and four-electrode configurations or arrays available for resistivity tomography (Zhou and Greenhalgh, 2000a). These configurations have distinctive merits in field measurement over the more common pole-pole electrode array. They can yield a satisfactory image with inversion processing. Specifically, the crosshole bipole-bipole *AM-BN* configuration (one current electrode *A* and one potential electrode *M* at a spacing *a* are set up in one borehole and another current electrode *B* and potential electrode *N* with the same spacing a are located in the other borehole) has the following advantages:

1. a current electrode placed in each borehole ensures that the current flows though the inter-well space of interest and that the signal levels are high;
2. with no requirement of using remote electrodes there is far less noise pick up;
3. it completely satisfies reciprocity;
4. it provides adjustable sensitivity with different electrode spacings a;

5. there is no singularity problem in the calculation of apparent resistivity and
6. it leads to easy acquisition of field data in build-up areas.

Therefore the crosshole bipole-bipole *AM-BN* configuration was employed in all crosshole surveys at the Bolivar site.

Another very important reason for using the bipole-bipole configuration was that we had to complete a few time-lapse surveys in a few months time, and any remote electrode placed on the surface could directly affect the resistivity changes of the area above the T2 aquifer (from a depth of 100m to the surface) into the survey data, eg. rainfall effect. This definitely makes the survey data interpretation more difficult. So we decided to use the bipole-bipole configuration for all crosshole resistivity surveys.

We built up two multi-electrode cables, one for each borehole. There are three electrodes on each cable, separated at 14m intervals, as shown in Figure 10.5. The bottom electrode is always used as a current electrode and the other two on each cable are used as potential electrodes. So for each depth position, we have one single current I measured between the two current electrodes A and B, and two potentials measured between M1 and N1 (14m interval from the current electrode), and between M2 and N2 (28m interval from the current electrode), respectively.

In each well, the access space is from 102m depth to 156m depth. So there are only 21 positions for AM=14m spacing (eg. A from 116m to 156m and M1 from 102m to 142m) and 14 positions for AM=28m spacing (eg. A from 130m to 156m and M2 from 102m to 128m) when the electrode depth measurement increment is 2 meters. It is the same for BN in the other borehole.

The crosshole multiple scanning method (refer to Section 7.4) was used in all surveys. So in total we obtained 21×21=441 data for the 14m spacing and 14×14=196 data for the 28m spacing in each single crosshole survey. The total number of data obtained is 637 potential measurements for each crosshole multiple scanning.

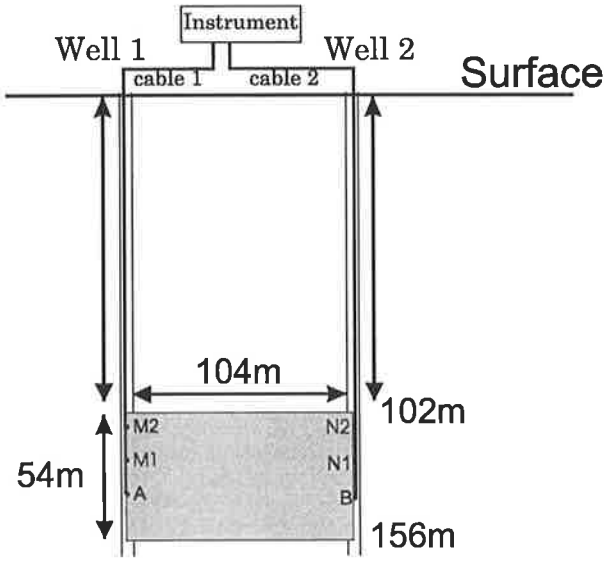

Figure 10.5 The cross section of the cross well resistivity multiscanning layout for all surveys in Phase I. A and B are current electrodes, and M1, M2, N1 and N2 are potential electrodes.

10.2.2 Survey Data

Three surveys were conducted in this phase and four crosshole multiple scannings were completed for each survey. So in total, 12 sets of crosshole multiple scanning data were obtained. As mentioned above, in each set of data, there are 441 data points for the 14m spacing and 196 data points for the 28m spacing.

In order to control the data quality, we repeated the readings at a few different depths by using the same supply voltage, changing supply voltage or swap the current and potential electrodes during the surveys to check the reading repeatibity and reciprocity. The maximum errors of reading repeatibity and reciprocity are 3% and the average errors are smaller than 2%for the three surveys.

For demonstration purposes, the part of the survey data between Well 19442 and 19443 in the first survey of Phase I are listed in Table 10.1 for 14m spacing, and in Table 10.2 for 28m spacing, respectively. From the tables, one can easily understand the operation procedure of the crosshole multiple scanning method since the depth positions of all four electrodes are listed in the tables. Voltage (mV) and current (mA) are recorded for each data point. Then apparent resistivity can be calculated from the data in the tables for each point, using formulas given in Chapter 2. All other crosshole survey data will not be displayed here due to space limitations.

Table 10.1 The resistivity survey data (14m separation) between Well 19442 and Well 19443 in the first survey. C1, P1, C2 and P2 are the depths of four electrodes.

No.	P1 (m)	C1 (m)	P2 (m)	C2 (m)	Potential (mV)	Current (mA)
1	142	156	142	156	161.3	1451.5
2	142	156	140	154	166.3	1449.7
3	142	156	138	152	165	1447.2
4	142	156	136	150	168.8	1470.6
5	142	156	134	148	171.1	1452.4
6	142	156	132	146	175.8	1451.1
7	142	156	130	144	185.2	1411.1
8	142	156	128	142	173.4	1396.1
9	142	156	126	140	172.2	1440
10	142	156	124	138	172.8	1425.6
11	142	156	122	136	172.4	1410.4
12	142	156	120	134	176.6	1401.2
13	142	156	118	132	174.5	1413.3
14	142	156	116	130	191.8	1413.9
15	142	156	114	128	203.9	1422.2
16	142	156	112	126	197.6	1414.6
17	142	156	110	124	197.7	1387.7
18	142	156	108	122	197.7	1427.4
19	142	156	106	120	201.8	1365.4
20	142	156	104	118	206	1357.9
21	142	156	102	116	207.7	1364.4
22	140	154	102	116	210.4	1360
23	140	154	104	118	211.9	1363.7
24	140	154	106	120	206.5	1356.6
25	140	154	108	122	203.7	1425.3
26	140	154	110	124	204.9	1390.3
27	140	154	112	126	205.7	1402.1
28	140	154	114	128	210.4	1399.2
29	140	154	116	130	204.9	1376
30	140	154	118	132	184.5	1398.3
31	140	154	120	134	183.6	1396.1
32	140	154	122	136	184.1	1408.6
33	140	154	124	138	184.5	1420.7
34	140	154	126	140	183.8	1428.3
35	140	154	128	142	185	1379.5
36	140	154	130	144	197.7	1406.7
37	140	154	132	146	188.3	1435.3
38	140	154	134	148	181	1428.1
39	140	154	136	150	181.6	1446.7
40	140	154	138	152	180.4	1441.2
41	140	154	140	154	184.3	1434.5
42	140	154	142	156	180.4	1426.5
43	138	152	142	156	183.6	1425
44	138	152	140	154	186.8	1424.7
45	138	152	138	152	184	1434.2
46	138	152	136	150	186.5	1443.4
47	138	152	134	148	187.5	1431.2
48	138	152	132	146	193.2	1438.2
49	138	152	130	144	200.3	1446.5
50	138	152	128	142	196.6	1389.8

51	138	152	126	140	190.2	1442.7
52	138	152	124	138	192.2	1436
53	138	152	122	136	190.2	1385.6
54	138	152	120	134	191.4	1405.6
55	138	152	118	132	191.5	1400.4
56	138	152	116	130	212.8	1373.3
57	138	152	114	128	214	1396.2
58	138	152	112	126	210.6	1406.6
59	138	152	110	124	210.3	1382.2
60	138	152	108	122	209.7	1417.3
61	138	152	106	120	214.1	1355.2
62	138	152	104	118	218.4	1356.2
63	138	152	102	116	219.7	1355.5
64	136	150	102	116	217.2	1344.8
65	136	150	104	118	217.3	1342.3
66	136	150	106	120	211.9	1344.3
67	136	150	108	122	208.5	1404.1
68	136	150	110	124	208.3	1375.2
69	136	150	112	126	209.5	1385
70	136	150	114	128	216.4	1395.1
71	136	150	116	130	212.2	1381.1
72	136	150	118	132	190.6	1369.3
73	136	150	120	134	189.7	1383.9
74	136	150	122	136	190.2	1375
75	136	150	124	138	191.3	1420.3
76	136	150	126	140	189.1	1426.8
77	136	150	128	142	193.9	1365.9
78	136	150	130	144	200.5	1424.3
79	136	150	132	146	192.7	1429.8
80	136	150	134	148	185.1	1420.1
...	...	...	...	...	...	...
...	...	...	...	...	...	...
410	104	118	122	136	211.6	1361.6
411	104	118	124	138	213.1	1359.2
412	104	118	126	140	212.1	1372.5
413	104	118	128	142	221.1	1312.3
414	104	118	130	144	219.7	1363.5
415	104	118	132	146	214.2	1343.6
416	104	118	134	148	209	1373.5
417	104	118	136	150	210.6	1342.9
418	104	118	138	152	206.2	1361.6
419	104	118	140	154	209.7	1364.2
420	104	118	142	156	205.5	1364.2
421	102	116	142	156	202.5	1337.4
422	102	116	140	154	204.3	1332.9
423	102	116	138	152	203.2	1309.3
424	102	116	136	150	207.6	1312
425	102	116	134	148	203.7	1351.4
426	102	116	132	146	211.1	1315.3
427	102	116	130	144	219.3	1334.2
428	102	116	128	142	214.6	1285.3
429	102	116	126	140	204.2	1341.9
430	102	116	124	138	210.1	1344.7

431	102	116	122	136	207	1341.6
432	102	116	120	134	208	1320.3
433	102	116	118	132	206	1312.6
434	102	116	116	130	210.4	1321.2
435	102	116	114	128	230.2	1320.2
436	102	116	112	126	221.5	1316.2
437	102	116	110	124	224.1	1326.6
438	102	116	108	122	224.4	1310.6
439	102	116	106	120	225.7	1324.4
440	102	116	104	118	230.2	1262.4
441	102	116	102	116	230.3	1270.1

Table 10.2 The resistivity survey data (28m separation) between Well 19442 and Well 19443 in the first survey. C1, P1, C2 and P2 are the depths of four electrodes.

No.	P1 (m)	C1 (m)	P2 (m)	C2 (m)	Potential (mV)	Current (mA)
1	128	156	128	156	40.8	817.8
2	128	156	126	154	41	830.6
3	128	156	124	152	40.7	817.3
4	128	156	122	150	40.8	810.3
5	128	156	120	148	40.8	816.2
6	128	156	118	146	41.1	815.9
7	128	156	116	144	42.1	815.3
8	128	156	114	142	41.6	800.8
9	128	156	112	140	42.2	816.5
10	128	156	110	138	42.4	824.1
11	128	156	108	136	41.2	811.3
12	128	156	106	134	41.5	816.2
13	128	156	104	132	38.7	750.2
14	128	156	102	130	40.3	778.5
15	126	154	102	130	40.8	777.2
16	126	154	104	132	38.7	746
17	126	154	106	134	41.7	809.7
18	126	154	108	136	41.6	806.6
19	126	154	110	138	42.5	813.4
20	126	154	112	140	42.6	814.2
21	126	154	114	142	41.7	796.5
22	126	154	116	144	42	808.5
23	126	154	118	146	41.3	810.4
24	126	154	120	148	41.1	808.2
25	126	154	122	150	40.6	798.9
26	126	154	124	152	41.1	819.4
27	126	154	126	154	40.9	820.1
28	126	154	128	156	40.4	804.6
29	124	152	128	156	40.9	800
30	124	152	126	154	40.9	813.2
31	124	152	124	152	40.9	804.7
32	124	152	122	150	41.1	800.5
33	124	152	120	148	41	798.6
34	124	152	118	146	41.1	801
35	124	152	116	144	41.8	790.6
36	124	152	114	142	42	794.9
37	124	152	112	140	41.8	793.9

38	124	152	110	138	42.3	806
39	124	152	108	136	41.4	795.8
40	124	152	106	134	41.6	799.1
41	124	152	104	132	38.7	738.6
42	124	152	102	130	40.6	763.8
43	122	150	102	130	40.8	771.2
44	122	150	104	132	38.9	746.5
45	122	150	106	134	41.4	800.9
46	122	150	108	136	41.3	796.7
47	122	150	110	138	42.4	807.8
48	122	150	112	140	42.1	800.9
49	122	150	114	142	42.1	797.3
50	122	150	116	144	42	807.2
51	122	150	118	146	41.4	807.3
52	122	150	120	148	41.3	807.2
53	122	150	122	150	40.9	800.2
54	122	150	124	152	41.2	816.2
55	122	150	126	154	41	815.9
56	122	150	128	156	41	802.5
57	120	148	128	156	41	799.4
58	120	148	126	154	41.3	809.5
59	120	148	124	152	41.2	808.3
60	120	148	122	150	41.1	799.9
61	120	148	120	148	41.1	796.7
62	120	148	118	146	41.5	804.7
63	120	148	116	144	42.4	801.7
64	120	148	114	142	42.1	791.7
65	120	148	112	140	42.2	796.2
66	120	148	110	138	42.1	800.1
...	...	...	...	...	...	...
...	...	...	...	...	...	...
170	104	132	126	154	40.3	797.5
171	104	132	124	152	40.3	792.7
172	104	132	122	150	40.8	790
173	104	132	120	148	40.1	782.4
174	104	132	118	146	40.4	782.7
175	104	132	116	144	41.3	786.6
176	104	132	114	142	41	770
177	104	132	112	140	41.3	783.3
178	104	132	110	138	41.2	783.8
179	104	132	108	136	40.6	778.6
180	104	132	106	134	40.7	784.7
181	104	132	104	132	38	728.3
182	104	132	102	130	39.2	747.3
183	102	130	102	130	40.4	724.7
184	102	130	104	132	39.4	710.7
185	102	130	106	134	41.9	759.2
186	102	130	108	136	42.3	761.7
187	102	130	110	138	43.1	771.7
188	102	130	112	140	42.8	764.4
189	102	130	114	142	42.5	749.3
190	102	130	116	144	42.3	759.2
191	102	130	118	146	41.6	758.5

192	102	130	120	148	41.7	760.2
193	102	130	122	150	41.9	764
194	102	130	124	152	41.6	766.7
195	102	130	126	154	41.5	768.5
196	102	130	128	156	41.7	758.6

For the surface resistivity survey, the data can be displayed in the form of a pseudosection. One can obtain a lot of information from the pseudosection, even without modelling and inversion. However for borehole survey data, it is hard to display the survey data properly and to link the electric response with the subsurface geology. In other words, after the electric responses (potential and current) are obtained in a crosshole survey, the question arises: where do you place the data on a 2-D map? This has greatly limited the use of the electric resistivity method in borehole surveys. Currently the only solution is to undertake a geophysical inversion.

Before inversion, we need to check the survey data and to do some preliminary analyses on data. So we introduced a 2-D display method to illustrate all survey data for each set of crosshole multiple scanning data. We call it a 2-D **pseudo depth profile** for the bipole-bipole configuration, since both axes in the profile represent depths. The pseudo depth profile is explained in detail below.

Four sets of measured currents and potentials of the third survey in Phase I for the 14m spacing are shown in **pseudo depth profile format** in Figures 10.6 and 10.7, respectively. The horizontal axis is the depth of one electrode (current or potential electrode) in one well and the numbers on the right for each of the profiles are the depths of the corresponding electrode in the other well. For example, in diagram (a) of Figure 10.7, the horizontal axis shows the depth of the POTENTIAL electrode M1 in well 19444 and the numbers on the right side of the profiles shows the depths of the POTENTIAL electrode N1 in well 19442. But in diagram (b) of Figure 10.6, the horizontal axis shows the depth of the CURRENT electrode A in well 19444 and the numbers on the right side of the profiles shows the depths of the CURRENT electrode B in well 19442. The scale of the profiles in each graph is shown on the top the graph. But each profile on the graph is separated by a small amount in the vertical direction from its adjacent profiles in order to show all profiles clearly on the one graph. This 2-D pseudo depth profile does not show the absolute variable value of each data point, but rather shows the relative variable change along profile or depth.

After the measured current and potential are obtained, the apparent resistivity can be calculated with formula (2.15A), to remove the electrode geometry and current factors. Then the apparent resistivity can be displayed in the pseudo depth profile format as used for the current and potential data. Figure 10.8 shows the calculated apparent resistivity pseudo depth profiles of the third survey in Phase I at the 14m spacing.

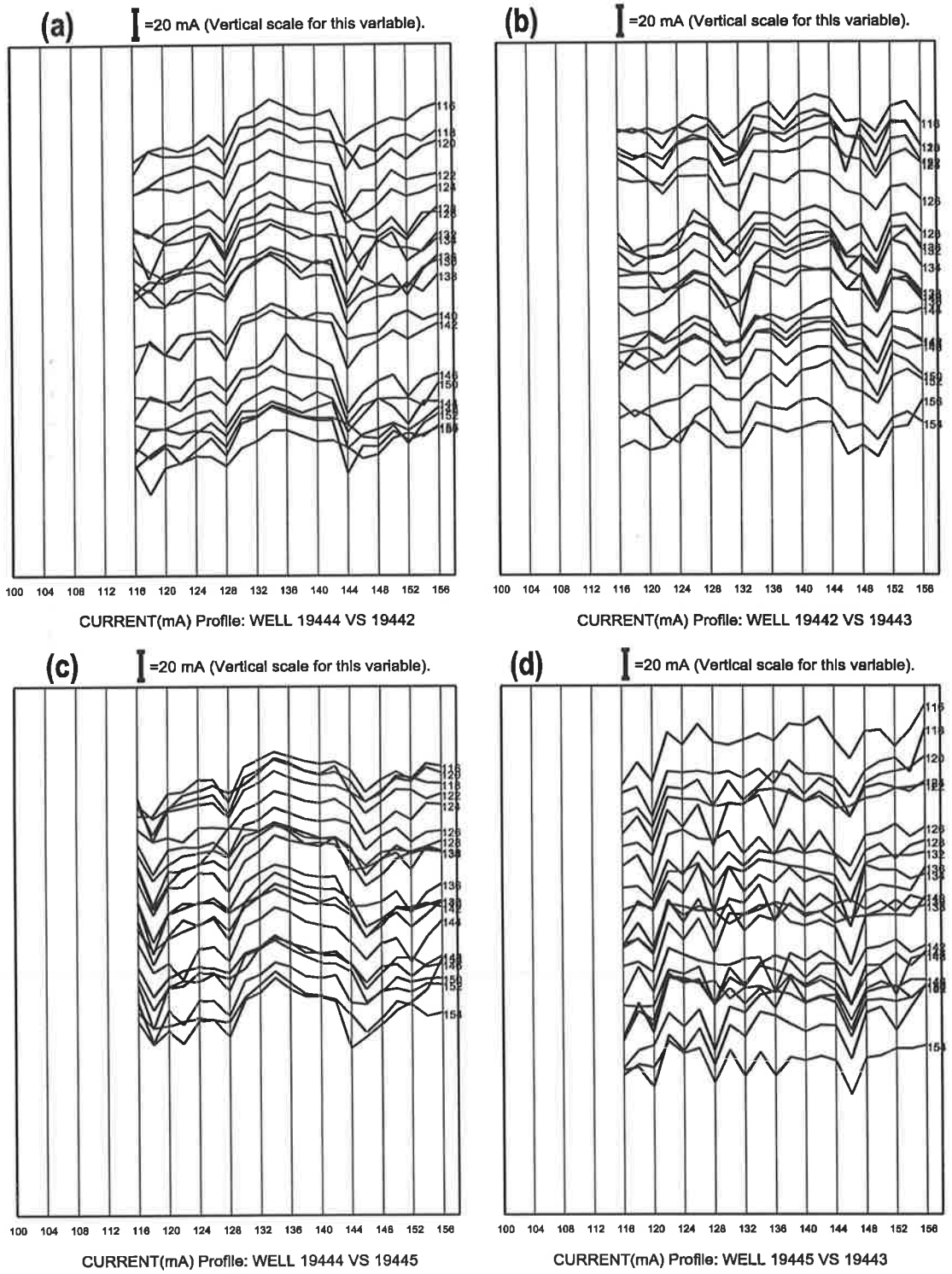

Figure 10.6 The currect pseudo depth profiles (14m separation) of the third crosshole resistivity survey in Phase I.

Note that the data point positioning is not the same as in the current and potential data display. Because there are four depth positions (A, B, M and N) for each apparent resistivity

calculation and there are only two depth axes in the pseudo depth profile, we have to reduce the four depth positions into two by picking the mid-point of the two electrodes in each well as the display depth. So the horizontal axis of the apparent resistivity pseudo depth profiles is for the mid-point of electrodes A and M1 and the numbers on the right hand side of profile are for the mid-point of electrodes B and N1.

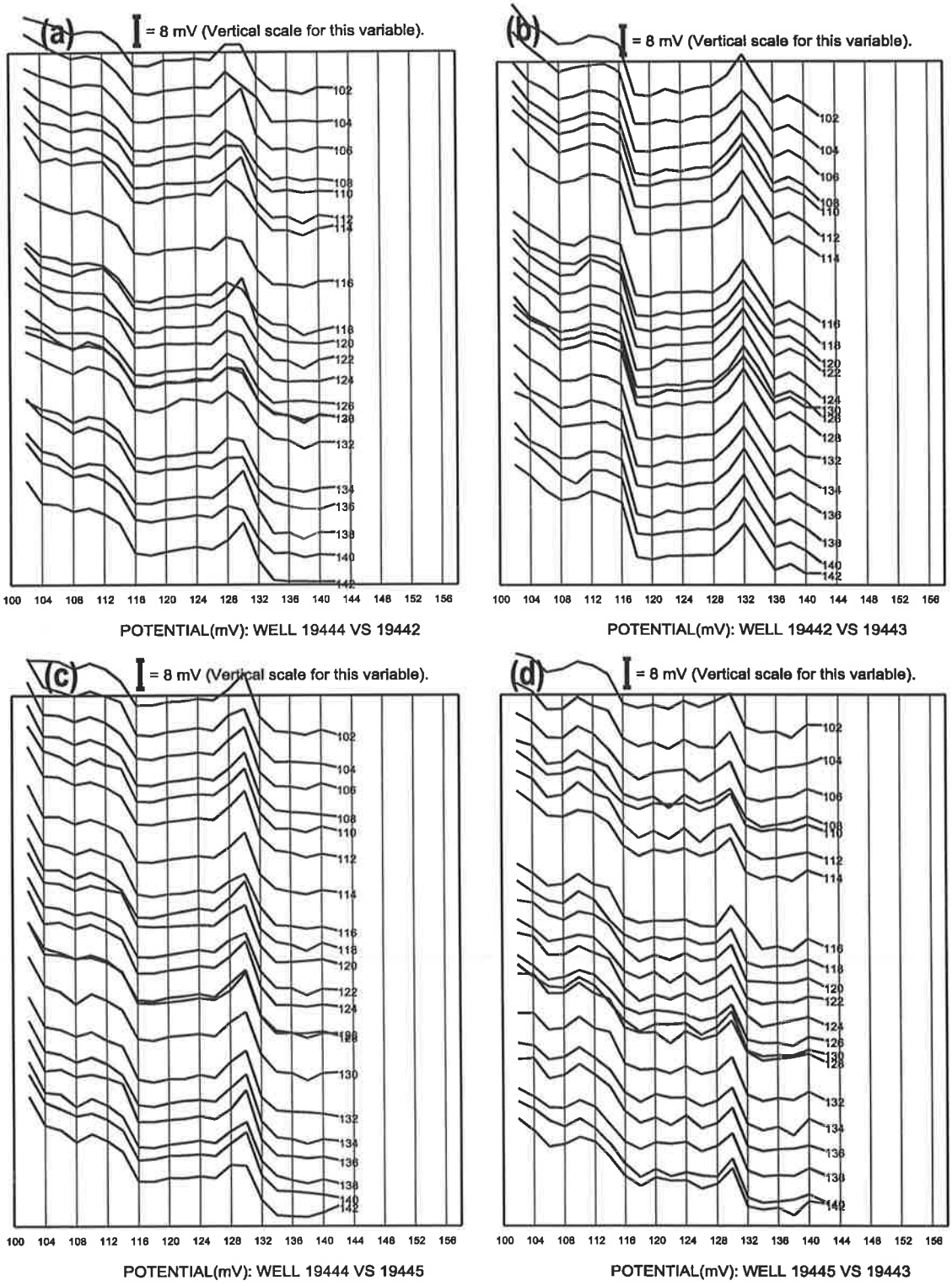

Figure 10.7 The potential pseudo depth profiles (14m separation) of the third crosshole survey in Phase I.

From Figure 10.6 and Figure 10.7, one can see that the current and potential profiles are not very stable. This may be caused by some random factors, such as battery voltage, local contact of electrodes, and so on. But the ratio between potential measurement and current measurement is stable, since the potential difference between potential electrodes M and N is mainly affected by the injected current and the resistivity distribution in the subsurface.

In other words, if the resistivity distribution in the sub-surface remains unchanged, increasing the current level will raise the potential proportionately. This is the reason that the calculated apparent resistivity profiles, as shown in Figure 10.8, looks much more stable than the potential and current profiles.

All three kinds of pseudo depth profiles: current, potential and apparent resistivity profiles, can be used to check data quality and complete some preliminary interpretation. This is why I produced the profiles. The next section will explain how I use the profiles to complete some of my interpretations.

From the above figures, one can see the profile change pattern along the horizontal axis (depths in one well). This pattern clearly shows the relative variable change near one well. For example, in Figure 10.7 (a), the potential values suddenly decrease in all profiles at a depth of 116m (horizontal axis of the figure). This means the resistivity at that position of the well 19442 suddenly changes. However, it is hard to see the pattern in the other well from the above figures. So we swapped the two depth axes to show the profile patterns in the other well. Figure 10.9 shows the swapped result of Figure 10.7. Now we can see the potential change pattern in the other well. By comparing Figure 10.7 with Figure 10.9, one can see that the variable change patterns in the two figures are different since they show the potential pattern changes in the different wells. For example, graph (a) in Figure 10.7 shows the potential change pattern in well 19444; graph (a) in Figure 10.9 shows potential change pattern in well 19442, although they are the same set of data.

For this reason, we can swap the two depth axes in all pseudo depth profiles to show the change pattern in different wells.

As mentioned earlier, 12 (3x4) sets of crosshole multiple scanning results were obtained (two different spacing in each scanning) in Phase I. So there are in total 72 (12 sets x 3 variables x 2spacing) pseudo depth profiles for potential, current and apparent resistivity respectively. To

save space, I only show some representative pseudo depth profiles here.

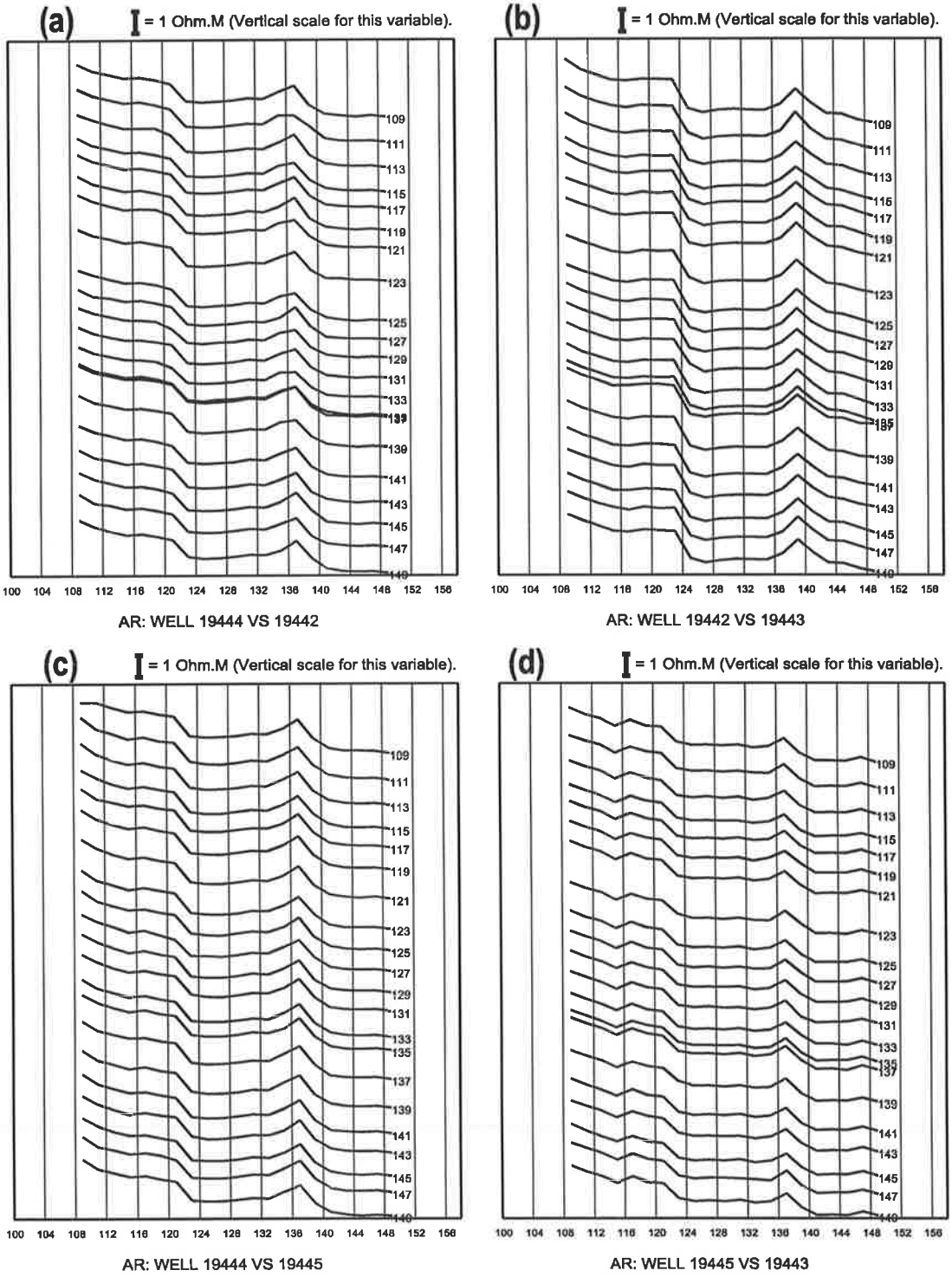

Figure 10.8 The AR pseudo depth profiles (14m separation) of the third crosshole survey in Phase I.

In some pseudo depth profiles, the sudden changes in the potential and current profiles can be seen, for example in (a) and (b) of Figure 10.10. These sudden changes in profiles are due to battery changes. After a battery was changed, the output voltage from both the new battery and the power booster are normally higher and the output current follows as well. The

measured potential goes up too. However, the calculated apparent resistivity removes most of the effect. From the apparent resistivity profile (calculated from the data on the above figures) shown in (c) of Figure 10.10, it is hard to see the sudden jump due to the battery voltage change. However relative more dynamic changes in each apparent resistivity profile are shown in the figures.

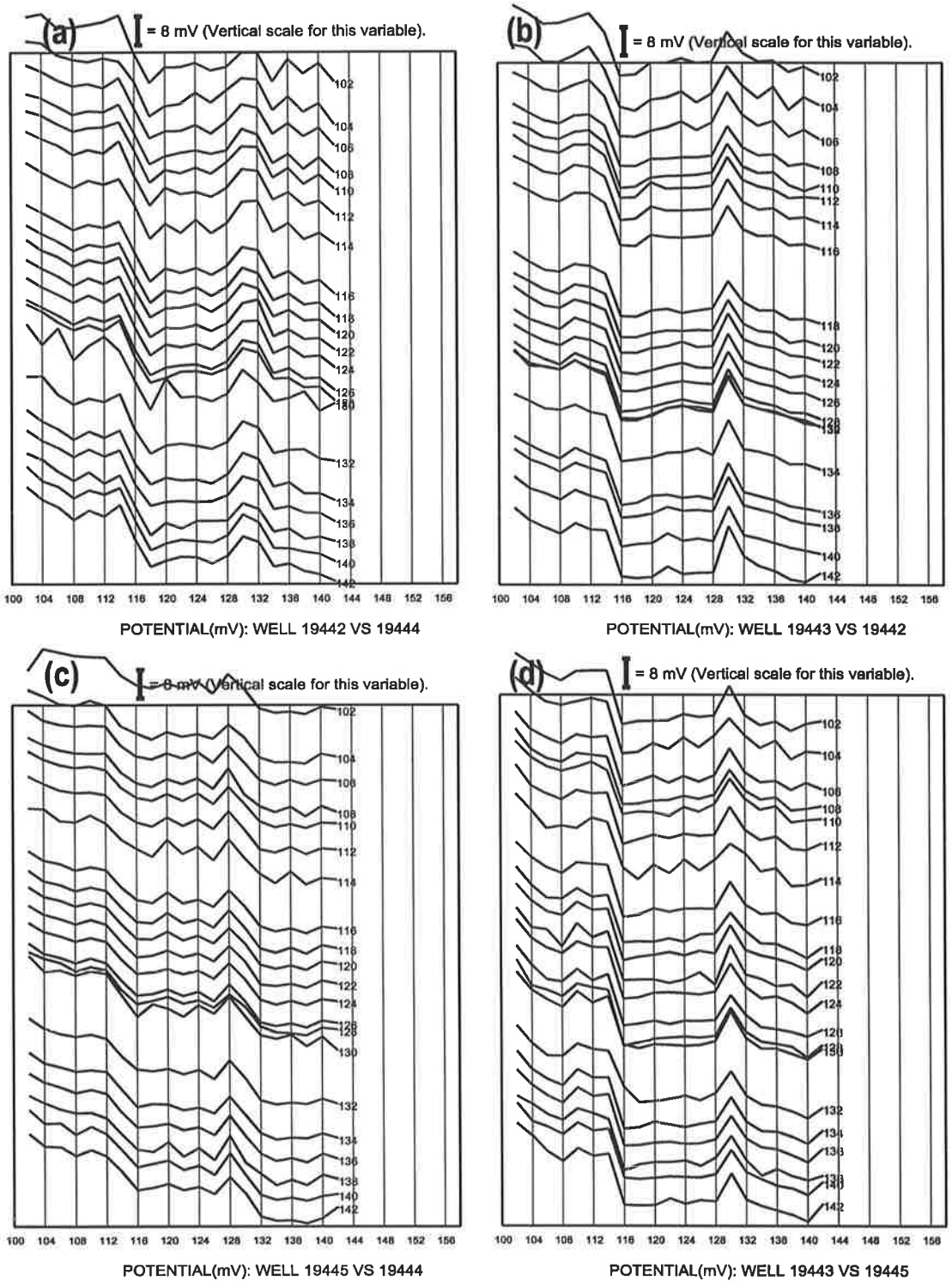

Figure 10.9 The potential pseudo depth profiles (14m separation) of the third crosshole survey in Phase I. The horizontal axis vs vertical axis in the figure is just the opposite to that in Figure 10.7.

From these pseudo profiles, we see that most of potential data have a downward trend with depth, while the current data have an upward trend with depth. Both trends show the resistivity distribution in this range decreases with depth.

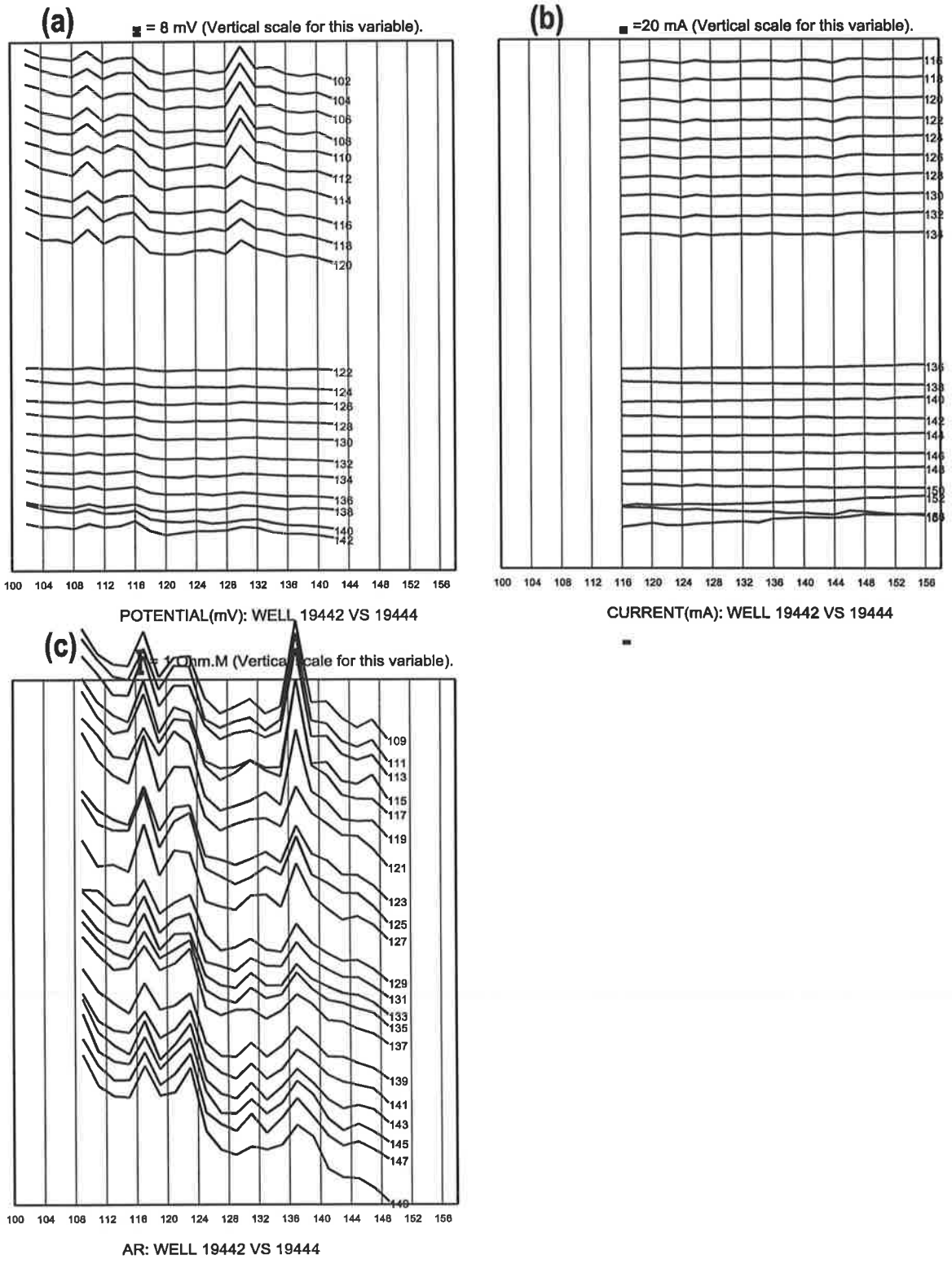

Figure 10.10 One set of pseudo depth profiles (14m separation) of the first crosshole survey.

In order to control the data quality, we repeated the readings by changing the supply voltage or checked the readings by reciprocity during the measurements. The maximum error is 3% for the three sets of data.

10.3 INTERPRETATION

A 2.5-D FEM resistivity forward modelling and inversion program was developed for some tests on crosshole imaging (see Chapters 3 and 4). The program is very good and an important tool for interpreting the resistivity crosshole survey data, as shown in the latter sections. Besides the program, a few new analysis techniques are developed for interpreting the crosshole survey data.

I classify the ways I used to interpret the resistivity data into three methods. The first one is to compare and analyse the potential, current and the calculated apparent resistivity (from the crosshole multiple scanning data) directly. The second one is to calculate the 3-D resistivity distribution from the scanning data, using our newly developed 3-D resistivity imaging program (Zhou & Greenhalgh, 2001). The last method is 2.5-D resistivity inversion. All these methods will be discussed in detail in the following sections.

10.3.1 What Resistivity Change Do We Expect After Higher Resistivity Water Is Injected into the Aquifer?

From laboratory and borehole electric measurements (Pavilic, 2000), we know that the resistivity of the underground water is about 2.7Ωm and that of the injected reclaimed water is about 4.63Ωm. The ratio between the two is 4.63/2.7=1.71. This means that the average resistivity of the T2 aquifer will definitely increase after the reclaimed water is injected into it. This is the basic idea used to interpret the resistivity survey data.

To understand the effect of the injected water, many numerical resistivity modelling and inversion experiments have been done to simulate the resistivity survey response of the higher resistivity water injection in Phase I. The details of the numerical experiments and conclusions are given in Chapter 8.

From Chapter 8, we know that the injected relative higher resistivity water definitely causes an observable AR increase in the resistivity crosshole multiple scanning surveys. However the AR increase rate is small, less than 10% on average, until just before the injected water reaches the two survey wells. Specifically, the increase rate for the 14m separation is about

5% on average only. So it may be very hard to pick up these apparent resistivity changes in a practical survey since many other factors may affect the survey data.

From the inversion results of the numerical forward modelling data, it can be seen that the resistivity distribution near both boreholes can normally be recovered with the 14m and 28m configurations. But the resistivity distribution in the middle part between the two wells is not very clear because of the limitation of the number of the survey data and the restricted survey geometry. So keep in mind that the inversion results from the survey data may not be that reliable due to the above reasons.

From Figure 10.2, we know that only 35ML of reclaimed water had been injected into T2 aquifer in Phase I. From the cores we obtained from the drilling, we know that the average porosity in the T2 aquifer is about 0.45. I assume the height of the T2 aquifer is about 60m. So I produced the following Table 10.3 to predict the minimum radius the injected fresh water can expand into from the central injection well after the 35ML water was injected, assuming simple cylindrical spreading. From the table, the injected water may reach a maximum radius of 61m from the injection well. So we assume that the injected fresh water can not reach the four observation wells situated on the circumference of a circle of radius 75 meters.

Table 10.3 The calculated minimum radius the injected fresh water can expend to from the central injection well after the 35ML water was injected.

Volume(m3)	Height(m)	Porosity	Minimum R (m)
35000	60	0.1	43.10
35000	60	0.2	30.47
35000	60	0.3	24.88
35000	60	0.4	21.55
35000	60	0.5	19.27
35000	50	0.1	47.21
35000	50	0.2	33.38
35000	50	0.5	21.11
35000	50	0.4	23.61
35000	50	0.5	21.11
35000	40	0.3	30.47
35000	40	0.4	26.39
35000	40	0.5	23.60
35000	40	0.4	26.39
35000	40	0.5	23.60
35000	30	0.1	60.95
35000	30	0.2	43.10
35000	30	0.3	35.19

35000	30	0.4	30.47
35000	30	0.5	27.25

10.3.2 Direct Method

The direct method interprets the observed current, potential and calculated apparent resistivity by analysing the data profiles and comparing the profiles with the simple numerical modelling result to obtain a preliminary resistivity distribution image for the survey area. This method is partially based on understanding of some simple numerical modelling results.

10.3.2.1 Turning point and profile patterns

From the test results described in Section 8.2.1, all resistivity interfaces between two resistivity layers will cause sudden value changes in current and potential measurements. These experiments also show that the potential and current response curves will be continuous profiles if the resistivity distribution is uniform or smoothly changing. Therefore by finding the sudden turning points in the measured potential and current profiles, one can identify resistivity interfaces easily. Take Figure 10.11 (the potential profiles and current profiles between Wells 19442 and 19443) as an example. In both graphs, one can see a sharp turning point at depth 132m on the horizontal axis. This means that there is resistivity interface in the vicinity of this depth.

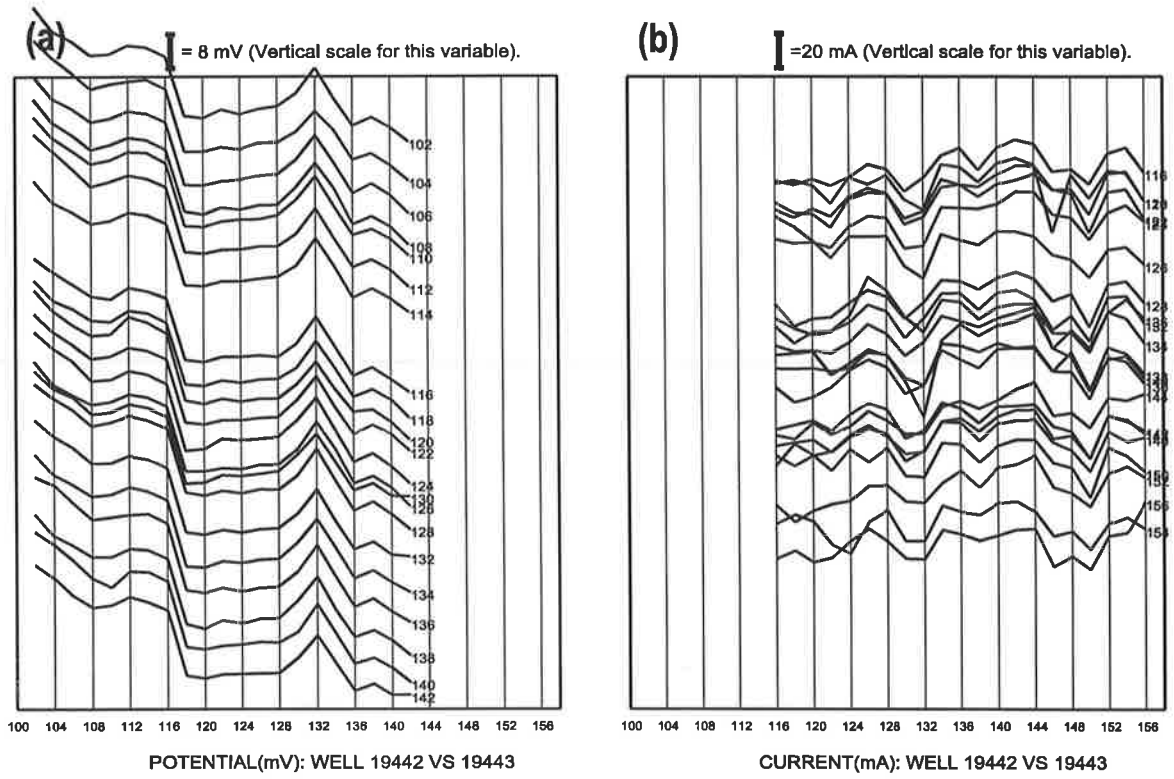

Figure 10.11 The pseudo depth potential and current profiles (14m spacing) between Wells 19442 and 19443 of the third crosshole survey.

As mentioned in chapter 7, if one pair of electrodes (for example. A and M) are fixed in one well and the another pair of electrodes (for example B and N) move from top to bottom in the second well, the apparent resistivity profile will mainly show the resistivity changes along the second well. Then if A and M are moved to another point and the above procedure repeated, another apparent resistivity profile can be obtained. These two profiles should be very similar in shape because they both mainly reflect the resistivity changes near the second well. Therefore, after a crosshole multiple scanning survey is complete, all potential profiles should have a similar shape and all current profiles should have a similar shape as well. This can be clearly seen from most of the potential and current pseudo depth profiles. But due to the complex practical situation, survey profiles may have some changes in shape. However, if all errors (or data noise) are random, by averaging all profiles in each data set, one can obtain a clear profile for a well.

In order to find these turning points easier, all profiles of potential and current variables in each set of multiple scanning data are summed to obtain a profile of average values according to the above principle. This average can reduce the noise effect and show the turning point more clearly. For instance, Figure 10.12 shows the average profiles of Figure 10.11. One can more easily pick up the turning points from Figure 10.12 than from Figure 10.11. From the figures, one can find a common turning point at a depth of about 130m in almost all profiles of the two figures. This proves two things: 1) there is a resistivity interface or a thin layer at this depth; 2) the geological structure in the T2 Aquifer is flat-lying, since all profiles have a similar pattern and the turning points in each profile are at similar depth positions.

By analysing all potential and current profiles (not included in the thesis for reason of space economy), there are at least two other very important turning points: one is at about depth 116m (from potential profiles) and one is at about 145m (from current profiles). Together with the turning point at about depth 130m, there are in total three turning points or resistivity interfaces. Comparing with the well logs shown in Figure 6.6, I find that the turning point positions match with the well logs.

The accuracy of the position of the resistivity interfaces from the turning point is very high since they are directly related to the electrode positions. The position of these resistivity interfaces or turning points are very important in setting up models for modelling and inversion.

Figure 10.12 The averaged profiles from the pseudo depth potential and current profiles shown in Figure 10.11.

10.3.2.2 Possible resistivity structure according to the modelling result

After the measured potential and current data were obtained, apparent resistivity data were calculated and plotted in pseudo depth profile format. From the pseudo depth apparent resistivity profiles (a sample of the many is given in Figure 10.10), we can see that all these profiles are pretty stable and less noisy, although the current data and some potential data are noisy. All turning points in the apparent resistivity profiles can not be used directly since the depth positions on the horizontal axis are the mid-point position of the two electrodes (potential and current electrodes in the same well). From all apparent resistivity profiles, one can see that the basic profile trend is a decreasing one. This means that the resistivity decreases with depth in the T2 Aquifer. This matches with the well log results (shown in Figure 6.6) and the electrical conductivity measurements (shown in Figure 6.8).

How to directly interpret the apparent resistivity profiles is a difficult task since no-one has (1) displayed apparent resistivity data like this before, (2) interpreted this kind of data before, and (3) completed this kind of experiment before.

From all these apparent resistivity profiles, I found a common pattern: three main 'continuously changed' segments (the first one is from depth 109 to 123m, the second is from

depth 125 to 133m and the last one is from depth 135 to 145m), as shown in Figure 10.13. Then we used our 2.5-D resistivity modelling program to simulate a three-layer model and tried to produce some matched apparent resistivity profiles. Since the middle segment in the apparent resistivity profiles is lower than the enclosing layers, I assumed the true resistivity in the middle layer to be the lowest in the three-layer sequence. The modelling result surprised me: the apparent resistivity profile pattern went the another way; the middle segment was higher. Then I changed the resistivity in the middle layer to be higher than layers either side and the program produced a very similar curve pattern (shown in Figure 3.11) to the field survey apparent resistivity profiles. For details on modelling parameters, please refer to Section 3.3.5.2. So from this modelling experiment, I suggest that there is a thin (about 2 to 3 metres thick) higher resistivity layer at about depth 130m.

The above features reflect vertical heterogeneity and imply the horizontally uniform resistivity structure of the T2-aquifer for the Bolivar site.

10.3.2.3 Apparent resistivity relative change between surveys

By using the above two techniques, we can obtain some useful resistivity distribution information. However, our goal is to detect the flow paths of the injected fresh water. So we have to use the time-lapse surveys to find the resistivity distribution changes between the surveys. Then the flow paths of the injected fresh water can be deduced.

To find the injected fresh water flow paths, the calculated apparent resistivities from the measured data at the different stages have to be compared to delineate the apparent resistivity change in the different areas and depths. To achieve this, we first calculated the average apparent resistivity for each set of data and for each electrode separation spacing. For instance, I calculated the average apparent resistivities for the first set of data (Well 19444 vs 19442) in the first survey for the 14m spacing and the 28m spacing data, respectively. The two values are 17.8Ω.m and 12.1Ω.m respectively. Then the average relative change (ARC) of the average apparent resistivities between two time-sequential surveys for every crosshole multiple scanning data with different spacings were calculated. Table 10.4 shows the calculated average apparent resistivities and ARC for all crosshole scanning data in Phase I.

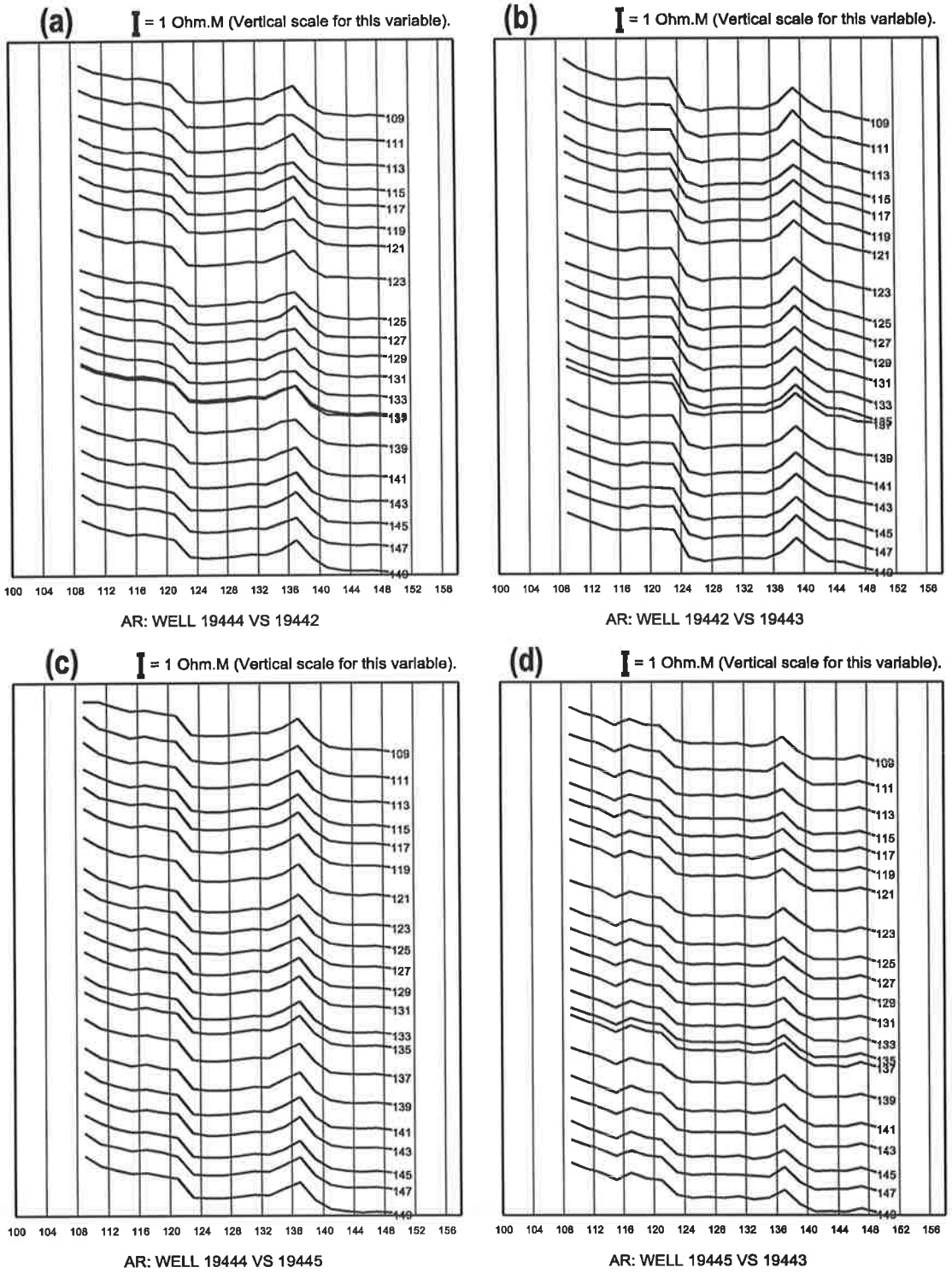

Figure 10.13 The pseudo depth AR profiles (14m spacing) of the third crosshole survey.

Table 10.4 The minimum, maximum, average apparent resistivity and the apparent resistivity relative change of the 3 time-lapse surveys in the first water injection phase. The apparent resistivity unit is Ohm.m.

Survey No.	Well 1 VS Well 2	Electrode Spacing	AR-MIN	AR-MAX	AR-MEAN	AR Increase (%)
1	Well 19444 VS 19442	14m	13.2	23.0	17.8	
1	Well 19442 VS 19443	14m	11.2	18.4	15.1	
1	Well 19444 VS 19445	14m	10.4	14.9	12.2	

1	Well 19445 VS 19443	14m	10.8	15.7	13.1	
2	Well 19444 VS 19442	14m	9.9	14.6	11.4	-35.6
2	Well 19442 VS 19443	14m	10.1	14.9	12.2	-19.0
2	Well 19444 VS 19445	14m	9.9	14.4	11.7	-3.4
2	Well 19445 VS 19443	14m	10.1	14.7	11.9	-8.8
3	Well 19444 VS 19442	14m	9.9	14.9	12.1	6.1
3	Well 19442 VS 19443	14m	10.2	15.4	12.3	1.0
3	Well 19444 VS 19445	14m	10.4	15.8	12.6	7.6
3	Well 19445 VS 19443	14m	10.6	15.5	12.5	5.0
1	Well 19444 VS 19442	28m	11.4	13.1	12.1	
1	Well 19442 VS 19443	28m	11.5	13.2	12.2	
1	Well 19444 VS 19445	28m	11.6	12.6	12.1	
1	Well 19445 VS 19443	28m	11.7	12.8	12.2	
2	Well 19444 VS 19442	28m	15.4	18.7	16.6	37.9
2	Well 19442 VS 19443	28m	13.7	16.8	15.1	24.1
2	Well 19444 VS 19445	28m	11.9	13.1	12.4	2.8
2	Well 19445 VS 19443	28m	13.0	15.3	14.1	15.6
3	Well 19444 VS 19442	28m	11.5	13.2	12.2	-26.4
3	Well 19442 VS 19443	28m	11.7	13.1	12.4	-18.0
3	Well 19444 VS 19445	28m	12.7	14.4	13.4	7.6
3	Well 19445 VS 19443	28m	12.0	13.6	12.7	-9.8

From the average apparent resistivities in the above table, we know that the range of the apparent resistivity in all these surveys is from about 10Ω.m to 20Ω.m. So the real resistivity distribution in the area should not differ very much from this range since the apparent resistivity is a kind of bulk effect of all resistivities in the volume under investigation. This helps us select the resistivity modelling parameters for the numerical modelling experiments.

As for surface resistivity surveying, the larger the distance between A and M or B and N, the deeper the penetration. The 14m spacing data normally show more local resistivity variations in the vicinity of the boreholes. But the 28m spacing data are more likely affected by changes in the interwell medium.

By analysing the average apparent resistivities (AAR) of the first survey in the table, it can be seen that the AARs for the 28m spacing are about 12Ω.m, but the AARs for the 14m spacing are in range from 12Ω.m to 17.8Ω.m, which is a little unusual compared with the data from the other two surveys in Phase I, since the AARs of the other two surveys (14m spacing) are much lower than those in the first survey. This may be due to the first survey being conducted just after the drilling of the four wells was finished. We know that the 14m

spacing data are more likely effected by local resistivity changes. Any material used in the drilling procedure, such as water or acid, may change the local resistivity distribution. So the reliability of the first survey (14m spacing) data is in doubt, especially for the first two crosshole multiple scannings.

By comparing the AARs between the first survey and the second survey, one can find that the AARs for the 14m spacing data decrease from 3.5% to 36%, but the AARs for the 28m spacing data increase from 3% to 38%. This is matched with the borehole EC data (refer to Figure 6.10), which shows the electrical conductivity in the observation wells increases after water injection. This means that the survey data is satisfactory. The AAR increase for the 28m spacing is expected and is reasonable since the injected higher resistivity water should cause a resistivity increase in this area and the 28m spacing data is more sensitive to the resistivity change in the area further away from the observation wells.

However the AAR decrease for the 14m spacing is hard to interpret although we know the 14m spacing data is more sensitive to the resistivity change in the local area of the boreholes. From the numerical modeling experiments (refer to Chapter 8), we know that the apparent resistivity for both the 14m and 28m spacing should increase after higher resistivity water is injected. The water injection had possibly pushed the deep more saline and more conductive water in the observation wells upwards, causing the local resistivity decrease. This mostly reflects the movement of the saline groundwater and the local pressure change; both may cause the resistivity decrease. The large AAR decreases between Well 19444 and 19442, and between Well 19442 and 19443 are very possibly due to the drilling operations.

From the average relative change (ARC) percentage for the 28m spacing between the first and the second surveys, it can be seen that the three ARC percentages are over 15% and only one (Well 19444 VS 19445) is lower than 3%. This may imply that the injected water mainly went in three directions (southeast, southwest and northwest).

From the AARs of the first survey (before water injection) and the third survey (after 9 weeks of stopping the injection), it is clear that the 14m spacing AARs do not change much, but the 28m spacing AARs drop considerably. The AARs of the third survey drop to almost the same level as before water injection. This means that after the water injection stopped, the injected water mixed with the original underground water and the resistivity in the subsurface volume returned to the original level.

10.3.3 3-D Imaging Method

In order to obtain the basic resistivity distribution for the Bolivar site, we applied the 3-D approximate imaging method (Chapter 4) to all three surveys in Phase I. Two images were produced for each survey. The first one used all the 14m spacing and 28m spacing apparent resistivity data (in total, 2548 points) and the second one used only the 28m-spacing apparent resistivity data (in total, 784 points). Figure 10.14 shows all three imaging results for the three surveys with all 14m and 28m spacing data. Figure 10.15 shows all three imaging results for the three surveys with only the 28m spacing data. Three X-Y sections, at depth 102m, 128m and 156m respectively, are shown for each imaging result.

From the imaging results shown in Figure 10.14, one can see that the resistivity decreases almost anywhere with time or from one survey to other. This is true between the second survey and the third survey since the injected higher resistivity water may mix with the original underground water or flow to other regions after 9 weeks time. So the resistivity in the region became smaller. From the numerical modelling experiments shown in Chapter 8, we know that the resistivity in the region should go up after the higher resistivity water was injected. The resistivity change between two imaging results of the first survey and the second survey is a decrease. This does not match with our modelling experiments at all. However, from the statistical data shown in Table 10.4, it can be seen that the apparent resistivity of all the 14m spacing data between the first survey and the second survey went down, but the apparent resistivity of all the 28m spacing data between the two surveys went up. As we know, the 14m spacing data is mainly affected by the local resistivity change, but the 28m spacing data is more likely affected by resistivity changes remote from the borehole. As mentioned before, the first survey was completed just after the wells were drilled. So some of 14m spacing data of the first survey may be greatly affected by the local resistivity change produced by the drilling procedure. Also the number (1764 points) of the 14m spacing data points is many more than the number (784 points) of the 28m spacing data points. As such, the 14m spacing data may dominate the whole image results. Besides, we are more interested in the remote resistivity changes in this case, since the injected water can reach only about half way to the observation wells. So I removed the 14m spacing data and used only the 28m spacing data to complete another imaging experiment. The imaging results, shown in Figure 10.15, are very good.

From Figure 10.15, we can see that the resistivity in the region went up after the higher resistivity water was injected; then the resistivity decreases almost everywhere after the water injection stopped. The former is consistent with our modelling experiments and is reasonable.

From the imaging result of the first survey, it is clear that the resistivity in the whole region is almost uniform and about 12Ω.m. The resistivity in the northwest region is slightly higher than that in the southeast side. This is because the salinity concentration in the northwest is a little lower than that in the southeast (refer to Figure 6.4 for details). After the higher resistivity water was injected into the T2 Aquifer, the resistivity distribution had a large change. From the imaging result of the second survey, we can see that the resistivity increased dramatically in all directions except the northeast. This may imply that the injected water spread in all directions except the northeast. Keep in mind that the resistivity distribution near the observation wells is somewhat artificial.

From the above, we can see that the imaging results from only the 28m spacing data are more reliable and reasonable than the images from the 14m and the 28m spacing data combined.

10.3.4 2.5-D Inversion Method

From the above section, we know that the imaging method gives us the approximate or average resistivity distribution map, from which we can deduce the injected water flow direction horizontally. However, this map does not tell us through which layer (in the vertical succession) the injected water flows. Resistivity inversion can possibly resolve this problem.

In order to reveal the freshwater plume and flow paths, ideally, one should perform 3-D tomographic inversion (eg. Park 1998) based on the resistivity anomaly image. But for this case, it needs a huge computer resource for inverting the large number of data (each set has 2548 data) and in dealing with the large dimension of the site (200m × 200m × 160m, or 100 × 100 × 80 = 800000 cells as cell size is 2m × 2m × 2m). So it is still not a practical method. Hence a 2.5-D inversion program was developed and used (B. Zhou and S. Greenhalgh, 1999) for this project.

Based on the resistivity anomaly images, we implemented 2.5-D tomographical inversions with the field data. Theoretically, if the observed data contains enough sampling points and a good coverage for a target between boreholes, the tomographical reconstruction should involve a complete 2-D inversion—divide the crosshole section into small-size cells, then apply an inversion algorithm to reconstruct the 2-D resistivity model. But, in some cases, the defects of the data (limited coverage and noise contamination), may defeat the proper reconstruction of the small-size model. By the field data inversion experiments, we found that the 2-D model reconstruction showed poor horizontal resolution due to the limited data

coverage in the *xz*-plane and poor survey geometry configuration. This has been shown in my numerical forward modelling and inversion experiments in Chapter 8.

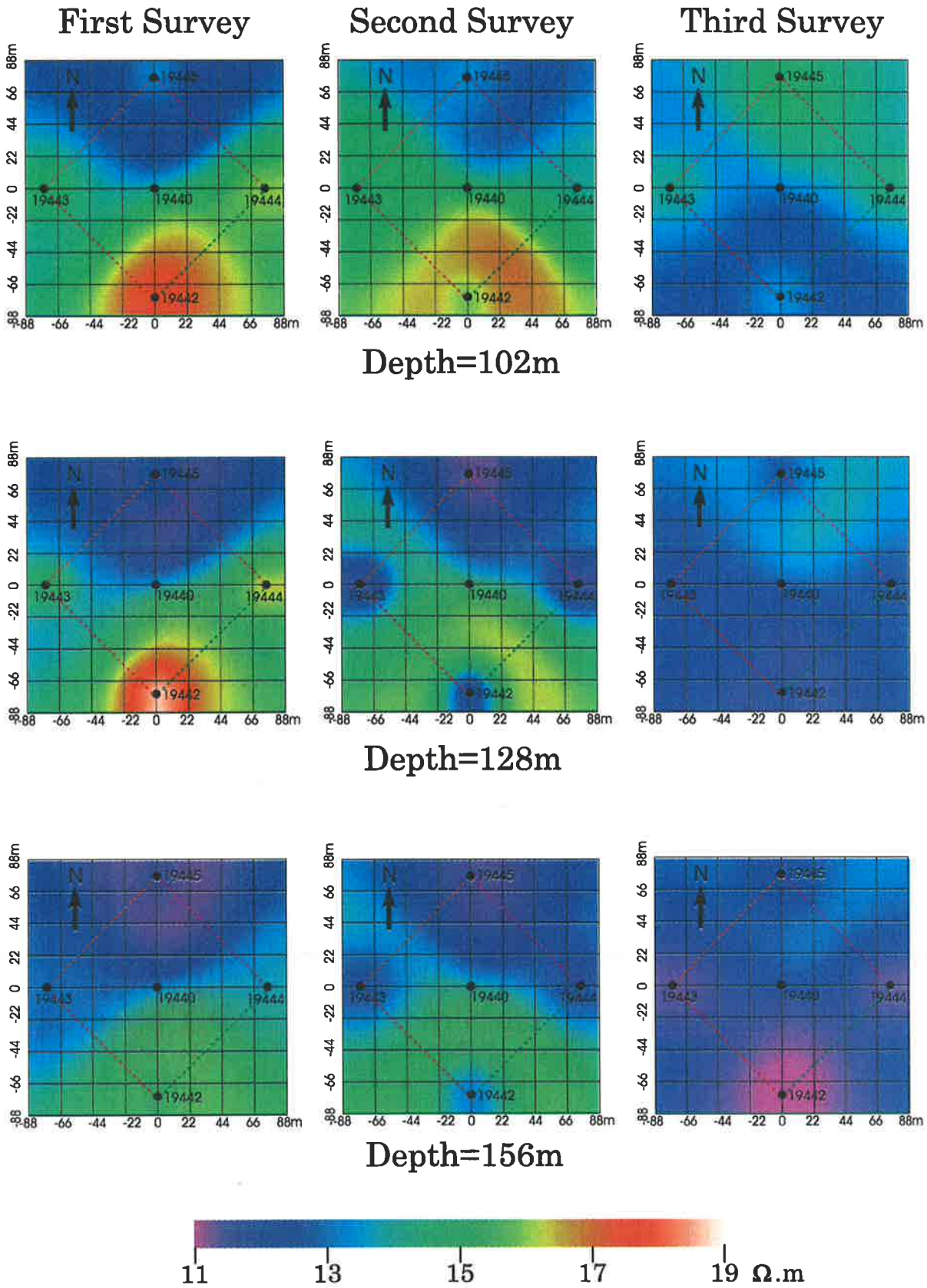

Figure 10.14 The imaging results from the three survey data (with both 14m and 28m spacing data) in Phase I. Three X-Y horizontal sections are shown for each imaging result.

From the imaging result of the third survey, one can see that the resistivity dropped greatly after 9 weeks from stopping water injection. The resistivity level is almost restored to the

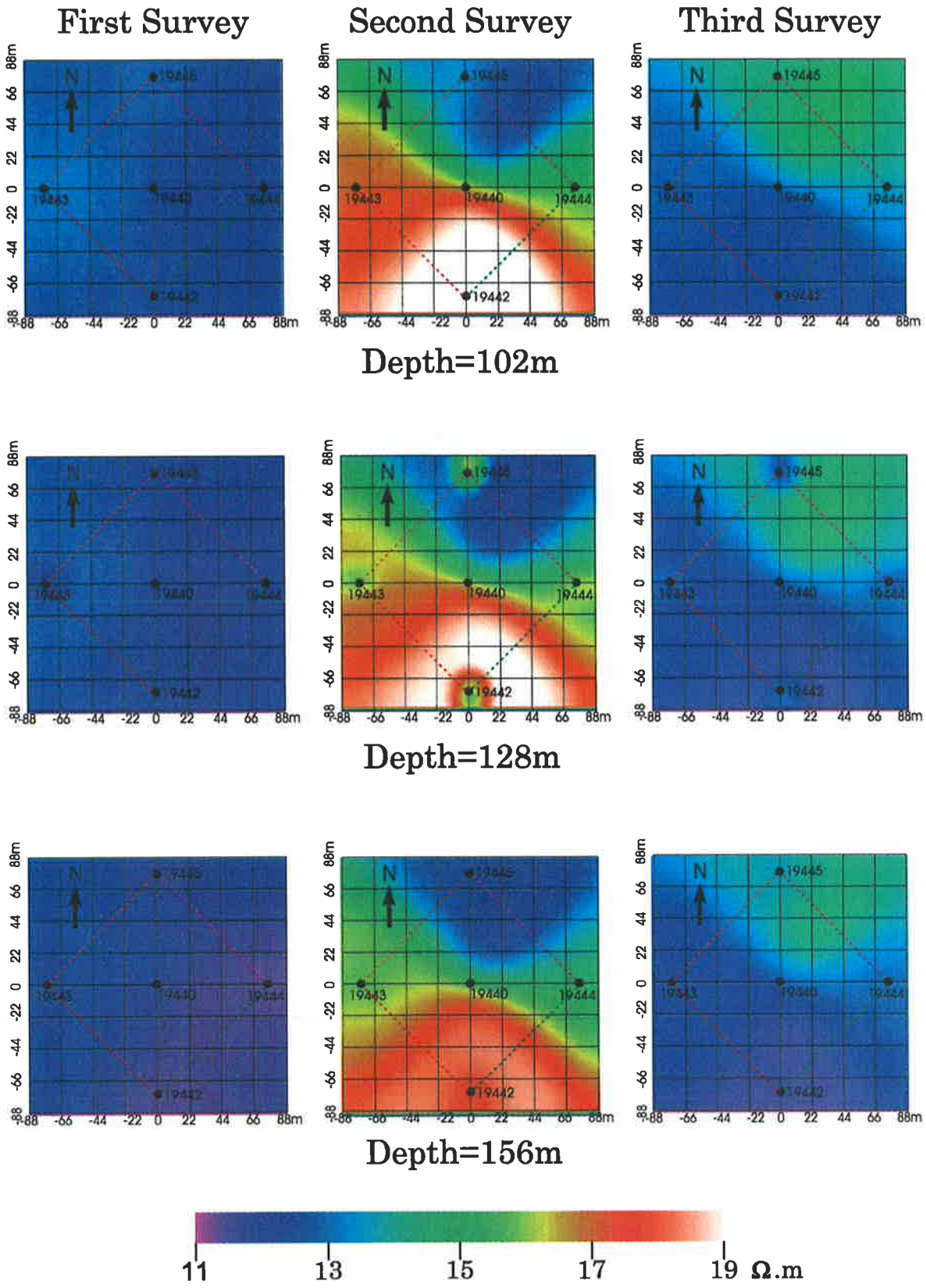

Figure 10.15 The imaging results from three survey data (with only 28m data) in Phase I. Three X-Y horizontal sections are shown for each imaging result.

original level. This is because the injected higher resistivity water has mixed with the underground water or has moved into other regions.

The 2.5-D resistivity inversions have been completed for the three surveys and 12 sets of the multiple scanning data in phase I. The 12 inversion results from both the 14m and 28m spacing survey data are shown from Figure 10.16 to Figure 10.18. From Figure 10.16, one can see that the initial resistivity distribution in the region is almost uniform horizontally.

There is not much change in resistivity between any two wells except the high resistivity distribution near the boreholes in images c) and d). That may be a result of the local resistivity changes due to the drilling operations. As we can see from Table 10.4 the average apparent resistivity from the 14m spacing data between the two pairs of wells are relatively high (15 to 18 Ω.m), but the average apparent resistivity from the 28m spacing data are much lower. So this implies that the resistivity only in the vicinity of the wells may be high and at other places it may be low. The inversion results (c) and d) of Figure 10.16) shows this to be the case. From the inversion results from the second survey data (shown in Figure 10.17), one can see that the resistivity distribution in the region is not uniform horizontally any more, especially, in a) and c) of Figure 10.17. This means that the injected fresh water did make some contribution to the resistivity distribution in the region.

By comparing the results in Figure 10.17 with the results in Figure 10.16, one part of wells at a time, we find that the resistivity distribution changed greatly in all inversions except in b) (between Well 19445 and Well 19444). The inversion results show the resistivity increases between Well 19443 and Well 19445, Well 19443 and Well 19442, and Well 19442 and Well 19444. This is consistent with the results I obtained from the 3-D imaging technique and means that the injected water mainly flowed in all directions except the northeast.

In diagram d) of Figure 10.17, there is a high resistivity band on the top of the aquifer. This may mean that the injected water has reached almost the two observation wells. From Table 10.3, we know that this is not possible, if water flows uniformly in all directions. However, as discussed above, the injected water may mainly flow in one or two directions. Under such circumstances, it is possible that the injected water reached close to some wells. Besides, if the water can only flow through the top part of the aquifer (with higher permeability), the possibility of "break-through" is even higher. It is also noticeable that the resistivity near all wells is lower than in other places. This matches with our summary statistical data (shown in Table 10.4) and the electric conductivity logging (shown in Figure 6.8). After 9 weeks from

stopping water injection, the resistivity distribution in the T2 Aquifer is returned to the original (almost) horizontal uniform situation after water mixing and moving. This is clearly shown from the inversion results in Figure 10.18.

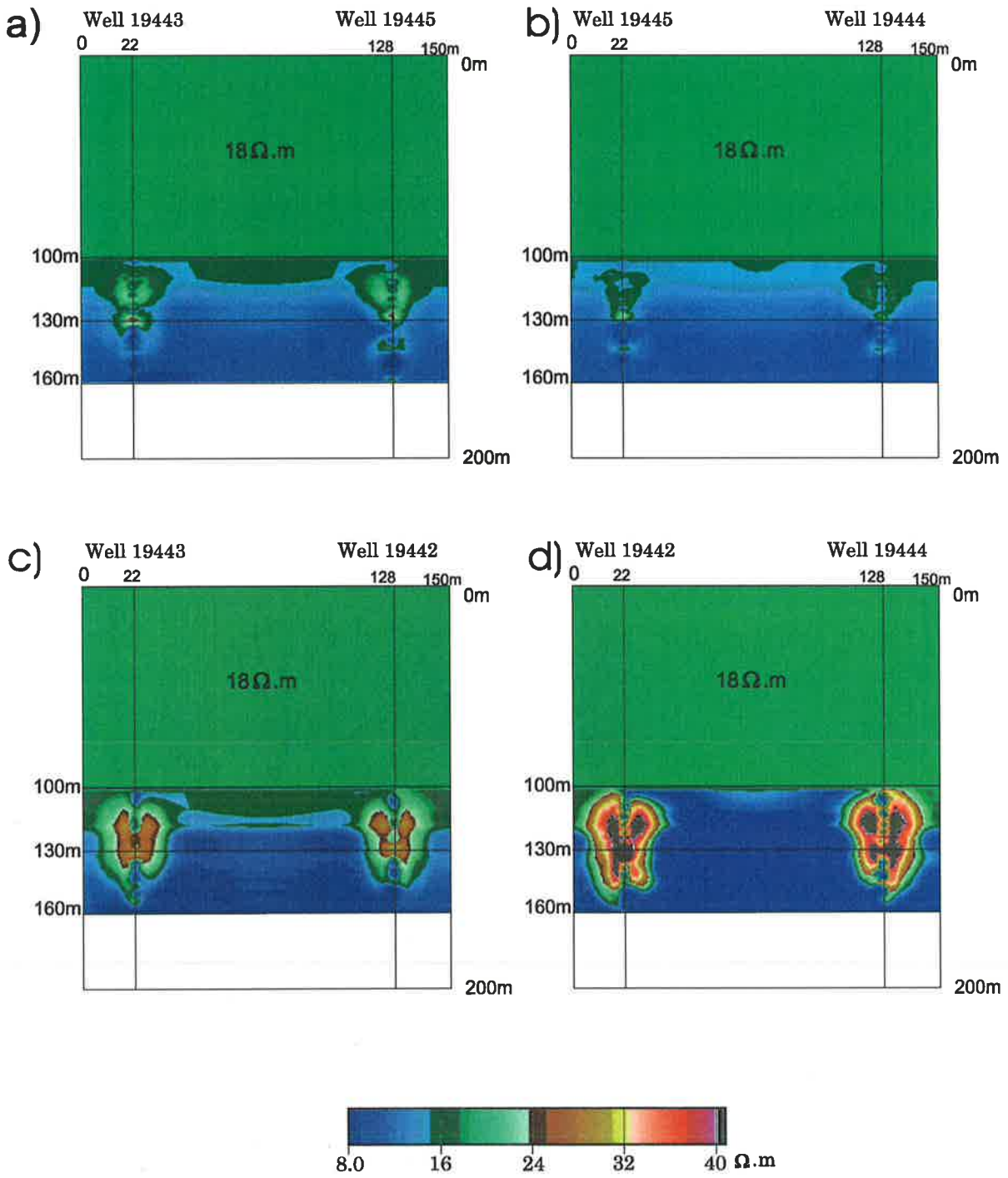

Figure 10.16 The inversion results from the first survey data with survey layouts overlain. Both 14m and 28m spacing data were used for the inversions.

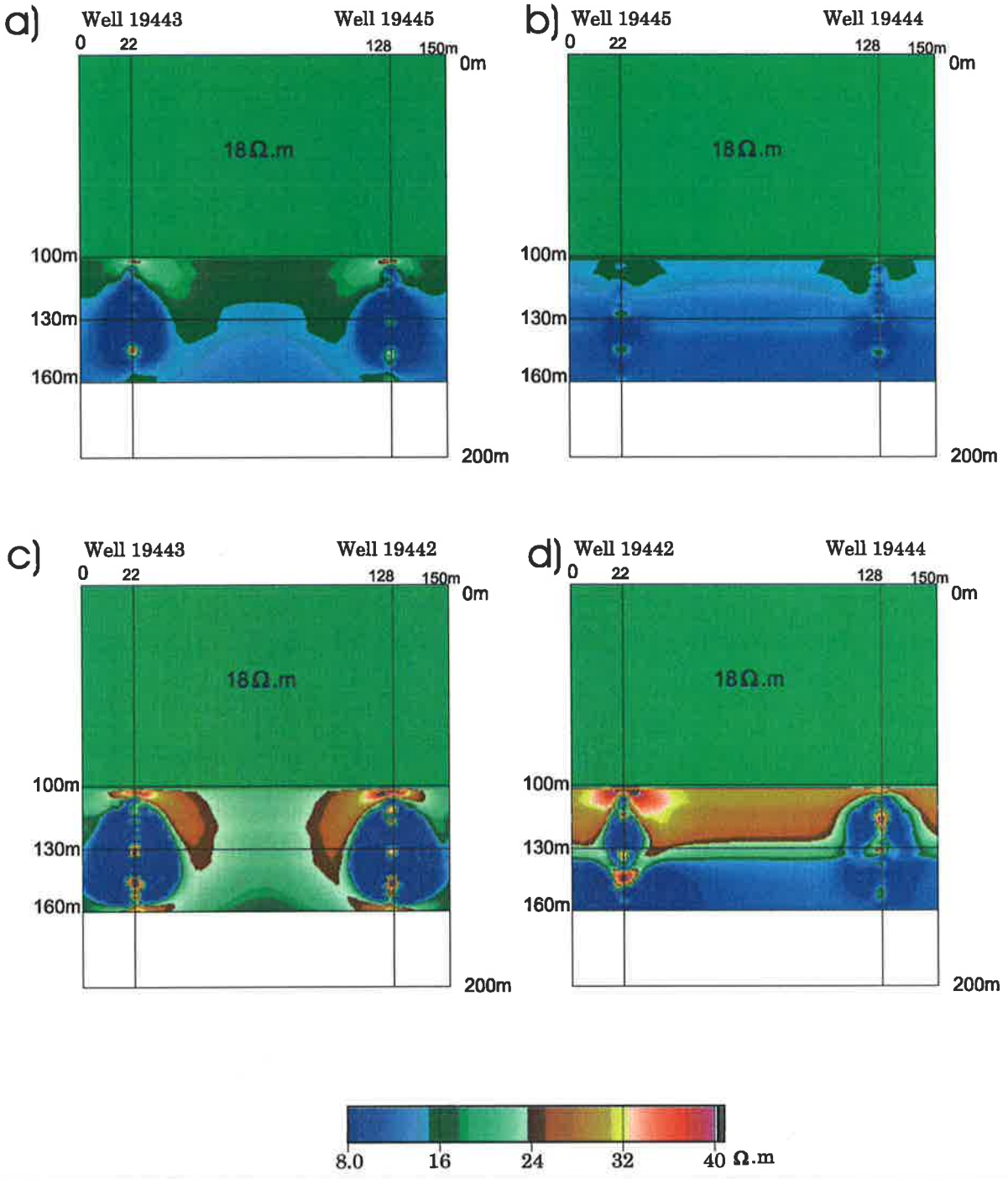

Figure 10.17 The inversion results from the second survey data with survey layouts overlain. Both 14m and 28m spacing data were used for the inversions.

For the same reason as in the previous section (imaging method), I completed another 12 inversions with only the 28m spacing data for each set of multiple scanning data. The results are shown in Figures 10.19 to 10.21. From the figures, we can see that the results are very similar to the inversion results from the combined 14m and the 28m data, except for some strong near-well effects from the 14m spacing data in the above results. For example, the high resistivity distribution near well 19442 and 19444 in d) of Figure 10.16 and the low

resistivity distribution near well 19443 and 19442 in c) of Figure 10.17.

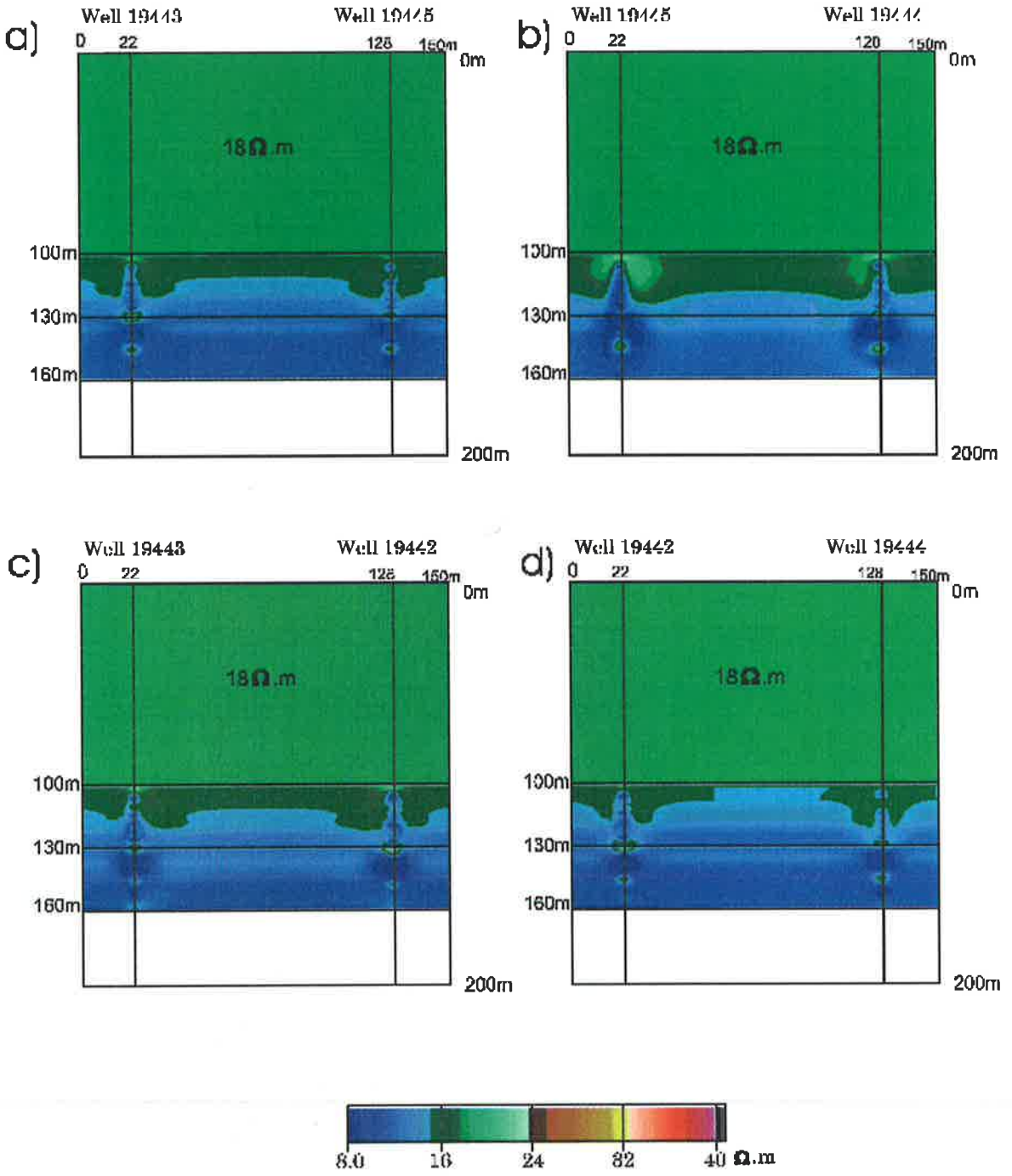

Figure 10.18 The inversion results from the third survey data with survey layouts overlain. Both 14m and 28m spacing data were used for the inversions.

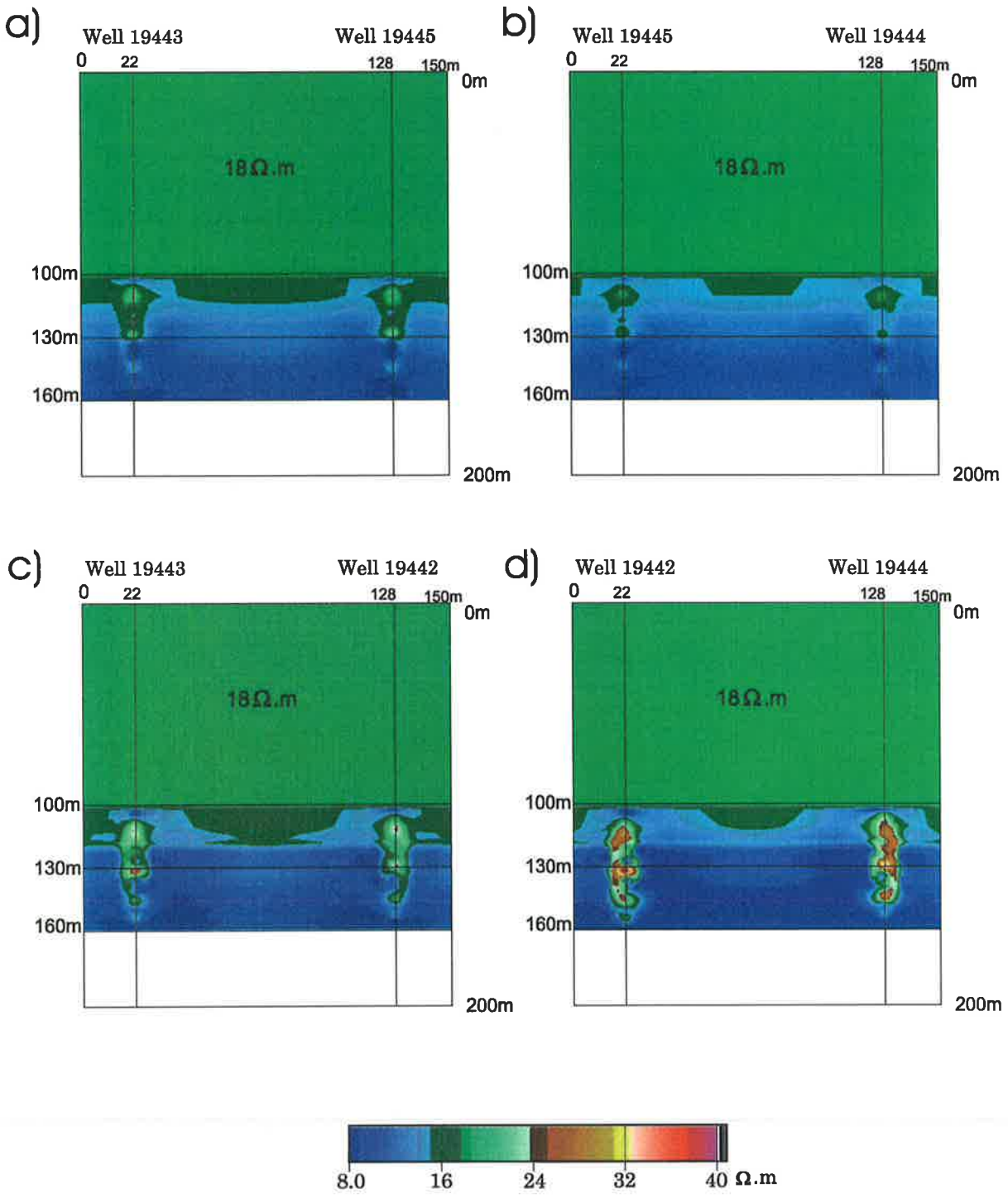

Figure 10.19 The inversion results from the first survey data with survey layouts overlain. Only 28m spacing data were used for the inversions.

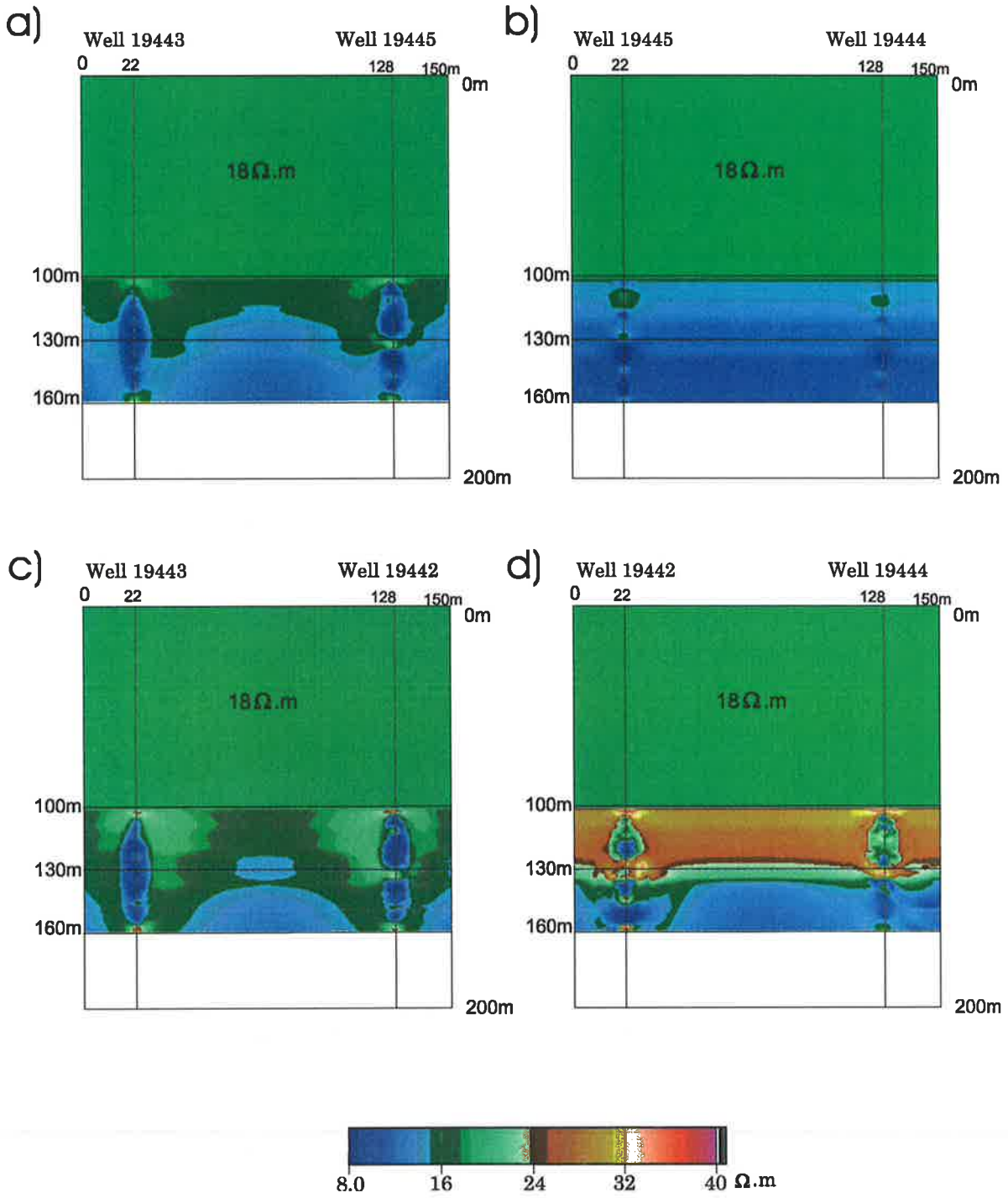

Figure 10.20 The inversion results from the second survey data with survey layouts overlain. Only 28m spacing data were used for the inversions.

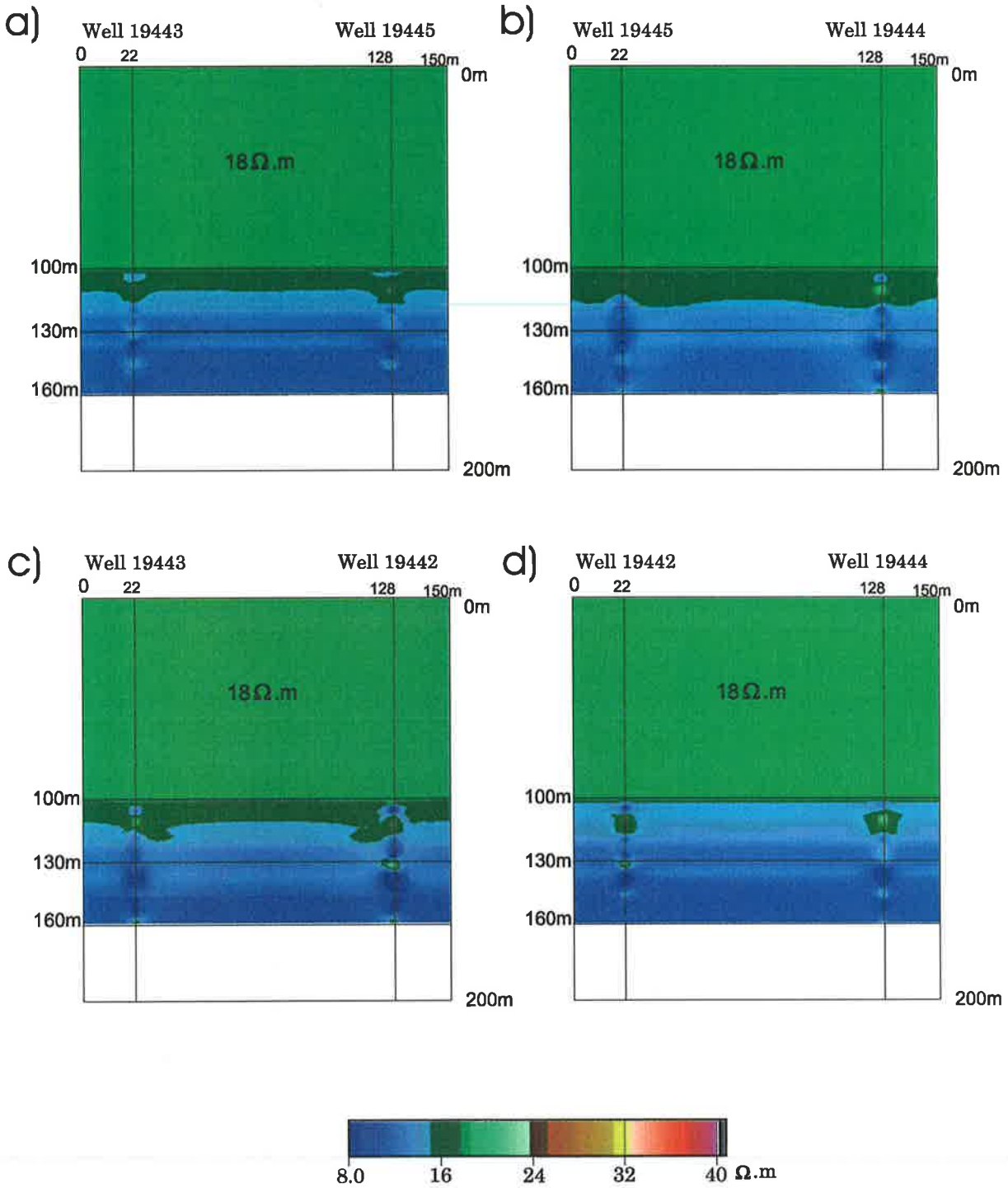

Figure 10.21 The inversion results from the third survey data with survey layouts overlain. Only the 28m spacing data were used for the inversions.

After each inversion, the original observed apparent resistivity and the apparent resistivity of the final inversion model were output. So the residual error and the relative percentage error are calculated to check the accuracy of the inversion. The relative percentage error was calculated with the following formula

$$relative\_percentage\_error = \frac{residual\_error}{observed\_AR} x100\%$$
$$= \frac{observed\_AR - final\_modelling\_AR}{observed\_AR} x100\%$$

where AR stands for apparent resistivity.

Figure 10.22 shows the output of the original observed apparent resistivity and final modelling apparent resistivity for the inversion between Well 19442 and Well 19444 in the second survey. Figure 10.23 shows the residual error and the relative error percentage for this inversion. The other inversions have similar error levels to this one. The average relative inversion error percentages for all inversions are smaller than 1 percent. So the inversion accuracy is reasonable.

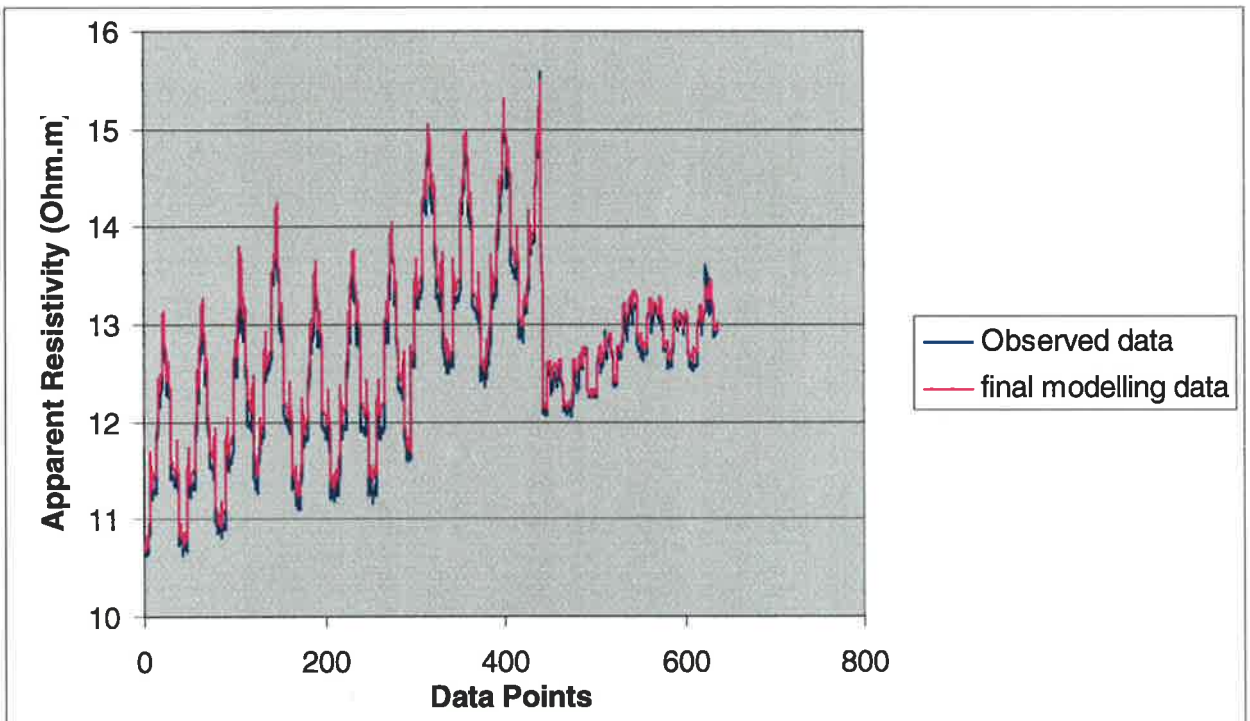

Fifure 10.22 The graph shows both the original observed data and the final modelling data for the inverion between Well 19442 and 19444 in the second survey.

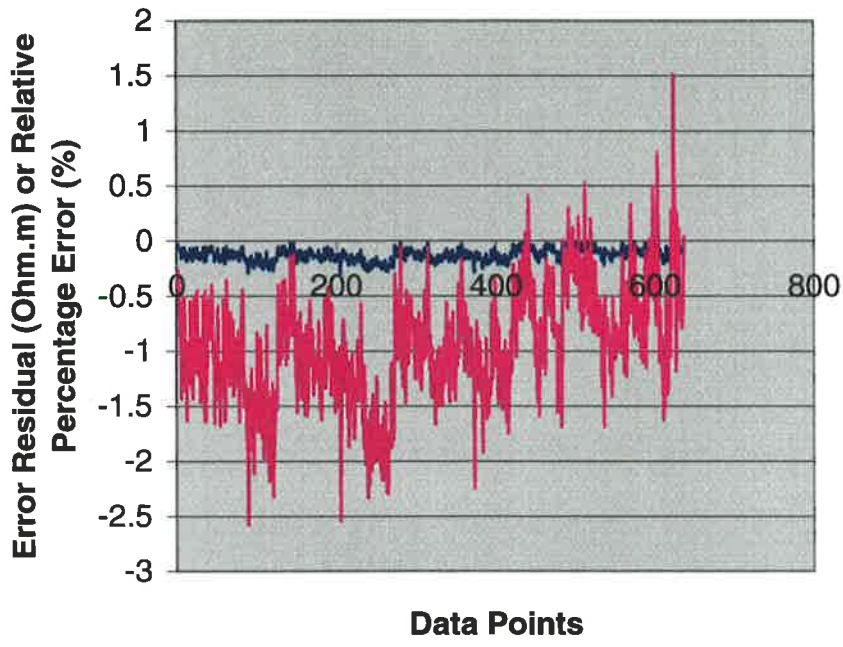

Figure 10.23 The graph shows the inversion residual error and relative percentage error for the inversion between Well 19442 and Well 19444 in the second survey.

10.4 CONCLUSIONS

The Aquifer Storage and Recover (ASR) research project commenced in July 1997 at the Bolivar site on the Northern Adelaide Plains in South Australia. The water injection period is split into two phases. Only 30ML water was injected in the Phase I and about 220ML water was injected in Phase II. The field resistivity surveys and data interpretation for Phase I were discussed in the chapter.

In total, three field tomographic resistivity surveys (before, during and after water injection) and 12 sets of crosshole multiple scannings (4 sets in each survey) were completed in Phase I. A specified crosshole bipole-biole *AM-BN* configuration was applied in each crosshole multiple scanning. The field acquisition proved that the configuration is available for crosshole resistivity measurement and good for the project.

A new display method: pseudo depth profile- was developed to display the crosshole bipole-bipole survey data. All voltage, current and calculated apparent resistivity data can be displayed with the method. From the pseudo depth profile, one can easily check and analyze the survey data.

Three methods: direct method, imaging method and inversion method, were used to interpret the survey data. All of them are capable of extracting some useful information from the survey data. The conclusions from the three methods support each other.

By analyzing the survey data, modeling experiments and comparing with other survey and experimental data, I reached the following conclusion:

1. Before the water was injected, the resistivity distribution in the T2 aquifer was stable and horizontally uniform. The resistivity value was about 12 Ω.m.
2. The injected higher resistivity water did affect the resistivity distribution in the region. The resistivity increase can clearly be seen from the both imaging results and the inversion results.
3. The injected water flowed outwards in all directions except the northeast. From the inversion results, we may assume that the water mainly went to the south.
4. After 9 weeks of stopping water injection, the resistivity distribution had returned to the original state.
5. There is a thin high resistivity layer near depth 130m. Almost all inversion results show a large relative high resistivity anomaly at this depth near the well. Unfortunately it is impossible to invert for the thin layer between two widely spread wells with restricted access data.
6. The resistivity decreases with depth in the region.

Chapter 11

RESISTIVITY SURVEYS AND INTERPRETATION - PHASE II

11.1 INTRODUCTION

The ASR fresh water injection was split into two phases. In this chapter, I will examine the resistivity data obtained in Phase II, which started in April 2000 and stopped in April 2001. Four crosshole tomography resistivity surveys were executed in Phase II. The survey dates and water injection progress in this phase are shown in Figure 11.1. The first survey was carried from 17/4/00 to 22/4/00, during the pumping test but before the formal water injection started in the second phase. The second survey was completed from 15/9/00 to 20/9/00, and the third survey was done from 18/12/00 to 22/12/00. Both were during the formal water injection period. The last survey in this phase was done from 27/3/01 to 1/04/01, just before the water injection ceased.

As distinct from the three surveys completed in Phase I, all four crosshole resistivity surveys in Phase II were conducted with four different pairs of wells. The crosshole resistivity multiple scannings in this phase were carried out in the radial direction (between the central observation well 19450, and the other four observation wells situated on the circumference of a circle of radius 75 meters, centred on the injection well), instead of on the four chords, as shown in Figure 11.2.

11.2 DATA ACQUISITION

11.2.1 Survey Configuration

The same survey configuration and procedure were used in all four surveys in this phase. Since all crosshole resistivity multiple scannings were completed in the radial direction in all four surveys, the distance between two observation wells in each multiple scanning was reduced from 106m (on chord) to 75m, as shown in Figure 11.2. The available depth access range in all surveys was still 54m from 102m to 156m depth. Again the crosshole bipole-

bipole *AM-BN* configuration was employed in all surveys. Figure 11.3 shows the cross section of the survey configuration between two wells.

Figure 11.1 The water injection progress graph for Phase II, with the four survey dates.

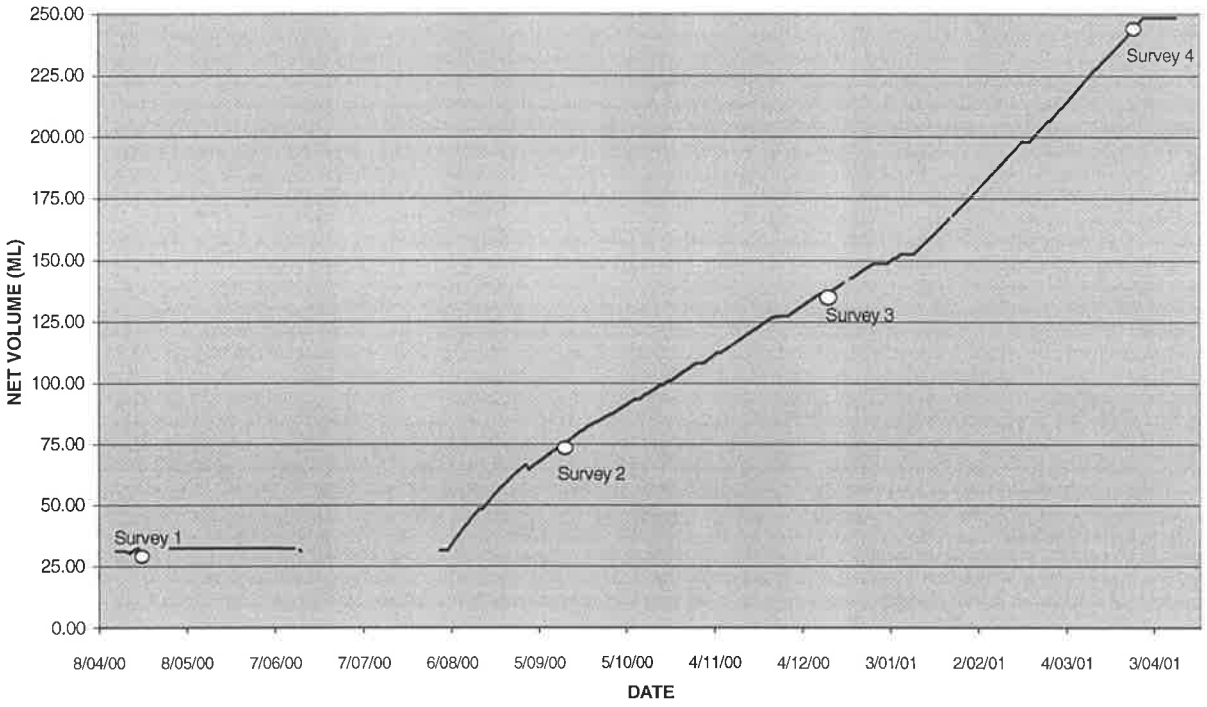

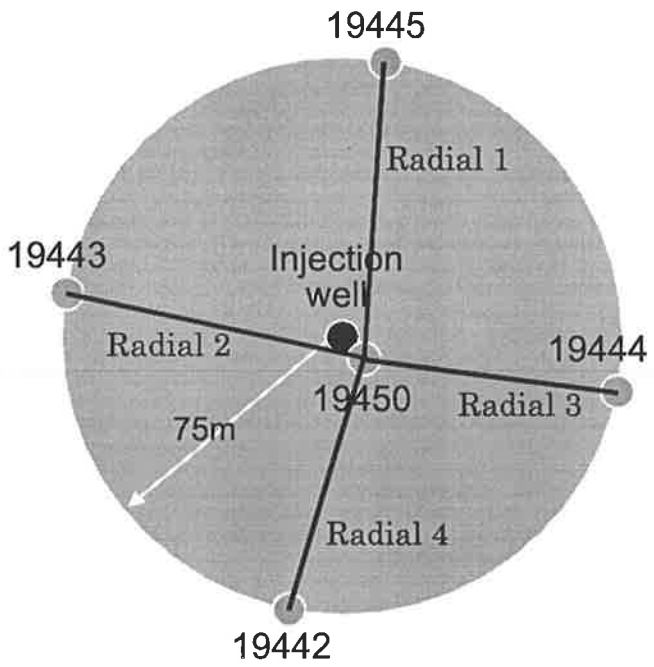

Figure 11.2 The surface layout of the four crosshole resistivity surveys in Phase II. Four crosshole resistivity multiple scannings, on radii 1, 2, 3 and 4, were conducted in each survey.

It common with Phase I, at each depth position, we used two pairs of potential and current measurements for the 14m spacing and the 28m spacing, respectively. So in each crosshole multiple scanning between two wells, there were 21×21=441 data measurements for the 14m spacing and 14×14=196 data measurements for the 28m spacing. The total number of data points obtained was 637 for each crosshole multiple scanning.

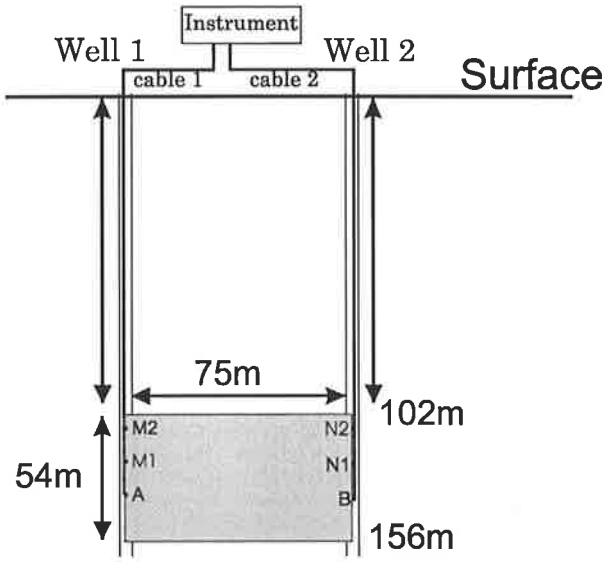

Figure 11.3 The cross section of the crosshole resistivity multiple scanning layout for all surveys in Phase II. A and B are current electrodes, and M1, M2, N1 and N2 are potential electrodes.

11.2.2 Survey Data

In total 16 (4 surveys x 4 scannings) sets of crosshole multiple scanning measurements were obtained in Phase II, and 96 (16 sets x 3 variables x 2 spacing) pseudo depth profiles were produced for potential, current and apparent resistivity respectively. To save space here, only some of the 96 pseudo depth profiles are displayed in this thesis.

From the 96 profiles, it was found that as a whole, the quality of survey data in Phase II is better than that of Phase I. All potential and apparent resistivity profiles in Phase II are fairly clean and stable. The current profiles are better as well, although they are still a bit noisy compared with the potential and apparent resistivity profiles. The improvement in data quality is partly due to the increased experience of the survey crew in this crosshole resistivity imaging. Large potential and current jumps, due to changing a battery, can still be seen in some profiles. But the apparent resistivity profile calculated from the current and potential profiles looks good. However one strange thing happened in the potential data between Well 19443 and Well 19450 in the second survey. A large gap or jump can be seen in the potential

profiles (shown in Figure 11.4 (a)) between profile 114 (the number on the right side of profile) and 116. However there is no gap or jump in the corresponding current profiles (Figure 11.4 (b)). Such, a large gap is produced in the calculated apparent resistivity profiles (Figure 11.4 (c)). This means that the measured data may have some error, which made the calculated apparent resistivities much higher. I have not found what caused this problem. I did not remove the data, but I keep an eye on it when I interpret the data.

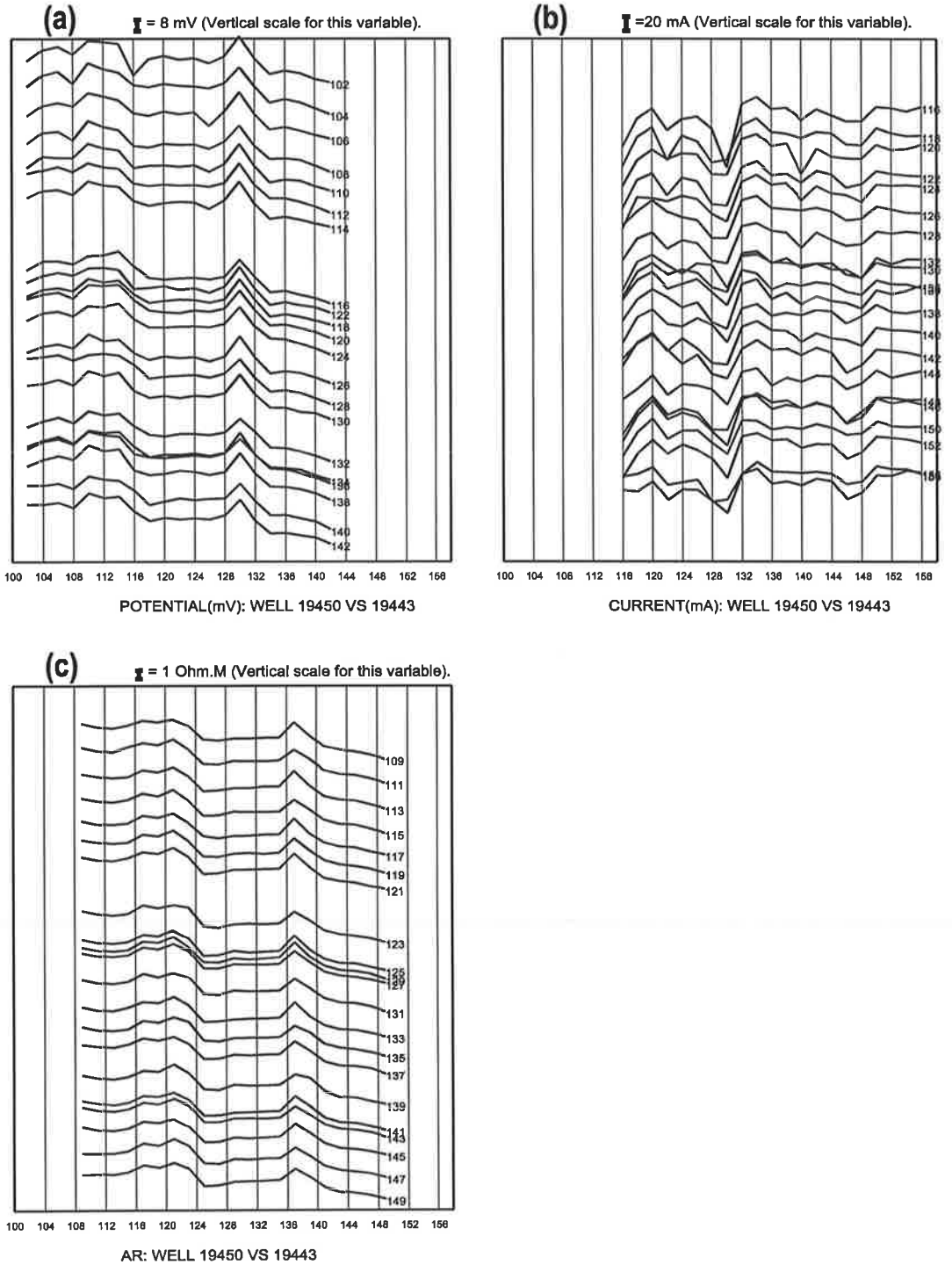

Figure 11.4 The pseudo depth profiles (14m spacing) between Well 19450 and 19443 of the second crosshole survey in Phase II.

By comparing the apparent resistivity profiles in Phase I with those in Phase II, one can see that all profiles exhibit a similar pattern. This means that the geological structure in the T2 Aquifer is almost flat or horizontally uniform. However, from just these profiles alone, it is too hard to directly deduce the resistivity distribution in the region.

The average apparent resistivities and relative changes between consecutive surveys were calculated for each crosshole multiple scanning, and for each 14m and 28m spacing, respectively. All these statistical data are listed in Table 11.1 for later use.

Table 11.1 The minimum, maximum, average apparent resistivity and the apparent resistivity relative change of the 4 time-lapse surveys.

Survey No.	Well 1 VS Well2	Electrode Spacing	AR-MIN	AR-MAX	AR-MEAN	AR Increase (%)
1	Well 19442 VS 19450	14m	13.48	19.23	16.40	
1	Well 19443 VS 19450	14m	13.18	19.68	16.32	
1	Well 19444 VS 19450	14m	12.14	18.29	14.90	
1	Well 19445 VS 19450	14m	12.55	19.48	16.03	
2	Well 19442 VS 19450	14m	14.19	22.29	17.36	5.86
2	Well 19443 VS 19450	14m	20.58	31.85	25.85	58.41
2	Well 19444 VS 19450	14m	13.43	23.44	18.44	23.75
2	Well 19445 VS 19450	14m	14.15	20.90	17.43	8.70
3	Well 19442 VS 19450	14m	12.36	18.21	15.49	-10.81
3	Well 19443 VS 19450	14m	13.00	18.84	16.01	-38.06
3	Well 19444 VS 19450	14m	12.51	18.61	15.66	-15.06
3	Well 19445 VS 19450	14m	12.91	18.71	15.68	-10.05
4	Well 19442 VS 19450	14m	13.86	20.58	17.43	12.55
4	Well 19443 VS 19450	14m	12.93	19.23	16.21	1.21
4	Well 19444 VS 19450	14m	12.93	19.24	16.23	3.66
4	Well 19445 VS 19450	14m	14.59	21.60	18.09	15.39
1	Well 19442 VS 19450	28m	15.47	20.16	17.31	
1	Well 19443 VS 19450	28m	16.58	20.91	18.10	
1	Well 19444 VS 19450	28m	14.03	16.79	15.16	
1	Well 19445 VS 19450	28m	15.81	19.93	17.41	
2	Well 19442 VS 19450	28m	14.98	20.56	16.59	-4.17
2	Well 19443 VS 19450	28m	15.56	19.52	17.11	-5.47
2	Well 19444 VS 19450	28m	15.34	18.35	15.58	2.74
2	Well 19445 VS 19450	28m	15.85	19.52	17.31	-0.58
3	Well 19442 VS 19450	28m	13.83	16.57	15.08	-9.09
3	Well 19443 VS 19450	28m	14.57	17.66	15.93	-6.86
3	Well 19444 VS 19450	28m	13.93	16.55	15.24	-2.19
3	Well 19445 VS 19450	28m	14.38	16.94	15.57	-10.02

4	Well 19442 VS 19450	28m	15.19	18.95	16.94	12.29
4	Well 19443 VS 19450	28m	14.97	19.44	16.66	4.55
4	Well 19444 VS 19450	28m	14.84	18.21	16.48	8.15
4	Well 19445 VS 19450	28m	15.74	19.46	17.57	12.86

11.3 INTERPRETATION

Once again the three methods: the direct method, the imaging method and the inversion method, were used to interpret the survey data. They are discussed in detail in the following sections. Before the interpretation of the survey data, numerous resistivity modelling and inversion experiments were done to help the interpretation. The next section discusses the experiments and significance of the results.

11.3.1 What Resistivity Change Do We Expect After Higher Resistivity Water Is Injected Into The Aquifer?

As discussed in the previous chapter, we know that the average resistivity of the T2 Aquifer will definitely increase after the higher resistivity water is injected into it.

To understand the effect of the injected water, I have completed many numerical resistivity modelling and inversion experiments to simulate the resistivity response of the higher resistivity water injection in Phase II. The details of these experiments and the conclusions reached are given in Chapter 9. From that chapter, we know that the injected higher resistivity water definitely causes an observable AR increase in the resistivity crosshole multiple scanning surveys. From the inversion results of the numerical modelling data, it was seen that the resistivity distribution near both boreholes could normally be imaged. However the resistivity change details between the two wells can not be clearly inverted due to the relatively small electrode spacing used (compared with the distance between two survey wells) and too few data points.

From Figure 11.1, we know that an additional 215ML reclaimed water was injected into the T2 aquifer in Phase II, after the 35ML water that was injected in Phase I. Using the same expanding cylinder method as used in the last chapter, I produced Table 11.2 to find the minimum radius that the 215ML injected fresh water volume can expand into from the central injection well, based on the assumption of simple uniform spreading. The different entries in the table correspond to different assumed formation porosities and thicknesses (height) of the permeable zone in the aquifer. From the measurements of the well core, we know that the

porosity in the T2 Aquifer is about 0.45. The first 35ML of water were not considered here since this volume may have moved to other places already, or mixed with the underground water.

Table 11.2 The calculated minimum radius the injected fresh water can expand into from the central injection well.

Volume(m3)	Height(m)	Porosity	Minimum R (m)
215000	60	0.3	61.7
215000	60	0.4	53.4
215000	60	0.5	47.8
215000	50	0.3	67.6
215000	50	0.4	58.5
215000	50	0.5	52.3
215000	40	0.3	75.5
215000	40	0.4	65.4
215000	40	0.5	58.5
215000	**30**	**0.3**	**87.2**
215000	30	0.4	75.5
215000	30	0.5	67.6
150000	60	0.3	51.5
150000	60	0.4	44.6
150000	60	0.5	39.9
150000	50	0.3	56.4
150000	50	0.4	48.9
150000	50	0.5	43.7
150000	40	0.3	63.1
150000	40	0.4	54.6
150000	40	0.5	48.9
150000	**30**	**0.3**	**72.9**
150000	30	0.4	63.1
150000	30	0.5	56.4
100000	60	0.3	42.1
100000	60	0.4	36.4
100000	60	0.5	32.6
100000	50	0.3	46.1
100000	50	0.4	39.9
100000	50	0.5	35.7
100000	40	0.3	51.5
100000	40	0.4	44.6
100000	40	0.5	39.9

100000	**30**	**0.3**	**59.5**
100000	30	0.4	51.5
100000	30	0.5	46.1

From the table, we can see that the injected water might reach all observation wells on the 75m radius after 215 ML water was injected. It is even possible that the injected water reached some observation wells after 150ML of water was injected, since the permeability in different directions and different layers in the T2 Aquifer varies. However, it seems unlikely that the water reached the 75m wells after only 100ML water was injected. From the core samples of the observation wells, we know that the permeability at the top of the T2 Aquifer is larger than at the bottom (Pavelic, 2001). So the injected fresh water should reach at least some of the four observation wells situated on the circumference of a circle of radius 75 meters after 215 ML water was injected.

11.3.2 Direct Method

11.3.2.1 Turning point and profile patterns

In keeping with the observation of Chapter 10, we again find some turning points from the potential and current profiles to help identify some resistivity interfaces between adjacent resistivity layers.

By comparing the potential and current profiles of both Phase I and Phase II, we can see that they are similar. Turning point positions in the profiles are at almost the same positions. The two turning points at depth 116m and depth 130m are obvious. Another turning point at depth 146m is recognisable in the current profiles. As stated earlier, this is consistent with the well log result shown in Figure 6.6.

From the 2.5-D inversion results (for both the 14m and 28m spacing data) shown later, one can see that (1) there is a relative high resistivity spot at a depth of about 130m in almost all inversion results; (2) there is an interface at a depth of about 130m in most inversion results, which divides the T2 Aquifer into the two parts – an upper and a lower zone.

All potential profiles from the different pairs of wells in this phase have similar patterns and all current and potential profiles have similar patterns as well. This supports the conclusion reached in the previous chapter: that the geological structure in the T2 Aquifer is sedimentary or flat.

11.3.2.2 Possible resistivity structure according to the model result

A common profile pattern can be seen from all apparent resistivity profiles. It is the same as that from Phase I: three main 'continuously changed' segments (the first one is from depth 109 to 123m, the second is from depth 125 to 133m and the last one is from depth 135 to 145m). Then the 2.5-D resistivity modelling experiments (see Section 3.3.5.2) proved that there is thin high resistivity layer at a depth of 130m. As mentioned above, almost all inversion results show a relative high resistivity spot at this depth. This spot in fact is a thin higher resistivity layer. According to the modelling and inversion experiments in Chapter 9, it is impossible to invert such thin layers with the given survey geometry and so few survey data points.

11.3.2.3 Apparent resistivity relative change between surveys

From Table 11.1, it can be seen that the mean apparent resistivities (AR-MEANs) are not as expected for a continuous increase of higher resistivity fluid during water injection. About half of the ARs increases are negative. However the continuous increase of the AR-MEANs with increasing fresh water injection is based on a theoretical calculation. In practice, there are many factors that could affect the AR-MEANs.

To solve the puzzle, I first examined the measured resistivity data of the injected water. Before the water was injected into the T2 Aquifer, the conductivity of the water was measured routinely. Figure 11.5 shows the recorded water resistivity data (converted from the well log conductivity data) over the period of the survey dates. From the figure, one can see that the resistivity changes are: high->low->low->high. This is consistent with most of the AR-MEANs changes in Table 11.1, since the AR-MEANs show the same change pattern, except the AR-MEAN change (the 14m spacing only) from the first survey to the second survey. So the conductivity changes of the injected water indeed affected the AR-MEANs. This is because the resistivity decrease of the injected water in the central observation well (4m away from the injection well) definitely caused the apparent resistivity decrease.

Then I examined the average local resistivity change curves of the four observation wells on the circumference of a circle of radius 75 meters. The four curves are overlain with the survey dates in Figures 11.6 to 11.9. From the figures, we can see that a common feature of all four figures is that the true water resistivity in these four observation wells on the 75m radius during the first survey is much lower than the one during the second survey. This lower local water resistivity in these four observation wells during the first survey made the survey apparent resistivity lower too, especially in the data for the 14m spacing. This is the

main reason why the AR-MEANs for the 14m spacing data of the first survey are lower than the AR-MEANs for the second survey.

Figure 11.5 The recorded resistivity change of the injected water during PhaseII.

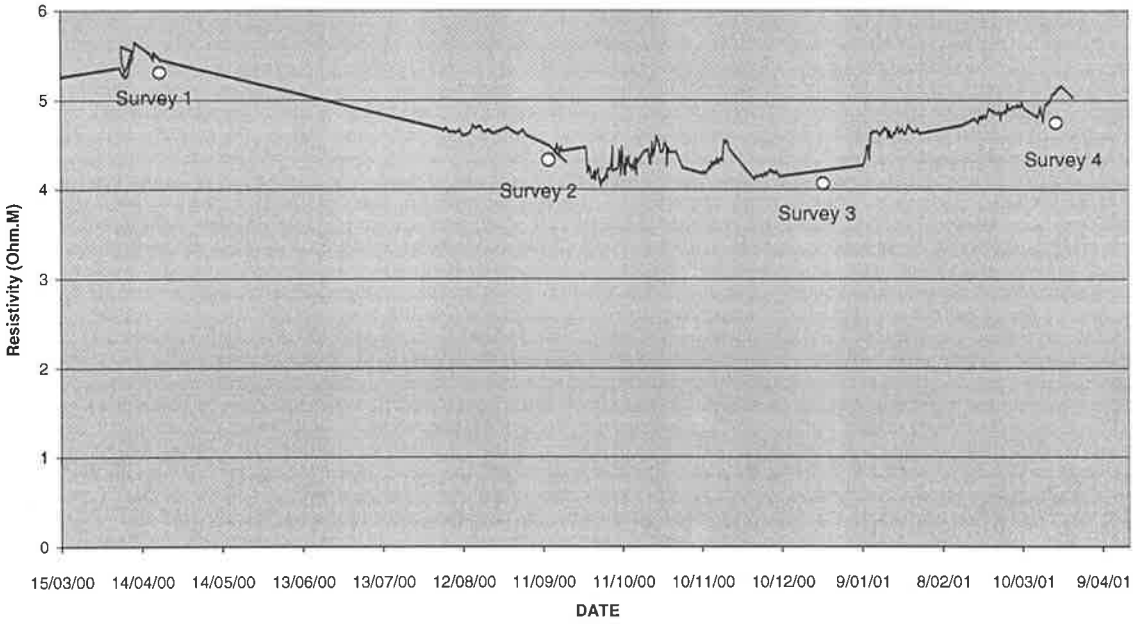

Figure 11.6 The local water resistivity change curve with time in Well 19442.

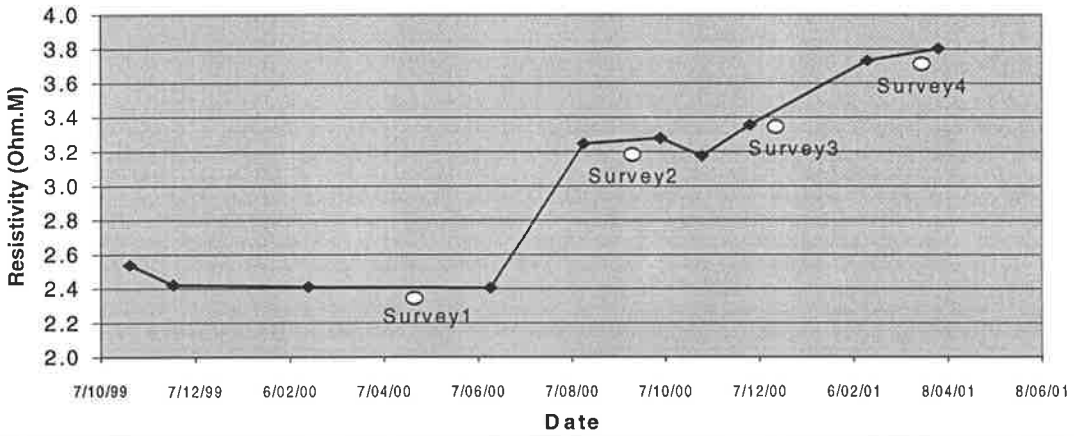

Figure 11.7 The local water resistivity change curve with time in Well 19443.

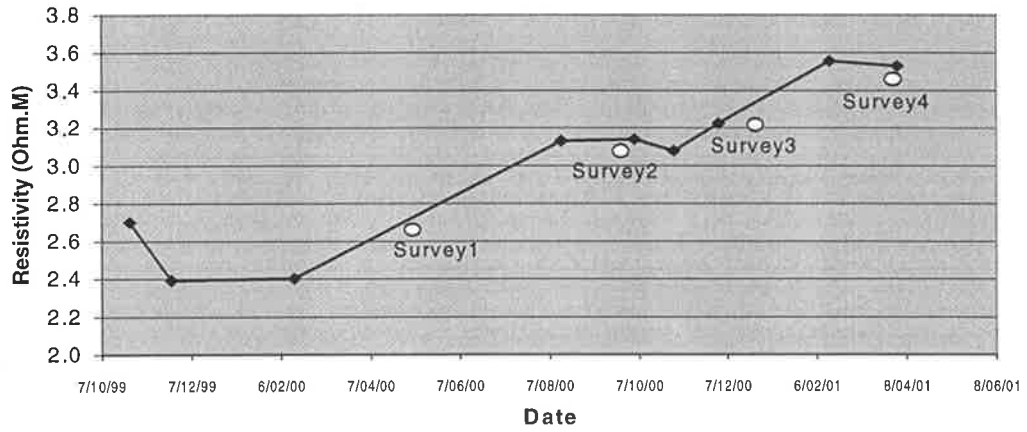

Figure 11.8 The local water resistivity change curve with time in Well 19444.

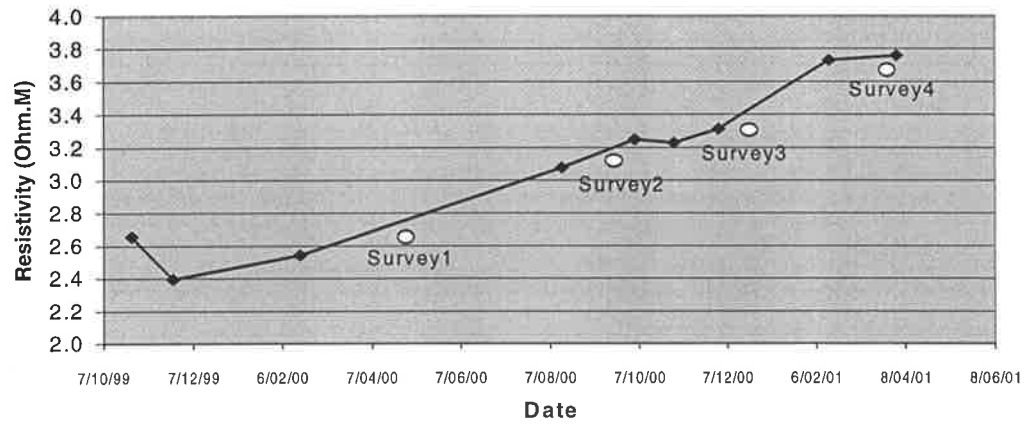

Figure 11.9 The local water resistivity change curve with time in Well 19445.

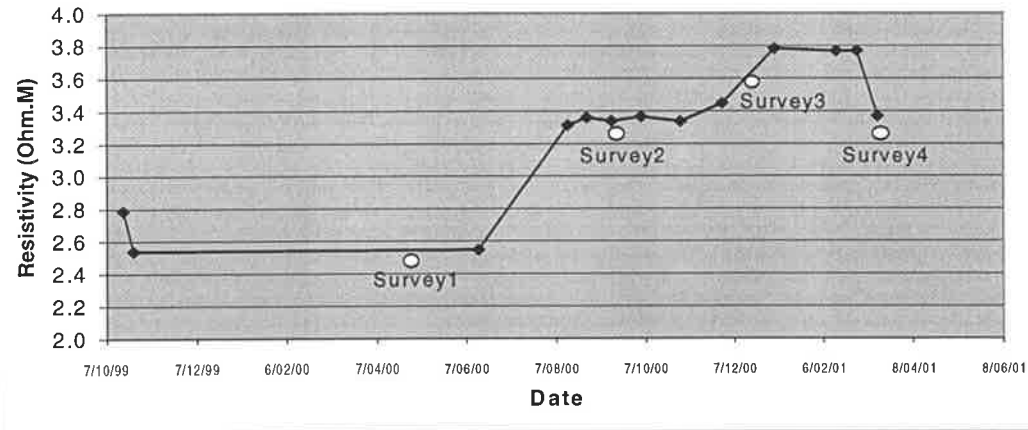

11.3.3 3-D Imaging Method

All four-survey data were imaged with our 3-D imaging program. Two images were produced for each survey, the first one used both the 14m spacing data and the 28m spacing data, while the second one used only the 28m-spacing data. All imaging results are shown from Figures 11.10 to 11.13. For ease of comparison, there are three imaging results in each figure.

A common feature of all imaging results is that the resistivity deceases with depth. Each imaging result was produced from 4 sets of crosshole multiple scanning data. In each set of the crosshole multiple scanning data, it related two wells, one is the central observation well and the other is a well on the circumference of a circle of radius 75 meters. So from the 3-D imaging algorithm, I know that the resistivity distribution near the central well in the imaged results is always affected by all survey data, and it shows a mixed effect from the 4 crosshole multiple scannings. As such, the central part of the imaging results is always not very low and not very high. However, the resistivity distribution near the other wells is mainly dependent on the crosshole multiple scanning data between the central well and the well in question and is closely associated with the AR-MEANs in Table 11.1. For example, in the first survey, the AR-MEANs of both the 14m and 28m spacing data between Well 19443 and Well 19450 are much larger than the AR-MEANs of the other sets of survey data. So the imaging results of the first survey show a high to the east.

Figures 11.10 and 11.11 show all four imaging results for the four surveys with all 14m and 28m spacing data. The imaging result of the first survey shows a high in the west, a low in the east, and intermediate values in the south and the north. This matches with the AR-MEANs in Table 11.1. The imaging result of the second survey shows a high in the west, near Well 19443. This is consistent with the AR-MEAN in Table 11.1. But this is spurious and is due to data error, since the voltage data for this multiple scanning (for 14m spacing only) has a large jump (refer to section 11.2.2).

Figures 11.12 and 11.13 shows all four imaging results for the four surveys with only the 28m spacing data. All these results are similar to the images produced from the combined 14m and 28m spacing data, except in the left part of the imaging result of the second survey. Since there are some errors in the 14m spacing data (between Well 19443 and Well 19450) of the second survey (mentioned in Section 11.2.2), the imaging result from the 28m spacing data

alone is different from and more reliable than the imaging result from both data sets taken together.

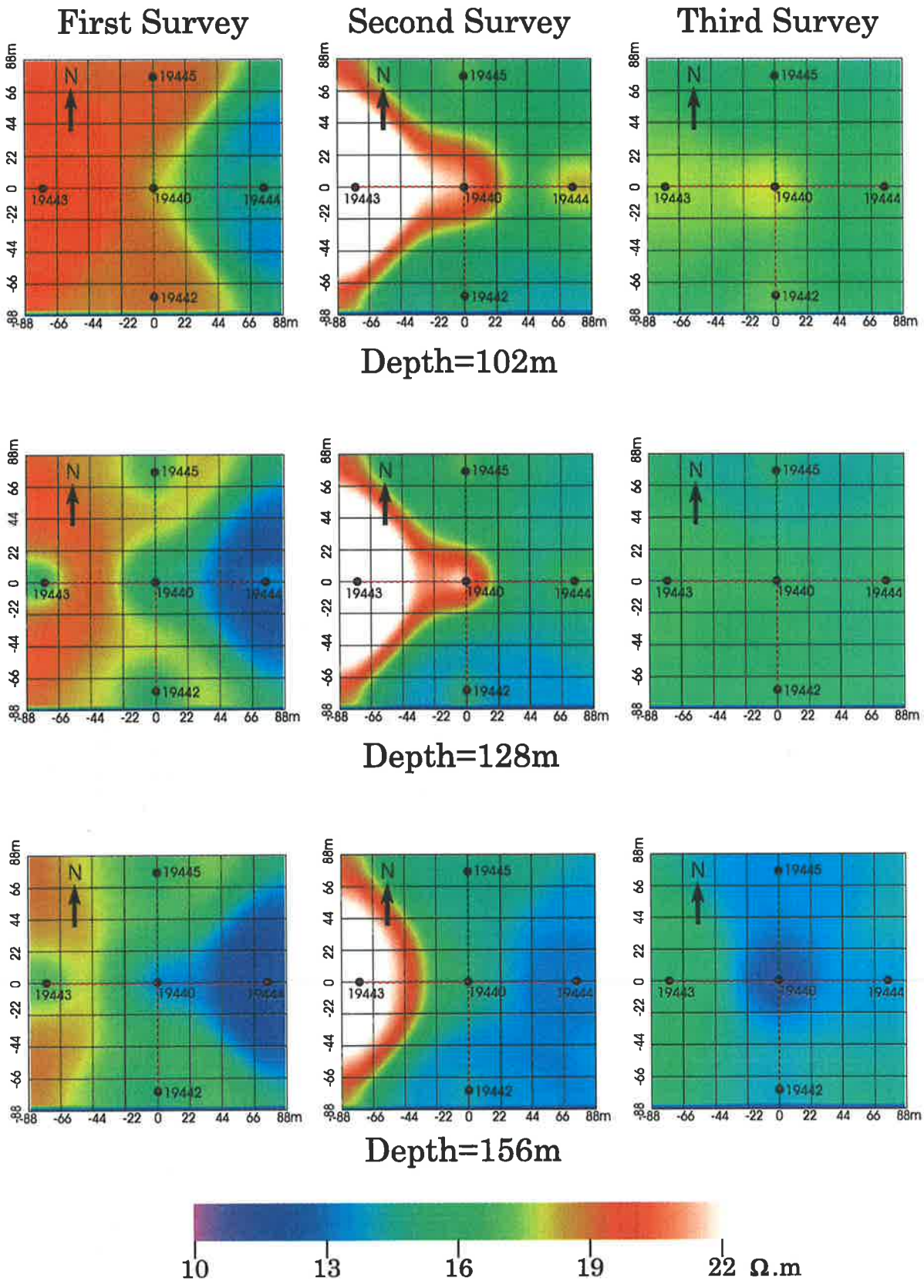

Figure 11.10 The imaging results for the surveys one, two and three (with both 14m and 28m spacing data) in Phase II. Three X-Y horizontal sections are shown for each imaging result.

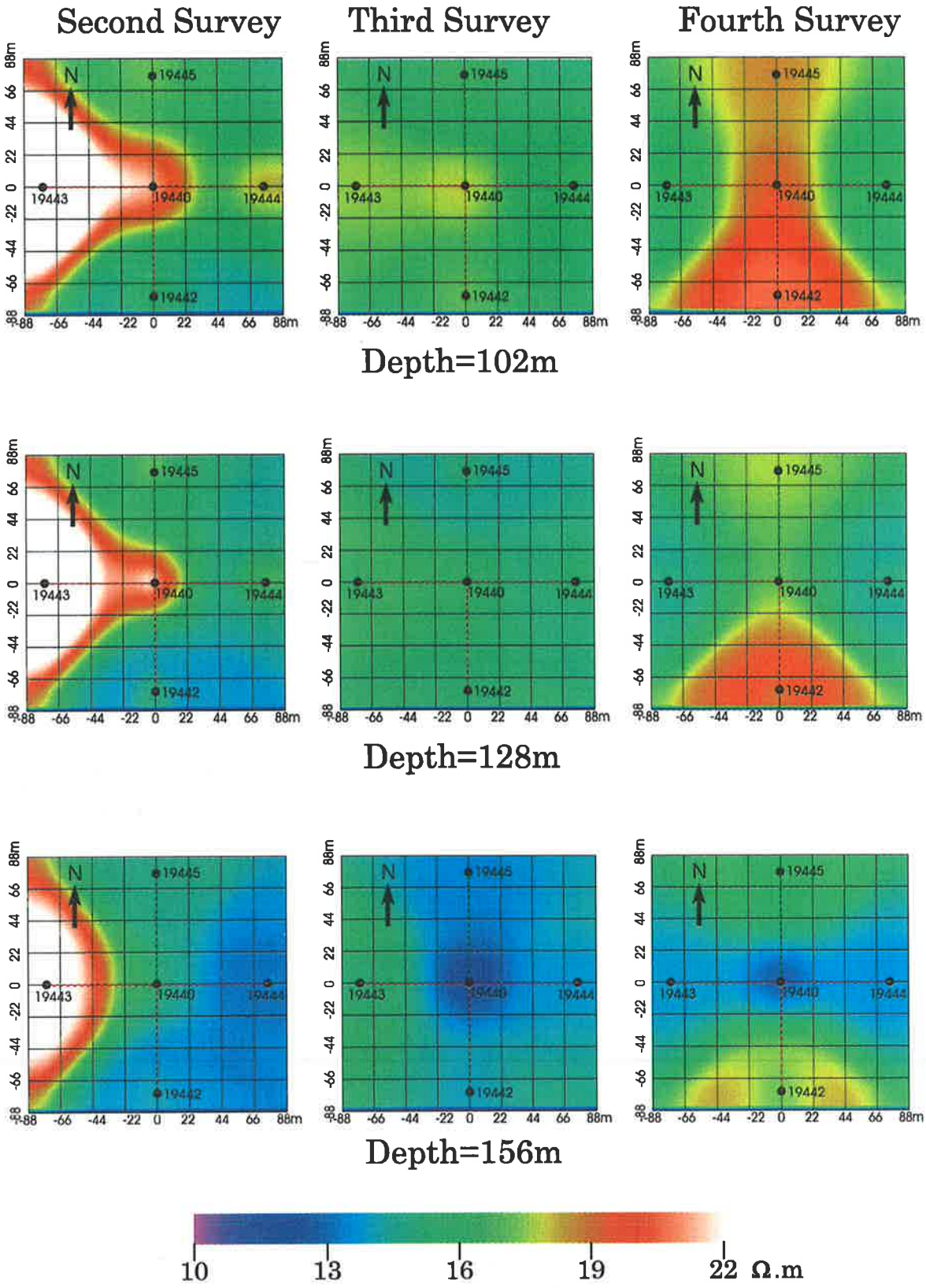

Figure 11.11 The imaging results for the surveys two, three and four (with both 14m and 28m spacing data) in Phase II. Three X-Y horizontal sections are shown for each imaging result.

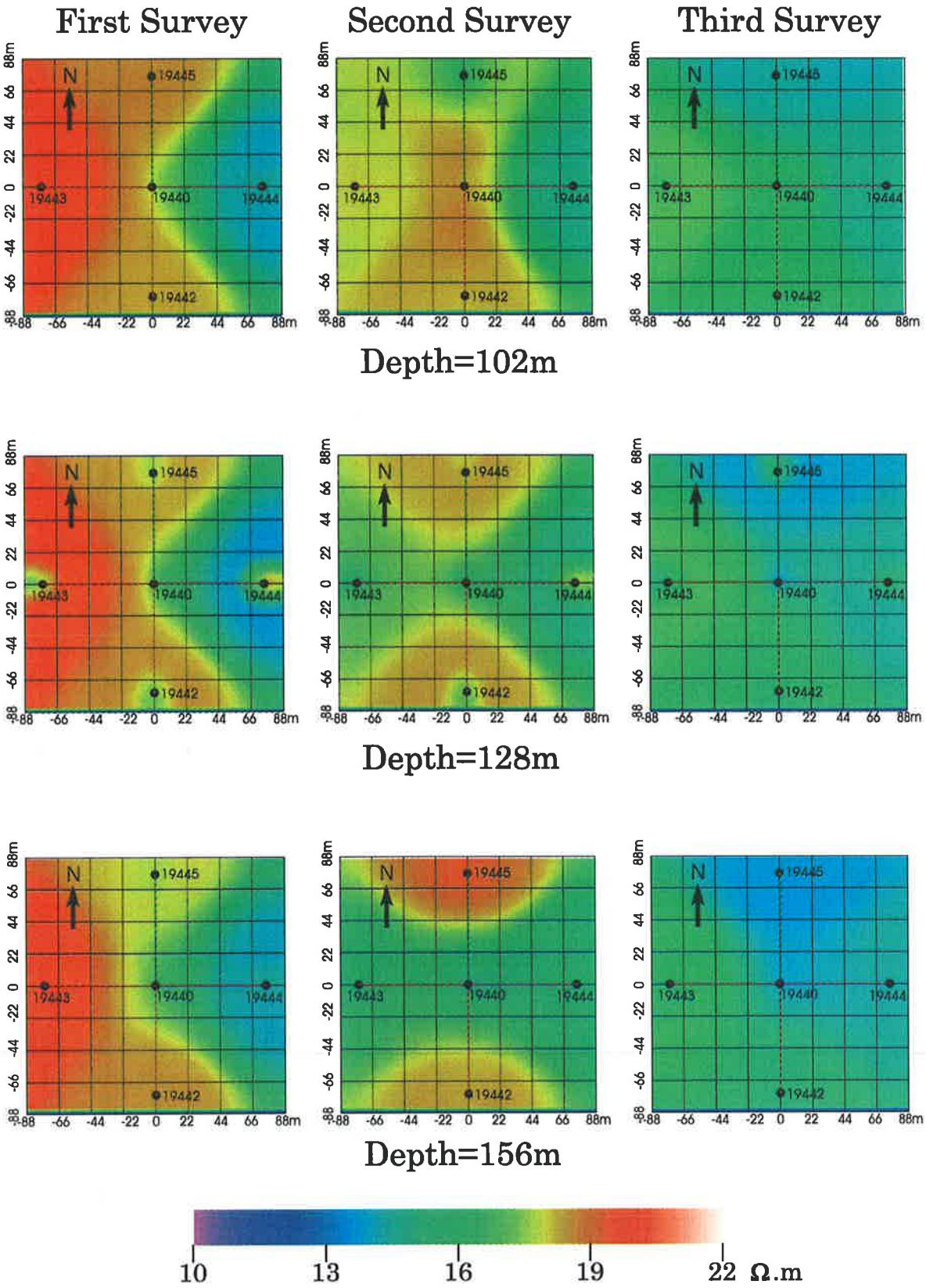

Figure 11.12 The imaging results for the surveys one, two and three (with only 28m spacing data) in Phase II. Three X-Y horizontal sections are shown for each imaging result.

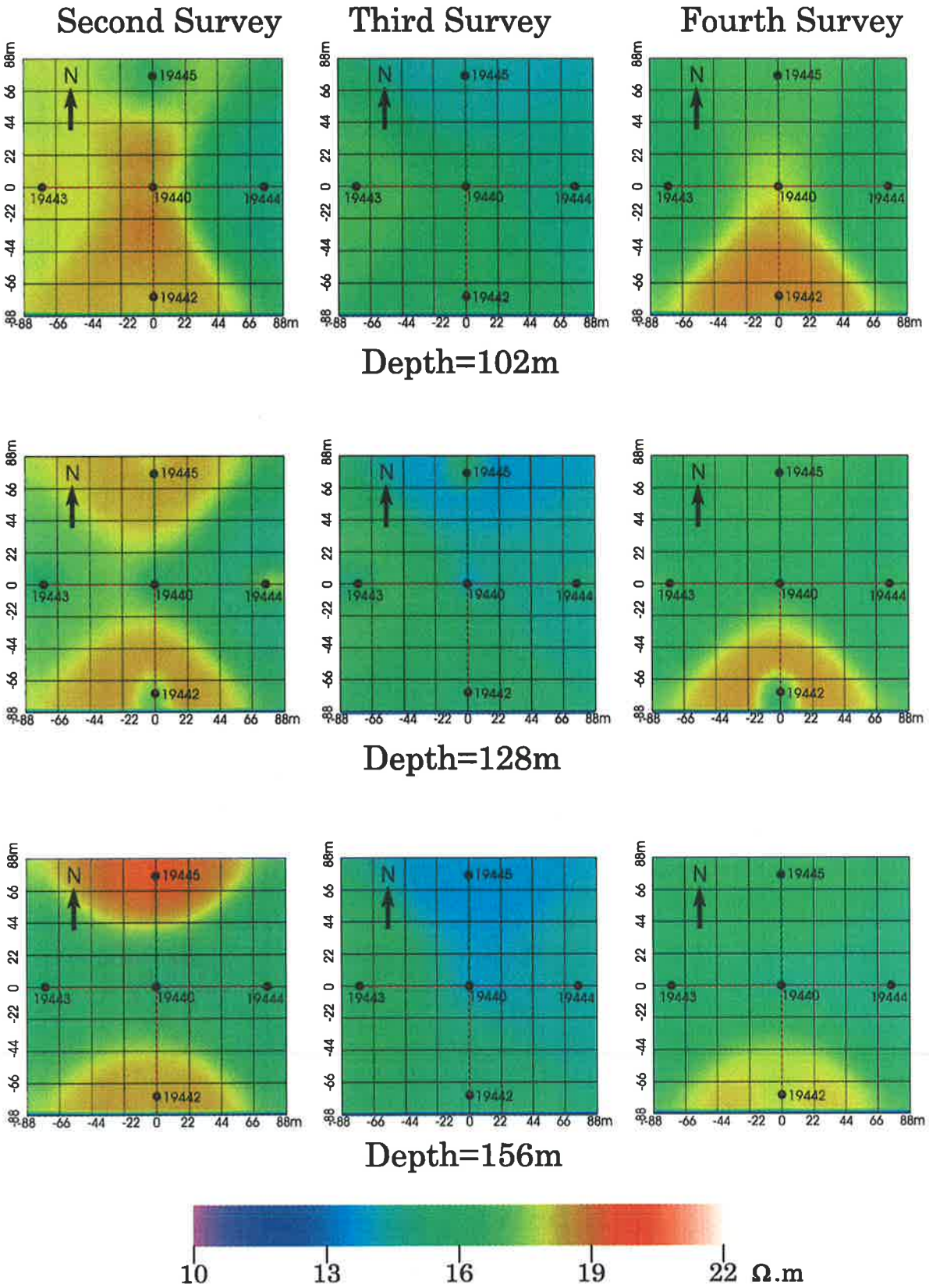

Figure 11.13 The imaging results for the surveys two, three and four (with only 28m spacing data) in Phase II. Three X-Y horizontal sections are shown for each imaging result.

11.3.4 2.5-D Inversion Method

All 16 sets of field data (4 surveys x 4 multiple scannings in each survey) were inverted with both the 14m and 28m spacing data. Results are shown in Figures 11.14 to 11.17. Another 16 inversion results produced from the 28m spacing data alone to remove the local resistivity effect, are shown in Figures 11.18 to 11.21.

From Figure 11.1, we know that the first survey was done prior to water injection. So the inversion results in Figure 11.14 (with the 14m and the 28m data of the first survey) show no anomaly in the middle part of the results except the inversion result (on the right) between Well 19444 and Well19450, which shows the trend of a high-in-the-east and a low-in-the-west. From the inversion results of the 28m spacing data (shown in Figure 11.18), it can be seen that the resistivity distribution in the east is slightly higher than in the west. But the resistivity distribution looks flat over the whole range since this survey was done prior to water injection.

The second survey was done just after the net volume of the injected water reached 35ML (refer to Figure 11.1). From the inversion results shown in Figures 11.15 and 11.19, the water injection effect is obvious. One can see that the high resistivity part expands outwardly from the central Well 19450 in all inversions in the second survey. By comparing the inversion results (Figure 11.19) of the 28m spacing data alone with the inversion results (Figure 11.15) of both the 14m and 28m spacing data, one can see that the former is a little better since it does not contain as much local resistivity effect (around the borehole) which mainly influences the 14m spacing data. From the inversion results of the second survey, one can also see that the high resistivity expansion from the central region started at the top of the T2 Aquifer. This is consistent with the permeability characteristics in the region. The permeability in the top of the T2 aquifer is higher than the bottom sector of the T2 aquifer (Pavelic, 2001). So the injected water will preferentially pass through the top part of the aquifer first.

Apart from the 5 observation wells we used, four additional closely spaced monitoring wells (from 19446 to 19449) were drilled in the south, 50m away from the injection well; and a further four monitoring wells (from 19180 to 19183) were drilled in the north, 50m away from the injection well. The locations of the eight wells along a N-S profile are shown in Figure 11.22. These eight wells are mainly used to monitor the "break-through" of the injected water at different depths in the south and in the north by measuring temperature, water conductivity and water content changes. According to the water conductivity and water

content change records, we know that the injected water broke through Wells 19449, 19447, 19183, and 19181 in early October 2000. This means that it took about two months for the injected water to travel about 50m horizontally. If the injected water continues to travels at the same speed, it should take another 2.5 months for the injected water to reach the 75m wells, since $((75m)^2*h*\pi)/((50m)^2*h*\pi)=2.25$ (where h is the assumed height the water can pass through). According to the calculation, the injected water should have reached the 75m wells in about late December 2000.

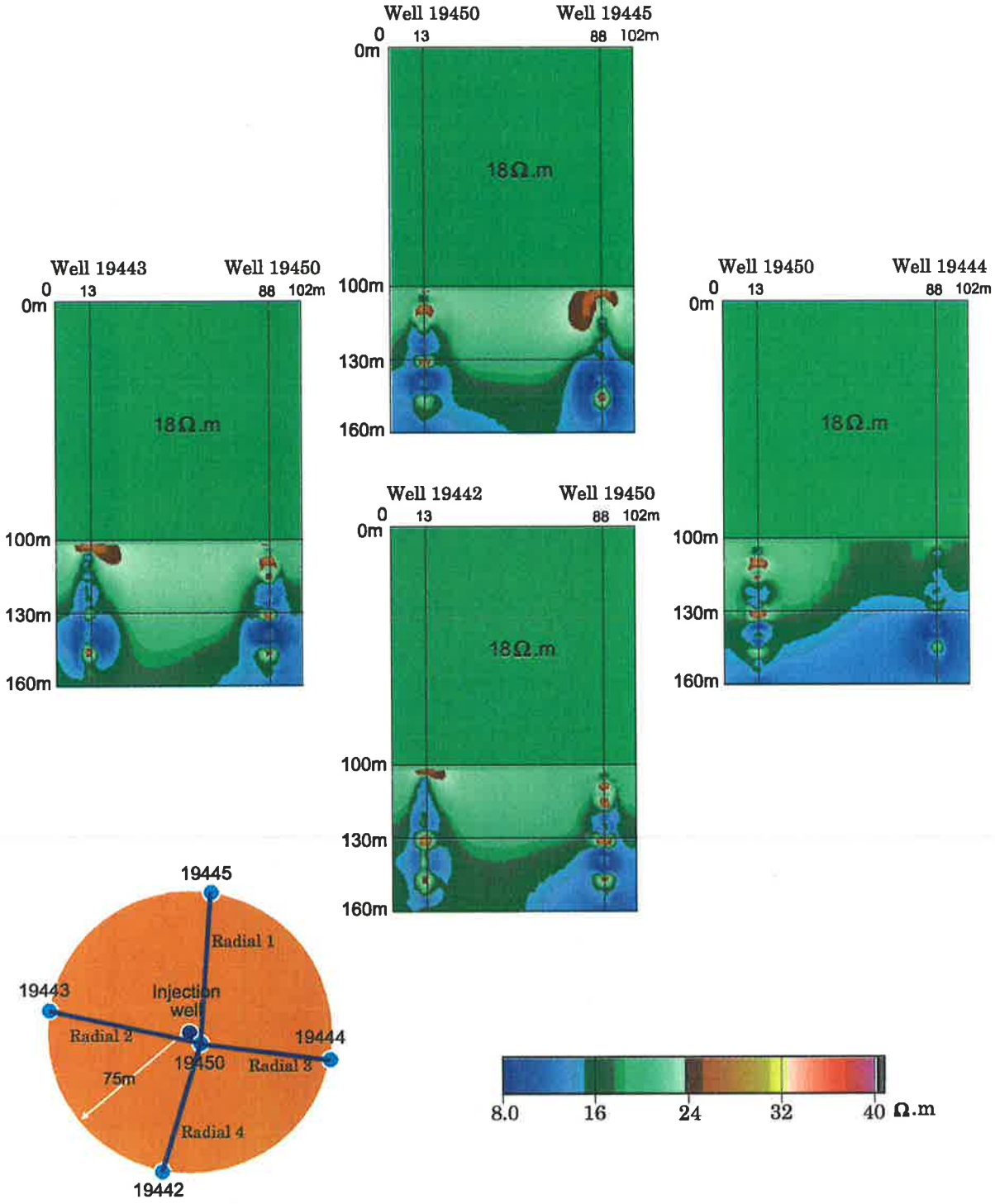

Figure 11.14 The inversion results from the data of the first survey in Phase II with survey layouts overlain. Both 14m and 28m spacing data were used for the inversions.

From the inversion experiments of the numerical modelling data (refer to Chapter 9), we know that when the injected water reaches close to the other observation well, the inverted resistivity distribution becomes a little bit flat, not high near one well and low near the other well. When the injected water reaches the other observation well, the inverted resistivity distribution becomes flat and the inverted resistivity values increase significantly.

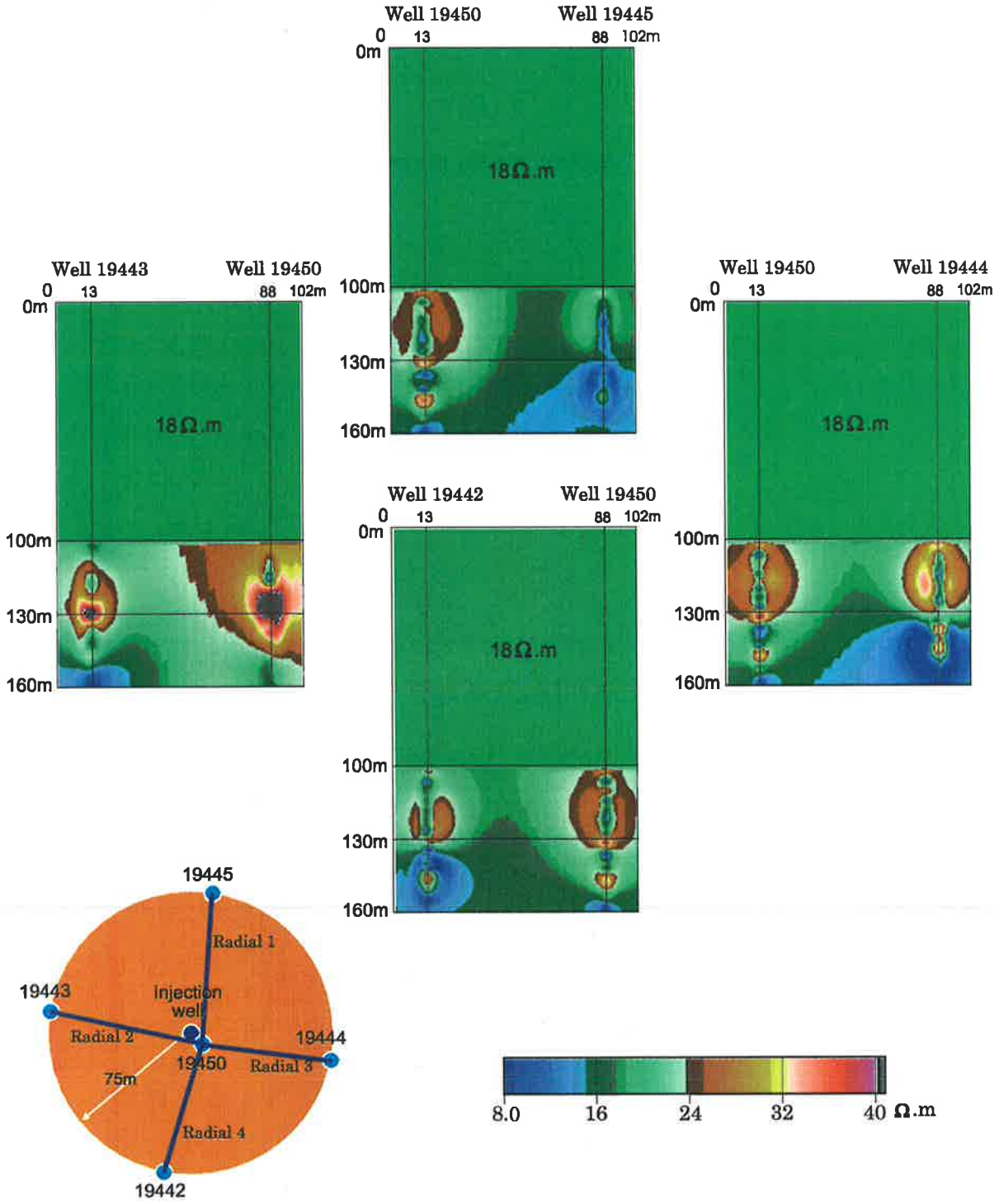

Figure 11.15 The inversion results from the data of the second survey in Phase II with survey layouts overlain. Both 14m and 28m spacing data were used for the inversions.

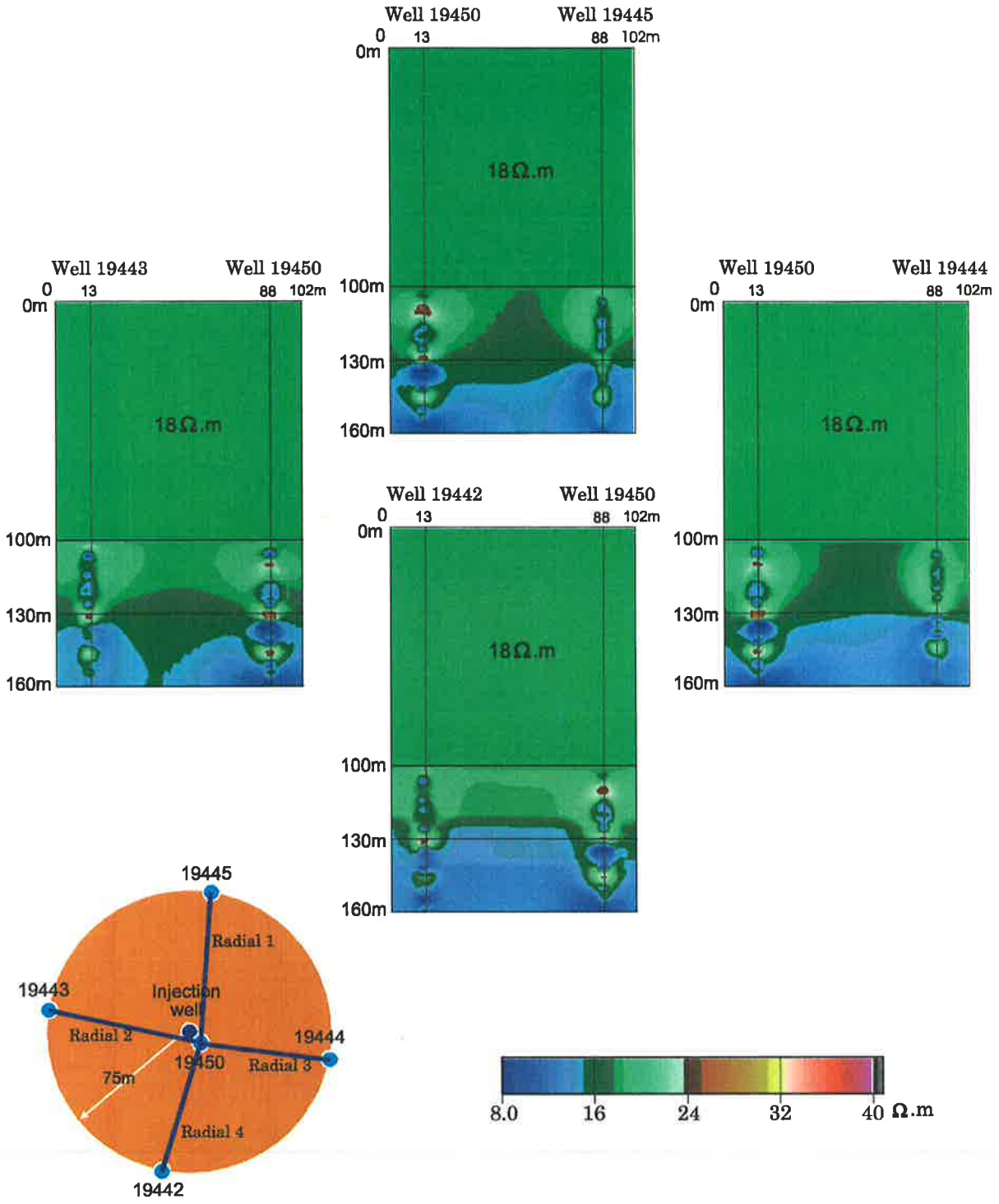

Figure 11.16 The inversion results from the data of the third survey in Phase II with survey layouts overlain. Both 14m and 28m spacing data were used for the inversions.

The third survey was done from 18/12/00 to 22/12/00. According to the above calculation, the injected water may have reached the 75m wells at this time. By examining the inversion results in Figures 11.16 and 11.20 and using the above summary of my numerical inversion experiments, I think the injected water nearly reached Well 19442, since the inversion results between Well 19442 and 19450 show a flat feature and the inverted true resistivity was relatively "not high". I do not think that the injected water reached the other three wells, since

the inversion results of these three sets of data still show that the higher resistivity water was expanding from the injection well outwards. This is apparent from the inversion results of both the 14m+28m data and the 28m spacing data alone.

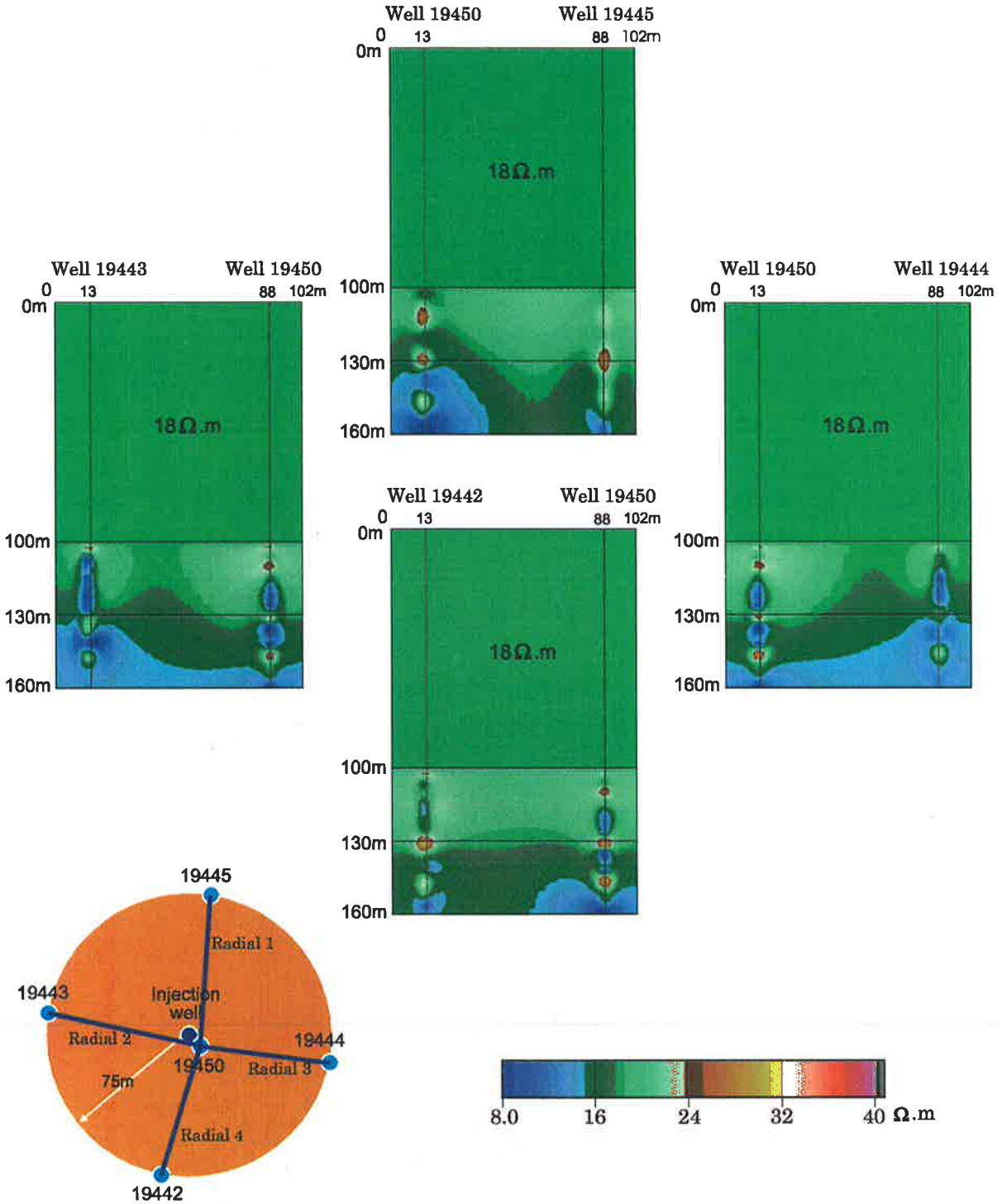

Figure 11.17 The inversion results from the data of the fourth survey in Phase II with survey layouts overlain. Both 14m and 28m spacing data were used for the inversions.

Comparing the inversion results between the third survey and the fourth survey, one can see that the inverted resistivities between Well 19442 and 19450, and between Well 19445 and

19450 in the fourth survey are relatively much higher than the inverted resitivities in the third survey. Also the inverted resistivity distribution between these two pairs of wells in the fourth survey shows the flat feature. Therefore I think that the injected water has fully reached Wells 19442 and 19445. However, the inversion results of the other two pairs of wells still show the water expanding feature, or high resistivity near the injection well expanding outwards. So I do not believe that the injected water came close to Well 19443 and 19444.

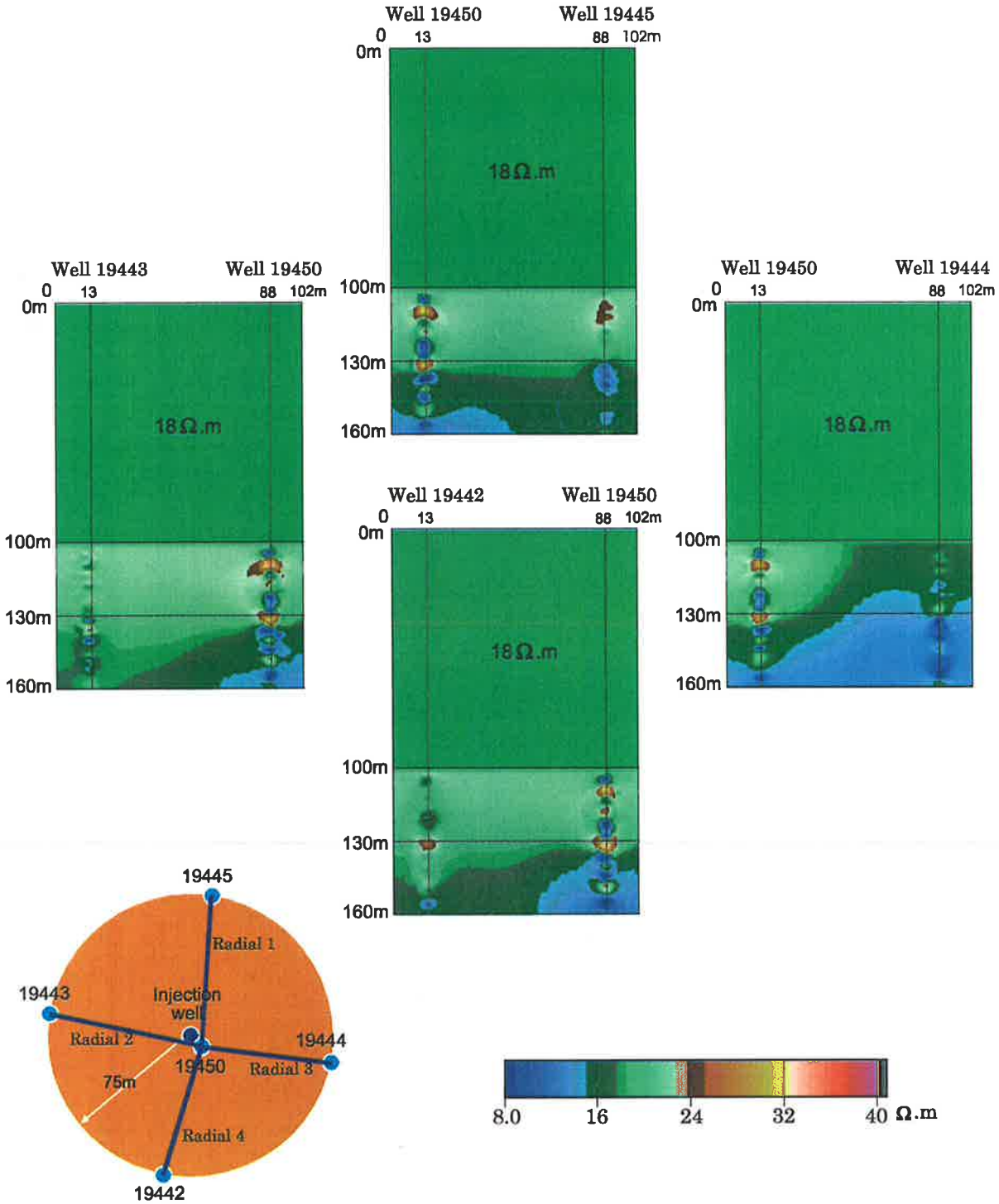

Figure 11.18 The inversion results from the data of the first survey in Phase II with survey layouts overlain. Only 28m spacing data were used for the inversions.

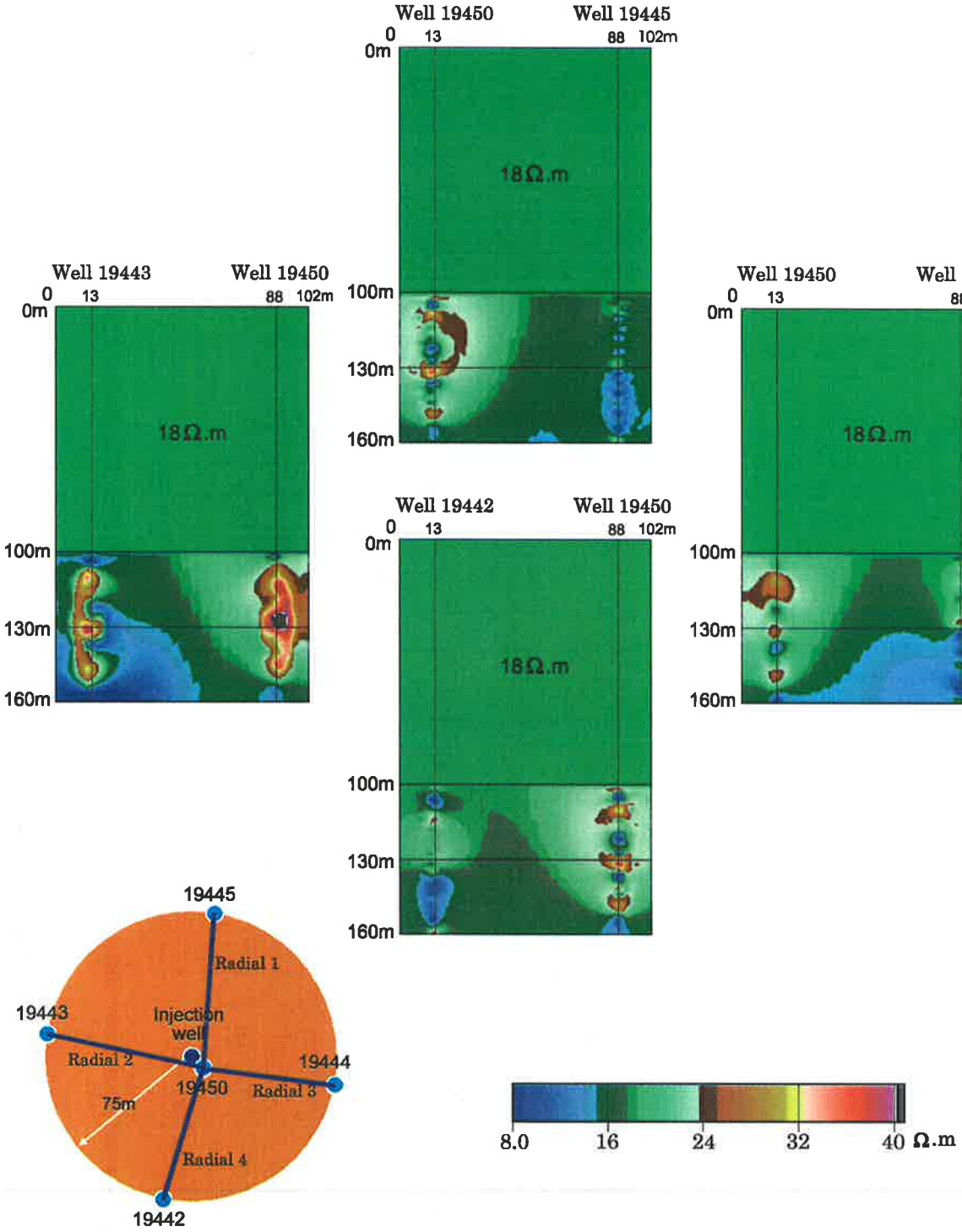

Figure 11.19 The inversion results from the data of the second survey in Phase II with survey layouts overlain. Only 28m spacing data were used for the inversions.

By examining all inversion results, one can find that the depth 130m is a special point. Firstly, there is a relative high resistivity spot near each well at this depth in almost all inversion results. This means that there is a thin high resistivity layer at this depth. This supports the conclusion obtained in Section 11.3.2.2. According to my experiments, it is impossible to invert this thin layer with such a poor survey configuration and so few data points (as a result of the restricted access range in partially cased holes). Secondly, in most of

the inversion results, one can see that the T2 aquifer is divided into two parts, separated at a depth of around 130m.

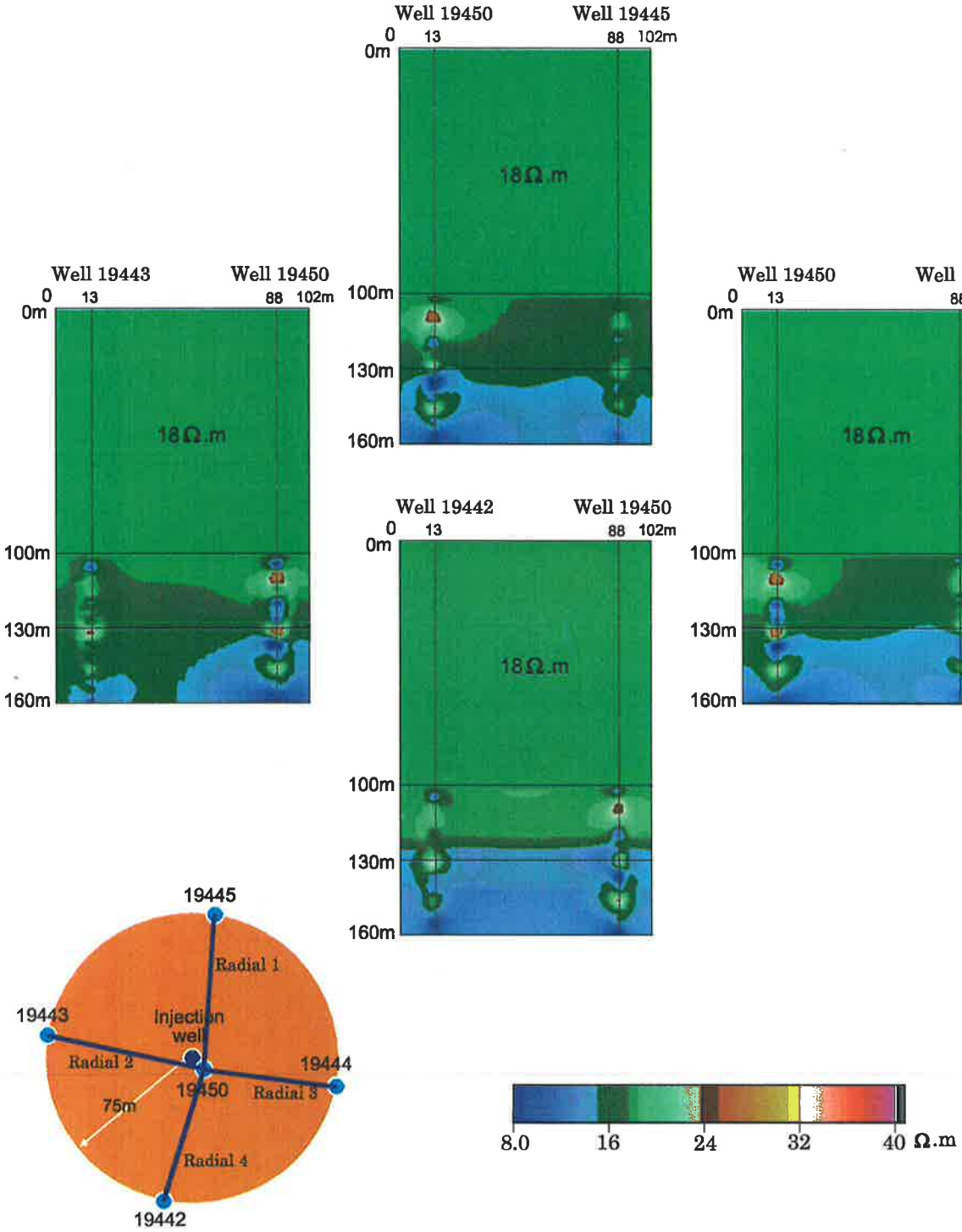

Figure 11.20 The inversion results from the data of the third survey in Phase II with survey layouts overlain. Only 28m spacing data were used for the inversions.

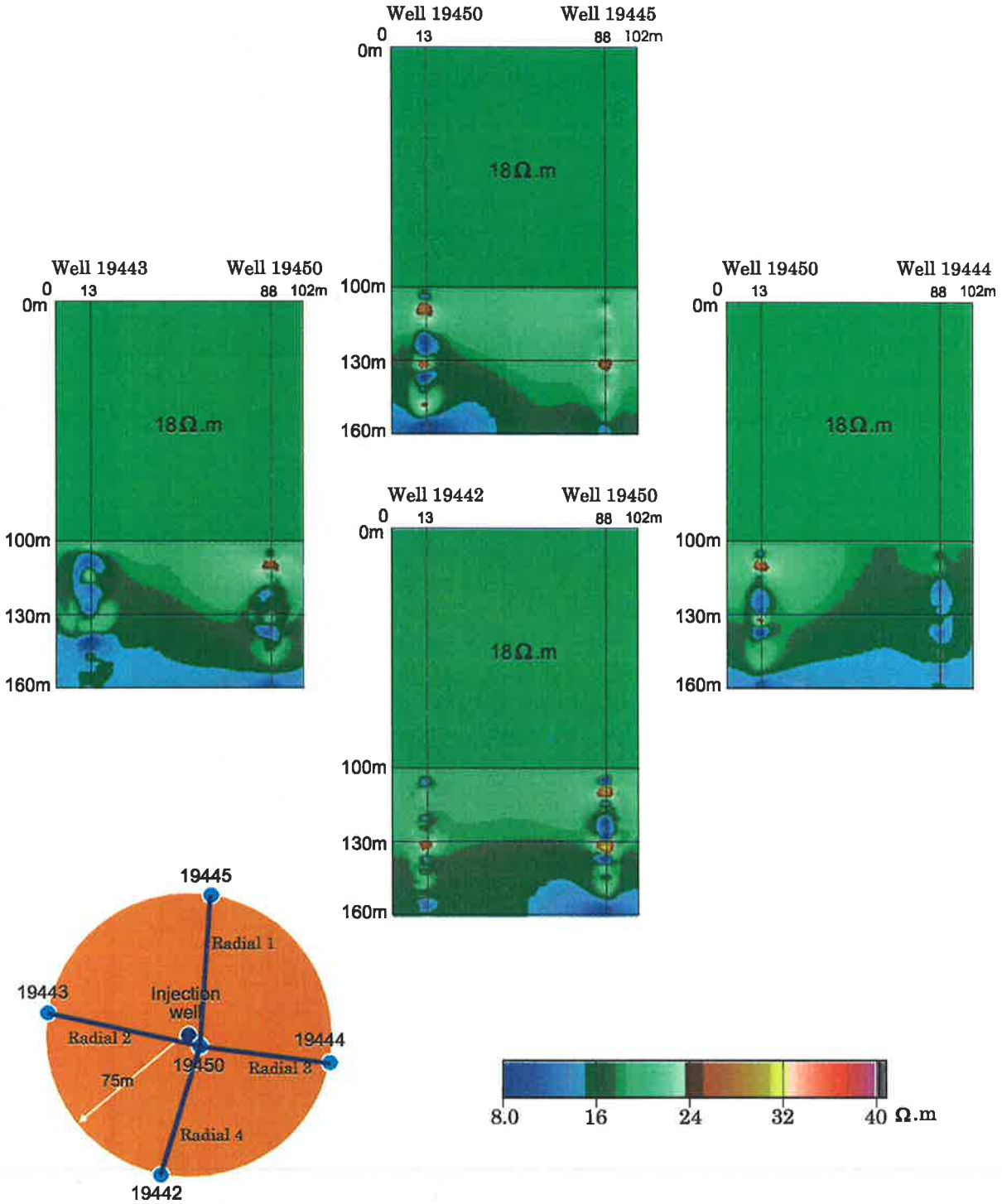

Figure 11.21 The inversion results from the data of the fourth survey in Phase II with survey layouts overlain. Only 28m spacing data were used for the inversions.

The residual error and the relative error percentage for all inversions in this phase were calculated to check the accuracy of the inversion. The average relative error percentages for all inversions are similar to those in Phase I. They are smaller than 1 percent. So the inversion accuracy is reasonable.

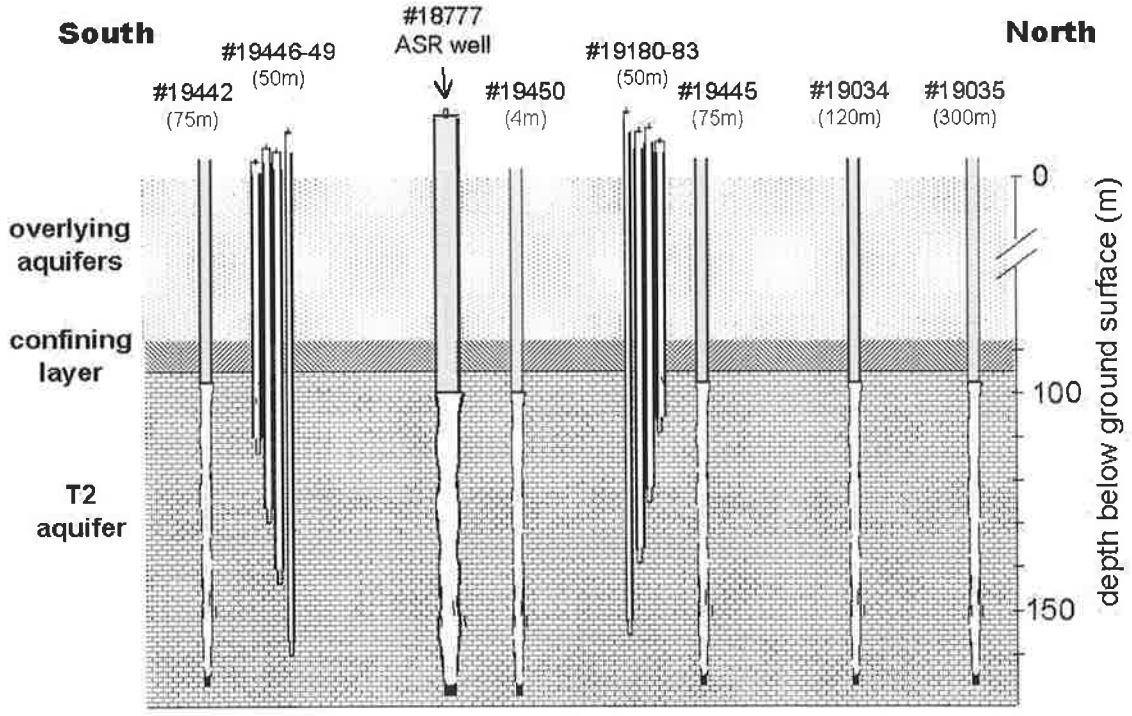

Figure 11.22 Simplified vertical section showing location of observation and monitoring wells

11.4 CONCLUSIONS

Four field tomography resistivity surveys were conducted at different stages of the water injection and 16 sets of multiple spacing 'crosshole multiple scannings' (4 sets in each survey) were completed during Phase II of the Bolivar experiment. The same crosshole bipole-biole *AM-BN* configuration as used in Phase I was applied to each crosshole multiple scanning. But different pairs of wells were used for the four surveys. All crosshole resistivity multiple scannings in this phase were completed in the radial direction, instead of on the four chords.

The same three methods as used in the last chapter were employed to interpret the survey data in the phase. The three methods interpret the survey data from different points of view. The conclusions from the three methods support each other. However, the inversion method can give more detail and a more accurate interpretation. It is a very necessary tool for interpreting crosshole resistivity survey data.

In conclusion, according to the above interpretation, it appears that the injected water flows in all directions, but mainly flows towards the south and the north; the injected water reached Well 19445 and Well 19442 between the third survey and the fourth survey; the injected

water did not reach Well 19443 and Well 19444. In general, the resistivity distribution in the region decreases with depth. There is a thin high resistivity layer at a depth of 130m, which separates the T2 aquifer into two parts.

Chapter 12

CONCLUSIONS AND DISCUSSION

12.1 CONCLUSIONS

The primary objective of this study was to develop a suitable resistivity imaging method to dynamically monitor the water flow direction in an Aquifer Storage and Recovery (ASR) trial project in Adelaide, after fresh water was injected into the T2 Aquifer, at a depth of 100m below the surface. This project involved electrical resistivity theory, resistivity numerical modelling and electrical inversion program development and experiments, building of a fully automatic resistivity physical modelling system, conducting crosshole resistivity field surveys, as well as undertaking field data processing, inversion and interpretation. So this PhD investigation was a comprehensive application research project.

In Chapters 1 and 2, I reviewed the basic theory of the resistivity method, and derived all of the formulas needed for the later chapters. I also reviewed the popular surface resistivity methods, different survey configurations, and some crosshole resistivity research work.

In Chapters 3 and 4, I reviewed the methods and theory used in numerical resistivity modelling and inversion. Then following the PhD work of B. Zhou, I completely rederived all formulas for 2.5-D resistivity modelling and inversion in order to thoroughly understand his work, and to modify his programs for my project. I also derived the formulas for 3-D resistivity modelling and developed the 3-D resistivity modelling program by myself. Numerous numerical resistivity modelling and inversion experiments were conducted in the chapters to validate the programs and to understand what sort of results to be expected at the field site. The inversions work well when the data acquisition geometry is favourable, but have difficulty with situation like the Bolivar experiment when access is restricted due to casing and the possible electrode spacings are small relative to the well spacing.

Initially, I planed to build a fully automatic 3-D physical resistivity modelling system with a large water tank to be used in the project. Using my knowledge of electronics and microcontrollers, I designed the 3-D physical resistivity modelling system myself with some help from an electronics technician and a mechanical technician. To obtain high efficiency for the physical modelling, the system was designed to be fully automatic, which includes

automatic positioning of electrodes, automatic current injection (on and off) and automatic data logging. All mechanical parts, including the water tank, 3-D electrode moving system (stepper motors, steel axes and mechanical support) and position measurements, were completely finished and tested with a manual stepper motor control box. The power box for providing injection current was completed by myself and tested. It works fine. The design of the power control (on/off) box, stepper motor control box and the main control box are finished and all printed circuit boards have been made for assembling. Unfortunately, I did not completely finish building the system mainly due to the lack of time and technical support.

This ASR project involved a lot of electrical field experiments. Before the water injection started, numerous surface, surface-to-borehole and borehole-to-borehole electrical field experiments were conducted. These experiments helped us understand the resistivity distribution in the region and find a better crosshole resistivity survey configuration for the ASR project. The crosshole bipole-bipole *AM-BN* configuration was chosen for all our crosshole surveys. There are two main advantages of this configuration. One is that there is no singularity problem in the calculation of apparent resistivity and it is easy to operate. The second one is that the survey data is less affected by the resistivity distribution changes outside of the survey region. This is especially very important for the time-lapse surveys, otherwise the resistivity changes outside of the survey region have to be considered when the survey data is interpreted. Since the resistivity contrast before and after water injection is not large, this is even more important to us.

To interpret the field data, many numerical resistivity modelling and inversion experiments were conducted and the sensitivity distributions for the electrical configurations used in the project were calculated. The experiments were designed to simulate the field surveys and some special model effects, such as the borehole water effect in a crosshole survey and the possibility of inverting a vertical contact of two layers between two wells. The calculated sensitivity distributions for the bipole-bipole configuration illustrate how useful the configuration is for the relatively wide well separations used in our tomography experiments. A closer well spacing will be preferable. The modelling and inversion experiments for the field surveys are very helpful in interpreting the field surveys, especially for the Bolivar time-lapse crosshole resistivity surveys. These experiments also discovered some very interesting things, such as turning points in an apparent resistivity profile and pseudo depth profile patterns.

Since only a few researchers (Slater et al., 2000; Spies and Robert, 1995) have completed this kind of field research work before, I had to develop my own survey design, data display method, data processing method, and my own data interpretation scheme, which is the most difficult part. The decision to drill the four observation wells on the circumference of a circle of radius 75 meters was beyond my control. This made the distance between two wells much larger than the accessible range in each well. So this posed a problem for data inversion, with the limited survey coverage.

In total, seven time-lapse crosshole resistivity tomography surveys were completed at the different stages of the water injection. A lot of data were collected and processed. Three interpretation tools were used for the interpretation of the field data. Firstly, all survey data were plotted in the pseudo depth profile format for checking and basic analysis. From the profiles, I checked all data to remove some bad points, found common turning points and analysed profile patterns. Secondly, I used our 3-D approximate imaging program to produce a 3-D resistivity distribution image. From the image, I obtained the basic resistivity distribution in the region. Lastly, the field data were inverted for each pair of boreholes with our modified 2.5-D inversion program. Then the final interpretation was based on the inversion results. The interpretations of the inversion results were supported by other scientific monitoring data, such as well log patterns, time-lapse conductivity measurements, and basically matched with them rather well. By comparing the inversion results in the different stages of the water injection, I deduced the possible water flow directions among different stages. I am confident about the survey data interpretation result.

All inversion results from both numerical and field data gave a clear resistivity distribution near the wells, but not in the middle part of the section. This mainly is due to the following two reasons. The first one is that the accessible range (54m) in each well is much smaller than the distance (104m in Phase I and 75m in Phase II) between two wells, which is supported by the calculated sensitivity distributions in Section 8.3 and Section 9.3. This greatly limited the inversion capability. The second is that the number of the data points (637 for the both 14m and 28m data or 196 for the only 28m data) for each inversion is much less than the number of cells (1560 in Phase I and 1180 in Phase II) in the survey region. So these inversions are purely underdetermined.

12.2 DISCUSSION

From the experience I gained during this project, I think that resistivity inversion is a very necessary tool for crosshole resistivity data interpretation. There is no better way to analyse and interpret the data properly and accurately. It provides reasonably accurate interpretation if the quality of the survey data is good, and it can also be done almost automatically. However, the inversion has some stringent requirements: a large mount of data and the right survey configuration. To obtain a lot of electric data for an inversion is a very hard and time-consuming task with a standard electrical survey instrument. It took us one full day to obtain 637 data points and it took at least four full days for a single survey. So to develop a fully automatic survey system for borehole resistivity surveying is very important. This kind of system will have two other advantages: 1) reduce the local (near-well) resistivity change effect on the survey data since it uses much less time to finish a survey; 2) enable the completion of a survey before the wells become blocked, (which is proportional to time, especially as casing is not allowed in the resistivity survey wells). To build and use this kind system is my ultimate goal.

The right crosshole resistivity survey configuration is very important for the resistivity inversion. From my experience, the accessible depth range (uncased) in each well should be at least as large as the distance between the two wells, in order to obtain a good inversion result. Multiple spacing acquisition between two electrodes in the same well is much better than single spacing acquisition. This is similar to surface resistivity surveying. The largest spacing in the multiple spacing acquisition should be at least as large as the half distance between the two wells. This will obtain more information about the middle part of two wells and will produce a better inversion result for the interwell medium. A sensitivity distribution for an electrical configuration is a good tool to use if the array is suitable for practical situations.

As mentioned before, I did not finish building the 3-D fully automatic physical laboratory resistivity modelling system. The plan is for someone to complete it later since about 80% of the work have been done. After it is built, it will be a very useful and helpful tool for research, teaching and routine commercial surveying. It will be very easy to use as well, since it is fully automatic.

Bibliography

Apparao, A., and Roy, A., 1969, Resistivity model experiments, *Geoexploration, 7*, 45-54.

Apparao, A., and Roy, A., 1971, Resistivity model experiments, *Geoexploration, 9*, 195-205.

Apparao, A., 1979, Model tank experiments on resolution of resistivity anomalies obtained over buried conducting dykes - Inline and broadside profiling: *Geophys. Prosp.*, **27**, 835-847.

Archie, G. E., 1942. The electric resistivity log as an aid in determining some reservoir characteristics. *Tran. AIME* **146**, 54-62.

Asch, T., and Morrison, H.F., 1989, Mapping and monitoring electrical resistivity with surface and subsurface electrode arrays, *Geophysics*, **54**, 235-244.

Barker, R D, 1988, Resistivity soundings in engineering investigations with the offset Wenner technique, *Geophysics*, Vol **38**, p. 355-366

Barker, R. D., 1990, Investigation of groundwater salinity by geophysical methods, in Ward, S. H., Ed., *Geotechnical and Environmental Geophysics*, **02**: Soc. of Expl. Geophys., 201-211.

Barker, R. and Moore, J., 1998, The application of time-lapse electrical tomography in groundwater studies: *The Leading Edge*, **17**, no. 10, 1454-1458.

Benson, A. K., Payne, K. L. and Stubben, M. A., 1997, Mapping groundwater contamination using DC resistivity and VLF geophysical methods - A case study: *Geophysics*, **62**, 80-86.

Bevc, D., and Morrison, H.F., 1991, Borehole-to-surface electrical resistivity monitoring of a salt water injection experiment, *Geophysics*, **56**, 769-777.

Bhattacharya, P. and H. Patra, 1968, Direct current geoelectrical sounding: Elsevier Publishing Company, New York, 133 pp.

Binley, A., G. Cassiani, R. Middleton and P. Winship, 2001a, Hydraulic Parameterisation aided by cross-borehole radar and resistivity imaging, In: Proc, 7th Meeting of the Environment and Engineering Geophysics Society (European Section), Birmingham, UK., 2001, p188-189.

Binley, A., P. Winship and M. Pokar, 2001b, Cross borehole radar and resistivity tomography: A comparison of techniques in unsaturated sandstone, In: Proc., Symp. Applications of Geophysics to Engineering and Environmental Problem (SAGEEP2001), Environmental and Engineering Geophysical Society, Denver, CO.

Binley, A., W. Daily and A. Ramirez, 1997, Detecting leaks from environmental barriers using electrical current imaging, J. Env. And Eng. Geophysics, Vol. 2(1), p11-19.

Binley, A., B. Shaw and S. Henry-Poulter, 1996, Flow pathways in porous media: Electrical resistance tomography and dye staining image verification, *Measurement Science and Technology,* **Vol. 7(3),** p384-390.

Buselli, G. and Lu, K., 2000, Detection of groundwater contamination with induced polarisation and resistivity methods using a 64-channel receiver, 62nd Mtg. Eur. Assn. Geosci. Eng., Session:D0007.

Boerner, E., and Holladay, J. S., 1990, Approximate Fréchet derivative in inductive electromagnetic soundings, *Geophysics* **55**, 1589-1595.

Chunduru, R., Sen, M. K., and Stoffa, P. L, 1996, 2-D resistivity inversion using spline parameterization and simulated annealing, *Geophysics,* **61,** 151-161.

Coggon, J. H., 1971, Electromagnetic and electrical modeling by the finite element method, *Geophysics*, **36**, 132-155.

Daily, W., A. Ramirez, D. LaBrecque and W. Barber, 1995, Electrical resistance tomography experiments at the Oregon Graduate Institute, *Applied Geophysics*, **33**, 227-237.

Daily, W., and Owen, E., 1991, Cross-borehole resistivity tomography, *Geophysics*, **56**, 1228-1235.

Daniels, J. J., 1977, Three-dimensional resistivity and induced-polarisation modeling using buried electrodes, *Geophysics*, **42**, 1006-1019.

Das, U. C., and Parnasis, D. S., 1987, Resistivity and induced polarization responses of arbitrarily shaped 3-D bodies in a two-layered earth, *Geophysical Prospecting,* **35**, 98-109.

Dasey, G. R., & Acworth, R. I., 2000. The use of borehole tomography to image the saline interface – A case study from New South Wales, Australia. In Olivier Sililo etal (eds) Proceedings of the XXX IAH Congress on Groundwater – Past Achievements and Further Challenges.

de Lima, O.A.L. & Niwas, S., 2000, Estimation of hydraulic parameters of sghaly sandstone aquifers from geoelectrical measurements, *Hydrology*, Vol **235**, 12-26.

Dey, A., and Morrison, H. F., 1979a, Resistivity modeling for arbitrarily shaped two-dimensional structure, *Geophysical Prospecting,* **27**, 106-136.

Dey, A., and Morrison, H. F., 1979b, Resistivity modeling for arbitrarily shaped three-dimensional structure, *Geophysics,* **44**, 753-780.

Dillon, P.J., Pavelic, P., Wright, M., Peter, P. and Nefiodovas, A. 2001. Small-scale heterogeneity and anisotropy of a confined carbonate aquifer from triaxial tests on core samples. *Proc IAH XXXI Congress*, Munich, Sept. 2001.

Dobrin M., 1988, Introduction to Geophysical Prospecting, McGraw-Hill Book Company, New York, 752pp.

Ebraheen, AAM, Senosy, MM & Dahab, K.A., 1997, Geoelctrical an dhydrogeological studies for delineating groundwater contamination due to salt water intrusion in the northern part of the Nile Delata, Egypt, Groundwater, Vol 35, 216-227

Frangos, W., 1994, Electrical detection of leaks in lined waste ponds, 64th Ann. Internat. Mtg. Soc. of Expl. Geophys., 648-651.

Gerges, N. Z., 1996, Proposals for injecting effluent for aquifer storage and recovery scheme, *Proceedings of An International Symposium on Artificial recharge of Groundwater*, Helsinki, Finland.

Greenhalgh, S., Zhe, J. and Zhou B. 2001. A trial of cross-hole electric imaging for monitoring aquifer artificial recharge. Proc IAH XXXI Congress, Munich, Sept 2001.

Goudswaard, W., 1957, On the effect of the tank wall material on geoelectrical model experiments, *Geophys. Prosp.*, **5**, 272-281.

Hauck, C. and Vonder Muhll, D., 1999, Using DC resistivity tomography to detect and characterise mountain permafrost, 61st Mtg. Eur. Assn. Geosci. Eng., Session:2015.

Hobbs, B. A., 1992, 2D resistivity modelling using parallel processing, 54th Mtg. Eur. Assn. of Expl. Geophys., 634-635.

Holcombe, H. T., and Jiracek, G. R., 1984, Three-dimensional terrain corrections in resistivity surveys, *Geophysics*, **49**, 439-452.

Jackson, P. D., 1981, Focussed electrical resistivity arrays - Some theoretical and practical experiments: *Geophys. Prosp.*, **29**, 601-626.

Jakosky, J. J., 1961, Exploration Geophysics. Trija Publishing Co., Newport Beach, 1195 pp.

James, B. A., 1985, Efficient microcomputer-based finite difference resistivity modeling via Polozhii decomposition, *Geophysics*, **50**, 443-465.

Joshi, M. S., Gupta, O. P. and Negi, J. G., 1984, Scale-model response of a thin vertical conductor below a conductive inductive or laterally inhomogeneous overburden layer: *Geophysics*, **49**, 2159-2165.

Karwatowski, J. and Habberjam, G. M., 1981, A tunnel resolution investigation using an automated resistivity tank analog: *Geophys. Prosp.*, **29**, 891-905.

Keller, G. V., and F. C. Frischknecht, 1966, Electrical Methods in Geophysical Prospecting: Pergamon Press, New York, 517 pp.

Kemna, A. and A. Binley, 1996, Complex electrical resistivity tomography for contaminant plume delineation, In: Proc. 2nd Meeting of the Environmental and Engineering Geophysics Society, Nantes, 2-5, September, 1996, p196-199.

Kenneth, H. H., 1975, The Finite Element Method for Engineers, Wiley Interscience, USA, 107pp.

Kumata, M., Chiba, A. and Kubota, R., 1993, Model tank experiments for basic study on resistivity tomography, 63rd Ann. Internat. Mtg. Soc. of Expl. Geophys., 1309-1311.

Kumata, M., Li, H., and Chiba, A., 1995, Physical model simulation tests for resistivity tomography: 65th International Meeting of SEG, Expanded Abstracts, 1309-1311.

Kunetz, G., 1966, Principles of direct current resistivity prospecting: Gebruder Borntraeger, Berlin, 103 pp.

LaBrecque, D., Miletto, M., Daily, W., Ramirez, A., and Owen, E., 1996, The effects of " Occam" inversion of resistivity tomography data, *Geophysics*, **61**, 538-548.

Lee, T., 1975, An integral equation and its solution for some two and three-dimensional problems in resistivity and induced polarization, *Geophys. J.*, **42**, 81-95.

Lesur, V., Cuer, M., and Straub, A., 1999, 2-D and 3-D interpretation of electrical tomography measurements, Part1: The forward problem, *Geophysics,* **64,** 386-395.

Lesur, V., Cuer, M., and Straub, A., 1999, 2-D and 3-D interpretation of electrical tomography measurements, Part2: The inverse problem, *Geophysics,* **64,** 396-402.

Loke, M. H., and Barker R. D., 1996, Rapid least-squares inversion of apparent resistivity pseudosections by a quasi-Newton method, *Geophysical Prospecting*, **44**, 131-152.

Lowry, T., Allen, M. B., and Shive, P. N., 1989, Singularity removal: A refinement of resistivity modeling techniques, *Geophysics*, **54**, 766-774.

Mares, S., 1984, Introduction to Applied Geophysics: D. Reidel Publishing Company, Dordrecht/Boston/Lancaster, 265pp.

McCartre, W.J. & Desmazer, P., 1997, Soil characterisation using electrical measurements, Geotechnique, Vol. 47, 179-184.

McGillivray, P. R., and Oldenbury, D.W., 1990, Method for calculating Fréchet derivatives for the non-linear inverse problem: a comparative study, *Geophysical Prospecting*, **38**, 499-524.

Meekes, J. A. C., 1993, Overview geophysical techniques for groundwater and environmental applications, 55th Mtg. Eur. Assn. of Expl. Geophys., Session:D041.

Middleton, R. T. and A. M. Binley, 2001, Characterisation of unsaturated zone recharge mechanisms using 3-D cross-borehole electrical resistivity tomography imaging: A comparison from the permo-triassic sandstone and cretaceous chalk aquifers in Yorkshire, England, In: Proc. 7th Meeting of the Environment and Engineering Geophysics Society (European Section), Birmingham, UK., 2001, p202-203.

Mooney, H.M., 1980, Handbook of Engineering Geophysics volume 2: Electrical Resistivity, Bison Instruments, Minneapolis.

Mufti, I. R., 1976, Finite difference resistivity modeling for arbitrary shaped two-dimensional structures, *Geophysics*, **41**, 62-78.

Mundry, E., 1984, Geoelectical model calculations for two-dimensional resistivity distributions, *Geophysical Prospecting*, **32**, 124-131.

Odins, J. A., Williams, R. M. and O'Neill, D. J., 1985, Use of geophysics for the location of saline groundwater inflow to the Murray river east of Mildura: 4th Geophysical Conference, Austr. Soc. Expl. Geophys., 16, 256-258.

Okabe, M., 1981, Boundary element method for the arbitrary inhomogeneity problem in electrical prospecting, *Geophysical Prospecting*, **29**, 39-59.

Osiensky, J. L., & Donaldson, P., 1995, Electrical flow through an aquifer for contaminant source leak detection and delineation of plume evolution, Hydrology, Vol 169, 243-263

Pantholu, T.V., Krishraiah, C. & Shirke, J. M., 2001, Detection of seepage paths in earth dams using self potential and electrical resistivity methods, Engineering Geology, Vol 59, 281-296

Park, S. K., and Van, G. P., 1991, Inversion of pole-pole data for 3-D resistivity structure beneath arrays of electrodes, *Geophysics*, **56**, 951-960.

Park, S. K., 1998, Fluid migration in the vadose zone from 3-D inversion of resistivity monitoring data, *Geophysics*, **63**, 41-51.

Parkhomenko, K., 1967, Electrical Properties of Rocks: Plenum Press, New York, 314pp.

Pridmore, D., Hohmann, G. W., Ward, S. H., and Sill, W. R., 1981, An investigation of finite element modeling for electrical and electromagnetic modeling data in three dimensions, *Geophysics*, **46**, 1009-1024.

Pritchard, J. I. and Renick, H., Jr., 1981, Today's exploration capability of electrical method surveys, 51st Ann. Internat. Mtg. Soc. of Expl. Geophys., Session:P3.1.

Pyne, R.D.G., 1995, Groundwater Recharge and Wells: A guide to aquifer storage recovery. Lewis Publisher, CRC Press, 376p.

Queralt, J. P., and Marcuello, A., 1991, 2-D resistivity modeling: An approach to arrays parallel to the strike direction, *Geophysics*, **56**, 941-950.

Ramirez, A., W. Daily, A. Binley, D. LaBreque and D. Roelant, 1996, Detection of leaks in underground storage tanks using electrical resistance method, *J. Env., and Eng. Geophysics,* **Vol. 1(3),** 189-203.

Ritz, M., Robain, H., Pervago, E., Albouy, Y., Camerlynck, C., Descloitres, M. and Mariko, A., 1999, Improvement to resistivity pseudosection modelling by removal of near-surface inhomogeneity effects: application to a soil system in south Cameroon: *Geophys. Prosp.,* **47**, 85-101.

Roy, A. and Apparao, A., 1971, Depth of investigation in direct-current methods: *Geophysics*, **36**, 943-959.

Roy, A. and Apparao, A., 1976, Laboratory results in resistivity logging : *Geophys. Prosp.*, **24**, 123-140.

Roy, A., 1978, Discussion of 'A modified pseudosection for resistivity and induced-polarization', by Edwards, L. S.: *Geophysics*, **43**, 1275-1276.

Sandberg, S. K., 1993, Examples of resolution improvement in geoelectrical soundings applied to groundwater investigations: *Geophys. Prosp.,* **41**, 207-228.

Sasaki, Y., 1994, 3-D resistivity inversion using the finite element method, *Geophysics*, **59**, 1839-1848.

Shima, H. and Saito, H., 1988, Application of resistivity tomography for detection of faults and evaluation of their hydraulic continuity: Some numerical experiments, 58th Ann. Internat. Mtg. Soc. of Expl. Geophys., Session:EM1.4.

Shima, H., 1992, 2-D and 3-D resistivity imaging reconstruction using crosshole data, *Geophysics*, **55**, 682-694.

Sill, W. R. and Sjostrom, K. J., 1990, Groundwater flow direction from borehole-to-surface electrical measurements, 60th Ann. Internat. Mtg. Soc. of Expl. Geophys., 535-537.

Singh, J., Jha and Gupta, 1971, Model tank experiments for resistivity measurements on non-conducting and conducting sheets, *Pure & Applied Geophys.*, **85**, 90-106.

Slater, L., A. Binley, W. Daily and R. Johnson, 2000, Cross-hole electrical imaging of a controlled saline tracer injection, *J. Applied Geophysics*, **44**, 85-102.

Slater, L., A. Binley and D. Brown, 1997a, Electrical imaging of the response of fractures to ground water salinity change, *Ground Water*, **35(3)**, 436-442.

Slater, L., M. D. Zaidman, A. M. Binley and L. J. West, 1997b, Electrical imaging of tracer migration in unsaturated East Yorkshire Chalk, *Hydrology and Earth System Sciences,* **Vol. 1(2),** 291-302.

Slater, L., D. Brown and A. Binley, 1996, Determination of hydraulically conductive pathways in fractured limestone using cross-borehole electrical resistivity tomography, *European Journal of Environmental and Engineering Geophysics*, Vol. 1 (1), p35-52.

Smith, N. C., and Vozoff, K., 1984, Two-dimensional DC resistivity inversion for dipole-dipole data, *IEEE Trans. Geoscience Rem. Sens.*, **GE-22**, 21-28.

Snyder, D. D., 1976, A method for modeling the resistivity and IP response of two-dimensional bodies, *Geophysics*, **41**, 997-1015.

Spies, B. R. and Ellis, R. G., 1995, Cross-borehole resistivity tomography of a pilot-scale, in-situ vitrification test: *Geophysics*, **60**, 886-898.

Spitzer, K., 1995, A 3-D finite-difference algorithm for DC resistivity modeling using conjugate gradient methods, *Geophys. J. Int.*, **123**, 903-914.

Spitzer, K. and Kumpel, H. -J., 1997, 3D FD resistivity modelling and sensitivity analyses applied to a highly resistive phonolitic body: *Geophys. Prosp.*, **45**, 963-982.

Stewart, D. I., West, L. J., Johnston, S. R. and Binley, A. M., 1997, Electrokinetic transport in natural soil cores, In Eds. Gourmans, J. J. J. M., Senden, G. J. and van der Sloot, H. A.: Waste Materials in Construction. *Studies in Environmental Science* **71**, 689-698.

Telford, W. M., L. P. Geldart, and R. E. Sheriff, 1990, Applied Geophysics (second edition): Cambridge University Press, Cambridge, 522 pp.

Topfer, K. D., 1972, Schlumberger measurements over undulating structures (model structures), *Geoexploration* **10**, 41-51.

Urish, D. W., 1983, The practical application of surface electrical resistivity to detect groundwater pollution, *Groundwater*, **Vol. 21**, p. 144-152

West, L. J., Stewart, D. I., Binley, A. M. and Shaw, B., 1997, Resistivity imaging of electrokinetic transport in soil, Geoenvironmental Engineering (Proceedings of International Conference on Geoenvironmental Engineering, held in Cardiff, September, 1997), Thomas Telford, 565-574.

White, P. A., 1994, Electrode arrays for measuring groundwater flow direction and velocity : *Geophysics*, **59**, 192-201. (* Erratum in GEO-59-7-1172.)

Worthington, M. H., 1984, An introduction to geophysical tomography: *First Break,* **02**, no. 11, 20-27.

Xu, S. Z., Gao, Z. C., and Zhao, S. K., 1988, An integral formulation for three-dimensional terrain modeling for resistivity surveys, *Geophysics*, **53**, 546-552.

Yang, C.-H., Tong, L. T. and Jeng, L. -W., 1994, Locating groundwater at selected sites by geoelectric methods, 64th Ann. Internat. Mtg. Soc. of Expl. Geophys., 652-654.

Yang, C.-H. and Lee, W. -F., 1998, Using resistivity sounding and geostatistics to aid in hydrogeological studies in the Choshuichi alluvial fan, Taiwan, 68th Ann. Internat. Mtg: Soc. of Expl. Geophys., 832-835.

Yi, M. -J., Kim, J. -H., Chung, S. -H. and Cho, I. -K., 1997, The borehole effect in imaging the Earth using resistivity tomography, 59th Mtg. Eur. Assn. Geosci. Eng., Session:P079.P079.

Zhao, S., and Yedlin, M., 1996, Some refinements on the finite-difference method for 3-D dc resistivity modeling, *Geophysics*, **61**, 1301-1307.

Zhou, B., Greenhalgh, S., and Sinadinovski, C., 1992, Iterative algorithm for the damped minimum norm, least squares and constrained problem in seismic tomography, *Exploration Geophysics*, **23**, 497-505.

Zhou, B., and Greenhalgh, S., 1995, A fast approach to Fréchet derivative computation for resistivity imaging with different electrode arrays, *Geotomography* Vol.III *Fracture Imaging,* Society of Exploration Geophysicists of Japan, 252-264.

Zhou, B., and Greenhalgh, S.A., 1997, A Synthetic study on crosshole resistivity imaging with different electrode arrays, *Exploration Geophysics*, **28**, 1-5.

Zhou, B., 1998, Crosshole resistivity and acoustic velocity imaging: 2.5D Helmholtz equation modelling and inversion, PhD thesis, The University of Adelaide.

Zhou, B., and Greenhalgh, S.A., 1998a, Composite boundary-valued solution of 2.5-D Green's function for arbitrary acoustic media, *Geophysics*, **63**, 1813-1823.

Zhou, B., and Greenhalgh, S.A., 1998b, A damping method for 2.5-D Green's function for arbitrary acoustic media, *Geophys. J. Int.*, **133**, 111-120.

Zhou, B., and Greenhalgh, S.A., 1998c, Crosshole acoustic velocity imaging with full-waveform spectral data: 2.5-D numerical simulations, *Exploration Geophysics*, **29**, 680-684.

Zhou, B., and Greenhalgh, S.A., 1999, Explicit expressions and numerical calculations for the Frechet and second derivatives in 2.5-D Helmholtz equation inversion, *Geophysical Prospecting*, **47**, 443-468.

Zhou, B. and Greenhalgh, S. A., 2000, Cross-hole resistivity tomography using different electrode configurations: *Geophys. Prosp.*, **48**, 887-912.

Zhou, B., and Greenhalgh, S.A., 2001, Finite element three-dimensional direct current resistivity modelling: accuracy and efficiency consideration, *Geophys. J. Int.,* **145**, 676-688.

Zhou, B., and Greenhalgh, S.A., 2002, A rapid 2D/3D crosshole resistivity imaging using analytic sensitivity function, *Geophysics,* **67**, p755-765.

Zimmer, U., 1999, Resistivity inversion in the presence of water saturated fractures, 61st Mtg. Eur. Assn. Geosci. Eng., Session:2014.